Self-Assembly of Multiple Soft Matter Systems

By

Beatriz Ioatzin Ríos de Anda

H.H. Wills Physics Laboratory
University of Bristol

A dissertation submitted to the University of Bristol in accordance with the requirements of the degree of Doctor of Philosophy in the Faculty of Physics.

September 2018

Word count: 41138

Abstract

Self-assembly is an exciting process to be exploited for the fabrication of hierarchical sophisticated functional materials with countless technological and medical applications. However, the lack of full understanding of the mechanisms and conditions that yield these structures, has limited its broad use. In this work, we focus on the study of a variety of self-assembling systems with different interactions between the components, along with their final architectures, as an effort to further comprehend the actual self-building process.

The first system consists of a binary mixture of hard spheres with a size ratio of 0.39. This mixture was investigated experimentally through particle-resolved studies. Complementary computational work provided insights into the dynamics of the system. Non-equilibrium interstitial solid solutions in coexistence with a fluid phase were found for both experiments and simulations. Here, the large particles form a close-packed mixture of fcc and hcp lattices, whereas the small ones occupy randomly some of the available octahedral sites of the crystalline phase. Although, these are the predicted stable configurations, the composition analysis showed a mismatch between these results and the predictions at equilibrium. This is likely a consequence to poor solubility of the small componentss in the close-packed ordered structure. Thus, our interstitial solid solutions remain long-lived and out-of-equilibrium.

The second system is composed by one-component particles with long Debye screening lengths, that form crystals at packing fractions as low as ϕ = 0.015. The Yukawa theory was used to study the phase behaviour of the system. Good agreement was found for the prediction of fluid and solid phases for concentrations ϕ < 0.015: the freezing point and bcc configuration of the solid phases match the model predictions. However, for higher packing fractions, the expected fcc lattice was not present, but a persistent bcc crystal was found. This could be due to lack of system equilibration and the influence of the sample square confinement.

A mixture of fluorescent proteins with short-range attractions constitutes the third system. This was used to produce bi-continuous gels with distinctive protein domains through salt addition. Several strategies along with protein surface modification were followed. Due to complex protein interactions, the target structures were successfully produced only when one gel was formed before the other. Additionally, control over the coverage of the original gel was also achieved. To our knowledge, this is the first realisation of these bi-continuous gel structures where the proteins retain their functional configuration.

Finally, core shell fluorescent silica magnetic nanoparticles were developed to constitute a magnetic responsive component of a binary system, where the other species are bare silica particles. The aim was to deposit iron oxide nanoparticles on the surface of fluorescent silica spheres and coat them with a silica shell. Although the decoration of the core with magnetic nanoparticles was successful, further attempts to coat them with a silica shell to provide stabilisation only produced aggregates. However, the dynamics of the clusters were effectively altered using an external magnetic field, showing the potential of these particles for further studies.

Al dragón, no temas
se lo vence con paciencia
la paciencia de los árboles bajo la tormenta.

–Moisés Villaseńor

Caminante, son tus huellas
el camino y nada más;
caminante, no hay camino,
se hace camino al andar.

–Antonio Machado

Por y para mamá, papá, Agus, Ponis y mi Churry,
quienes me inspiraron, apoyaron
y caminaron conmigo,
continuamente, constantemente,
invariablemente. Siempre.

Con mi más profundo amor, gracias.

Acknowledgements

Being a Ph.D. student in Bristol was a splendid and challenging experience. Throughout my work, many people were involved directly or indirectly in shaping my development as a scientist, it would have been impossible for me to go through it without them. Here is a small tribute to these amazing personalities.

First and foremost, I would like to express my deepest gratitude to my supervisor Paddy Royall for giving me the great opportunity and resources to develop my skills. His expertise, hard work, generous guidance, understanding, patience and support made this work possible. It has been a great pleasure to work with him, *he knows so much about these things*.

I would like to express my sincere gratitude to all the different groups I had the invaluable opportunity to work with. In particular, I would like to thank Richard Shear for the collaboration built regarding the crystallisation of binary mixtures of hard spheres. Also, I would like to thank Steve Whitelam and Jeff Urban at the Molecular Foundry, University of Berkeley and their correspondent group members for allowing me to work with them. In particular, many thanks to Jason Forster and Alyssa Brand for their invaluable help in the synthesis of iron oxide nanoparticles. Finally, my gratitude extends to Ross Anderson, along with members of his group, specially to Angélique Coutable for all her immeasurable help with the expression and manipulation of the proteins.

Additionally, I would like to thank Jeroen van Duijneveldt for providing advice, chemicals and letting me use equipment from his lab. Also, many thanks to John Russo and Brian Vincent who were always willing to provide helpful advice during my project. My deepest gratitude goes to Germinal Magro who kindly helped with the vast number of chemical procedures I was always trying. I acknowledge Jon Jones and Jean-Charles Eloi and the Electron Microscopy Unit for training and access to the SEM and TEM equipments.

I am highly indebted to all my past and present group mates who I am very proud to call *friends*. Thank you all for your wonderful and kind assistance, help and suggestions throughout the project. It has been a great honour to share G39, the labs, the going-outs and group meetings with you. Max, Azaima, Rattachai, Jun, Francesco, Josh, Nick, Peter, James, Abraham, Julien, Kate and Chris, you made it all worth it and I will keep all our memories fondly.

I am grateful beyond measure to all my friends and family here and in Mexico. Thank you for all your love, help and encouragement through these years. Thank you for always being a source for inspiration and for never letting me give up. In particular, thanks to my beloved friends Andrea, Andrea, Liliana, Danni, May, Gerardo, Karina and Dan. Special thanks to my family in the UK: Liz, David, Mat, Bob, Esmee, Ian, Steph, Andrew and Julien. Thank you for ever being so kind, for caring so much and for being a vital support.

Finalmente, agradezco profundamente a Conacyt por el apoyo económico y la asistencia. Estoy en deuda con todos los mexicanos. Espero éste y mi futuro desempeño esté a la altura de la inmensa oportunidad que me han obsequiado.

Author's declaration

I declare that the work in this dissertation was carried out in accordance with the requirements of the University's Regulations and Code of Practice for Research Degree Programmes and that it has not been submitted for any other academic award. Except where indicated by specific reference in the text, the work is the candidate's own work. Work done in collaboration with, or with the assistance of, others, is indicated as such. Any views expressed in the dissertation are those of the author.

SIGNED: ..... DATE: .....

Publications

Ioatzin Ríos de Anda, Antonia Statt, Francesco Turci, and C. Patrick Royall. Low-Density Crystals in Charged Colloids: Comparison with Yukawa Theory. *Contributions to Plasma Physics*. 55:172 (2015)

Ioatzin Ríos de Anda, Francesco Turci, Richard P. Sear and C. Patrick Royall. Long-lived non-equilibrium interstitial solid solutions in binary mixtures. *The Journal of Chemical Physics*. 147: 124504 (2017)

Table of Contents

Page

List of Tables

List of Figures

Figure **Page**

CHAPTER 1

INTRODUCTION

1.1 Self-Assembly

Self-assembly is the spontaneous guided organisation of disordered pre-existing materials in hierarchically ordered or functional systems. It is reversible and can be triggered and controlled through direct specific component interactions and/or indirect interactions from their environments [1, 2, 3]. This process can be found throughout nature, from the molecular to the planetary scale [4]. The assemblies found in nature are complex, sophisticated, highly efficient and specific. Moreover, they exhibit self-repair, self-replication and adaptability processes [5]. They are therefore an important source of inspiration for the architecture of novel materials with promising functionalities in the nano and micron scale.

Tibbits has proposed that in order to achieve the construction of such materials, four requirements need to be fulfilled: 1) the system constituents need to be simple materials, 2) with programmable parts, where 3) a force or energy can be easily applied for self-assembly activation and that 4) the system can correct errors or avoid redundancy [5].

The building blocks used in nature start with atoms and molecules, where we still do not have the means or understanding for fine manipulation. However, an attractive alternative are *colloidal systems*, where species with sizes in the nano and micron-scale are dispersed in a medium. This size range endows them two main advantages: on the one hand, they are large enough to be effectively observed using microscopy techniques; their assembly processes can be followed –and potentially controlled –in real space and time; and characterisation of their final architectures is possible [4, 6]. On the other hand, colloidal species are still small enough to experience Brownian motion, typical of atomic and molecular systems, thus they might be considered their analogs [6]. Due to the latter characteristic, colloidal dispersions can also be employed as model systems to study the fundamental phenomena involved in the self-assembly

process [4].

Colloidal particles typically interact with each other through weak interactions including: van der Waals attractions, electrostatic interactions, hydrogen bonding, hydrophilic/hydro-phobic interactions or ion-paring interactions, where the bond energies range from 0.4 to ~8 k_BT [4, 6, 7]. Thus, thermal fluctuations of such energy values are enough to drive the activation of these interactions and trigger particle organisation. The individual properties of the components and the medium will determine the type of interactions. Thus, particle design is essential to yield the desired structures [4]. Additionally, a new type of self-driven particles has been developed recently. These particles do not rely on thermal fluctuations and instead intrinsic energy sources are the driving motion force [6].

These properties of colloidal systems satisfy the above requirements proposed by Tibbits [5]. Therefore colloidal species stand out as promising building blocks for a myriad of functional devices with novel physical, chemical and biological properties. Their applications extend from robotics, optical, photonics, electronics, magnetic, energy storage, to enzymatic, ion transportation, antimicrobial, drug and gene transportation, or cancer treatments [4]. Moreover, the use of self-assembly as a tool for yielding these materials has several advantages that include high quality through low cost and scalable processes with high reproducibility [8].

Research dedicated to the design as well as the cheap and scalable production of functional colloidal particles is fast growing. An impressive variety of particles with different sizes, shapes, interactions and functions is now available. Additionally, a large number of self-assembly methods have also been described [7, 9]. Both scientific advances are focused on programmed self-assembly, where the components of the system carry information or characteristics to yield the desired architecture or purpose [1].

However, we still lack a full comprehension of the mechanisms involved in self-building as well as the tools for understanding and finely controlling these processes [3].

In the upcoming chapters, different colloidal systems with a variety of interactions are studied in an effort to further understand their self-built process and characterise their final structures. In addition, we study experimentally a theoretical new route for the self-assembly of out-of-equilibrium systems, where the mechanism and final assemblies resemble nature's far from equilibrium processes.

1.2 Thesis Structure and Outline

This thesis is organised as follows: in Chapter 2 we review the theoretical background of colloidal suspensions and their applications as analogs of atomic and molecular systems to study self-assembly. It also includes the colloidal interactions and colloidal systems relevant for this work. We introduce in Chapter 3 all the experimental and simulation techniques used throughout this work. In the following chapters we present the results of the different colloidal systems

studied. We have organised these systems according to their complexity. In Chapter 4 we study the interstitial solid solutions formed by a binary mixture with hard spheres interactions. We continue with the study the crystal formation by a mono-component system with long-range repulsion interactions in chapter 5. In Chapters 6 and 7 we discuss the realisation of *critical soft matter* using two different systems. In Chapter 6 the binary system consists of fluorescent proteins with short-range attractions, whereas in Chapter 7 we focus on the synthesis of core shell fluorescent silica magnetic nanoparticles. Finally, in Chapter 8 we recapitulate the main results and conclusions of each individual system studied, along with their outlook.

CHAPTER 2

COLLOIDAL DISPERSIONS

2.1 Introduction

Colloidal dispersions are heterogenous systems with a dispersed phase that consists of solid particles, liquid droplets or gas bubbles, immersed in a continuum dispersing medium, which can be a solid, a liquid, a plasma or a gas [10]. They are ubiquitous systems ranging from paints, inks, emulsions, pharmaceutical products and biological systems [11, 10]. The term 'colloid' derives from the Greek word for *glue-like* coined by Thomas Graham in 1861, when he observed that particles in an aqueous solution did not pass through a membrane and did not fully sediment.

The sizes of the dispersed component range between a few nanometers to several micrometers in any of their dimensions. They have acquired interest as they can serve as model systems to atomic and molecular self-assembly phenomena, i.e., they can form fluid, crystalline and glassy phases. Moreover, since they present larger dimensions and larger time scales than molecules and atoms, their phenomenology is accessible to investigate experimentally, that is to say, they can be directly visualised through microscopy techniques and tracked through image processing. Furthermore, the interactions, sizes, composition and shapes of colloidal particles can be easily designed, modified and manipulated, in order to mimic the ones from atomic and molecular systems. In addition, with the new synthesis and manipulation techniques that have been developed in the last years, the application fields of colloidal systems have vastly diversified, ranging from electronics, electrophoretic displays, solar panels, photonic crystals to drug and gene therapy delivery or tissue scaffolding [12, 13, 14, 15, 16].

The similarity between phase transitions of colloidal dispersions and those of atomic or molecular systems is a result of one of the principal characteristics of the former: their dynamics. Due to thermal motion, the molecules of the solvent continuously collide with the dispersed colloidal particles. Since the sizes of the colloidal particles are relatively small, they are affected

by these collisions which results in a random movement of the particles, known as *Brownian motion*. This type of motion was first described by Robert Brown, who observed microscopically the random movement of pollen particles in water in 1827 [13, 14, 15, 16]. The conclusion that such phenomena was a result of thermal motion and its mathematical explanation were described by Albert Einstein and William Sutherland [13] almost a century later.

In colloidal dispersions, the suspended species interact with the solvent molecules in two ways: the aforementioned solvent-particle collisions and the frictional forces that arise as the particles move in the fluid. The former produces the random displacement of the particles, whereas the latter causes a drag force opposite to the particles' motion. This drag force can be expressed through the dimensionless Reynolds number as follows:

$$Re = \frac{\rho v \sigma}{2\eta} \tag{2.1}$$

thus this magnitude depends on the diameter of the colloidal species, σ, their velocities, v, as well as on the density, ρ, and viscosity, η, of the dispersion medium. Additionally, from the equation we can see that the numerator is related to the inertial forces (through the density), in contrast with the denominator, which is related to viscosity forces. So, through the Reynolds number, one can characterise the nature of the dynamics of the system depending on the contributions of each of these forces. Colloidal dispersions typically present low Re values, which indicate that viscosity forces dominate in these systems. In this regime, the drag force, F_S, is given by Stoke's Law:

$$F_S = 3\pi\eta\sigma v \tag{2.2}$$

On the other hand, as stated before, due to the bombarding of solvent molecules on the colloids, they experience a random motion which can be considered as a random walk, where the steps are equal and uncorrelated. If we consider Brownian motion (in a whole) as a random walk, then the time average and the mean displacement are both zero. However, the mean square displacement in a random walk is proportional to the number of steps taken and hence, to time following:

$$\langle (\Delta r(t))^2 \rangle = \alpha t \tag{2.3}$$

Both Einstein and Sutherland determined independently the value of the constant of proportionality α by solving the equation of motion for a colloidal sphere:

$$m\frac{dv}{dt} = \mathscr{F}(t) \tag{2.4}$$

where *m* is the mass of the particle and $\mathscr{F}(t)$ the force acting on the particle as a result of the impacts from the solvent molecules. $\mathscr{F}(t)$ can be written as the sum of two parts. The first one corresponds to the viscous drag *-v/*ϵ, where ϵ is the *mobility* of the system or the drift acquired by the particle through an 'external' force, with ϵ is given following the Stoke's Law, $\epsilon = 1/(3\pi\eta\sigma)$. The second part corresponds to a 'rapidly fluctuating' part *F(t)*. Thus, we can rewrite equation 2.4 as:

$$m\frac{dv}{dt} + \frac{v}{\epsilon} = F(t) \tag{2.5}$$

The final result is that the mean squared displacement of a colloidal particle in 3d is diffusive and can be obtained through:

$$\langle(\Delta r(t))^2\rangle = 6Dt \tag{2.6}$$

where, *D* is the Stokes-Einstein diffusion constant given by:

$$D = \frac{k_B T}{3\pi\eta\sigma} \tag{2.7}$$

here k_B is the Botzmann constant and *T* is the absolute temperature. This magnitude then characterises the mobility of colloidal species: larger constant values correspond to faster particles' diffusion. Finally, through the numerator we can see the dependence of the motion on the atomic properties of matter: $k_\mathrm{B} = R/N_A$, where *R* is the gas constant and N_A the Avogadro's number.

Colloidal suspensions are also subjected to gravity which produces sedimentation. As such, in addition to their Brownian motion, another parameter that differentiates a colloidal suspension from other type of dispersions is the *Péclet number*. This is a dimensionless magnitude that relates the sedimentation time of a colloidal particle with the time it takes for it to diffuse its own diameter, or Brownian time:

$$P\acute{e} = \frac{\tau_{sed}}{\tau_B} \tag{2.8}$$

here $\tau_{sed} = \sigma/v_{sed}$, where v_{sed} is the sedimentation velocity and is in turn given by $v_{sed} = \Delta\rho g/3\pi\eta\sigma_H$, with σ_H describing the hydrodynamic radius, i.e., the apparent size of the hydrated/solvated particle. On the other hand, $\tau_B = \sigma^3\pi\eta/8k_BT$. Thus, values of Pé < 1 indicate that Brownian dynamics dominate the system and hence, the dispersion csan be classified as colloidal. Conversely, for Pé > 10 gravity dominates the dynamics of the particles and thus the suspension is instead classified as granular, where particles are not subjected to thermal motion, which in turn changes the behaviour of the suspension [15, 17].

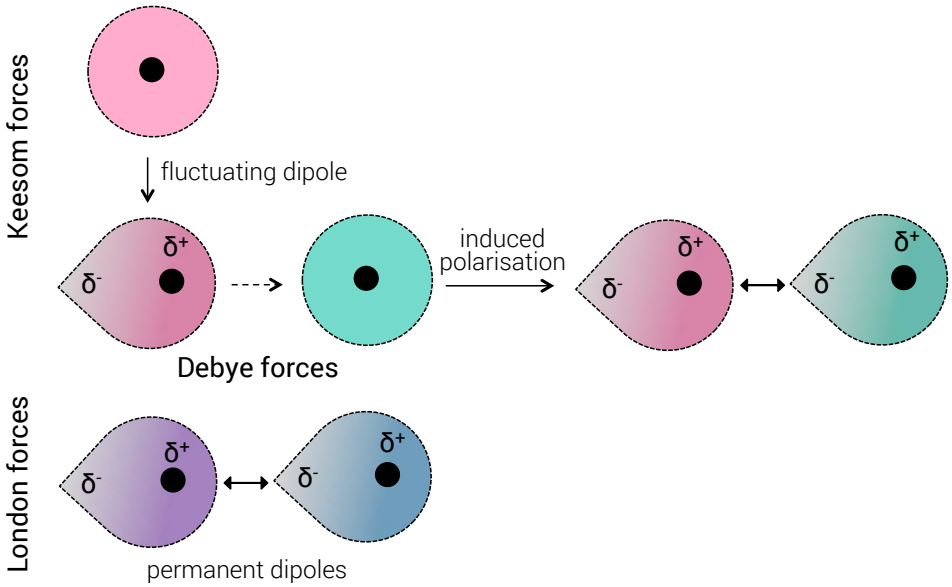

Figure 2.1: Classification of the attractive van der Waals forces. Particles in a colloidal dispersion are attracted to each other due to temporary or permanent dipole moments (δ). See text for details.

2.2 Colloidal Interactions

During Brownian motion, colloidal particles will also collide with each other. According to the combination of attractive or repulsive forces involved, the system can form non-dispersible aggregates or stable dispersions. As discussed earlier, one of the main advantages of colloidal systems is the feasibility of controlling these interactions to yield the desired behaviour. In this section we will limit the description of the interactions relevant for this work, which include van der Waals attractions, electrostatic repulsions, hard sphere behaviour, long-range attractions and the type and range of interactions required to yield critical soft matter.

2.2.1 Van der Waals Attraction Forces

For the majority of colloidal suspensions, the attraction and further aggregation of the particles is a consequence of van der Waals forces. Here, molecules present temporary or permanent dipole moments which generate electric fields that polarise neighbouring molecules and thus, induce a correlated dipole moment. The interaction between these dipole moments is attractive. According to the molecules involved in the interaction, van der Waals forces can be categorised in Keesom forces, Debye forces and London (dispersion) forces, as shown in Fig. 2.9. In the first one, neutral molecules become polarised due to electron fluctuations within the molecules, which in turn will induce the polarisation of neighbouring neutral molecules. In Debye forces, molecules with permanent dipole polarise nearby neutral molecules. Finally, London forces take place between molecules with permanent dipoles (Fig. 2.9). van der Waals interactions are short

ranged and vary with the molecules separation, *r*, to the negative sixth power [18, 16, 19, 15]. van der Waals forces are not restricted to molecular species, and are also relevant for macroscopic systems. The pair potential for these interactions between spherical colloids can be found by integrating the atomic pair contributions over the volumes of the two species, giving:

$$U_{vdW}(r) = -\frac{A_H}{12}\left[\frac{\sigma^2}{r^2-\sigma^2} + \frac{\sigma^2}{r^2} + 2ln\left(\frac{r^2-\sigma^2}{r^2}\right)\right] \tag{2.9}$$

where σ is the particle size and A_H the Hamaker constant [18, 10, 16, 15]. The latter is a material property [14] and can be approximately obtained using Lifshitz's approach, where the forces between large bodies are treated as continuous media:

$$A_{123} = \frac{3}{4}k_B T\left(\frac{\epsilon_1-\epsilon_3}{\epsilon_1+\epsilon_3}\right)\left(\frac{\epsilon_2-\epsilon_3}{\epsilon_2+\epsilon_3}\right) + \frac{3h\nu}{8\sqrt{2}}\frac{(n_1^2-n_3^2)(n_2^2-n_3^2)}{\sqrt{(n_1^2+n_3^2)(n_2^2+n_3^2)}\left(\sqrt{(n_1^2+n_3^2)}+\sqrt{(n_2^2+n_3^2)}\right)} \tag{2.10}$$

where A_{123} refers to the Hamaker combination of two bodies (1,2) interacting with their medium (3), k_B is the Boltzmann constant, T the absolute temperature, h is the Planck constant, ν the frequency of fluctuation, and n_i and ϵ_i are the refractive index and the dielectric constant of each component, respectively [18].

The relevant result from this equation is that if the difference in refractive index or dielectric constant is close to zero, the Hamaker constant can be dramatically reduced and hence van der Waals forces can be neglected. Thanks to such dependence of the Hamaker constant on these characteristics of the material, the attraction of colloidal systems can be effectively manipulated. Indeed, we will use refractive index matching between our colloidal species and their respective solvents to avoid these short range interactions in the systems studied herein and thus prevent aggregation.

However, refractive index matching is not always possible and since van der Waals forces arise from polarisability, they cannot be suppressed completely. Moreover, particle aggregates have a reduced surface area and thus a lower interfacial energy in comparison with the same 'free' species. Hence, the aggregated state is energetically favourable [16]. In order to avoid unstable samples and undesired particle aggregation, repulsive counteracting interactions need to be added to the systems. Two main approaches in this regard have been taken: charge and steric stabilisation.

2.2.2 Colloidal Particles Stabilisation

When colloidal particles are dispersed in a solution, they often acquire an electrostatic charge originated through ion dissociation from the particle surface. These charges have the same sign for the particles and thus they repel each other, inhibiting van der Waals attractions and stabilising the dispersion. On the other hand, spontaneous ion dissociation also occurs in the solvent.

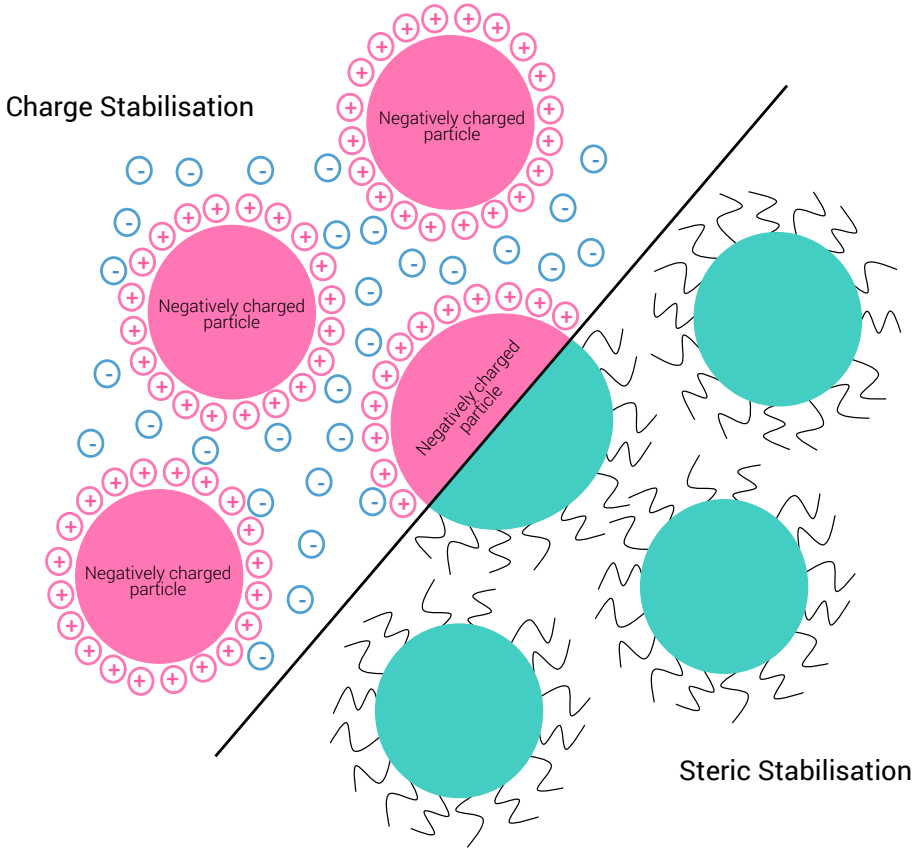

Figure 2.2: Colloidal Stabilisation. Left: charge stabilisation via co-ion adsorption and counter ion double layer. The pink particles are negatively charged. Right: steric stabilisation via adsorbed or chemically grafted polymer chains on the surface of the particles [11, 16, 15].

In the absence of colloidal particles, these ions are free to diffuse in the solution. However, when colloidal charged species are present, these ions might be affected by electrostatic forces, resulting in ion association on the surface of the particles. This then forms an ion cloud around the particles known as double layer, shown in Fig. 2.2 on the right panel. The same phenomenon occurs when salts are added to the solution.

When the ion cloud is missing, the charged colloids repel each other through Coulombic interactions. *Per contra*, when ions are present in the solution, they change the form of the interaction by screening the colloidal charge. The altered interaction can be described by solving the Debye-Hückel equation of Yukawa form [16]:

$$U_{Yukawa}(r) = \epsilon_{Yukawa} \frac{e^{-\kappa(r-\sigma)}}{r/\sigma} \tag{2.11}$$

where ϵ_{Yukawa} is the potential at contact given by:

$$\epsilon_{Yukawa} = \frac{Z^2}{\left(1+\frac{\kappa\sigma}{2}\right)^2}\frac{\lambda_B}{\sigma}k_BT \tag{2.12}$$

where Z is the colloid charge (evaluated in elementary charge units), σ is the particles' diameter, and κ is the inverse Debye screening length ($\kappa = \lambda_D^{-1}$) calculated through:

$$\kappa = \sqrt{4\pi\lambda_B\rho_{ion}}, \tag{2.13}$$

with ρ_{ion} being the number density of monovalent ions. Thus, the Debye screening length defines the thickness of the surrounding double layer of counter ions. Finally the Bjerrum length represents the distance at which the interaction energy between two electronic charges equals k_BT, and can be obtained through

$$\lambda_B = \frac{e^2}{4\pi\epsilon_0\epsilon_r} \tag{2.14}$$

where e is the electronic charge, ϵ_0 the permittivity of free space, and ϵ_r the dielectric constant [20, 21, 16, 15].

However, these electrostatic repulsions, while desired to avoid aggregation, might also create long-range repulsions between the particles. Nevertheless, from equation 2.13 we can see that by changing the ion concentration in the solvent, ρ_{ion}, usually through salt addition, we can tune the magnitude of the Debye length and thus the electrostatic interactions between the particles. Indeed, in Chapter 4 we saturate the salt concentration in our system in order to reduce the Debye length so that electrostatic repulsions only occur at very short range, which allows the system to behave approximately like hard spheres.

A second option to avoid particle aggregation is steric stabilisation, where short polymer chains are chemically grafted or adsorbed on the surface of the particles, as shown in Fig. 2.2 in turquoise on the left panel [16, 15]. When dispersed in an good solvent, the grafted polymer chains extend away from the colloidal surface in a stretched conformation. Now, when two coated particles come close, their polymer chains either interdigitate with each other or undergo some compression. In both cases, the possible polymer conformations within the interaction zone will be restricted as the volume available for the polymer chains when overlapped or compressed is reduced. Such loss of conformational freedom causes a reduction in the entropy of the polymer chains, which in turn increases the free energy. The way the system minimises this free energy is by excluding the overlapping polymer regions. Thus, the colloidal repulsion is entropically driven and, if larger than the van der Waals forces, the attraction can be overcome. The range of the repulsion and hence the particle interactions, can be manipulated through the polymer length [11, 16, 15].

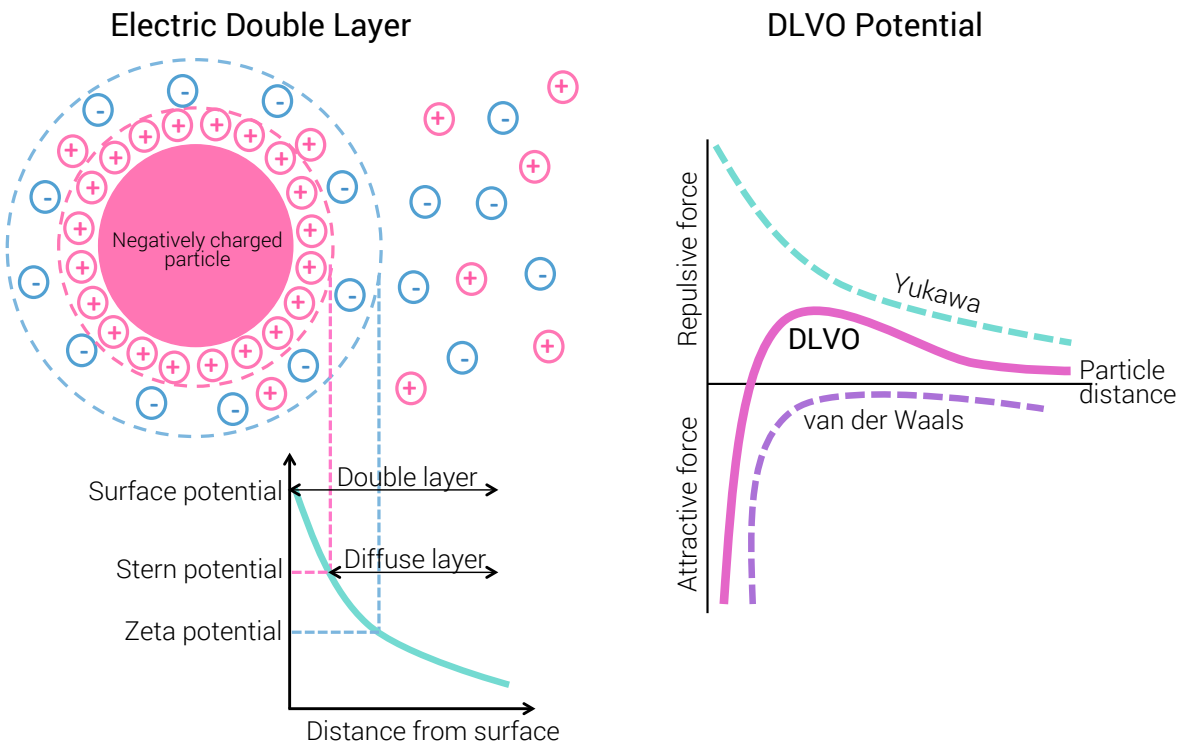

Figure 2.3: Electric Double Layer and the DLVO Potential. Left: schematic representation of the electric double layer formed by counter (pink) and co-ions (blue). The pink particles are negatively charged. Right: schematic diagram of the Derjaguin-Landau-Verwey-Overbeek interaction potential, shown as the sum of the Yukawa (turquoise) and van der Waals (violet) potentials [11, 16, 15].

2.2.3 Electrostatic Interactions

As already discussed, suspended colloidal particles may acquire a surface charge originating from ion adsorption on the surface of the particles from ionic species in the solvent. Ions with the same charge as the colloidal particle (co-ions) are depleted from the surface and/or a layer of counter-ions (with opposite charge), also coming from the solvent, accumulate around the colloidal particle surface, creating a so-called electrical double layer, as shown in Fig. 2.3 right panel. Close to the particle, the concentration of counter-ions is large, however, said ions diffuse as they extend away from the particle [10], as shown in Fig. 2.3 right panel. Here, the first layer formed by the counter-ions is known as the Stern potential, whereas the layer formed by co-ions is known as the Zeta potential (Fig. 2.3, right). This distribution is important as it affects the interaction of the components in the suspension. An expression that allows us to describe such interactions is the Poisson-Boltzmann (PB) equation, which consists of two components: first, Boltzmann distributions govern the ion concentration and diffusion. Second, the Poisson equation relates the variation in electrostatic potential to the charge density. Thus, from the PB equation an expression to describe the electrostatic potential interaction to characterise the overlap of the two double layers can be derived. Indeed, the interactions between charged

particles are successfully described by the Derjaguin-Landau-Verwey-Overbeek (DLVO) theory [21, 16, 15, 20, 10], derived from the linear part of the aforementioned PB equation. Here, the interaction potential results from a combination of the previously defined van der Waals attraction forces, the screened Coulomb repulsion, and thus is given by

$$U_{DLVO}(r) = U_{vdW}(r) + U_{Yukawa}(r) \tag{2.15}$$

where U_{vdW}(r) and U_{Yukawa}(r) are defined above in equations 2.1 and 2.11, respectively [21, 15, 16, 20]. A typical DLVO potential is illustrated as the solid violet line in Fig. 2.3 right panel, where the contributions from each attractive and repulsive potential are also shown in dashed lines.

Phase diagrams of charged repulsive systems have been obtained in experiments and simulations. Here the interactions are dependent on both the concentration of particles and the magnitude of the screening length, which can be altered through salt addition. In general, crystallisation occurs at lower packing fractions (ϕ) than the corresponding volume fraction of hard spheres, which will be reviewed in the following section. Indeed, as discussed in Chapter 5, such packing fractions can be as low as ϕ = 0.015 [22]. Typically, for small screening lengths, a fluid is stable at low ϕ followed by face-centered cubic (fcc) crystals as the concentration increases. For larger screening lengths, however, a body-centered-cubic (bcc) stable crystal preludes the fcc configuration [10].

2.2.4 Hard Sphere Interactions

The simplest pair interaction that uncharged colloidal particles can experience is of hard spheres. Here, the particles only interact at contact, where the potential is infinite as the species cannot overlap. The potential is zero for any other distances larger than the particle diameter, i.e., there is no attraction between the particles, as shown in Fig. 2.4 left panel [15, 16, 10]. As the concentration of the particles in the system increases, the system configuration transitions from disordered to dense-fluid-like to crystalline arrangement. Although there is a loss in configurational entropy as the system gets more organised, it is compensated by the increase of the local entropy, since the particles have larger local volumes to explore in an ordered lattice. Thus, it is energetically favourable for the system to crystallise, with entropy as the driving force [23, 15, 16, 14]. This transition from a disordered to an organised arrangement is analogous to a liquid crystal transition [14]. The relevant parameter for this type of interaction is the concentration, or packing fraction, ϕ, of the system, obtained by calculating the volume space occupied by the particles as follows:

$$\phi = \frac{\pi\sigma^3}{6}\frac{N}{V} \tag{2.16}$$

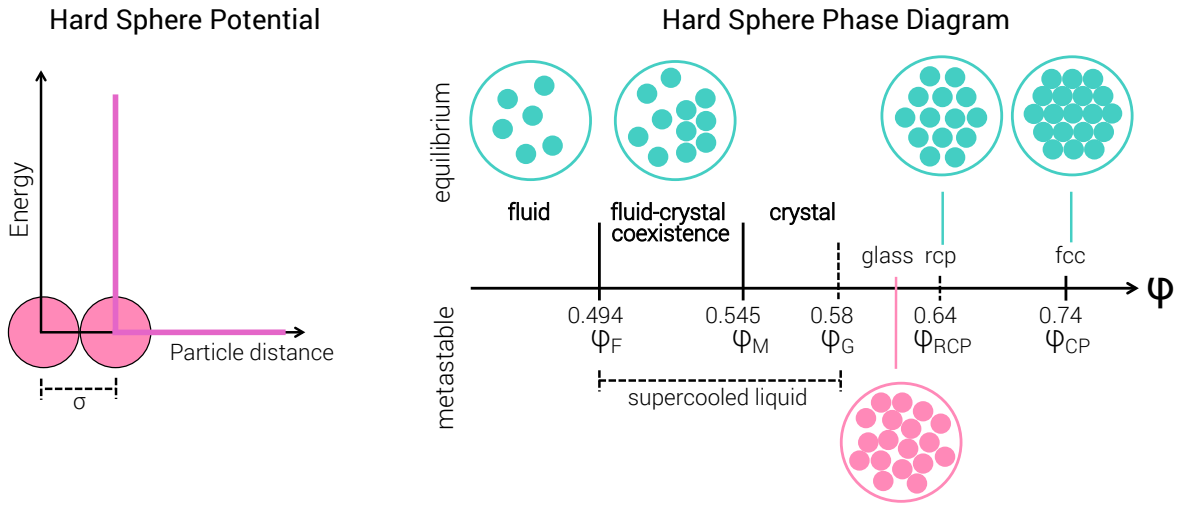

Figure 2.4: Hard spheres. Left panel: steep repulsive hard sphere potential interaction, where the no attraction is present and only infinite repulsion exists at contact (σ = particle diameter). Right: phase diagram of hard sphere particles as a function of volume fraction, ϕ. Equilibrium states are indicated in turquoise above the axis, whereas out-of-equilibrium states are shown below the axis and in pink. The freezing (ϕ_F), melting (ϕ_M), glass (ϕ_G), random close packing (ϕ_{RCP}) and close packing (ϕ_{CP}) volume fraction transitions are also indicated [16, 15].

where N is the number of particles and V the total volume of the system [16].

For ideal hard spheres, i.e., monodispersed particles, computer simulations predicted the different phases found as the packing fraction increases and they are illustrated in Fig. 2.4 right panel. The equilibrium configurations are shown in turquoise above the axis, where we can see that at low packing fractions, the system behaves as a fluid showing no long-range order. However, when the concentration reaches $0.494 < \phi < 0.545$, the system phase separates into a fluid at $\phi_F = 0.494$ and a crystal at $\phi_M = 0.545$, known as the freezing and melting volume fractions, respectively. Above ϕ_M the whole system is crystalline and further increase in the concentration only increases the density of the crystal. If the particles pack randomly as close as possible, then the maximum packing fraction achievable is $\phi_{RCP} = 0.64$ (random close packing). However, the maximum (most efficient) packing occurs at $\phi_{CP} = 0.74$, which corresponds to the close-packed crystalline volume fraction (see Fig. 2.4) [14, 15, 16, 24]. There are two types of close-packed crystalline structures that the system might acquire: face-centered cubic (fcc) and hexagonal close packed (hcp), with an energetic difference of 0.001 k_BT [14, 25, 26]. The structural difference between these phases is illustrated in Fig. 2.5. A first ordered layer is generated and there are two possible ways in which subsequent layers can follow: in fcc the layers have an *abcabc* stacking, whereas hcp layers have an *abab* sequence [14].

Additionally, metastable phases have also been predicted at $\sim \phi_F = 0.58$, which are known as colloidal glasses. Although the characteristics and properties of this phase are relevant, they are out of the scope of the present work.

Hard spheres were *nearly* realised experimentally by Pusey and van Megen in 1986 [27]. They

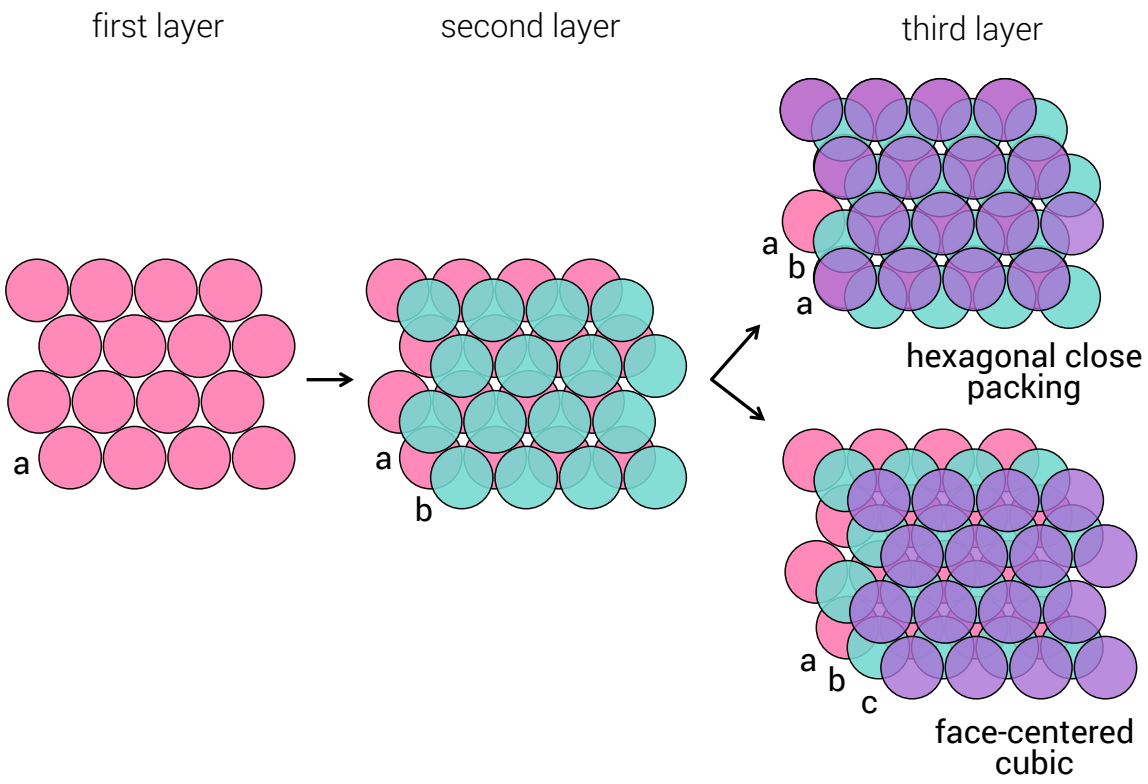

Figure 2.5: Face-centered cubic (fcc) and hexagonal close packed (hcp) configurations, where the difference between these is the stacking sequence. hcp first (a) and third layer (c) are aligned and the stacking cycles between the two equivalent shifted positions (abab). In fcc the third layer is no longer aligned with the fist and thus the structure contains three types of planes (abcabc) [14].

used sterically stabilised polymethylmethacrylate (PMMA) particles with poly-12-hydroxystearic acid. The particles had a 610 nm of diameter and were suspended in a refractive index matched decalin and carbon disulphide solution (2.66:1 volume ratio). Their system showed to crystallise nearly at the packing fractions mentioned above and displayed the correspondent phases. Moreover, they even observed a colloidal glass (long-lived amorphous structures) at the predicted particle concentration [27]. Thus, colloidal dispersions can be used as model system to study these phase transitions.

It is important to highlight that although experimental systems of hard sphere behave very closely to theoretical and computational predictions, large experimental errors are always present [16, 15]. . True monodispersed systems can not be produced through the currently available procedures and there is always some size distribution of the particles obtained. The way to characterise such distribution is by calculating the polydispersity as the ratio of the standard deviation and the mean of the particle sizes (often expressed as a percentage):

$$s = \frac{\sqrt{\langle \sigma^2 \rangle - \langle \sigma \rangle^2}}{\langle \sigma \rangle} \tag{2.17}$$

Both computational and experimental studies have shown changes in the melting and freezing packing fractions as the polydispersity increases. Furthermore, crystallisation does not occur when the system presents a polysdispersity above 0.06 in experimentally accessible timescales [23]. Indeed, highly polydispersed systems are popularly used to form and study glasses. On the other hand, "softness" in particle-particle interactions are inherent to experimental systems, due to finite compressibility of the polymer coatings or small charges and hence they will *always* be present [28, 27, 16, 15].

2.2.5 Binary Hard Spheres

Hard sphere multicomponent systems have also been described, with binary mixtures being the most studied. In these mixtures, the particles only differ on their sizes, with σ_{L} and σ_{S} for the larger and smaller diameter, respectively. From a theoretical point of view, binary hard spheres constitute the simplest model to study the self-assembly of mixtures, which include salts and metal alloys [29, 30]. Moreover, colloidal superlattices have promising applications as photonic crystals with potential optical properties [31, 32, 33].

Due to the size difference, binary hard spheres present a richer phase behaviour over their mono-component counterparts [30]. The force driving crystallisation is still the higher entropy of the crystalline phase at high densities in comparison with the fluid phase [32, 30]. Thus the richer assemblies formed arise from the size ratio of the components, γ ($\gamma = \sigma_{\mathrm{S}}/\sigma_{\mathrm{L}}$), their stoichiometry ($\mathrm{N}_S/\mathrm{N}_L$) and the total packing fraction of the system [31, 34].

Theoretical, computational and experimental work has been devoted to the study of the behaviour of these mixtures. Theory has proposed a variety of possible assemblies that can be formed according to γ and the packing fractions of each component [31, 24, 32, 26, 13, 35, 29, 30].

The main stable structures found in computer simulations at different γ and stoichiometries are illustrated in Fig. 2.6 [24, 26, 13, 32, 35, 29, 30]. Here, stable phases at moderate size differences (γ = 0.95-0.85) correspond to fcc solid solutions, where the crystalline order is composed by random distribution of large and small particles without leaving vacancies [29, 30]. On the other hand, for γ = 0.85-0.76, particle phase separation occurs and the crystalline structures found are fcc composed only by large or small particles ($\mathrm{fcc}_{\mathrm{L/S}}$). These are in coexistence with so-called Laves phases, which are analogues of $MgZn_2$, $MgCu_2$ and $MgNi_2$ salts [36, 32, 35, 30]. These three structures present the same maximum packing fraction (ϕ_{max}=0.710 at $\gamma\sim$ 0.816), and only differ on the free energies by around 10^{-3} k_BT per particle at ϕ=0.6 and γ = 0.82. $MgZn_2$ has the lowest free energy (7.436 k_BT), followed by $MgNi_2$ (7.438 k_BT) and $MgCu_2$ (7.439 k_BT) [32, 35, 30]. Although the maximum packing fraction of these structures is not larger than the correspondent of one-component systems, their higher symmetry in comparison with other better packed configurations, seems to be more favourable for stability [13, 32].

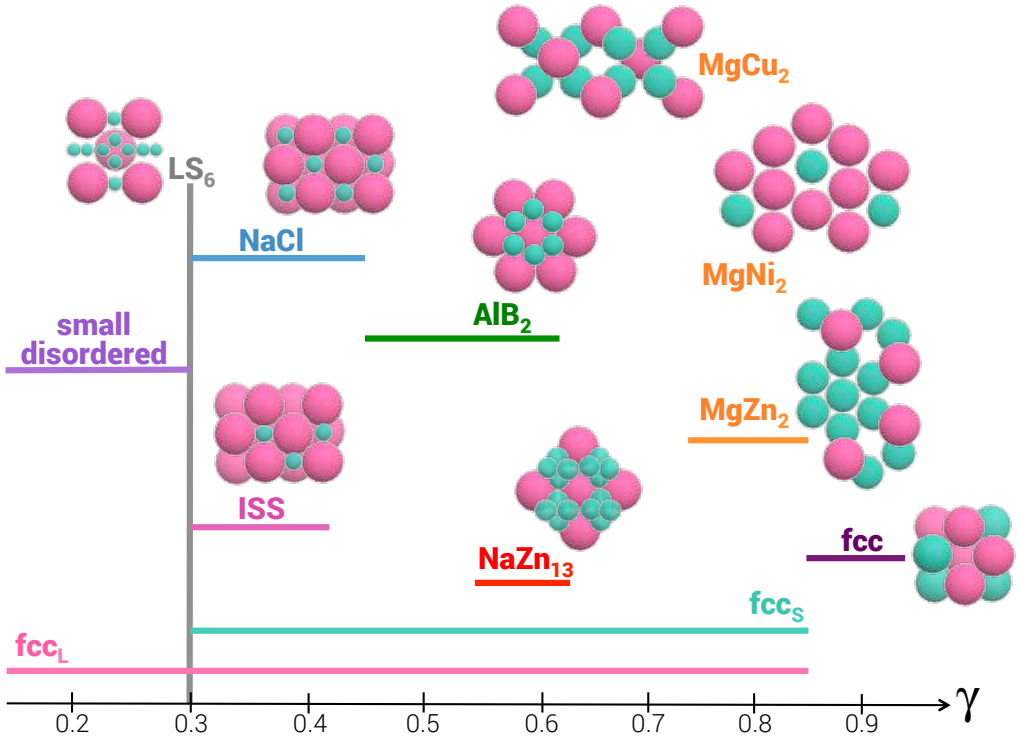

Figure 2.6: Illustrations of the variety of the main stable crystalline phases found computationally for binary mixtures according to their size ratio ($\gamma = \sigma_S/\sigma_{Ls}$) at different mixture stoichiometries [24, 26, 13, 32, 35, 29, 30]. fcc corresponds to a solid solution, where both components are randomly mixed without vacancies, whereas $fcc_{L/S}$ stand for fcc structures formed only by large (L) or small (S) particles. ISS correspond to interstitial solid solutions. See text for details.

At γ = 0.74, no Laves phases were found leaving only fcc_L and fcc_S crystals [32, 30]. At larger size discrepancies, $\gamma \sim$ 0.62, besides the fcc_L and fcc_S crystals an analogue structure to $NaZn_{13}$ appeared, with ϕ_{max}=0.738 at $\gamma \sim$ 0.558 [24]. In addition to these three structures, from $\gamma \sim$ 0.61-0.54 an AlB_2 crystal (ϕ_{max}=0.779 at $\gamma \sim$ 0.577) is also observed [36, 37, 24, 30].

However, when the small species are half the size of the large ones (γ = 0.5), $NaZn_{13}$ is no longer observed. At γ = 0.45 a NaCl-type structure appears. From γ = 0.42-0.4, fcc_L, fcc_S, NaCl and tunable interstitial solid solutions (ISS) are the stable configurations. In the latter, the smaller particles are located randomly within the interstitial sites of a fcc crystal formed solely by the large species, and are analogues of metal alloys. Moreover, the filling of the interstices can be modified from 0 (fcc_L) to 1 (NaCl configuration) [26, 13]. In addition to all these structures, at γ = 0.3 a structure with LS_6 configuration was observed. This configuration has no atomic prototype [30, 26, 13].

Finally, at very large size differences (γ = 0.2-0.033) only fcc_L with disordered small species were observed [38, 30].

In experiments NaCl, AlB_2, LS_3, $CaCu_5$, $MgZn_2$, and CsCl-type crystals have been obtained for charged [39] and DNA functionalised particles [33], as well as for solvent evaporation [40]

and for layer-by-layer deposition methods [34], amongst several others. Moreover, using combinations of semiconductor, metallic and magnetic nanoparticles, along with charge control over the particles and solvent evaporation, Shevchenko and coworkers found more than 10 different binary nanoparticle superlattices. These included CuAu, Cu_3Au, Fe_4C, CaB_6-type configurations, which have not been reported before [41].

However for hard sphere systems, experimental realisation of the predicted variety of structures has been more challenging. Binary crystals were first observed in Murray and Sanders examination of Brazilian gem opals formed by silica spheres with γ = 0.58. They analysed replicas of gem opal sections under electron microscopy and found two different structures with AlB_2 and $NaZn_{13}$-type crystals. The former is shown in Fig. 2.7 (a) [37, 42].

Pioneering experimental work carried out by Bartlett, *et al.* was able to replicate the structures observed by Sanders and Murray. They obtained similar AlB_2 and $NaZn_{13}$-type configurations using density and refractive index matched sterically stable PMMA particles at γ = 0.58 [43, 24]. The former crystalline structure is shown in Fig. 2.7 (b). Complementary work on this front was performed by Hunt *et al.* Using a related system, they also studied γ = 0.72, 0.52, 0.42 and 0.39 through optical powder-diffraction techniques [31]. For the smallest particle size difference (γ = 0.72) the authors only found crystals formed solely of small or large particles along with amorphous configurations. For γ = 0.52, AlB_2 and $NaZn_{13}$-type crystals were obtained in addition to crystalline arrangements formed only by small or large species and an amorphous phase. These are in agreement with theory and simulation predictions. Reducing γ to 0.42 seemed to destabilise the crystalline phases observed at the previous size ratio and only crystals of small particles and potentially binary crystals (with a NaCl/NiAs-type configuration) were observed. Finally, at the largest particle dissimilarity (γ = 0.39) the range of compositions of the amorphous phase was bigger than for γ = 0.41 and again, potentially NaCl/NiAs crystalline structures were found. Interestingly, for all the ratios tested, at certain compositions (generally when the concentration of both species is significant) crystallisation was suppressed and an amorphous phase, not predicted in theory, appeared. This is likely to arise from kinetic factors. Additionally, a fluid phase was always in coexistence with any of the structures found [31].

Finally, ISS have been successfully obtained through sedimentation experiments using a mixture of core-shell silica colloids at γ = 0.3 and stoichiometry, $n \sim 0.3$, with n=N_S/N_L, as shown in Fig. 2.7 (c) [26, 13].

The difficulty in obtaining experimentally crystals of hard spheres, along with the appearance of an amorphous phase [31], might be mainly due to inherent polydispersity of the components along with the difficulty to obtain close-packed structures. The latter might be a consequence of slow kinetics, compositional fluctuations and differences in sedimentation rates between the particles. This can lead to the appearance of non-equilibrium factors absent in simulations [24].

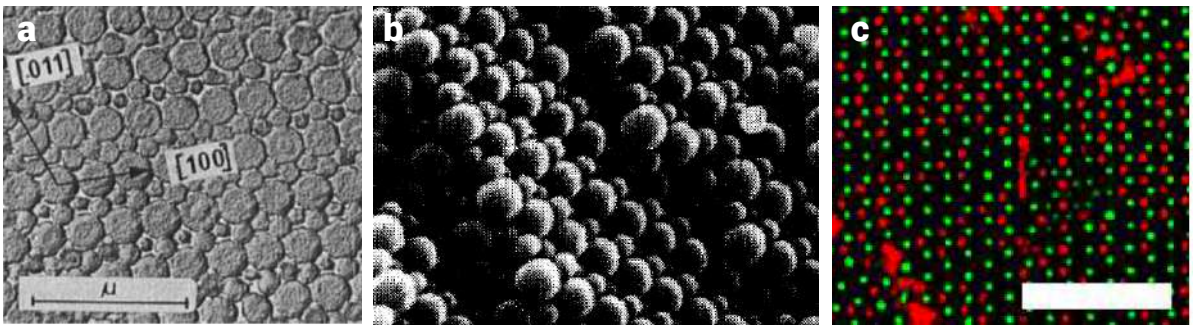

Figure 2.7: Images of some binary crystals obtained experimentally. a. Electron micrograph of the first binary crystals observed in Brazilian opal gems with size ratio (γ =σ_S/σ_L) = 0.58 observed by Sanders and Murray with a AlB_2-type arrangement. Modified from [37]. b. Scanning electron micrograph of a AlB2-type crystals formed by sterically stabilised PMMA particles with γ = 0.58, N_S/N_L = 0.16 and ϕ = 0.536. Modified from Bartlett *et al.* [43]. c. Confocal images of a mixture of core-shell silica nanoparticles forming interstitial solid solutions with γ = 0.58, N_S/N_L = 0.3 found by Filion and coauthors. Scale bar: 10 mum. Modified form [13].

2.2.6 Attractive Interactions

In previous sections, we have already addressed weak short-range attractive interactions as a consequence of van der Waals forces and how to avoid them from causing particle aggregation. However, there are some instances in which either weak or strong attractive interactions are desired. In these kind of interactions, two approaching particles experience attractive forces that grow in strength as they come closer together, until a critical separation is reached when repulsive forces from volume exclusion, charge or polymer coating prevent further approach. This is illustrated in Fig. 2.8 left panel, where short-range weak attractions are shown in pink and long-range strong attractions are illustrated in turquoise. Under these conditions, the system will also develop from a disordered to a condensed phase transition, similar to the one undergone by atomic and molecular systems, like argon [44, 14].

Examples of phase diagrams of attractive interactions are illustrated for short (pink) and long-range (turquoise) attractions in Fig. 2.8 right panel. Here, when the interactions are weak, the system undergoes a liquid-solid transition. As the strength of the interactions increase, the system undergoes a gas-liquid transition. In colloidal dispersions these phases co-exist and are observed as poor and rich particle regions. If the coexisting packing fraction of the liquid is dense enough, the system can form an ordered equilibrium state to lower its free energy. However, if the strength of the attraction is too large, then it becomes harder to reach equilibrium: the stronger two particles enter into contact, the harder it would be for them to un-stick and try other configurations. These arrangements thus become long-lived even if they do not correspond to equilibrium configurations. As a result, so-called arrested structures like clusters, glasses or gels can be obtained [14].

Understanding attractive interactions in order to control and exploit them is vital to successfully using colloidal systems for technological applications. There are different strategies one

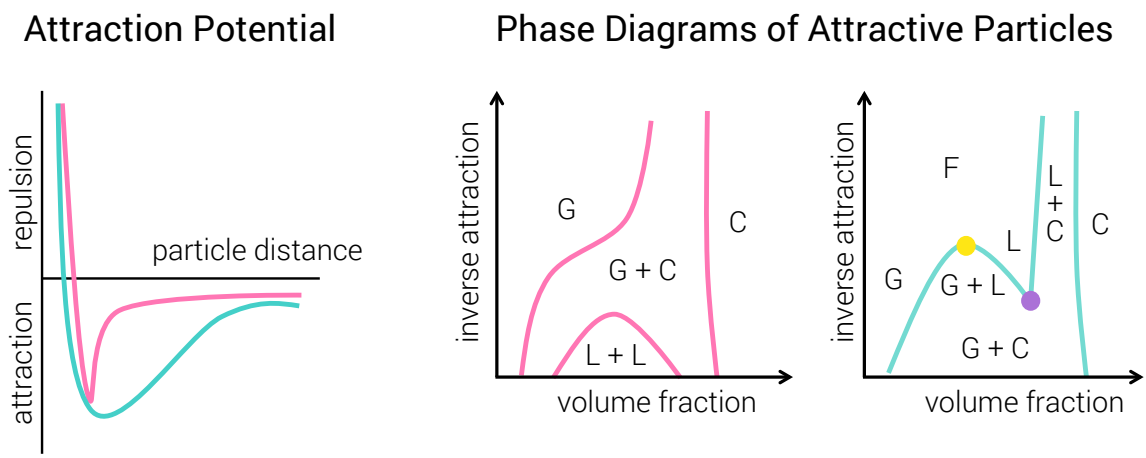

Figure 2.8: Attractive Interactions. Left panel: example of an attractive potential where the pink and turquoise colours represent short-range weak and long-range strong attraction potentials, respectively. Right: examples of phase diagrams of attractive interactions where the different gas (G), liquid (L), crystalline (C) and glass or gel (G) regions are indicated. The critical point and the triple point are highlighted as the yellow and purple circles, respectively. Also, the pink diagram corresponds to short-range attractions and the turquoise to long-range ones [44].

can follow to yield attractive interactions.

For colloidal systems, probably the most popular is the addition of non-adsorbing polymer, or depletant, to a colloidal dispersion of particles. Here, when two colloidal species come close to each other, their excluded volumes (or depletion zones) overlap, illustrated as the yellow zone in Fig. 2.9 (a). The overlap leaves only a little space in-between, which is not accessible to the polymer. In this situation, the polymer has more available volume, which minimises the free energy of the polymer. This results in an attractive force between the colloids in the presence of polymer, even when the intrinsic colloid-colloid and colloid-polymer interactions are both repulsive. Control over the strength and range of attraction forces can be obtained and modified independently by changing either the concentration or the size of the added polymer respectively [45, 46, 44, 47].

Adsorbing polymers, i.e., polymers that bind or anchor physically (and reversibly) to the surface of the colloidal species, can also induce attraction by forming bridges that link the particles as shown in Fig. 2.9 (b) [46]. However, less research has been devoted to these systems in comparison with their non-adsorbent counterparts. Experimental and computational studies have both found liquid-gel-liquid transitions for these systems. Here, as bridging polymer is added, the particles aggregate and form a gel. However, at a critical polymer concentration, the surface of the colloidal particle is saturated, forming a polymer monolayer around the particle and consequently they become stable again, i.e., they re-enter solution. [45, 46]

Additionally, specificity and directionality of the attraction can be provided to colloidal particles. This is the case of DNA chains grafted on the surface of colloidal species, for example. In these systems, particles will come together to form condensed phases through DNA hybridisation of complementary chains, hence, DNA strains act like particle linkers as illustrated in Fig 2.9

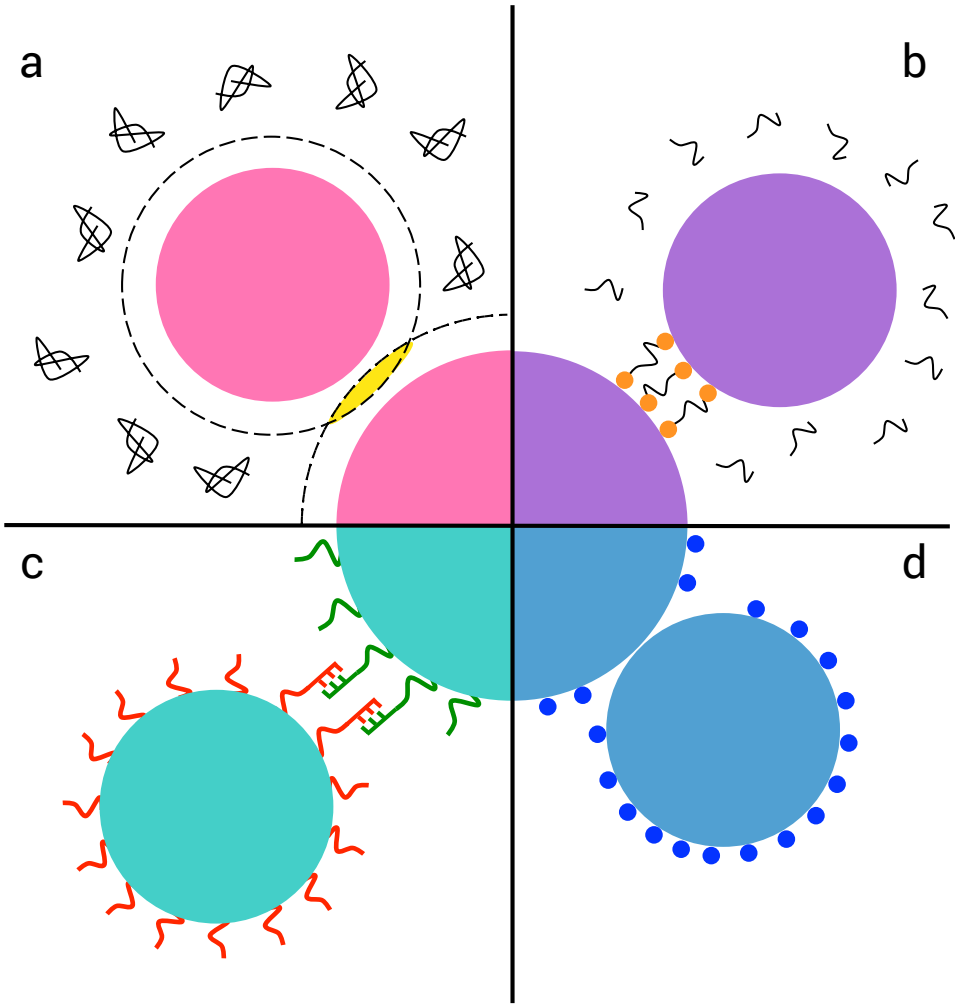

Figure 2.9: Different types of attractive Interactions. a) Depletion interactions with non-adsorbing polymers. b) Linking particles with physically adsorbing polymers. c) Particles linked through DNA hybridisation. c) Hydrophobic attractions. Polymers, water and DNA molecules are not drawn in scale. See text for details.

(c). The condensed phases formed in these systems might depend on the particle-DNA size and coverage ratio, where the former determines the packing of the species, whereas the latter determines the stability of the assembled structure. The final structure is the one that maximises DNA hybridisation. Additionally, the rate of hybridisation and de-hybridisation will also play an important role on the final assembly obtained [33, 48].

On the other hand, when the system is aqueous, complex couplings between water-colloid and water-water may arise. If the surface of the particle has affinity for water, it is considered hydrophilic. In these cases, strong binding of water molecules on the surface of the particles (surface hydration) stabilises the colloids through hydration repulsion [49]. *Per contra*, hydrophobic particles are the ones that have a lack of polar or ionic groups, or hydrogen-bonding moieties, thus, present no affinity for water [50]. In these cases, the orientation of water around the sur-

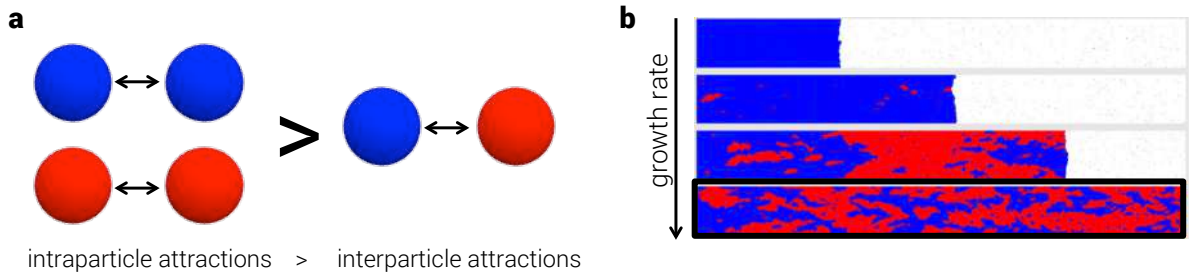

Figure 2.10: Critical Soft Matter. a) Whitelam and collaborators system composed by two species with different mutual attractions. b) 2d snapshots of de-mixed (top) and mixed (bottom) structures found by Whitelam *et al.*, as a function of increasing the growth rate (reproduced from [53].

face of hydrophobic particles is entropically unfavourable, since they have lower degrees of freedom at this vicinity, illustrated in Fig. 2.9 (d) as small blue circles. When two hydrophobic particles come together, the water molecules need to be displaced from the surface to the bulk water phase, which increases the water molecules entropy. Such increase of entropy might be the driving force for hydrophobic attractions, similar to the case of non-adsorbing polymers. In this case, the attractions can be long-range and stronger than van der Waals [50, 51]. These type of interactions are fairly complex, system dependent and very much affected by the presence of ionic species in the solution [49].

Finally, non-homogenous charge distribution on the surface of the particles might also lead to short-range attractions and hence cluster formation. These interactions are not that common and thus have been less investigated [52].

2.2.7 Critical Soft-Matter

As mentioned above, the ability to mimic self-assembly processes offers the attractive opportunity for the design and synthesis of new devices with novel properties. Nonetheless, nature functional materials usually involve multicomponent systems, where the particular properties of the components will determine the final characteristics of the material. Furthermore, achieving and maintaining these intricate structures and functions often occurs by operating far from equilibrium. This characteristic of natural systems presents an issue, since the current means and tools we possess to study these processes are based on equilibrium models. Consequently the prediction of the final assemblies that result from non-equilibrium processes is not yet possible.

Only recently, a new route for colloidal self-assembly was predicted theoretically by Whitelam *et. al* [53]. In their simulation study, the authors were able to predict and confirm the final assemblies of a mixture of monodisperse blue and red particles with slightly higher intraparticle attractions over interparticle attractions, i.e., blue-blue and red-red interactions are preferential over blue-red (Fig. 2.10 (a)). They modelled the growth dynamics of the assembly in 2d and 3d

by controlling the growth rate. Fig. 2.10 (b) reproduces their results. At low growth rates, the colour of the assembly is mostly blue, due to preferential blue particle 'deposition' to the sticky wall. This assembly suggests that the particles are phase separating, which is the expected assembly at equilibrium (Fig. 2.10 (b) top). As the growth rate increases, clusters of red particles start appearing. These regions grow in number and size as does the growth rate. The final mixed lattices obtained are thus out-of-equilibrium and resemble structures with particle component fluctuations typical of systems near their critical point (black square Fig. 2.10 (b)) [53]. These new assemblies were called then *critical soft matter* (CSM) and stand out as promising materials to reproduce nature's far-from-equilibrium processes, structures and functionalities. Moreover, by tuning the association rates, the sizes of the individual domains can be modified, which is relevant for the design of new technological devices.

In order to yield such materials then, a multicomponent system where the mutual attractions of the different components are higher than inter-species attractions is needed, along with fast and controllable cooling (association) rates.

2.3 Functional Nanostructured Materials

Complex, hierarchical, long-range ordered materials with building blocks in the nano and micro scale can be obtained by controlling and manipulating self-assembly processes. If the components of such structures present optical, magnetic, electric, chemical or biological properties, then the assemblies formed acquire potential for a myriad of applications in a great variety of fields, including photonics, energy transfer and storage, magnetic levitation, catalysis, drug delivery, tissue scaffolding, cancer treatment and gene transfection. Indeed, in the recent years, the synthesis and design of new materials and devices through fine control of the interactions of their components, has acquired major relevance within the fields of solid state physics, chemistry, engineering, materials science and biology [54, 55, 56].

To yield functional nanostructured materials, it is necessary to control the nano-block shapes, sizes and surface properties. Thus, the first objective of self-assembly strategies is to obtain components with specific dimensions and forms, which combined with specific surface properties (charge, hydrophobicity/hydrophilicity or functionality) will allow control over attractive and repulsive interactions to create integrated devices with specific ordering, length scales and functionalities [57].

Two functional building blocks relevant for the research work present herein will be the focus of the following sections.

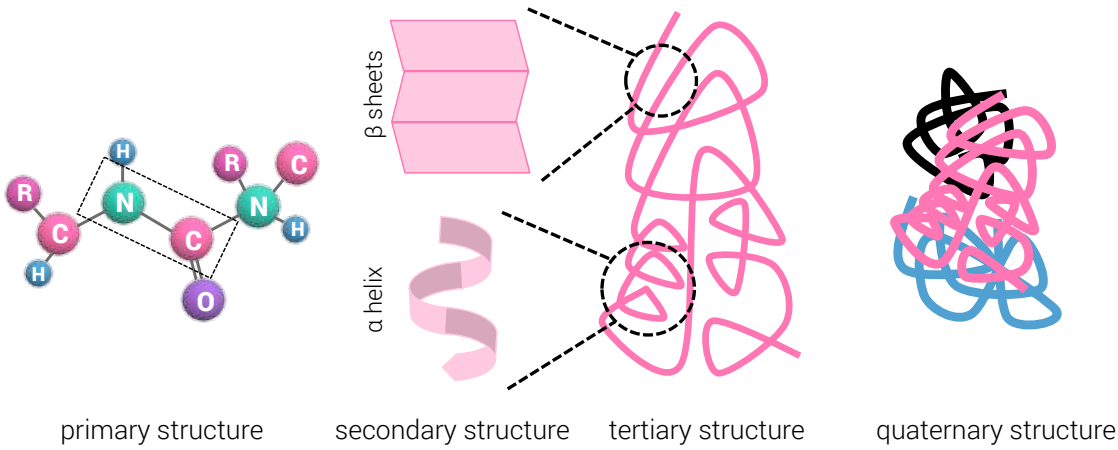

Figure 2.11: Scheme of the different protein structures, where two amino acids formed by carbon (C), nitrogen (N), oxygen (O), hydrogen (H) and a side chain (R) are shown linked through an amide bond highlighted in the rectangular square. β sheets and α helices are also depicted forming part of the 3-dimensional protein. Finally, three different coloured proteins form the quaternary structure.

2.3.1 Proteins for Functional Nanomaterials

Probably the most obvious source of inspiration for the design of functional materials at the nanoscale is nature itself. Indeed, the high level of complexity, specificity, efficiency and sophistication of nature's structures makes their building blocks (proteins, polymers, carbohydrates and lipids) an attractive possibility to be used for new human-manufactured devices. Of these, proteins are the species with the largest diversity of structures and functions, thus have the greatest potential to be exploited as the functional components for novel nanostructured materials [58, 59]. They are capable of carrying out structural, catalytic, transport, packaging, optical, specific recognition, electrical, information storage and metabolism functions [58]. A complete review of the vast catalogue of techniques and assemblies so-far achieved, using proteins as building blocks, can be found in Luo *et al.* [58].

Proteins are the largest components in number of living organisms and play a crucial role in the structure, function and maintenance of all cells. They are macromolecules formed by a large and specific sequence of amino acids, which is encrypted in the DNA and known as the *primary structure* of the protein [60]. Amino acids are molecules containing carboxyl (-COOH) and amine ($-NH_2$) functional groups, along with a side chain (R group), which is specific to each of the 20 amino acids available. These molecules are bound together through peptide (amide) bonds between the amino and carboxylic groups, as illustrated in Fig. 2.11. The R groups confer different hydrophobic, hydrophilic or amphiphilic properties to the sequence. Due to these characteristics, amino acid chains fold up in 2-dimensional shapes in aqueous media via hydrogen bonds forming so called 'β sheet' and 'α helix' structures, yielding the *secondary structure*. These in turn fold in 3-dimensional specific shapes, or *tertiary structure*, at which most proteins are functional. Sometimes, various proteins can bond together non-covalently to form even larger functional

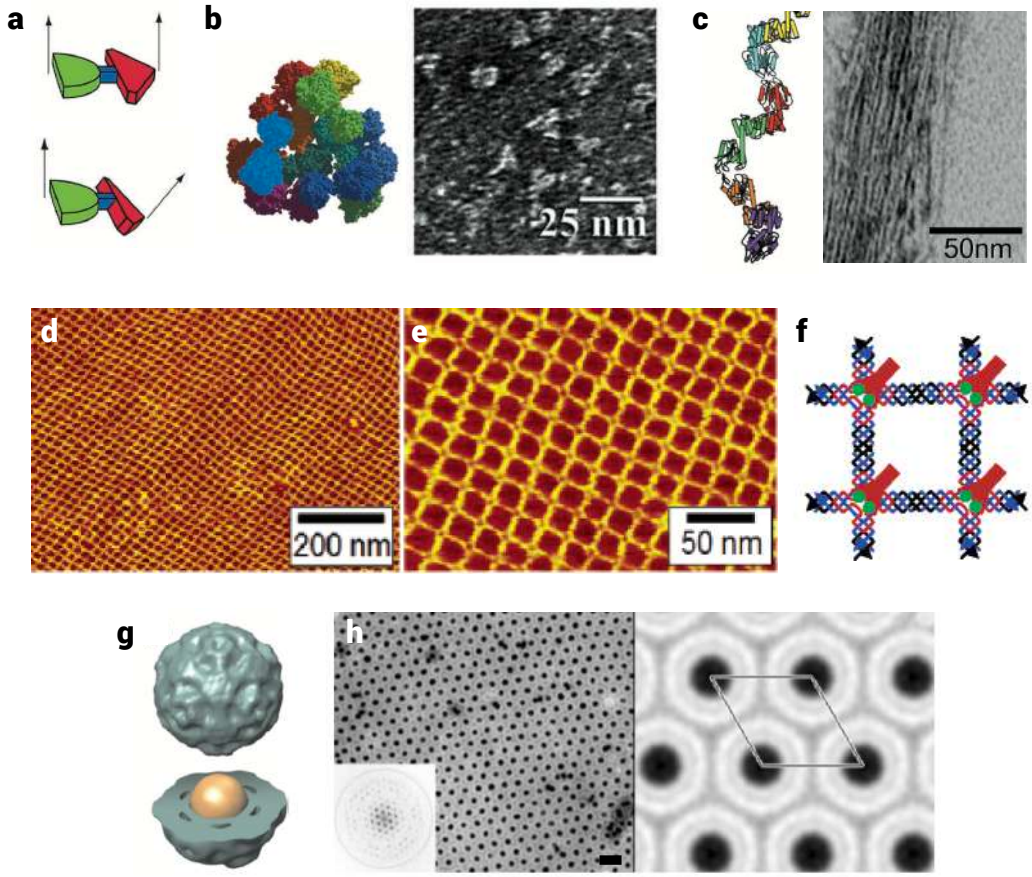

Figure 2.12: Examples of different nano-architectures comprised by proteins. (a-b) Fusion protein formed by two peptide subunits (a) that self-assemble into tetrahedral cages (b) or fibres (c), as shown by the models and transmission electron micrography images. Modified from [61]. (d-f) Atomic force microscopy image of a DNA 2-dimensional array (d-e), where antibodies have been deposited through fluorescein conjugation to the array (f, green circles) and further antibody recognition of the antigen (f, red y-shaped molecules). Modified from [62]. (g-h) Hybrid nanomaterials formed by a gold nanoparticle core coated with a shell formed by proteins of the capsid of the Brome Mosaic virus (g), forming a 2-dimensional crystal. Transmission electron micrography image of the assemblies (h left) is accompanied with their corresponding Fourier transform (insert) and Furrier projection maps (b right). Scale bar: 50 nm. Modified from [63].

aggregates constituting the *quaternary structure* [60, 59]. All these conformations are shown in Fig. 2.11.

Thus, the vast variety of functions carried out by proteins are specific and depend on the amino acid sequence encoded in the genome [59]. This particular characteristic constitutes an attractive feature to be exploited for the rational design of desired structures and functions using genetic technologies. Although complex and on its primary steps, computational design guided self-assembly combined with the production of genetic engineered DNA sequences for the expression of tailor-made proteins, are nowadays possible [58, 64].

Moreover, protein subunits (peptides) can be designed to self-assemble into functional architectures like nanofibers, nanocages, nanosheets and periodic arrays [65]. For example, Padilla

and collaborators [61], carefully chose and combined two small peptides through genetical manipulation to create a fusion protein, as illustrated in Fig. 2.12 (a). These proteins have the ability to associate with other copies of themselves to form highly symmetric shapes. With this method, they were able to fabricate two different architectures: tetrahedral cages and filaments. Fig. 2.12 (b) and (c) show both the models and the transmission electron microscopy image of the assemblies formed [61].

However, it remains challenging to fabricate well-organised complex, hierarchical and functional 2 or 3-dimensional structures. This arises from large difficulties of controlling the assembly process due to surface chemistry and structural symmetry [65]. An alternative to yield long-range protein architectures is to use of other biological molecules (like DNA) or inorganic materials as scaffolds for the self-assembly. For example, He and coauthors DNA-directed the self-assembly of antibodies into 2-dimensional arrays, as shown in Fig. 2.12 (d-f). Here, they first formed long-range DNA ordered tetragonal 2-dimensional arrays (Fig. 2.12 d-e), where the protein fluorescein was covalently conjugated with DNA, as shown in green on Fig. 2.12 (f). Fluorescein was used as the antigen for immobilisation of the fluorescein antibody (y-shaped red molecule Fig. 2.12 (f)), yielding antibody arrays with high density and symmetry [62].

Alternatively, proteins can be bound to inorganic nanoparticles and form crystalline structures, as demonstrated by Sun and collaborators [63], where proteins from the capsid of Brome Mosaic virus were used to encapsulate gold nanospheres functionalised with polyethylene glycol (Fig. 2.12 (g)). Here, the natural design of these capsid proteins to spontaneously self-assemble into shells was exploited to yield such hybrid materials. Since they presented a high degree of homogeneity, the particles were able to form 2-dimensional crystals, as shown in Fig. 2.12 (h). Moreover, they showed that these crystalline structures presented promising optical properties [63].

Another much less studied alternative to form nano-architectures using proteins is to treat them like colloidal patchy particles and yield condensed phases like gels, glasses and crystals. Proteins are indeed capable of presenting these phases when electrostatic repulsive forces are overcome by attractive interactions [66, 67, 68]. Furthermore, phase diagrams very similar to the one illustrated in Fig. 2.8 (turquoise) have been obtained for globular proteins [67, 68]. For protein solutions, the attractive forces can be controlled in different ways. The first one can be through protein design, which might involve protein improvements or mutations [69]. Additionally, phase transition in protein solutions can be a result of increasing protein concentration or of changes in the temperature, pH and ionic strength of the solution [67, 68]. Finally, it has been discovered recently that adding trivalent salts to the protein solution allows protein association and thus gel and crystal formation [66].

However, unlike most colloidal species, proteins present shape heterogeneity in addition to surface, charge, chemistry and hydrophilic/hydrophobic anisotropy [68, 66]. Moreover, most of the research dedicated to study proteins phase transitions has focused on protein aggregation

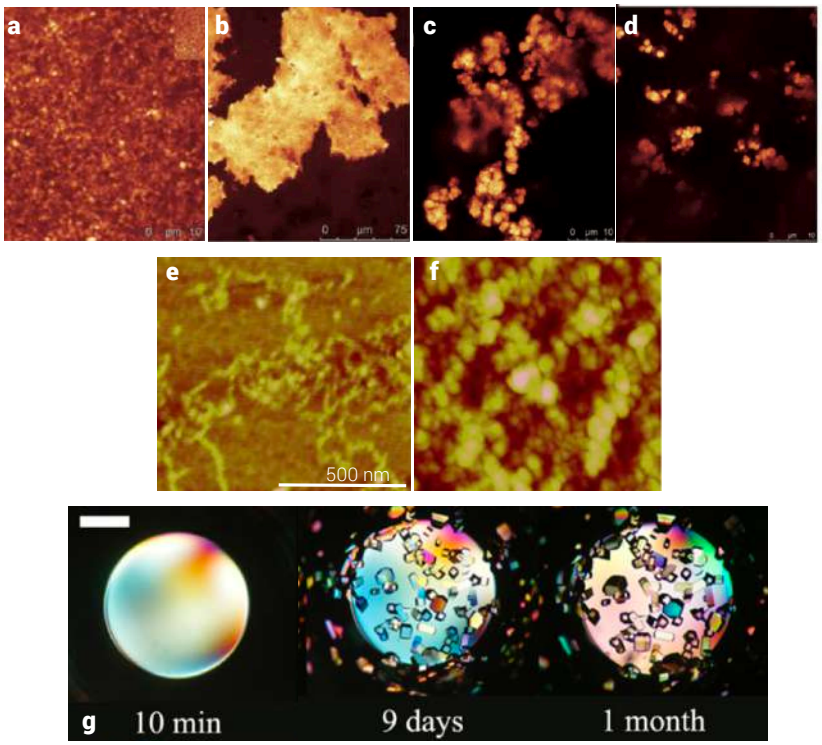

Figure 2.13: Examples of condensed phases formed by proteins. (a-d) Confocal microscopy images of fluorescently labelled wheat proteins aggregates formed during heat induced gelation at 90 °C at pH 6.8 (a), at pH 4.6 (b), at pH 6.8 plus shearing (c) and at pH 4.6 plus shearing. Modified from Singh *et al.* [70]. (e-f) Atomic force microscopy image of rice bran globulin when heated at 90 °C at pH 6.8 and 500 mM NaCl, showing the nanofibrils obtained (e) and a close up of the structures (f). Modified from Huang *et al.* [71]. (g) Optical microscope images of the time evolution of the crystal formation of lysozyme solutions at 23.6 mg/mL in 1.3 M of NaCl and 5 mM sodium phosphate at neutral pH and room temperature. Scale bar: 0.3 mm. Modified from Dumetz *et al.* [67].

in diseases like Parkinson's or Alzheimer's, food processing or on obtaining crystals for crystallography studies [68, 66, 67].

For example, Singh and collaborators studied the influence of pH or shear heat induced gelation (90 °C) on solutions of fluorescently labelled whey proteins (β-lactoglobulin, α-lactalbumin and bovine serum albumin) [70]. They obtained different aggregates and structures, illustrated in Fig. 2.13 (a-d). When the pH was maintained at 6.8 and no shearing was applied, the proteins aggregated into fine stranded networks (a), but when the pH was lowered to 4.6, the protein formed aggregates (b). When shearing was added, the proteins formed stranded gel aggregates for the higher pH (c) and particulate aggregates for the lower pH (d) [70].

Additionally, nanofibrils of rice bran globulin were obtained by Huang *et al.* through heating protein solutions at different salt concentrations. The structures formed were investigated through atomic force microscopy measurements and are shown in Fig. 2.13 (e-f). After heating at 90° C , at a pH of 2.0 and at NaCl concentrations between 100-500 mM, the architectures found consisted on linear fibrillar aggregates as shown in Fig. 2.13 (e), with a close up to show the dense 'granules' forming the network. The only difference between the various salt concen-

trations was that more branching was observed as the ionic strength of the solution increased [71].

Although several assemblies can be formed through these heating protocols followed by pH/ionic strength changes, proteins loose their functional conformation at high temperatures [70, 71], which limits the use of these methodologies and structures.

Obtaining suitable crystals like the ones shown in Fig. 2.13 (g) from highly pure supersaturated protein solutions is often desirable, since these structures can be used to elucidate protein's tertiary conformation through X-ray crystallography analysis and thus predict their specific function(s) [67, 66]. However, yielding these ordered structures is frequently complicated and the use of these potentially functional structures has been almost exclusively devoted to crystallography.

Due to the high complexity of the protein interactions, along with protein denaturation (lost of tertiary and thus functional structure) from temperature, pH and ionic strength modifications, this last self-assembly route has not been as broadly explored for the fabrication of functional nano-devices.

2.3.2 Magnetic Nanoparticles for Functional Nanomaterials

From the variety of functional inorganic materials, magnetic nanoparticles stand-out for their integration in devices to yield unique properties. Indeed, ordered structures of magnetic nanoparticles display different emergent properties from their isolated or bulk counterparts [55, 72]. Additionally, their spatial distribution within the assembly will also determine these properties [72]. For example, chains formed by iron oxide colloidal particles, have shown tunable photonic properties. On the other hand, 2-dimensional hexagonal monolayers of the same nanoparticles presented dipolar ferromagnetism [72]. These different structures can be obtained via dipole-dipole interactions which can be triggered and controlled remotely, reversibly and instantaneously by magnetic fields [55, 72]. Moreover, the interactions driving the self-assembly of these particles are directional, an thus, they provide a richer variety of structures that can be yield [56].

Magnetic nanoparticles are those that are influenced and manipulated through magnetic fields. Such behaviour is determined by their susceptibility (χ) and their permeability. The former describes the level of magnetisation ($M = \chi H$), whereas the latter characterises the magnetic induction change (B) induced by an external magnetic field (H). Based on their susceptibility, all materials can be classified intro three main groups: diamagnetic, paramagnetic or ferromagnetic. If the magnetic field induces a weak magnetic moment, the particles have a small and negative $\chi \sim$ -10^{-6} to 10^{-5} and are diamagnetic. Moreover, once the external field is removed, the particles do not show magnetic features. On the other hand, if the particles show a weak but positive susceptibility on the order of 10^{-5} to 10^{-3}, they are paramagnetic, which arises from unpaired electrons. In the absence of an external field, their dipoles are oriented randomly, however,

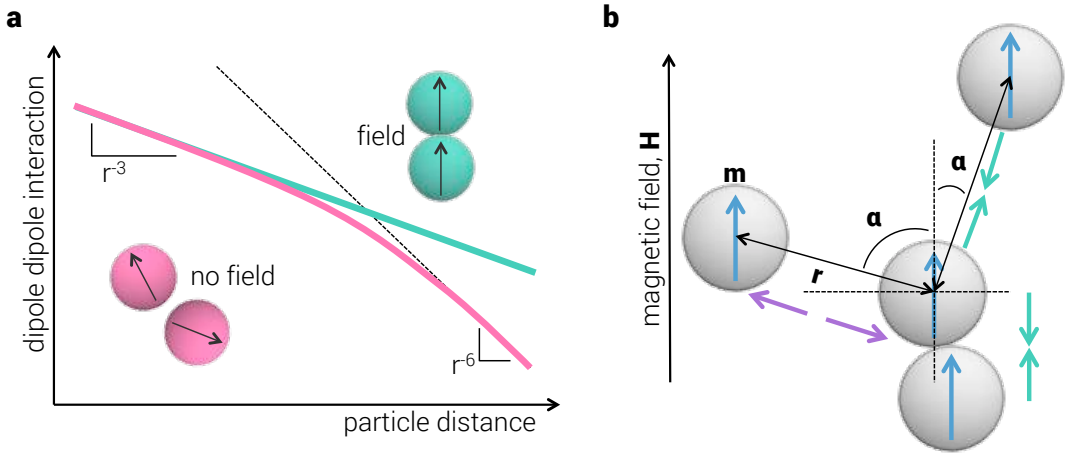

Figure 2.14: Magnetic nanoparticle interactions. a) Interaction potential of magnetic nanoparticles in dispersion (pink) and when an external magnetic field is applied (turquoise), reproduced from [56]. See text for full description. b) Dipoles induced by an external magnetic field (H), attractive forces appear when α < 50° (turquoise arrows), whereas repulsive forces appear when 50° < α < 9 ° (purple arrows).

once a magnetic field is applied, the magnetic moments align. Similar to the case before, once the external field is eliminated, their magnetic moment does not persist. Finally, if the particles present large susceptibilities $\chi \sim 10^{-2}$ and 10^{6}, they are classified as ferromagnetics and their magnetic properties persist even after the magnetic field has been removed [73].

When magnetic particles are exposed to an external magnetic field, they acquire magnetic moments, $m = \mu_0 \chi V H$, where μ_0 is the magnetic permeability of vacuum and V is the particle volume. From this expression we can see that the magnitude of m scales with the size of the particle [56].

Therefore, the driving force for attractive and repulsive forces amongst magnetic species originates from dipole-dipole interactions. The necessary work to bring two magnetic nanoparticles together to finite r separations can be described by the dipole-dipole interaction U_{dd}(r):

$$U_{dd}(\vec{r}) = \frac{m_1 \cdot m_2 - 3(m_1 \cdot \vec{r})(m_2 \cdot \vec{r})}{4\pi\mu_0 r^3} \tag{2.18}$$

where $\vec{r}$ corresponds to the vector parallel to the one connecting particle 1 and 2 [56]. Fig. 2.14 (a turquoise) shows the long-range interaction between the particles when exposed to an external field. When this is absent, at small particle separations, the interactions are strong and scale with r^{-3}, which causes alignment with neighbouring particles. However, as the distance increases, the magnetic moments become more disordered and their interaction can be described with Keesom interactions (see Section 2.2.1), which scales with r^{-6} (Fig. 2.14 (a pink)) [56].

Furthermore, magnetised particles can become small magnets due to their dipoles. The magnetic field generated by these dipoles varies with the particle separation to the negative

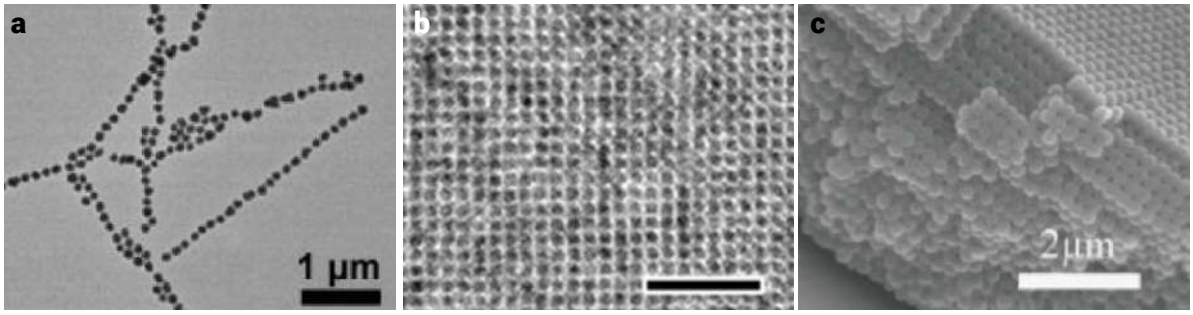

Figure 2.15: Different examples of assemblies formed by magnetic nanoparticles under the influence of a magnetic field. a) Transmission electron microscopy (TEM) of iron oxide-fluorescent carbon nanoparticles [77]. b) TEM maghemite nanocubes magnetic-induced superlattice (scale bar: 100 nm) [78]. c) Scanning electron microscopy of an 3-dimensional assembled colloidal crystal formed by elipsoids [79].

third power (r^{-3}) and the magnitude of m [56]. For spherical particles with the same m, the generated field is given by:

$$H = \frac{3\vec{r}(m \cdot \vec{r}) - m}{4\pi\mu_0 r^3} \tag{2.19}$$

Additionally, the interactions depend strongly on their relative orientation, described by α, which is the angle formed between the line connecting the centres of the particles and the direction of the magnetic field and takes values from 0 - 90° (Fig. 2.14 (b)) [56, 74, 75]. As such, the interactions between magnetised particles can be either attractive if they are 'parallel' to each other with α < 50°, or repulsive if they are 'antiparallel' where 50° < α < 90° [76, 56, 74, 75]. This illustrated in Fig. 2.14 (b) with the turquoise and purple arrows showing attractive and repulsive interactions, respectively. According to equation 7.4, for the parallel alignment, the interaction is given by $m^2/2\pi\mu_0 r^3$, twice as big as the antiparallel alignment given by $m^2/4\pi\mu_0 r^3$ [56].

Different field-induced arrangements of magnetic nanoparticles can be obtained and they arise once the attraction forces dominate other inter-particle forces, including van der Waals, dispersive and gravity forces [76]. The simplest arrangement that can be formed is the parallel alignment of the particles to the external field which generates linear chains or ring structures form dilute dispersions. These assemblies present a high aspect ratio and thus have potential as sensing probes, nanowires, drug/gene delivery carries, enhancers for magnetic resonance contrast and for cancer therapy [77, 80]. An example of these structures is illustrated in Fig. 2.15 (a). Here cubic iron oxide nanoparticles with ~ 25 nm per edge were assembled in chains under a magnetic field. The structure chains can be observed through transmission electron microscopy (Fig. 2.15 (a)) [77].

Stronger magnetic fields along with higher particle concentrations, might produce close-packed superlattices. Nanocrystal superlattices have important applications in semiconductor arrays and in high density storage devices [78]. An example of a long-range 2-dimensional array with high degree of translational and orientational order of cubic maghemite nanoparticles

is shown in Fig. 2.15 (b). Even higher order structures can be achieved, as shown by Ding and collaborators on their work on fabricating 3-dimensional photonic crystals with core-shell silica-iron oxide magnetic ellipsoids.The authors employed both an external magnetic field and solvent evaporation for the formation of the structures [79]. An image of the structures they found is shown in Fig. 2.15 (c).

On the other hand, magnetic nanostructures can also be obtained through template assisted methods, where physical and chemical substrates can be used to assemble nanoparticles in desired sizes, shapes and compositions [81, 56]. An example of such techniques is illustrated in Fig. 2.16, where Badini Confalonieri *et al* [81] produced a honey-comb type array through anodisation aluminium discs. Iron oxide nanoparticles are later spin-coated on the surface of the substrate and thus deposited on the template cuvettes, where they form individual clusters. The number of particles forming said aggregates depended on the size of the cuvette and generally if this number exceeded 10, the particles arranged in an hexagonal order. Moreover, they found different collective magnetic properties of these type of arrangements in comparison with the same particles arranged in a regular monolayer [81].

2.4 Summary

In this first chapter, the basic properties and interactions of colloidal dispersions have been described. They represent a powerful model system to investigate and understand fundamental physical phenomena, including crystallisation, vitrification and gelation. This is due to their sizes: they are small enough to behaviour similar to atoms and molecules, but are still large enough to be manipulated and observed in real space.

In addition, colloidal dispersions stand out as promising building blocks for the generation of functional devices with applications in a wide variety of fields, expanding from photonics and

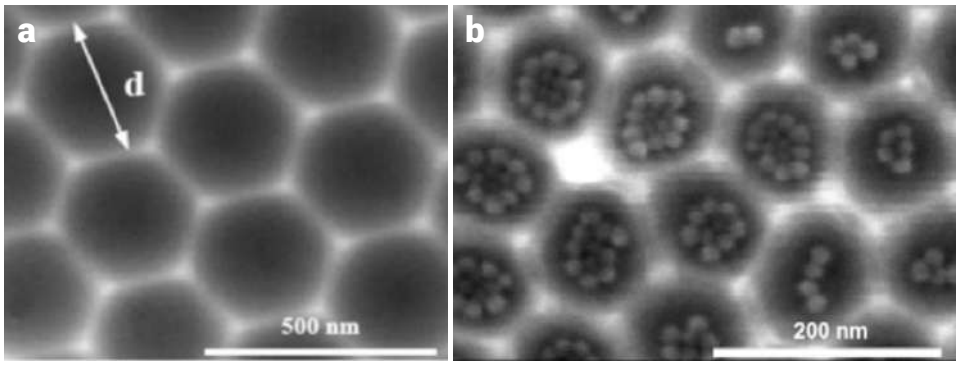

Figure 2.16: Individual clusters of magnetic nanoparticles formed using a template produced by Badini Confalonieri and collaborators. a) Scanning electron microscopy images of the aluminium patterned substrate. b) Scanning electron microscopy images of individual clusters of magnetic iron oxide nanoparticles [81].

electronics to cancer and gene therapy. Moreover, great progress on chemical and biological tools has allowed further development of routes to produce colloidal species with the desired sizes, shapes, and physical, chemical and biological properties to fulfil such purposes. However, in order to yield functional architectures, their self-assembly processes need to be fully understood to allow their manipulation.

The research presented in the forthcoming chapters investigates the self-assembly processes of multiple soft-matter systems with different component number, interactions and potential applications. These systems include hard sphere binary mixtures, particles with long Debye lengths, fluorescent protein solutions and core shell magnetic nanoparticles.

CHAPTER 3

Experimental and Simulation Techniques

Different experimental, characterisation and simulation techniques were employed within the present work to synthesise and describe the colloidal particles as well as to study the assemblies they form. More specifically, polymethylmetacrylate particles were previously obtained through dispersion polymerisation [82, 83] and their shape and sizes were determined using scanning electron microscopy. On the other hand, transmission electron microscopy was utilised to characterise the shape and size of metallic nanoparticles, whose synthesis procedure is detailed in Chapter 7. Proteins were produced through bacterial expression and purified from the cell culture through affinity chromatography, according to standard protocols. Confocal laser scanning microscopy was used to image the different assemblies obtained for each system. Finally, event driven molecular dynamics simulations [84] were performed to get further insights into the dynamics of the hard sphere binary system studied in Chapter 4.

In this chapter, the principles behind these variety of techniques will be briefly described.

3.1 Production of Colloidal Particles

Two different colloidal particles were used in this work. For the study of self-assembly of binary hard sphere mixtures (Chapter 4) and charged particles (Chapter 5), fluorescent polymethylmetacrylate (PMMA) particles were used. These particles were previously synthesised through emulsion polymerisation and are sterically stable through a layer of (PHSA) polymer hairs covalently bonded to the surface of the particles.

On the other hand, a mixture of fluorescent silica spheres and fluorescent magnetic silica particles were developed for the realisation of *Critical Soft Matter*. The details of the synthesis of the silica magnetic nanoparticles are described in Chapter 7.

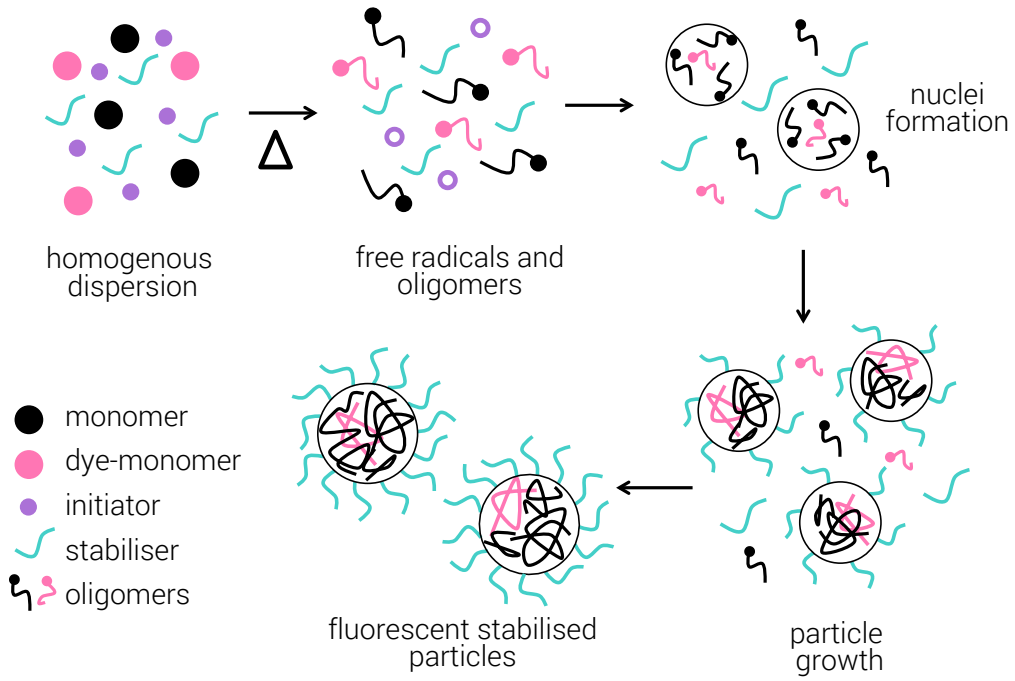

Figure 3.1: Dispersion polymerisation mechanism for the synthesis of polymethylmetacrylate (PMMA) particles. Refer to text for details.

3.1.1 Synthesis of Fluorescent Polymethylmetacrylate Particles

Rhodamine labeled polymethylmetacrylate (PMMA) particles coated with a layer of poly(12-hydroxystearic acid) (PHSA) polymer hairs were previously synthesised through dispersion polymerisation, whose mechanism is illustrated in Fig. 3.1.

In this type of reaction, the solvent used is a good one for the monomer, crosslinker, stabiliser and initiator, but a poor one for the polymerised product. For this particular synthesis, the monomer used was methylmetacrylate, the crosslinker methacrylic acid, the stabiliser PHSA and the initiator azobisisobutyronitrile (AIBN). The reaction starts with the thermal decomposition of AIBN at 75-80 ° C, which creates free radicals (open purple circles in Fig. 3.1) that trigger the polymerisation of methylmetacrylate (black circles in Fig. 3.1). The linear oligomers formed reach a critical molecular weight at which they are no longer soluble, they precipitate and then coagulate forming aggregates. These aggregates become nucleation centres where both the stabiliser (turquoise chain in Fig. 3.1) and more oligomers from the reaction medium are adsorbed and captured to form stable nuclei. At this stage, the number of nuclei is fixed with fairly narrow size distributions. Further particle growth takes place until all the monomers and oligomers are exhausted (Fig. 3.1)[85, 82, 83, 86].

Moreover, the particles can be fluorescently labelled through the addition of dyed monomers, which are composed of a fluorescent molecule and a coupling monomer, in this case rhodamine-B-isothiocyanate and aminostyrene, respectively. Here, styrene will also be polymerised and in-

corporated to the growing particles [82, 83], as shown in Fig. 3.1 as the pink oligomers.

Finally, control of the sizes can be achieved by changing the monomer, stabiliser and initiator concentrations and ratios [83].

3.2 Imaging of Colloidal Systems

Different microscopic techniques were employed to characterise the different kind of particles synthesised, both individually as well as their corresponding self-assembled structures. The selection of the technique was done according to the nature of the specimen as follows. Scanning electron microscopy was used to measure the sizes and polydispersity of PMMA particles, whereas transmission electron microscopy was used to measure and characterise the particles obtained on each of the different steps of the syntheses processes carried out for the fluorescent magnetic nanoparticles.

On the other hand, confocal laser scanning microscopy was used to obtain real-space and real-time information of the structures formed by all of our different systems (PMMA, fluorescent metallic nanoparticles and proteins).The presence of a fluorophore in the matrix of all the different kind of particles and the inherent fluorescence of the proteins, allowed this technique to be used.

3.2.1 Scanning Electron Microscopy

The scanning electron microscopy (SEM) belongs to a family of electron microscopes that are able to image and characterise different materials thanks to the interaction of the sample with a focused beam of specific energy range electrons. The main components of the equipment are shown in Fig. 3.2 and its principle is as follows. In order to produce an image, an electron beam is originated at the thermionic electron gun, which is then controlled, narrowed and directed to the sample under vacuum through a series of magnetic lenses. Once they reach the sample, the high-energy electrons (or primary electrons) will collide and interact with the corresponding electrons and nuclei of the specimen generating different type of signals which include secondary electrons, backscattered electrons, X-rays and visible light. From these, the signal detected by SEM is that produced by the secondary electrons, which are easily captured due to their low exit energy by a positively biased electron detector. They are then amplified and converted to an image pixel-by-pixel and line-by-line on the screen as the sample is scanned. Furthermore, since the yield of secondary electrons depends on the angle of incidence of the primary electrons in addition to a combination of enhanced emission at sharp borders of the features and shadow contrast due to incomplete collection of emitted electrons, SEM is able to provide information about the topography of the sample and thus gives three-dimensional information.

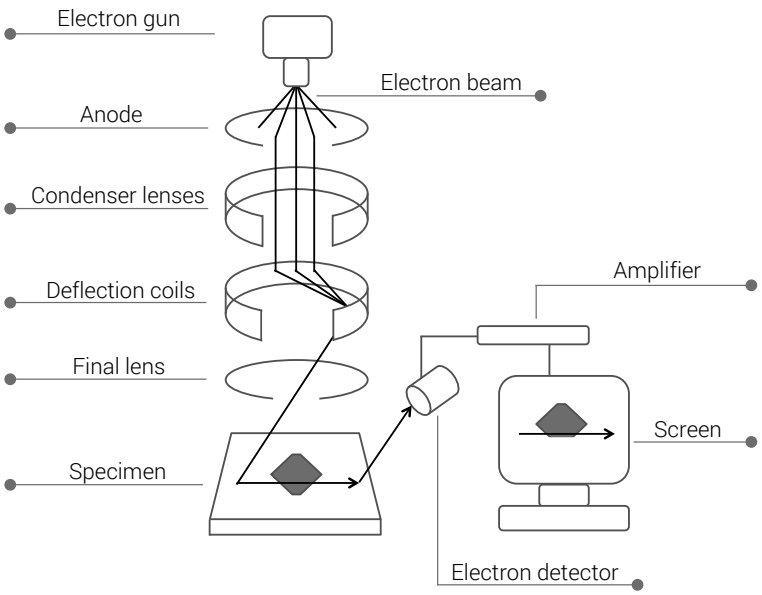

Figure 3.2: Schematic diagram of a standard scanning electron microscope, showing its most important components.

A slight drawback of this technique is the need for the sample to support high vacuum conditions, as well as the need for it to be dry and conductive. The latter limitation can be overcome by coating the sample with a thin layer of metal. SEM can achieve a resolution of 10 nm with magnifications of about 300000 times [87, 88, 89].

3.2.2 Transmission Electron Microscopy

Transmission electron microscopy (TEM), like SEM, utilises an accelerated electron beam and relies on the interaction of this with the sample. The electron beam is also generated by thermionic emission and this is directed and controlled by a series of electromagnetic lenses to reach the sample under vacuum conditions. In this case, however, the beam passes through a thin sample previously deposited in a carbon coated copper grid. The transmitted beam is then focused and projected onto a fluorescent screen, where a 2-dimension image is generated. The image is created due to differences on the contrast of the transmitted beam: areas covered by the sample will scatter the electrons strongly, preventing them from reaching the phosphorus screen and thus producing black spots. In areas with no sample, on the other hand, the electrons will be transmitted and then projected onto the screen to produce fluorescence. This means that the image generated is a negative of the real sample. Furthermore, different materials will scatter light more than others, producing more or less contrast on the final image. This principle was used to identify the successful coating of the metallic nanoparticles by silica. A scheme with all the main components of the apparatus is shown in Fig. 3.3. TEM can achieve resolutions as

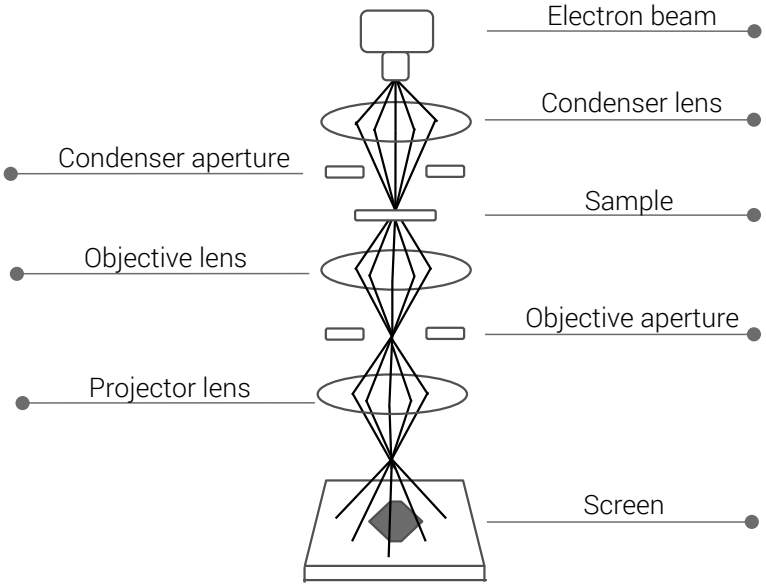

Figure 3.3: Schematic diagram of a typical transmission electron microscope, showing its main components.

high as 0.2-0.3 nm. Nevertheless, TEM presents similar limitations to SEM: the sample needs to be dry, vacuum resistant and in some cases, it needs to be coated for successful electron scattering [90, 89].

3.2.3 Confocal Laser Scanning Microscopy

The principle of the confocal laser scanning microcopy (CLSM) is similar to a conventional confocal microscopy, i.e., point-by-point illumination and exclusion of out-of-focus light emitted by the sample. However, in the former a laser beam is used instead of a lamp. A diagram illustrating the main components of a conventional CLSM is shown in Fig. 3.4. First, the laser light (purple lines in Fig. 3.4) is directed to the x-y scanner through a dichroic mirror, which selects the proper wavelength to excite the dye(s) (turquoise lines in Fig. 3.4). Then it passes through the microscope objective and reaches the sample, where the dye(s) is/are excited. Furthermore, more than one wavelength can be selected and thus mixtures of particles with different dyes can be imaged at the same time and independently. Only the fluorescent light emited from the specimen (solid pink lines in Fig. 3.4) is selected using emission filters. It then goes back to the dichroic mirror and passes through the pinhole, where light out of focus is prevented from reaching the detector (dashed lines in Fig. 3.4), increasing the resolution of the image. The pinhole is placed in the conjugate focal plane of the sample. Finally the on-focus emitted light is detected by the photomultimeter tube (PMT), which amplifies the signal.

Pixel-by-pixel and line-by-line 2-dimensional images and videos are possible thanks to the scanner, a series of mirrors that focus the laser beam across the sample. Three-dimensional

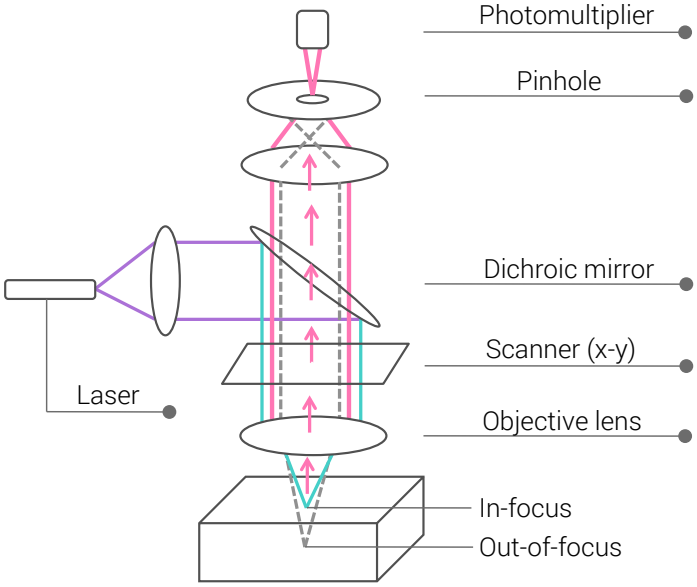

Figure 3.4: Schematic diagram of a typical confocal laser scanning microscope, showing its most important components. The purple solid lines represent the laser light that passes through the dichroic mirror that selects the appropriate wavelength to excite the dye (turquoise solid line) in the sample. The emitted line (pink solid line) from the plane of the sample is filtered and selected in the pinhole to reach the detector. The out of focus emitted light (dashed lines) is the rejected.

files are obtained by scanning one depth level at a time. The images and videos are reconstructed pixel by pixel and by combining the slices of each level [91, 89, 92].

3.3 Expression, Purification and Concentration of Fluorescent Proteins

Both eGFP and mCherry proteins were obtained through bacterial expression, followed by cell separation, cell lysis, centrifugation and selective purification of the proteins using a nickel column, as summarised in Fig. 3.5. The details of each step are described below.

3.3.1 Cellular Culture for the Expression of eGFP

Escherichia coli BL21 (DE3) competent cells were previously transformed with the DNA plasmid-pET45b(+)-eGFP. A plasmid is a small DNA molecule that can produce proteins autonomously using the cellular machinery. They can be artificially built and use as vehicles to insert foreign genetic material into a cell to produce proteins of interest [93]. In this case, pET45b(+) contains the genetic sequence to produce (or express) eGFP, a T7lac operator and a histidine tag, which will be relevant for the following steps.

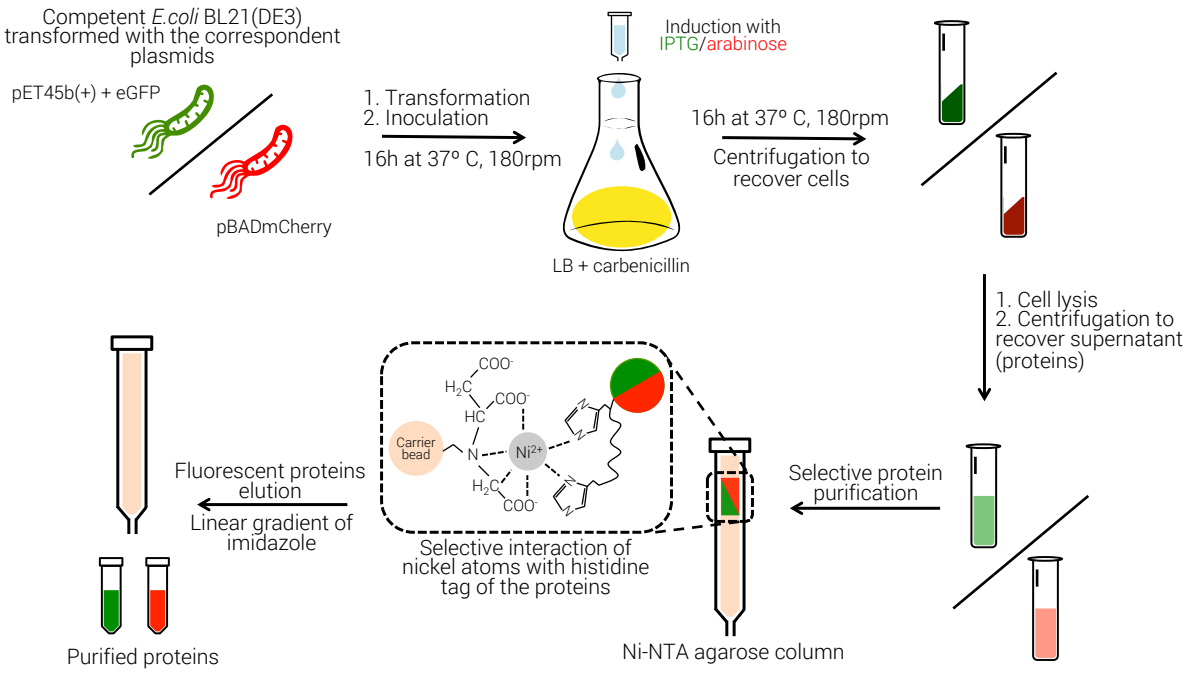

Figure 3.5: Schematic diagram of the steps followed for the expression and purification of both eGFP and mCherry fluorescent proteins. Transformed *E. coli* with the respective plasmid for eGFP or mCherry, were inoculated to a growth medium, until a desired concentration. Protein induction was then initiated through the addition of IPGT (for eGFP) or arabinose (for mCherry). After 16h of growth, the cells were pelleted through centrifugation. They were lysed and centrifuged to obtain the expressed proteins, which then were injected to a nickel column for purification. The insert shows the selective reaction of the histidine tag present in the protein with the immobilised nickel atom in the column. The bound proteins were eluted by adding an excess of imidazole buffer. Finally, they were dialysed against dH_2O. Refer to main text for the details.

First, a mini-culture was prepared by inoculating 100 mL of lysogeny broth (LB) and the antibiotic carbenicillin (50 μg/mL) with said bacterium. The culture was left to grow for 16 h at 37° C and 180 rpm. 20 mL of this culture were then used to inoculate 1 L of LB containing carbenicillin (50 μg/mL), which was left to grow under the same previous conditions. Change in the turbidity of the culture (optical density, OD) is related to cell growth and by measuring it, one can estimate the bacterial density. Thus, the OD_{600nm} was monitored and when it reached a value of 0.5-0.6, the production of eGFP was induced by adding 1 mM of Isopropyl β-D-1-thiogalactopyranoside (IPTG). This molecule binds preferentially to the active site of the lac repressor, an enzyme that inhibits the transcription of the lac operon present in the plasmid. So, when IPTG is added to the mixture, it prevents the lac repressor from blocking the transcription, which then allows the transcription of genes, including eGFP, in the lac operon [94].

After 1 h of induction time, the temperature was changed to 30° C, to de-accelerate cellular growth and increase protein expression. After 16 h of incubation, the cell culture was centrifuged at 4500 g for 15 min at 4° C. The supernantant obtained was discarded and the pellet was re-suspended in a lysis buffer (20 mM imidazole, 300 mM NaCl and 50 mM potassium phosphate

at pH 8.0) and stored at -20° C.

3.3.2 Cellular Culture for the Expression of mCherry

A very similar protocol to the above described was followed for the expression of mCherry. The DNA plasmid pBADmCherry was inserted into *E. coli* BL21 (DE3) competent cells. This plasmid contains the genetic sequence for the expression of mCherry. It also contains a histidine tag, but contrary to eGFP plasmid, it contains an arabinose promoter.

A mini-culture was also prepared by inoculating 100 mL of lysogeny broth (LB) and the antibiotic carbenicillin (50 μg/mL) with the mentioned *E. coli*. The culture was left to grow for 16 h at 37° C and 180 rpm. Equally, 20 mL of said culture were used to inoculate 1 L of LB with 50 μg/mL carbenicillin, which was then incubated as before. However, in this case the OD_{600nm} of the culture was closely monitored until it reached a value between 0.6-0.8, when mCherry expression was induced by adding arabinose from a 20% stock solution for a final concentration of 0.2%. Contrary to IPTG induction, in this case the arabinose promoter *ara* p_{BAD} is intrinsically off. However, once arabinose is added to the system, the protein AraC, bound to the promoter, senses the presence of the sugar and binds preferentially to it. This in turn liberates the DNA, which allows the expression of the proteins under *ara* p_{BAD} [95].

The rest of the steps followed are the same as the ones described above for eGFP.

3.3.3 Purification of Fluorescent Proteins

The purification technique used in this work is immobilised-metal affinity chromatography (IMAC), and is based on the affinity of transition metals (here nickel, Ni^{2+}) to histidine tags present in the proteins [96]. Said metal is bound to the porous agarose matrix of the purification column through the chelating ligand nitriloacetic acid (NTA). The coordination bond formed between NTA and Ni^{2+} leaves two valencies available for their interaction with the free pair of electrons from the nitrogen atoms of the imidazole rings of the histidine tag (His-tag) [96], as shown in the insert in Fig. 3.5.

The purification of both proteins followed the same protocol. Cells pellets were de-frozen and kept on ice, lysed by 3 sonication cycles of 30 seconds (Soniprep 150 plus MSE) and centrifuged at 18000 rpm (Sorvall SS34 rotor) at 4° C for 30 min. The supernatant was recovered and filtered through a 0.22 μm syringe filter (Millipore) and injected to a Ni-NTA agarose column (Qiagen) connected to an ÄKTA start purification system (GE Healthcare), in order to isolate the fluorescent proteins from the rest still present in the supernatant. The column had been previously equilibrated with the lysis buffer mentioned in the previous section. After the protein solution addition, the bound fluorescent proteins were washed with the same lysis buffer to elute unbound proteins. eGFP and mCherry were later eluted (extracted) with a linear gradient (0-100%) of a 500 mM imidazole, 300 mM NaCl, 50 mM potassium phosphate buffer at pH 8. This increasing gradient of imidazole creates an excess of said molecule, which displaces

the His-tag from the metal, and thus releases the protein. The recovered proteins were dialysed agains dH_2O for 16 h using a 10MWCo dialysis membrane. Finally, the proteins were collected and stored at -20° C.

3.3.4 Concentration of Fluorescent Proteins

Finally, the dialysed proteins were filtered through 0.22 μm syringe filter (Millipore) and concentrated to ~1 mL using protein 30 KDa concentrators (ThermoFisher Scientific) at 5000 rpm and 4° C for the time required to reach the desired volume.

The protein concentration was determined by measuring the absorbance at the excitation wavelength of each protein for several dilutions of the concentrated solution. The amount of protein can be obtained through the Beer-Lambert Law equation

$$A = L\epsilon c, \tag{3.1}$$

where A is the absorbance, L is the path length of the cell holder (usually 1 cm), ϵ the molar extinction coefficient and c is the concentration of the protein [97]. We measured the absorbance at λ_{eGFP} = 488 nm and λ_{mCherry} = 587 nm, where ϵ_{eGFP} = 56000 $M^{-1}cm^{-1}$ [98] and $\epsilon_{\text{mCherry}}$ = 72000 $M^{-1}cm^{-1}$ [99].

3.3.5 Protein Charge

The charge of the proteins was determined by measuring the zeta potential. The zeta potential is illustrated in Fig. 2.3 in Chapter 2.2.3 and it can be related the surface charge of the species when functional groups on their surface dissociate or ions from the solution adsorb onto them. From the figure, one can observe that the zeta potential is the one located in the boundary of the Stern and diffusive layer [100, 101]. We used the Zetasizer Nano ZS (Malvern) equipment that determines the zeta potential by measuring the electrophoretic mobility through:

$$\mu_e = \frac{2\epsilon\zeta f(\kappa a)}{3\eta} \tag{3.2}$$

where μ_e is the electrophoretic mobility obtained by dividing the protein velocity by the applied electric field strength, ϵ is the dielectric constant of the medium, ζ is the zeta potential, $f(\kappa a)$ is the Henry function evaluated at κa (ratio of the particle size and the Debye length) and η is viscosity of the medium [100, 102].

3.4 Event Driven Molecular Dynamics Simulations

The simulations carried out to study the dynamics of our binary mixtures in Chapter 4 were done using DynamO (DYNAMics of discrete Objects) [84], an open source simulation package based on event-driven molecular dynamics. In this type of molecular dynamics (MD) the trajectories of interacting particles are calculated according to elastic collision laws. Here, the particles travel with ballistic trajectories and thus they move in straight lines and preserve their velocity between impacts. Once the particles collide, their momenta need to be adjusted accordingly. In event-driven molecular dynamics all the particle collisions (events) are first identified and listed hierarchically according to when they will take place. The system is then evolved to the time of the first collision of said list. The momenta of the particles involved in this first event are updated and a new hierarchy list is created. This cycle is continued until sufficient events or the maximum simulation time have been completed [84, 103]. The advantage of using event-driven molecular dynamics is that only the momenta of the particles implicated in the collisions (or within the neighbourhood) need to be determined, reducing significantly the calculations and thus the computational and time costs [84].

The main properties of the system include the number of particles, their dimensions and mass along with their interactions, which are only hard-spheres for the work herein. Their position and velocity are adjusted as the simulation takes place. The velocity is set by the Andersen thermostat, so the temperature is the relevant parameter.

All the simulations performed in this work were conducted keeping constant the number of particles (N), the volume of the simulation box (V) and the temperature (T) of the system (NVT), using said Andersen thermostat [84, 103].

These simulations were performed to complement and get further insights into the experimental work of binary mixtures of hard spheres with different sizes, particularly the dynamics of the system. Therefore, the simulation conditions were chosen to mimic the ones from the experiments detailed in Chapter 4. As such, a size ratio of small and large particles of 0.39 was chosen, and the total packing fractions ranged from 0.52 to 0.64.

3.5 Acknowledgements

The expression and purification of both proteins was done in collaboration with Dr. Ross Anderson and Dr. Angélique Coutable in the School of Biochemistry at the University of Bristol. Dr. Coutable helped and supervised throughout all the different procedures.

On the other hand, the synthesis of iron-oxide nanoparticles was first carried out in collaboration with Dr. Steve Whitelam and Dr. Jeffrey Urban of the Molecular Foundry at the Lawrence Berkeley National Laboratory in Berkeley, California. Dr. Jason Forster, member of Dr. Urban's group, helped and supervised the synthesis of the metallic nanoparticles.

Chapter 4

Crystallisation of Binary Mixtures of Hard Spheres: Non-Equilibrium Interstitial Solid Solutions

Author Contributions: Based on the work published in article: I. Ríos de Anda, F. Turci, R. P. Sear and C. P. Royall, Long-Lived Non-Equilibrium Interstitial-Solid-Solutions in Binary Mixtures, Journal of Chemical Physics, 147,124504 (2017). The experiments, simulations and data analysis done for this paper were carried out by the first author. Data analysis of the experimental and simulation work was also done by the second author. Both, the third and fourth author supervised the work.

In this chapter we study binary mixtures of hard spheres where the particles differ on their diameters, giving a size ratio of 0.39. Binary hard spheres represent the next level of complexity for monodisperse systems with these type of interactions. We performed particle resolved experimental studies of the heterogeneous crystallisation of this system and further compared these results with molecular dynamics simulations of homogenous nucleation that mimic the experimental conditions. Interestingly, we observed that for both approaches the final structures correspond to *interstitial solid solutions*, where the ordered structure is made up by a mixture of closed-packed fcc and hcp lattices of the large particles, whilst the small species are located in a random fashion in the interstitial sites of the former. Our structures closely resemble the ones observed by Filion and collaborators at equilibrium, whose system had a size ratio of 0.4 [26]. However, the composition of our ISS was different: our simulation studies of said parameter and dynamics of the small particles, showed that the occupancy of the octahedral sites reaches a maximum of ~14% for most the packing fractions examined and that the small particles are immobile once located in the octahedral holes of the ordered structure, leading to long-lived non-equilibrium structures.

4.1 Introduction

As discussed earlier, the most explored experimental model system to study self-assembly and phase behaviour of atoms and molecules is colloidal hard spheres. In this system the particles only interact at contact at which they experience hard-core repulsions, since they cannot overlap [92, 13], as discussed in Chapter 2. Advances in microscopy have allowed for the study of the evolution of phase transitions and dynamics of these systems in real time and space. Furthermore, these systems have also been extensively studied in simulations, which have been able to successfully replicate the phenomena and assemblies found in experiments [13]. The simplest and most popular system of hard spheres is the one-component one. The extensive literature on this system in both experiments and simulations has identified the face-centered cubic (fcc) phase- often mixed with hexagonal close placking (hcp)- as the equilibrium structure. Additionally, entropy has been identified as the driving force yielding a phase transition: the loss of configurational order as the system becomes more ordered is compensated by the gain in local entropy, since under ordered configurations the particles have a larger local volume to explore. The study of the crystallisation of equal hard spheres is relevant for fundamental understanding of monodisperse systems, but also for applications in material science, metallurgy, energy and biotechnology [104, 105].

However, as the particles in this system are identical, the final equilibrium structure will remain fcc. Therefore, the study of the self-assembly process of polydisperse colloidal mixtures has acquired more interest, as these present a richer and more complex phase behaviour and assemblies than their monocomponent counterpart [106, 107, 108, 26, 31, 43]. The simplest polydisperse colloidal system is a *binary mixture of hard spheres*, formed by two populations of spheres of differing sizes, and thus they are the reference model to study phase transitions of mixtures [107, 108, 26, 31]. Just as the monodisperse case, crystallisation in binary mixtures of hard-spheres is driven entropically. Thus, the large diversity of assemblies arise– and depends– on the difference in size of the components, the composition of the mixture and the total concentration [13, 26, 109, 110].

Crystals of these systems were first identified in Brazilian gem opals by Sanders and Murray in 1978 [111]. These rocks are composed of silica particles and had an structure analogue to AlB_2 and $NaZn_{13}$ [111]. Nowadays, experimental and computational studies on two-component hard-spheres have produced a large variety of structures resembling the ones found in nature for different salts including NaCl, $NaZn_{13}$, AlB_2 [108, 43, 109, 31, 26]. Additionally, the Laves structures $MgCu_2$, $MgNi_2$, $MgZn_2$ [111, 26, 13] have also been predicted. Most recently, stable interstitial-solid-solutions which are analogs of metal alloys, have also been observed [26]. Thus binary mixtures of hard spheres represent ideal models to study the kinetic mechanisms of salt, metal alloys and bulk metallic glasses formation [26, 13, 112, 113]. In addition, such a big variety of equilibrium structures highlights their potential for promising applications in photonics, optics, semiconductors and structure design [108, 109, 26, 31].

Of particular interest is the study of interstitial solid solutions (ISS) which are amongst the toughest and most versatile crystalline materials [114]. ISS appear when the size ratio of the partilces, γ, is $\leqslant 0.4$ [115]. Unlike in binary crystals, in ISS the components do not form perfectly interpenetrating crystalline lattices. Instead, only one of the components forms the crystalline phase whilst the other fills randomly the interstitial spaces of the former [26, 13, 115]. Metal alloys are a good example of ISS, for instance steel, where the iron atoms form an ordered crystal lattice, with the smaller carbon atoms in the interstices [116]. Moreover, the occupancy of these sites confers steel its characteristic strength. Similarly, the presence of interstitial hydrogen on metallic lattices allows or enhances the superconductivity of the materials [117]. Thus, understanding the mechanisms that yield, and might improve or prevent the solubility of the small species in the crystalline lattice is of relevance for materials science and further technological applications of these alloys.

In spite of the great potential and interest in studying binary mixtures of hard spheres, only a few experimental studies have focused on their *crystallisation process*. One of the possible reasons for this is the great difficulty of obtaining close-packed ordered structures for these mixtures. It has been hypothesised that these limitations are caused by slow kinetics, caused by a competition of the growing crystal nuclei, as well as the compositional fluctuations that occur as a consequence of crystal formation. In addition, differences in sedimentation rates between the particles also play an important role in preventing crystallisation [118, 34, 31, 24].

Furthermore, these studies have also shown some discrepancies between the experimental observations and the predicted assemblies for particular size ratios and compositions, especially at concentrations near the glass transition [107, 26, 24]. More importantly, neither the kinetic contributions to crystallisation, nor the microscopic mechanisms that yield the ordering of mixtures are fully understood [36, 24], accentuating the complexity of these systems over monocomponent ones, and limiting their promising applications.

Based on the interest in understanding such crystallisation processes, our goal is to study experimentally the heterogeneous crystallisation of a mixture of colloidal hard spheres at the particle-resolved level and compare our results with previous predictions. Additionally, we use simulations to study the evolution of the crystals, in particular the dynamics of the small particles, and propose a mechanism for the crystal formation.

4.2 Methods

4.2.1 Experimental Techniques

Our experimental model consisted on sterically stabilised poly(methylmethacrylate) (PMMA) particles labelled with rhodamine and coumarin fluorescent dyes. The large particles had a size of σ_{L}=1700 nm and a polydispersity of 7%, whilst the small species had a diameter σ_{S}=669 nm and 7.8% of polydispersity, determined through scanning electron microscopy. Albeit the large

size distribution of the particles, we did observe heterogenous crystallisation when tested on their own. These dimensions yield a size ratio, ($\gamma = \sigma_{\mathrm{S}}/\sigma_{\mathrm{L}}$) of 0.39.

4.2.1.1 Sample Preparation

The particles were individually suspended in a solvent mixutre of 27% w/w cis-decahydronaphtalene (cis-decalin) and cyclohexyl bromide (CHB). This solution nearly matches the density and refractive index of the PMMA particles, thus reducing both the van der Waals attractions and gravitational sedimentation [28, 109, 119]. We added tetrabutylammonium bromide (TBAB) salt, that screens the charges of the particles through modulating the range of electrostatic interactions, due to its effect on the Debye screening length. This particular medium allows for hard-sphere behaviour [109, 119]. The suspensions were left to equilibrate for several hours and were mixed together to yield fixed equimolar suspensions (N_L/N_S=1) at different total volume fractions ϕ_{tot}, defined as $\phi_{\mathrm{tot}} = \phi_{\mathrm{L}} + \phi_{\mathrm{S}}$, where ϕ_{L} and ϕ_{L} correspond to the partial packing fractions of large and small particles, respectively. These were calculated based on the amount of particles and solvent weighed, following $\phi_{\mathrm{L/S}} = v_{\mathrm{L/S}}/(v_{\mathrm{L}} + v_{\mathrm{S}} + v_{\mathrm{solvent}})$.

4.2.1.2 Characterisation

After several hours of mixing, the samples were confined to squared capillaries of 0.50 x 0.50 mm (Vitrocom) and sealed on the ends with epoxy. Confocal laser scanning microscopy (CLSM - Leica SP5 fitted with a resonant scanner) was used to study the samples, using a NA 63x oil immersion objective. Two different channels were used at 543 nm and 488 nm for rhodamine and coumarin dyes, respectively. Scans of the capillary in the z axis were taken for 3D analysis of the structures, where care was taken to ensuring the pixel size was the same in all axes (0.125 μm/pixel).

4.2.1.3 Determining the Time Units

Particle resolved studies were conducted to study the crystalline structure [92]. The crystallisation time was calculated in Brownian time units of the large particles, that is, the time it takes for the large species to diffuse their own radius, given by $\tau_B = (\sigma_{\mathrm{L}}/2)^2/6D = 0.963s$, where D=0.125 μm/s is the diffusion constant for our system. Thus the Brownian time τ_B is our unit of time. Observations of the crystal formation were carried out for over a month, corresponding to 2.6×10^6 τ_B, and were made all along the length and height of the capillaries, which were kept in a vertical position.

4.2.2 Simulations

Hard sphere simulations were performed using the open-source event-driven molecular dynamics DynamO package [84, 120] in isothermal-isochoric (NVT) conditions for a binary mixture. De-

tails of this package are explained in Chapter 3.4. The total number of particles is $\mathrm{N_{tot}}$= 10 968, with an equal mass, m. The size and number ratio, as well as the final total particle densities were carefully chosen to match the ones from the experiments, thus γ= 0.39 and ϕ_{tot} from 0.52 to 0.64, respectively. A fluid system at ϕ_{tot} = 0.282 was used as the initial configuration, which was then linearly compressed following the Stillinger and Lubachevsky algorithm [121]. Once they reached the desired packing fraction, event-driven molecular dynamics is performed until we observed the formation and no further growth of interstitial solid solutions. Experimental studies have observed that colloidal particles stick irregularly on the walls of the cell in which they are contained, thus producing a random surface over which heterogeneous crystallisation takes place [122]. Since such a random monolayer is difficult to reproduce, we elected to conduct our simulations with periodic boundary conditions. However, future work focusing on simulating such environment and its influence over the kinetics of the system presented herein is worth pursuing.

4.2.3 Mapping Experimental and Simulation Times

Simulation times were scaled to the experimental data. We inferred our simulation τ_B through the previously described relationship τ_α= 2.597 τ_B, obtained by comparing event-driven MD simulations and colloidal experiments of a one-component hard sphere system at ϕ=0.38. In said study, the structural relaxation time τ_α of the simulations was found to equal 0.404 simulation time units [123]. Since this mapping corresponds to a one-component system, we calculated τ_α of our large species from the trajectories at the same packing fraction (ϕ_{tot}=0.38) in order to confirm that the relaxation of the large particles is similar in our binary system. Therefore, we computed the intermediate scattering function (ISF),

$$F(\mathbf{k}, t) = N^{-1} \langle \sum_{j=1}^{N} \exp[-i\mathbf{k} \cdot (x_j(t) - x_j(0)\rangle, \tag{4.1}$$

where $x_j(t)$ is the position of particle j at time t and k is the wavenumber. To characterise the mobility in the length scale of a large particle diameter, we evaluated $F(k, t)$ at the wavenumber $k = 2\pi/\sigma_{\mathrm{L}}$ [123, 124]. We obtained a value of τ_α=0.526 simulation time units, which is comparable to the one obtained by Royall *et al*. This confirms the validity of our approach and enables us to use the aforementioned relationship to infer the τ_B for our simulations.

4.2.4 Location of the Species in the Experiments

In order to determine the local ordering of the crystals formed in our experiments, we analysed separately the structures formed by each component through particle tracking. To locate the particles in the experiments, 3d data sets were directly analysed using the 'Colloids particle tracking' algorithm developed by Leocmach and Tanaka [125]. Briefly, the xyz coordinates of the

particles are determined by identifying Gaussian bright spots on the images, which correspond to the particles' centres.

4.2.5 Identification of the Type of Crystalline Structure

In order to identify the type of crystal formed in both our experiments and simulations, we followed Lechner and Dellago [126] and obtained the bond orientational order parameters (BOO), which are based on complex spherical harmonics. This analysis gives information of the particles' bond network based on the particles' proximity and arrangement, which can in turn be related to their degree and type of ordering, thus enabling us to differentiate between distinct crystalline phases. Based on previous predictions of crystalline structures for our size ratio [108, 31, 13], we focused on the locally averaged order parameters $\bar{q}_4$ and $\bar{q}_6$ for square and hexagonal orders, respectively. By averaging, these parameters take into account the effect of the second nearest neighbours, which distinguish more sharply amongst different arrangements [126], which was crucial in identifying the environment of the small particles, as will be shown later. The methodology followed is detailed elsewhere [126, 127, 22]. Firstly, we identified the nearest neighbours $N_b(i)$ for each particle i, regardless of its small or large nature. We did this by computing the pair distribution function, $g(r)$, of the systems, in order to find the contact distance between the closest large particles and used this distance as the cutoff. For the experiments said distance corresponded to $1.38\sigma_{\mathrm{L}}$, whereas for the simulations this number was $1.25\sigma_{\mathrm{L}}$. We also found this distance for perfect (by construction) NaCl-type lattice, which was of $1.1\sigma_{\mathrm{L}}$. Using said list of neighbours, the local order parameters, or Steinhardt bond orientational order parameters can be obtained [126]:

$$q_{lm}(i) = \frac{1}{N_b(i)} \sum_{j=-l}^{N_b(i)} Y_{lm}(r_{ij}) \tag{4.2}$$

and summing over all the harmonics:

$$q_l(i) = \sqrt{\frac{4\pi}{2l+1} \sum_{m=-l}^{l} |q_{lm}(i)|^2} \tag{4.3}$$

where $Y_{lm}(r_{ij})$ correspond to the spherical harmonics, l and m are integer parameters, the latter running from $m = -l$ to $m = +l$, and r_{ij} corresponds to the vector from particle i to particle j. However, these parameters only contain information about the first shell surrounding particle i. In order to obtain information about the second shell, and thus, the locally averaged order parameters, we need to sum over the list of $\tilde{N}_b(i)$ of particle i and the particle i itself, giving [126]:

$$\bar{q}_{lm}(i) = \frac{1}{\tilde{N}_b(i)} \sum_{k=0}^{\tilde{N}_b(i)} q_{lm}(k), \tag{4.4}$$

and again summing over all the harmonics we get [126]:

$$\bar{q}_l(i) = \sqrt{\frac{4\pi}{2l+1} \sum_{m=-l}^{l} |\bar{q}_{lm}(i)|^2} \tag{4.5}$$

4.2.6 Determination of the Lengthscale and Quality of Crystalline Ordering

In order to study the quality of the crystals found, we followed the analysis described by Fullerton and coworkers [128, 129] for identifying the length scales of the crystal domains in both our experiments and simulations. The typical crystalline domain size, N_Q, is an estimate of the average number of particles in a coherently ordered crystallite, and thus can be a measure of the quality of the ordered structure. The values taken by it will depend on the number of particles oriented in the same fashion: the longer the length scale of the ordered structure, the larger the number, and thus the quality of the crystal. It is given by $N_Q = N^{-1}\langle \vec{Q}^* \cdot \vec{Q} \rangle$, where N is the total number of particles. Here $\vec{Q} = \sum_{p=1}^{N} \vec{q}_6(p)$ is the sum over all particles of the normalised complex vector $\vec{q}_6(p)$, whose components are the spherical harmonics with l=6. $\vec{q}_6(p)$ normalisation is done by setting the average of $\vec{q}_6(p) \cdot \vec{q}_6(p)^* = 1$.

4.3 Results and Discussion

We present our results and analysis in three different sections. Firstly we identify and compare the type of crystalline structure and its quality in both our experiments and simulations. Next, we set our attention on the individual dynamics of the two species in both the fluid and the ordered phases in our simulations. And then, we compare the small particle composition of the ISS found with the ones reported previously at equilibrium for a system with a comparable size ratio. With these analyses, we finish by proposing a mechanism for the formation of the structures found.

4.3.1 Analysis of the Crystalline Structures: Identification of Interstitial Solid Solutions (ISS)

Filion and collaborators studied computationally a mixture of binary hard spehres with a size ratio comparable with ours, γ=0.4 [13]. They obtained the phase diagram at equilibrium, which is reproduced in Fig. 4.1 (a). Here, the diamonds represent our experimental state points for experimental heterogeneous nucleation, whereas the circles and triangles correspond to the simulation state points. According to the phase diagram, at equilibrium the structures consist of interstitial solid solutions (ISS) in coexistance with a fluid phase (F) [13]. The former structures consist of regular close-packed lattices formed by the large particles, with the small species

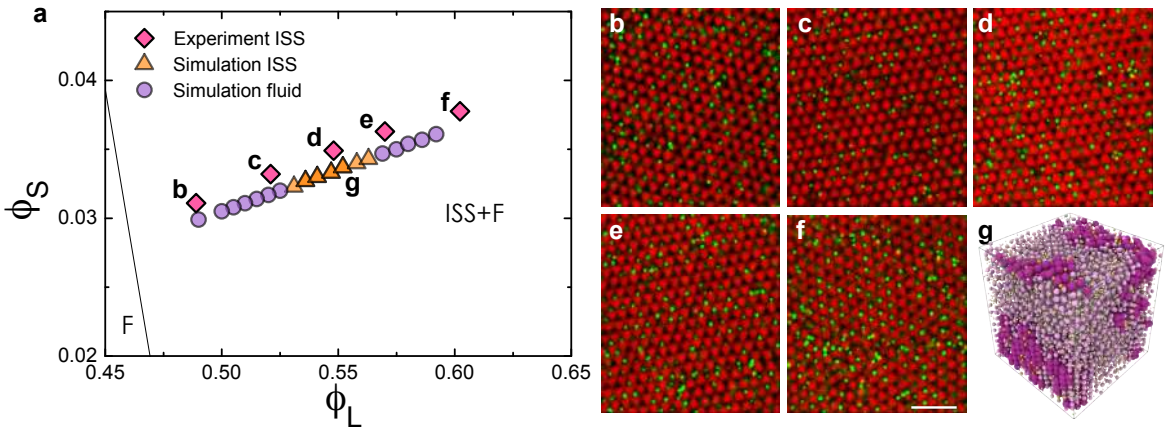

Figure 4.1: (a) Phase diagram obtained by Filion, *et al.* of binary hard spheres with a size ratio γ = 0.4 [13], in the ϕ_L-ϕ_S plane. The symbols represent our state points at a size ratio $\gamma = 0.39$, and number ratio of one as follows: diamonds: ISS from heterogenous nucleation experiments; purple circles: simulations that did not crystallise; orange triangles: ISS from simulations. (b-f) Characteristic snapshots of crystalline structures found on experiments for different ϕ_{tot}, the letters b to f in (a) indicate the position on the phase-diagram. The red and green colours are the large and small particles, respectively, and the scale bar = 10 μm. (g) ISS found in simulations with ϕ_{tot}=0.586, where ordered large and small particles are coloured purple and yellow, respectively, whereas fluid large and small particles appear in light pink and light yellow, respectively.

occupying randomly the octahedral sites of the ordered structures. It is worth noticing that the occupancy of said holes varies continuously with composition.

In agreement with the phase diagram, we observed in both our experiments and simulations, crystalline structures built up exclusively of the large particles with the small ones filling some but not all of the octahedral holes (Snapshots Fig. 4.1), regardless of the ϕ_{tot} and in coexistence with a disordered phase. Interestingly, the ϕ_{tot} range at which we observed crystalline structures in simulations was much smaller than in the experiments, extending only from ϕ_{tot}=0.563 to ϕ_{tot}=0.610 (Fig. 4.1 purple circles).

The reason for the disparity can be due to the different type of nucleation present in our experiments and simulations. In the former, the nucleation is heterogeneous, i.e., the crystals start growing parallel to the walls of the capillaries, with the fluid phase remaining far way from them [130]. On the contrary, in simulations the nucleation process starts in the bulk. The presence of a flat wall clearly facilitates nucleation [131] and thus our experiments present a larger ϕ_{tot} that crystallise.

In both cases, the ordered structures observed are stable ISS [132] on the time scales studied. In these structures, the crystals start nucleating from the fluid phase and form ordered close packed ones composed solely by the large particles, whereas the small species partially fill the interstices of it. This produces a difference in the composition of the two phases: the crystal being poor on small particles and the fluid being richer on them [133, 26]. These compositions are also different from the original equimolar fluid.

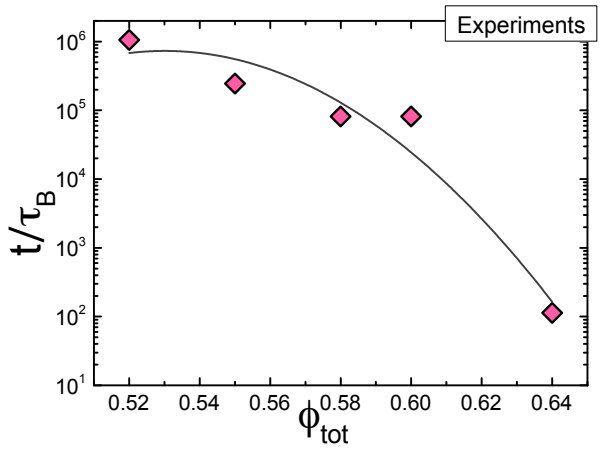

Figure 4.2: Experimental results of the heterogeneous crystallisation time of the binary system in terms of Brownian motion, τ_B. The line is a guide to the eye.

Additionally, we studied the heterogenous crystallisation of our experimental mixtures according to the total volume fractions $\phi_{\text{tot}} = \phi_L + \phi_S$. We found that higher ϕ_{tot} yields faster crystallisation rates, as shown in Fig. 4.2, which is in agreement with one component systems [104].

4.3.1.1 Local Structure of the Large Particles

According to the phase diagram shown above, the equilibrium structure for all of our samples is an interstitial solid solution in coexistence with a fluid phase [13]. In the ISS, the large particles are expected to form a random mixture of fcc and hcp lattices, known as random hexagonal close packing (rhcp). As aforementioned, this is also the case for monodisperse systems [104]. Such mixture is due to a very small free-energy difference between the two crystalline phases (only 0.001 $k_B T$) near coexistence [26, 13].

In order to determine if our ordered structures of large particles are indeed rhcp, we found the local bond-orientational order parameters for only the large particles in both our experiments and simulations. As explained before, these parameters can help us to sharply distinguish between different crystalline phases. The results of the analysis for both the experiments and simulations are summarised in Fig. 4.3 (a and b, respectively), where the plots show the population distribution of the particles in different regions that correspond to fcc and hcp lattices and the fluid phase (see Fig. 4.3 a, left), for all the total volume fractions tested. We also included a concentration of particles where we did not observe crystallisation in the simulations Fig. 4.3 (b, left) to further illustrate a purely fluid phase. The analysis shows that indeed our crystalline phases correspond to the predicted ones.

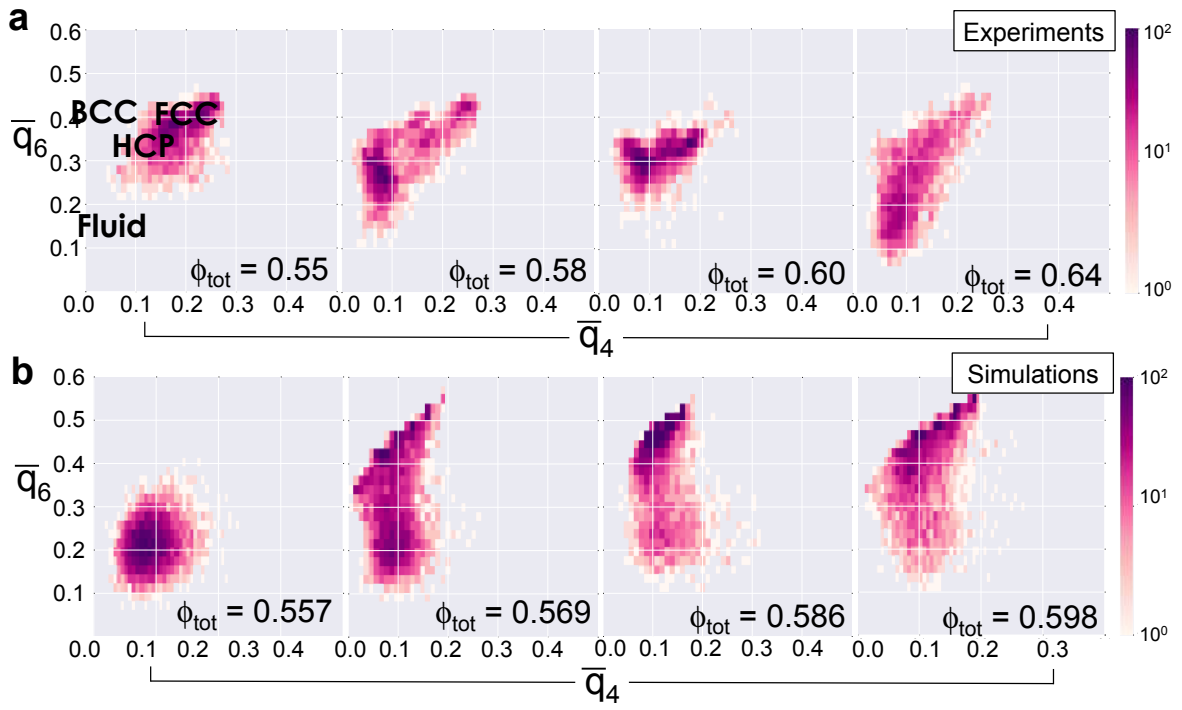

Figure 4.3: Bond orientational order parameter diagrams for the crystalline phases found in (a) experiments and (b) simulations. The graphs show a mixture of fcc, hcp crystalline lattices and fluid coexistence for different total volume fractions tested for both studies, all at final times. The simulations of the low ϕ_{tot}=0.557 is included to show the presence of only a liquid phase. The regions corresponding to perfect bcc, fcc, hcp lattices are shown in the top-left plot. Both parameters were calculated using only the large particles.

4.3.1.2 Local Environment of the Small Particles

As aforementioned, in the ISS the small particles are situated in the octahedral holes of the fcc and hcp lattices formed by large particles. Filion *et al.* found that for their smaller size ratio of 0.3, the small species present mobility through the lattice and are able to hop between interstitial holes and fill all the octahedral holes to yield a binary crystal [26], with two perfectly interpenetrating fcc lattices of the large and small species.

Nevertheless, for the larger size ratio of 0.4, Filion and coworkers also found that ISS are the stable assembly, and for this larger size ratio they do not report the formation of a perfect crystalline NaCl structure, nor they show the dynamics of the small particles like for γ=0.3 [13]. In our experiments with a similar size ratio of 0.39, we also identified only ISS, and we could not observe hopping of the small particles in direct imaging. In order to study the dynamics of the system, we needed to track the small particles at different stages of the crystallisation process and after the large particles had self-assembled, which we could not achieve due to bleaching of the dye, drifting of the sample and particularly, to limitations on tracking the motion of the small particles. Therefore, we decided to conduct hard sphere molecular dynamics simulations in order to overcome these limitations and quantify both the small sphere ordering and dynamics.

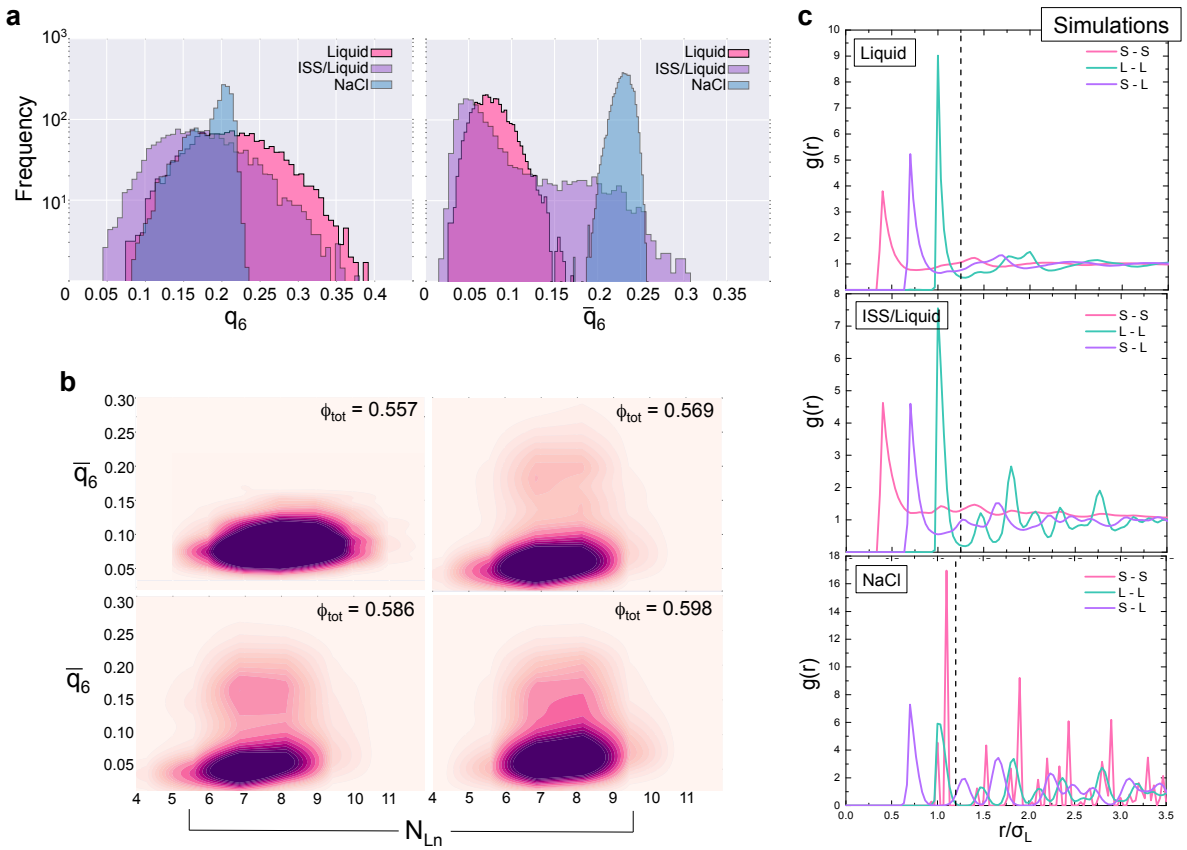

Figure 4.4: (a) Histograms of the bond orientational parameters q_6 (left) and $\bar{q}_6$ (right) values of the small particles at ϕ_{tot}=0.586 before crystallisation (pink) and after crystallisation (purple), compared with an equilibrated NaCl-type crystal at ϕ_{tot}=0.64 (blue), showing the ability of $\bar{q}_6$ to distinguish the local environment of the small particles. (b) Heat maps of the $\bar{q}_6$ values of the small particles and their corresponding number of neighbouring large particles (N_{Ln}) for different total volume fractions that crystallised in simulations, calculated following reference [125]. The plots show two populations: one below and one above $\bar{q}_6$ = 0.15. Note that ϕ_{tot}=0.557 does not crystallise. (c) Radial distribution functions of the liquid (top) and ISS/Liquid (middle) both at ϕ_{tot}=0.586, and NaCl-type crystal (bottom) at ϕ_{tot}=0.64. Each shows the small-small (S-S), large-large (L-L) and small-large (S-L) interactions. The dashed lines indicate the minimum corresponding to the small and large contact cutoff used for the BOO analysis.

As detailed above, the simulation conditions were carefully chosen so that they would mimic the experimental ones. It is important to mention that in the simulations, the movement of the particles is not Brownian. However, it has been shown that at higher concentrations (like the ones employed herein), there is not meaningful difference between these two types of dynamics [134], and thus the results can be compared directly.

Since the small particles are situated in the octahedral holes of the fcc and hcp lattices formed by large particles, no crystalline structure is detected when they are analysed on their own. However, studying their local environment can give us information about the vacancies (defects) found in our ISS, and how they might depend on the total volume fraction.

Using simulation data, we then calculated the BOO q_6 and $\bar{q}_6$ values for the small component in order to evaluate their local environment, i.e., determine if they are in the vicinit of a crystalline

region or a fluid phase (see Fig. 4.4(a) and (b)). In panel *a*, we compare the histograms of the q_6 (left) and $\bar{q}_6$ (right) values of particles in the liquid state (pink), in a state that is partially crystallised with remaining liquid (ISS-fluid coexistence, purple), and in a perfect (by construction) NaCl-type crystal (blue). It is clear that the parameter q_6 is not able to differentiate between the various configurations, unlike $\bar{q}_6$ which does distinguish between the liquid and the ISS state. So we use the Lechner-Dellago averaged $\bar{q}_6$ in order to identify the fluid or crystalline nature of the small particles. Since values of $\bar{q}_6$ above 0.15 are very rare in the liquid and dominant in a well-ordered NaCl structure $\bar{q}_6$ (see panel *a, left*), we stablished $\bar{q}_6$=0.15 as the cutoff value. Therefore, small particles with values below the cutoff correspond to small particles in the disordered phase, and vice versa.

To further demonstrate the validity of our approach, we obtained heat maps of the probability distribution of neighbouring large particles and $\bar{q}_6$, $p(N_{\mathrm{Ln}}, \bar{q}_6)$ for 4 states: one liquid (top-left) and three ISS/liquid mixtures, shown in Fig. 4.4(b). The samples with coexistent liquid and ISS show again two populations. The dominant one, with $\bar{q}_6 < 0.15$ is the liquid, but there is a smaller population with $\bar{q}_6 > 0.15$, which is consistent with values of $\bar{q}_6$ in the crystal. Moreover, particles with these latter values, have between 6 and 8 large-particle neighbours. Since in the NaCl structure each small is surrounded by 6 large-particle, our findings further support the association between the small particle population with $\bar{q}_6$>0.15 and the ISS. Note that the liquid sample (ϕ_{tot}=0.557) presents a broader N_{Ln} distribution– from 5 to 10. As described in the methods, our cutoff distance for the identification of neighbours was obtained by computing the pair distribution function, $g(r)$ of the small-small (S-S), small-large (S-L) and large-large (L-L) particle interactions in the liquid phase, the ISS/liquid case and for a perfect NaCl-type crystal (see Fig. 4.4(c)). The cutoff distance was established as the minimum corresponding to the contact distance between two large particles (L-L) (dotted line in Fig. 4.4(c)). Said distance is above the small-large (S-L) nearest neighbour distance (first minimum of purple curves), which might be the reason why we observed more than 6 neighbours.

4.3.1.3 Composition of the crystalline domains

Now that we can differentiate between crystalline and fluid small particles, we can follow the crystal growth by monitoring the number of crystalline large particles, N_{XL}, along with the number of small particles located in the octahedral holes (N_{XS}), according to their $\bar{q}_6$ values. These results are shown in Fig. 4.5 (a) and (b), respectively. Interestingly, we observe that both quantities increase and tend towards a plateau at very similar times, indicating no further crystal growth and suggesting no hopping of the small particles within the interstitial sites of the fcc and hcp lattices, as discussed previously [26].

Next, we calculated the ratio of N_{XL}/N_{XS} forming the ordered phase. We found two notable phenomena. Firstly, the octahedral holes are filled rapidly as the nucleation takes place (Fig. 4.5 (b)) with a maximum filling of the octahedral sites of around 14%, above ϕ_{tot}=0.586 (see Fig.

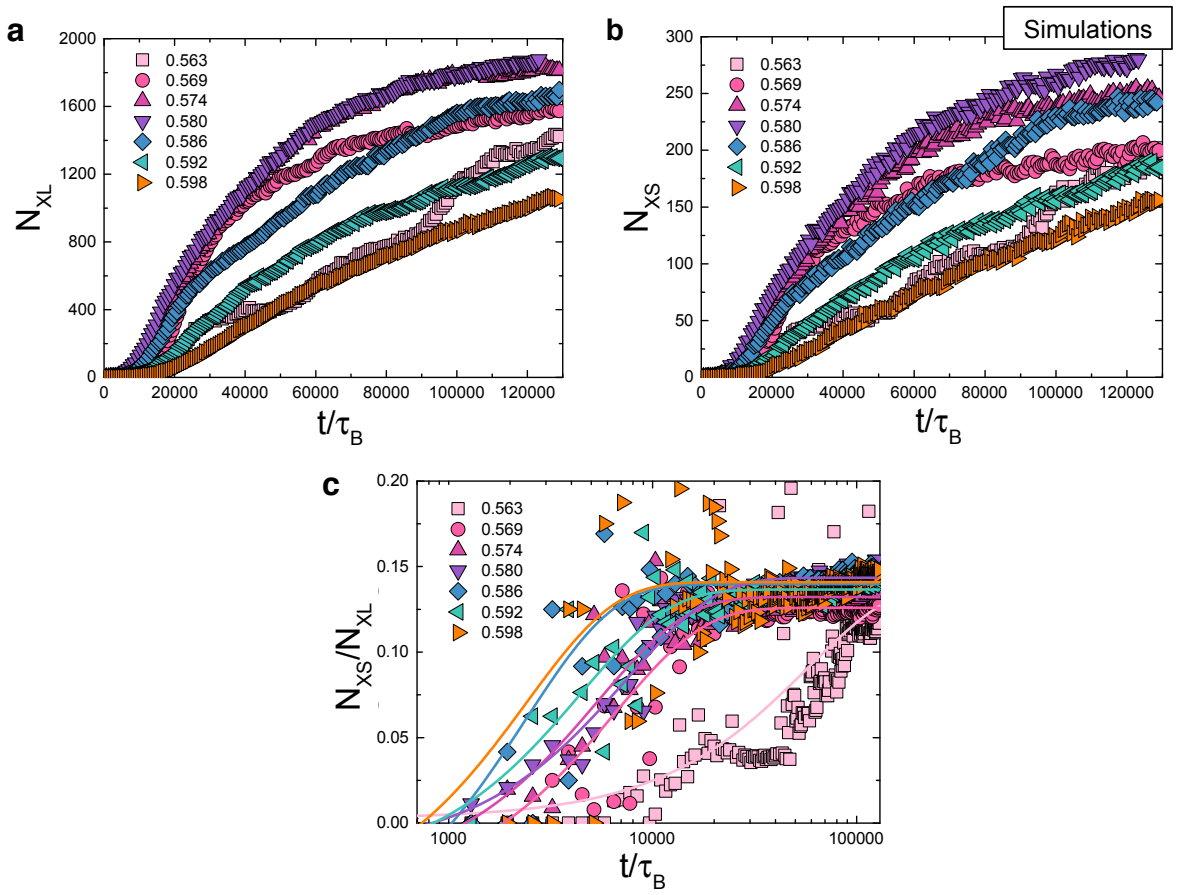

Figure 4.5: The numbers of large (a) and small (b) crystalline particles as a function of time in simulations. (c) evolution of the proportion of small crystalline particles relative to the large crystalline ones in simulations according to their ϕ_{tot}.The simulation time has been rescaled to Brownian time (see Methods for details).

4.8 (b)). Secondly, we observed no further changes in the proportion of crystalline particles, suggesting no further movement of the small particles, to either enter or leave the crystal. Since the number of small crystalline particles also reached a constant value, we infer that they become trapped (and immobilised) in the the ordered lattices once they are formed. We will explore in detail these phenomena.

4.3.1.4 Crystalline Domains in Experiments and Simulations: Evaluation of the Crystal Quality

To enrich the analysis of the crystals found, we evaluated their quality. One way to assess the quality is by identifying if the crystalline large particles are in one large crystalline domain, or if the system is polycrystalline. To do so, we follow the work by Klotsa and Jack [128, 129], where the authors defined the parameter N_Q which describes the size of coherent crystallites, i.e., the typical number of particles with the same direction in an ordered crystal. N_Q thus takes large values (close to N) the larger the amount of particles oriented in the same direction, *i.e.*, if they

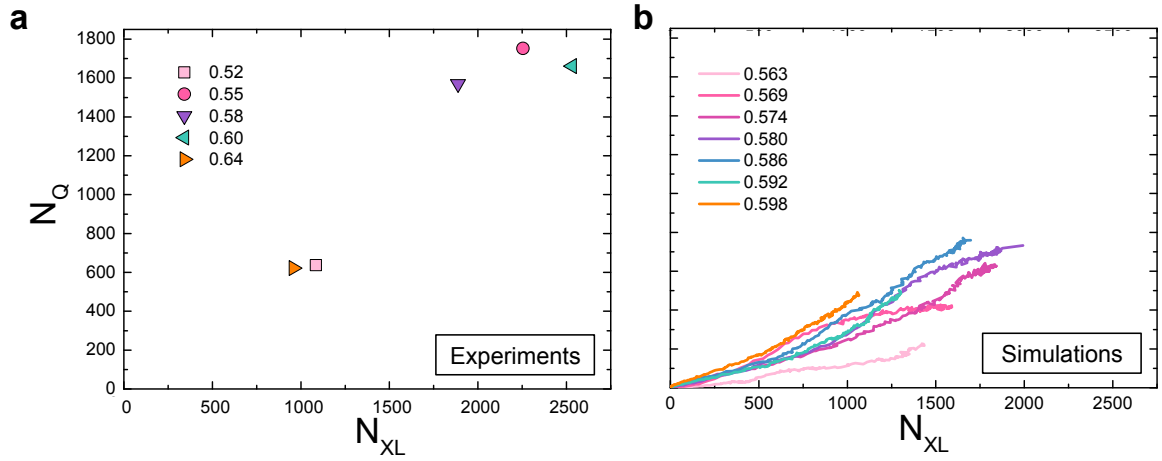

Figure 4.6: The characteristic size of the crystal domain(s), N_Q, as a function of the total number of large crystalline particles, N_{XL}. For the experiments, we show the final values as symbols, see key, whilst the computer simulations are shown as a curve corresponding to the evolution with time during crystallisation. The total number of large particles in the experiments is 2534, 2645, 2584, 2524 and 2244 for ϕ_{tot}=0.64, 0.60, 0.58, 0.55 and 0.52, respectively. On the other hand, for simulations the total number is 5,484 of large and 5,484 of small particles. From our N_Q values we can conclude that the quality of the crystals obtained in the experiments is higher than the simulations.

belong to the same cluster. We applied this analysis to both our experiments and simulations to determine which conditions yielded the crystaline domains with the highest coherence. In the case of the experiments, we analysed only the final structures formed by the large particles, whereas for the simulations, we were able to study the evolution of N_Q through the crystallisation of the different packing fractions.

The results are presented in Fig. 4.6, where we compare N_Q with the number of large crystalline particles, N_{XL}, for experiments (symbols) and simulations (curves). It is evident from these results that the size of the crystalline domains obtained from heterogeneous nucleation in the experiments is higher than the quality obtained from homogenous nucleation present in the simulations, as N_Q presents significantly larger values in the former for similar N_{XL}. Furthermore, the N_Q values for the experiments are close to the number of crystalline particles.

In the case of simulations, the numerical values of N_Q are significantly smaller than N_{XL} in all the samples, indicating that the domains of crystals are small and thus there is a presence of several clusters. Also, a non-monotonic behaviour of this value is noted, since the highest values of N_Q do not correspond to the largest values of crystalline large particles. This is evident for ϕ_{tot}=0.598, whose maximum N_Q surpasses the correspondent of ϕ_{tot}=0.563 and 0.569, that on the other hand, present a higher number of crystalline particles (Fig. 4.6 (b) orange, light pink, and pink lines, respectively). Interestingly, the dependence between these two parameters is not linear, with N_Q increasing faster than the crystal growth. A possible reason for this could be coalescence between the forming crystalline clusters. This can be observed for ϕ_{tot}=0.574 (Fig. 4.6 (b) dark pink line), who shows a faster increase of N_Q around $N_{XL} \sim \mathbf{1000}$, which could be a

consequence of two clusters merging to form a larger one.

Reasons for the difference of the quality of the crystals formed between the experiments and simulations include the presence of the flat walls of the capillaries, larger system sizes or the need for longer waiting times. Indeed, it has been observed that flat walls can act as a template that enhances nucleation and layering of the particles, which in turn improves the orientation of the crystal [104, 135]. On the other hand, estimations of the crystallisation time for our experiments for homogenous nucleation were found to be two orders of magnitude larger than the corresponding crystallisation time on our simulations, suggesting that longer waiting times are required for experimental homogenous crystallisation. This might be related to the higher polydispersity in the experimental system. Moreover, said time surpasses our limit for experimental timescale observations of a month ($2.6 \times 10^6\ \tau_B$), after which the sample becomes less stable due to solvent evaporation. Indeed, when experiments for homogenous nucleation were carried out, only one experiment underwent crystallisation, at ϕ_{tot}=0.55. Moreover, this only occurred in one experiment, which we were not able to replicate. Finally, the system size in the experiments is of order 10^5 times bigger than the simulations. Hence it seems likely that our experiments can crystallise over a wider range and form crystals with a greater quality due to a combination of the reasons mentioned above.

It is important to highlight again that the range of packing fractions that crystallised *on the simulation timescale* was smaller than that of the experiments (see Figs. 4.1 and 4.6). However, in both experiments and simulations there are packing fractions where a maximum amount of crystallisation was reached. In experiments we observe regions in the system where the majority of the particles analysed is identified as crystalline. For example, at $\phi_{\text{tot}} = 0.55, 0.58$ and 0.60 —see Fig. 4.6 (a), the fraction of crystalline large species is around 65% or above. On the other hand, the total amount of crystalline structure in the simulations is much smaller, reaching the highest amount around 18% at ϕ_{tot}=0.580, after which it decreases, as shown in Fig. 4.6 (b).

In addition, we also identified a need for a larger ϕ_{tot} to observe crystallisation in our binary system on the simulation timescale, ϕ_{tot}=0.563, in comparison with the one needed for one component systems of ϕ=0.53 [136]. Such difference might be due to a higher free-energy barrier to generate the necessary nuclei for crystallisation. On the other hand, the drop of the crystalline fraction of our system at ϕ_{tot} above 0.598, is similar to the one where one-component systems exhibit slow dynamics $\phi \simeq 0.58$ [113]. In the latter, such decrease is related to the particles moving more slowly as their concentration increases, requiring a longer time to rearrange in ordered structures. A similar and more dramatic trapping phenomenon could be happening here, where the particles do not move fast enough to rearrange and form ordered structures.

4.3.2 Study of the Dynamics of the System in Simulation

We continue to study the dynamics of both the large and small particles in our simulations. This we did in order to show whether or not there is an arrest on the dynamics once the maximum

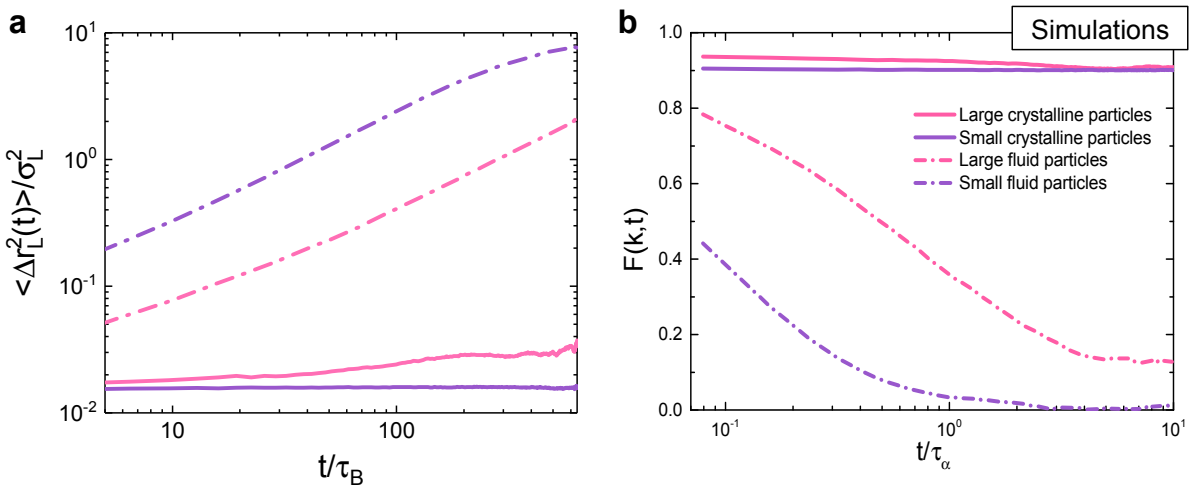

Figure 4.7: Mean square displacement (a) and intermediate scattering functions (b) from simulations at ϕ_{tot}=0.586. The large and small particles are shown in pink and purple, respectively. The continuous lines correspond to particles identified as crystalline, and dotted lines correspond to those identified as disordered. The simulations start at the end of a crystallisation simulation. Particles at the liquid-crystal boundary region were discarded in order to characterise only the crystalline and fluid particles.

amount of crystallisation has been reached. Thus, in order to prove that our small particles were indeed localised, we computed both the mean square displacement (MSD) and the intermediate scattering function (ISF) directly from the trajectories of both the large and small species geometrically selected in the liquid and crystalline phases for ϕ_{tot}=0.586.

Both parameters study the displacement of the particles at a time interval, t, as follows. MSD describes the averaged distance traveled by a particle experiencing Brownian motion [137], and is given by

$$\langle \Delta r_L^2(t) \rangle = \langle (r_L(t) - r_L(0))^2 \rangle \tag{4.6}$$

where r_L corresponds to the radius of the large particles.

On the other hand, the ISF, introduced in the Methods section as equation 4.1, describes how quickly the particles diffuse from their original positions. ISF typically start at 1 and decay as the particles in the system rearrange [123, 124]. We evaluated $F(k,t)$ at the wavenumber $k = 2\pi/\sigma_L$ to study the motion on the length scale of the diameter of the large particles.

The analysis was conducted at the final points of the simulation, once the ratio N_{XS}/N_{XL} remained constant. The results are summarised in Fig. 4.7. We observe that both the large and small particles in the liquid region diffuse (Fig. 4.7, dotted pink and purple lines, respectively), *i.e.* their MSD (a) and ISF (b) present a behaviour typical for a confined random walk and a fluid, respectively. In contrast, both species identified as crystalline do not show any movement, showed as a flat line close to zero in the MSD and as a non-decaying line on the ISF (Fig. 4.7, continuous lines). We can conclude therefore that indeed, once the crystalline lattices are formed, the small particles remain localised within the octahedral site of the crystal formed by the large particles;

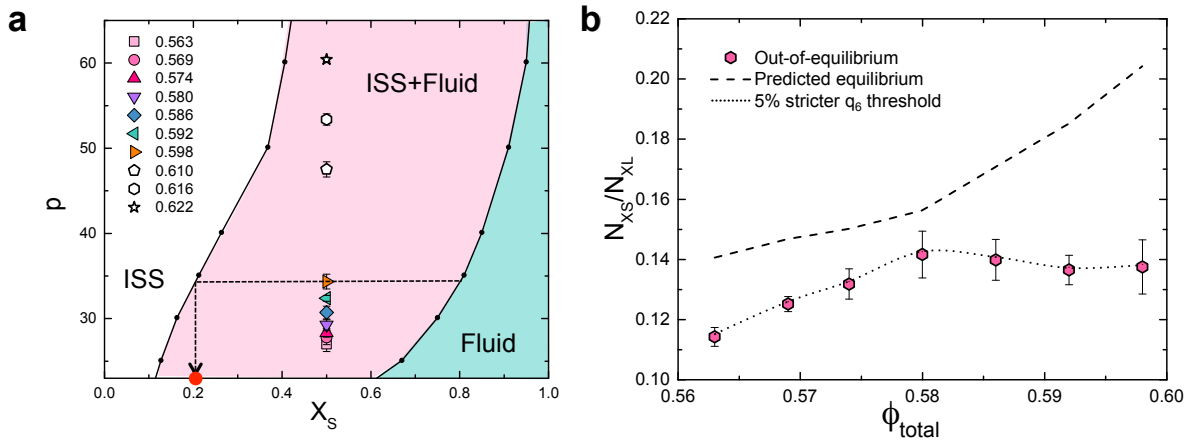

Figure 4.8: Comparison of our results with previous related work. (a) Phase diagram produced by Filion and coworkers [13] of a binary hard-sphere system with $\gamma = 0.4$, showing the reduced coexistence pressure $p = \beta P \sigma^3$, as a function of composition $X_S = N_S/(N_S+N_L)$. The filled symbols represent our state points where we observed ISS, whereas the empty symbols correspond to the conditions where, on our time scales, we did not observe crystallisation. The tie line and arrow are drawn to illustrate the interpolation process to obtain the small particle composition in the equilibrium ISS. (b) The crystal composition as a function of our system's volume fraction, ϕ_{total}. The dashed line corresponds to the equilibrium composition [13], and the hexagons are our simulation results. The error bars are the standard deviation of 8 runs, whereas the dotted line is the error obtained when using a 5% more strict $\tilde{q}_6$ threshold in the bond-orientational order analysis.

they are unable to hop and complete the occupancy of all the available octahedral holes, and thus our ISS remain as long-lived out-of-equilibrium structures.

4.3.3 Comparison of our Results with Previous Related Work

We finalise our analysis by comparing our results with previous work conducted on experiments and simulations of binary mixtures of hard spheres with γ=0.3 and 0.40.

From our simulation studies, we found that the small particles occupy the octahedral sites of the crystalline lattices in an incomplete fashion, forming dilute ISS with a consistent composition close to seven large particles per one small particle, much less than the one-to-one ratio in the original fluid phase. ISS have also been identified before in binary mixtures with a smaller size ratio of 0.3 compared to 0.39 here [26]. In this work, Filion and coauthors found that in order for the small particles to hop from one octahedral hole to the other to fill all the available octahedral holes– and form a binary crystal– they needed to access the adjacent tetrahedral hole first. This site has a size of ~0.225σ_L across at close-packing. Although slow, they found that their smaller particles could indeed hop and form a binary crystal. As proved in the previous section, this is not the case for our system.

For the system studied by Filion *et al.* with a size ratio of 0.4, the ISS equilibrium region in the phase diagram is larger than for 0.3. In order to confirm that our ISS are out-of-equilibrium, we compared the composition of small particles, $X_S = N_S/(N_S + N_L)$ of our simulations with the

equilibrium ones found by Filion [13]. Thus, we determined the final pressure in our simulations and located the results in the phase diagram (symbols in Fig. 4.8(a)). Then, using tie lines (which are horizontal here as the two phases have the same pressure) we calculated the composition of small particles of both the fluid and ISS phases at equilibrium, as shown by the dashed arrow in Fig. 4.8(a). Finally, we compare these values of X_S at equilibrium with the ones corresponding to our ISS, as shown in Fig. 4.8(b), where the dashed curve is the former, and both the symbols and the dotted curve are our results. The dotted curve corresponds to a 5% stricter $\bar{q}_6$ threshold in order to show that the phenomenon was independent of our chose of cutoff. Additionally, the error bars of the symbols correspond to the standard deviation of 8 different simulation runs. As can be observed, for all cases, the number of small particles within the crystalline structure is smaller than the one predicted for an ISS in equilibrium. Furthermore, this difference is large for systems at higher volume fractions.

Therefore, we can conclude that our ISS have not reached equilibrium, and presumably are out of equilibrium when they nucleate and grow. The possible explanation for this phenomenon is the following: as the large particles crystallise into ordered lattices, some of the small particles become trapped in the octahedral holes, forming the ISS. But under the conditions we study, further integration of the small particles into the growing crystal appears to be inefficient, resulting in the low number of small particles in the crystal. The ineffective occupancy of the available octahedral holes might be due to the crystalline phase being close-packed. Under these circumstances, the small particles do not have access the tetrahedral holes due to size constrictions and thus cannot reach the empty octahedral interstices. As a consequence, important compositional fluctuations arise on the remaining fluid, which becomes increasingly rich in the small species, as the crystal grows. Indeed, as shown in Fig. 4.8(a), increasing X_S will ultimately move the fluid out of the coexistence region and into the one-phase fluid region of the phase diagram. So, we believe this change in composition contributes to the growth of the crystal slowing and stopping. This results are in agreement with the suggestion that compositional fluctuations can slow and prevent crystal formation in binary crystals [108, 31].

4.4 Conclusions

We identified interstitial solid solutions in a binary hard sphere mixture with a size ratio of 0.39 through particle resolved experiments and simulations. Through the former, we were able to identify that the ordered structure consisted solely of the large species forming a close-packed mixture of fcc and hcp, with low crystallinity. On the other hand, the small particles occupy the octahedral sites of said lattices in an incomplete and random fashion. Simulations showed the same structures and allowed us to follow the crystallisation process and quantify the ISS composition. Simulations also allowed us to access the dynamics of the small particles once the crystal has formed and how they stop moving once the crystalline structure is formed. With

this information, we were able to propose a mechanism for the formation of the structures found as follows: the large particles crystallise independently from the small species, which in turn become rapidly trapped within the growing crystal, reaching maximum occupancy of the octahedral holes of ~14%, which is a smaller filling than the predicted at equilibrium conditions, particularly for total concentrations above 0.586. The exclusion of the small particles produces large compositional changes in the surrounding fluid which we believe prevents further crystal growth. Finally, we were able to show that the small species remain localised and are not able to penetrate the formed crystal nor to move within the octahedral holes due to size constrictions, and thus we obtained long-lived-out-of-equilibrium ISS.

Chapter 5

Crystallisation of Highly-Charged Particles: Low-Density Crystals

Author Contributions: This Chapter is based on the work published in the article: I. Ríos de Anda, A. Statt, F. Turci, and C.P. Royall, Low-Density Crystals in Charged Colloids: Comparison with Yukawa Theory, Contributions to Plasma Physics, 55, 172 (2015). The experimental section and calculations were carried out by the first author. Some data analysis of the experimental work was done by the second and third authors. The fourth author supervised the work.

In this chapter we study a highly charged colloidal system, i.e., with a long Debye screening length, which represents the next level of complexity for mono component systems with interactions different to hard spheres. It is believed that the charging of the colloidal particles arises from the spontaneous self-dissociation of the solvent and further interaction of the dissociated ions with the surface of the particles. Through particle-resolved studies, we observed that this system was able to crystallise at very low packing fractions $\phi \sim 0.015$. We quantitatively compared our system with the Yukawa model and found that the freezing point of our crystals is well described by said model. However, the structure analysis of the assemblies showed that the crystal formed for the highest packing fractions is not the fcc structure predicted, but bcc. Possible reasons for the discrepancy might include lack of full equilibration of the system, the Ostwald rule of stages and confinement.

5.1 Introduction

As mentioned previously, in colloidal dispersions the colloidal particles are not the only components as they are immersed in a solvent, where the counter-ions and salt-ions balance the electrostatic charge of the system [92]. In these cases the colloidal particles acquire a charge and the system can be described by soft repulsive interactions and they represent good model systems for studying metals, salts, dusty plasmas or even biological systems like proteins [10, 21, 138].

Nevertheless, the number of interacting species in the dispersions is too large to be taken into account. In order to facilitate the study of these systems, one can integrate out the degrees of freedom of the solvent and counter and salt-ions, and treat the dispersion as an *effective one-component* system where only the colloids are considered [139, 138]. If we first focus on the contributions of the solvent, we find that it only affects the dynamics of the colloids (the system is non-inertial on reasonable timescales) and has no impact on the equilibrium phase behaviour of the system [92]. Unlike the solution, the ions do need to be integrated out, and this can be successfully done using the DLVO approach [140].

For many cases, the interactions between charged colloids can be successfully described by the Derjaguin, Landau, Verwey and Overbeek (DLVO) model [140], where the colloidal species are treated as Yukawa particles and introduced in Chapter 2.2.3. In this model, both short-range attractive and electrostatic double-layer repulsive interactions are taken into account. The former interactions are due to van der Waals forces, whilst the latter arise from surface charges of the particles and the solvent counter-ions (screened Coulomb repulsion) [118, 21]. In the systems explored in this thesis, the van der Waals forces can be neglected due to refractive index matching and the steric stabilisation provided by polymer layer on our colloidal particles, as discussed previously (see Chapter 2.2.2). On the other hand, the electrostatic repulsion can be finely tuned by changing the amount of ions in the solvent, and thus the potential interaction can be modified from long-range repulsive, to short-range attractive or short-range repulsive [118, 39, 21], as already shown in the previous chapter. Control of these interactions allows the formation of more complex crystal ordering and phases transitions than one-component hard spheres and therefore represent a new level of complexity.

As such, the behaviour of many other similar systems highlighted above can then be successfully described [92, 141]. Indeed, as shown in Fig. 5.1, the behaviour of charged colloids and complex plasmas' can both be described by the DLVO model. Here, under the right conditions both systems exhibit phases characteristic of the Yukawa system: a fluid phase (f) and two crystalline structures: body-centred and face-centred cubic crystals (bcc and fcc, respectively). The model assumes that the electrostatic potential is weak enough that the linear Poisson-Boltzmann theory can be applied [138].

In the case when particle concentration in colloidal dispersions is high enough, steric interactions due to the finite particle size can become relevant [142], and thus it is appropriate to

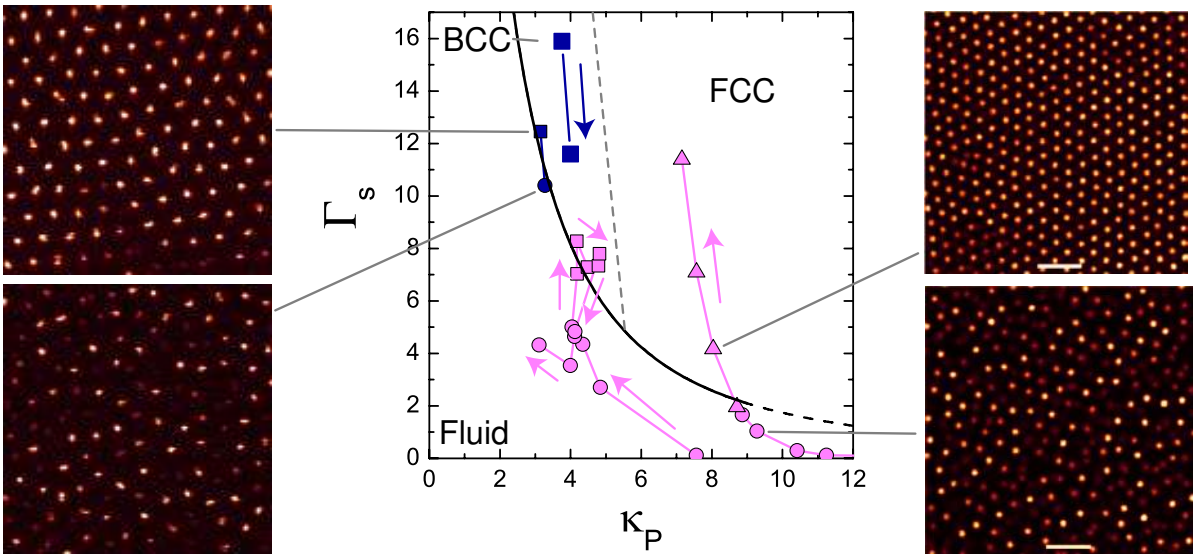

Figure 5.1: Phase diagram of Yukawa systems. The fluid-solid phase boundary (solid line) is the analytic approximation [Eq. 5.4], the dashed line at large κ_p denotes that its validity is limited by $\kappa_p < 10$. The dotted line indicates the approximate position of the bcc-fcc crystal boundary. Various crystallisation/melting experiments in colloidal dispersions (pink) [122, 143] and complex plasmas (blue) [144] are represented in the state points. Circles correspond to fluid phases, whereas squares and triangles indicate, bcc and fcc crystals, respectively. Arrows show the direction in which parameters varied during the experiments. Characteristic snapshots of observed fluid and crystalline phases are also shown [92].

include the hard-core $U_{\mathrm{hc}}(r)$. For the case of hard core Yukawa interaction, it reads

$$U(r) = U_{\mathrm{hc}}(r) + U_{Yukawa}(r), \tag{5.1}$$

$$U_{Yukawa}(r) = \epsilon_{Yukawa} \frac{\exp[-\kappa(r-\sigma)]}{r/\sigma}. \tag{5.2}$$

Here, as already described in Chapter 2.2.3 the potential at contact (when the colloids touch) is given by

$$\beta\epsilon_{Yukawa} = \frac{Z^2}{(1+\kappa\sigma/2)^2} \frac{\lambda_B}{\sigma}, \tag{5.3}$$

where Z is the colloid charge, σ is the particles' diameter, and κ is the inverse Debye screening length, that in turn depends on the number density of monovalent ions and, λ_B the Bjerrum length (see equations 2.13 and 2.14, respectively in Chapter 2.2.3).

Nonetheless, in their investigations of hard-core Yukawa phase diagrams, Hynninen and Dijkstra showed that the effect of the hard core was small when the electrostatic interaction was strong enough that crystallisation occurs at low colloid volume fractions ($\phi \lesssim 0.3$) [142]. In such systems, the colloids are ordered sufficiently apart from one another that short-range interactions become irrelevant. Under this conditions, the interaction parameters take values $\sim \beta\epsilon_{Yukawa} = 20$ and $\kappa\sigma = 1.0$. Thus, at lower concentrations, the system can be treated as a point

Yukawa system, which is also the case for complex plasmas, where particles are suspended in plasma [92]. Such point Yukawa treatment is convenient: when the hard core is neglected, the Yukawa parameters can be represented in a 2d plot [145, 146]. Following this phenomenon, herein we shall use the Yukawa screened Coulomb coupling parameter, Γ_s, and the scaled inverse Debye length, κ_p [92], which have already been introduced in Fig. 5.1 and will be defined in the following sections.

In the case when the system exhibits stronger interactions, (where the Poisson-Boltzmann theory is no longer valid), the pair interactions can still be treated with the Yukawa theory through a *renormalised* or *effective* charge that is smaller than the physical charge on the particles [147, 148, 138, 21], therefore, if the effective colloid charge can be obtained, a Yukawa behaviour is recovered.

However, behaviour inconsistent with the models has also been found. Particularly, "like charge attraction" has been observed, which appears as voids in the system or as crystalline close-packed clusters, resulting in colloid-rich and colloid-poor regions [149, 21]. Several studies for such phenomenon have counterintuitively concluded that the interactions between said particles were attractive, in spite of their like charge [150, 151, 152]. Nevertheless, experiments with optical tweezers showed no evidence of attraction, and suggest that the original observations from Ito and coworkers may have been affected by artefacts [153, 154]. The presence of voids could be a consequence of non-fluorescent impurities in the system, like dust, un-dyed polymer or glass [21, 122]. An alternative explanation explored by van Roij and collaborators considers the influence of the present salt ions: its entropy might drive phase separation and thus produce the observed "colloidal liquid" and "colloidal gas" [155, 156]. Moreover, under this explanation, the repulsion between the colloidal particles is maintained, and thus, the repulsive Yukawa form in Eq. 5.2 is satisfied. On the other hand, the effective one-component DLVO treatment fails to describe the entropic terms responsible for the phase separation, since the degrees of freedom of the salt ions are integrated out. Finally, the quantitative studies carried out by Yoshizawa, *et al.* of a binary system whose behaviour *is* expected to be fully described in a pure Yukawa picture, but in fact demixes, following van Roij's theory [138].

Lastly, colloidal systems immersed in water typically present ionic strengths on the order of $\gtrsim 10^{-7}$ Mol, which, in addition to counter-ion contributions, give a Debye screening length of $\kappa^{-1} \lesssim 300$ nm. Moreover, as stated above, for the system to behave purely as Yukawa, i.e., without significant contributions from the hard core or van der Waals interactions, the Debye length needs to be comparable (or larger than) the particle sizes, which makes particle resolved studies difficult, since the particles have sizes usually larger than a micron. Thus, it is difficult to accomplish such conditions in aqueous systems. However, in solvents with low dielectric constants, like cyclohexyl bromide, the ionic strength can reach values as small as 10^{-12} Mol, and thus the Debye length is sufficiently large so that micron-sized particles are separated enough for point Yukawa behaviour [122, 143]. Furthermore, in such systems the inter-particle spacing can reach

several microns, yielding colloidal crystals of exceptionally low concentrations [157, 122, 21]. Additionally, these systems have also shown to fail to crystallise and thus form arrested structures (glasses) at low colloidal densities [158], just like observed in aqueous systems [159].

In this chapter we consider the Yukawa parameters associated with such *low-density crystals* to make a quantitative comparison between the structures obtained at low packing fractions and the predictions of Yukawa theory through the equilibrium phase diagram [145, 146]. Firstly, we explain how we can make such a comparison and map our parameters to the Yukawa model. We then explain the suggested charging mechanism of our system. We continue with comparing our experimental results to the Yukawa parameters Γ_s and κ_p. We finally discuss the findings and explain any discrepancies between our results and the theory found.

5.1.1 Mapping to Yukawa theory

Figure 5.1 shows the Yukawa phase diagram in the Γ_s, κ_p plane where we compare literature values of charged colloidal particles [122, 143] and complex plasmas [144]. This comparison is viable since the colloidal particles illustrated on the right-hand side insets in Fig. 5.1 are 2 microns in size and thus are comparable to complex plasma experiments [92] showed on the left-hand side. This means that only the immersing medium is different between the two systems: a liquid solvent for the former and a plasma for the latter.

As described by Ivlev and collaborators [92], for Yukawa systems the freezing line can be calculated for κ_p < 10 through:

$$\Gamma_s(\kappa_p) = \frac{106}{1+\kappa_p+\frac{1}{2}\kappa_p^2} \tag{5.4}$$

where Γ_s is the screened coupling parameter and represents the Yukawa interaction evaluated at the mean inter particle separation $\rho^{-\frac{1}{3}}$ $[U_{Yukawa}(\rho^{-\frac{1}{3}})]$, where ρ is the particle number density, and κ_p is a scaled inverse Debye length, obtained through κ_p=$\kappa\sigma\rho^{-\frac{1}{3}}$ [92, 145, 146].

Due to the charging experienced by the particles, we can assume they acquire their maximum charge or their *saturated effective* charge, $Z_{\mathrm{sat}}^{\mathrm{eff}}$, which under charge renormalisation is approximately given by [92]:

$$Z_{\mathrm{eff}}^{\mathrm{sat}} = \frac{(2+\kappa\sigma)\sigma}{\lambda_B} \tag{5.5}$$

Finally, we can then estimate the number density of ions present ρ_{ion} as the sum of the effective charge number per colloidal particle due to the counter ions, $Z_{\mathrm{sat}}^{\mathrm{eff}}\rho$, and the number density of salt and background ions, ρ_{salt}, as:

$$\rho_{\mathrm{ion}} = Z_{\mathrm{eff}}^{\mathrm{sat}}\rho + \rho_{\mathrm{salt}} \tag{5.6}$$

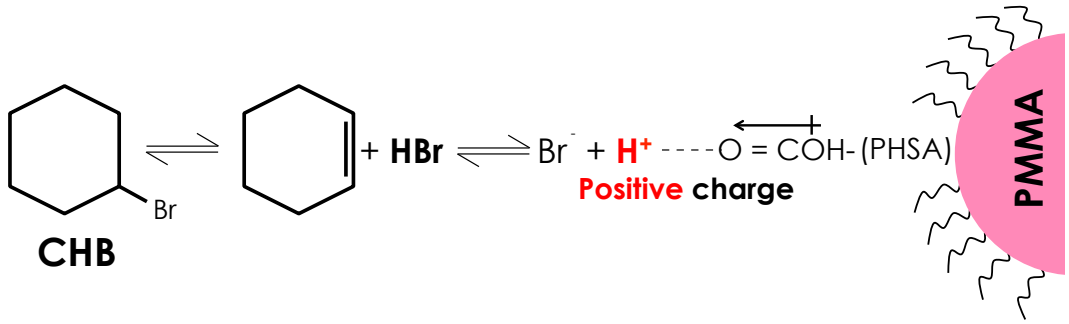

Figure 5.2: Proposed mechanism for the charging of PMMA particles in CHB, showing the partial decomposition of the solvent, which firstly partially self-dissociates in HBr. This in turn decomposes in H^+ and Br^{-1} ions. The former then interact with the polar carboxyl groups of the poly-12-hydroxystearic acid (PHSA) stabiliser on the surface of the particles, conferring them a positive charge.

It is important to highlight that although no salt was added, background ions arising from self-dissociation of the solvent might be present too. We include their contribution in ρ_{salt} and treat it as a free parameter. Assuming agreement with with the Yukawa freezing line, as will be discussed later, the value of $\rho_{\text{salt}} = 10^{-10}\ m^{-3}$, which corresponds to 8.3 nmol, consistent with previous work [21].

With these parameters, the Yukawa interaction can be evaluated at the mean inter particle separation from Eq. 5.3.

5.1.2 Particles Charging Mechanism

The colloidal system used in this chapter consists of similar fluorescently labeled and sterically stabilised spherical poly(methyl)methacrylate (PMMA) particles used in the previous chapter. They were synthesised previously by dispersion polymerisation and also contain poly(12-hydroxystearic acid) (PHSA) chemically grafted on the surface for steric stabilisation. However, in this case, the dry particles were resuspended only in cyclohexyl bromide (CHB), with a dielectric constant $\epsilon_{(\text{CHB})}$ = 7.92, which classifies it as a low polar solvent. Under these low polarity conditions, CHB spontaneously dissociates into cyclohexane and hydrobromic acid (HBr). The latter also partially dissociates into bromide ions and protons. Said protons then form an ion-dipole interaction with the polar carboxyl groups of the PHSA molecules and thus, confer a positive charge to the particles, as shown in Fig. 5.2 [21, 39].

5.2 Methods

5.2.1 Experimental Techniques

As aforementioned, the model used in the present chapter consists on PMMA colloidal particles stabilised with PHSA and fluorescently labelled with rhodamine dye. The particles have a

a diameter of σ = 2000 nm and a polydispersity of 5%, determined previously with static light scattering.

5.2.2 Sample Preparation

Different packing fractions of the particles were suspended in CHB, with a density ρ= 1.32 g/mL and a refractive index of 1.496. The latter closely matches the corresponding one of the colloidal particles of 1.4876, which then avoids attractions due to van der Waals interactions and allows bulk 3d imaging [122, 21]. Rectangular glass capillaries with internal dimensions of 0.10 x 1.00 mm (Vitocrom) were filled with the different suspensions and sealed on their ends with epoxy glue.

5.2.3 Characterisation

The samples were studied immediately after prepared through CLSM means before sedimentation occur due to differences in the density of the solvent and particles. The images were taken at 543 nm excitation and using the same NA 63x oil immersion objective, as indicated in the previous chapter. 2d data sets were recorded for qualitative imaging (512 x 512 pixels), along with a full scan of the capillary in the z direction for 3d data sets for particle tracking analysis. Similar care was taken to assure the pixel size was maintained equal in all axes (200 nm/pixel).

5.2.4 Location of the Particles

Tracking of the particles was also done through the analysis of the 3d scans obtained using the same algorithm described for the binary hard sphere system (Chapter 4.2.4) [125]. In this case, image manipulation techniques were used to reduce the noise and increase the contrast of the particles from the experimental datasets.

5.2.5 Identification of the Type of Crystalline Structure

The coordinates obtained via particle tracking were further used to analyse the level of ordering and crystalline structure of the different samples. Here we also employed the locally averaged order parameters $\bar{q}_4$ and $\bar{q}_6$ to distinguish square and hexagonal order of the crystals observed [126]. Said parameters have been previously detailed in Chapter 4.2.5. In this case, however, in order to identify the list of nearest neighbours $N_b(i)$ for each particle i, we performed a parameter-free detection through Voronoi tessellation of the sample volume.

In addition, we computed the $\bar{w}_4$ parameter, which allows further differentiation of the crystalline structure by being able to distinguish between hcp, fcc and bcc structures, as follows:

$$\bar{w}_l(i) = \frac{\sum_{m_1+m_2+m_3=0} \begin{pmatrix} l & l & l \\ m_1 & m_2 & m_3 \end{pmatrix} \bar{q}_{lm_1}(i)\bar{q}_{lm_2}(i)\bar{q}_{lm_3}(i)}{\left(\sum_{m=-l}^{l} |\bar{q}_{lm}(i)|^2\right)^{3/2}} \tag{5.7}$$

where the term in brackets is the Wigner 3-j symbol. The integers m_1, m_2 and m_3 take values from $-l$ to $+l$, however, only combinations with $m_1 + m_2 + m_3$ = 0 are allowed, on equation [126]. Only the bulk region of the 3d datasets was analysed, discarding about 2.5 μm thickness of the top, bottom and lateral edges of the sample.

5.3 Results and Discussion

We present our results and discussion in two different sections. We first compare and map our results with the Yukawa theory. We then focus on studying the crystalline ordering of the structures and contrast it with the model predictions. We finally conclude with analysing the validity of our approach and give the possible reasons for any discrepancies observed.

5.3.1 Phase Behaviour and Comparison with Yukawa Theory

The phase behaviour of our system, along with the comparison with Yukawa theory is shown as the green state points in Fig. 5.3, where the insets show the confocal images of the different phases identified. We firstly observe that the present system has allowed us to access a new region in the phase diagram in comparison with previous experiments mapped to Yukawa parameters (Γ_s, κ_p). Indeed, with our system we achieve Γ_s values above 60 (Fig. 5.3 e), when the largest value obtained previously was Γ_s =16. We then observe that our two lowest concentrations ϕ = 0.0055 and 0.01 can be identified as fluids (Fig. 5.3 (a) and (b), respectively), whereas the rest of the concentrations show an ordered phase (Fig. 5.3 (c-f)). We thus fit the ionic strength such that the fluid phases are consistent with the Yukawa prediction. As reported before, the low crystallisation concentration, compared with ϕ=0.494 of hard spheres, is a consequence of long-ranged Coulombic repulsions [21].

It can also be observed that the path followed by the state points in the (Γ_s, κ_p) space is not linear, curved or even monotonic. This can be explained through competing effects between the ionic strength and the packing fraction. In one hand, from Eq 5.6 we can see that the added salt ρ_{salt} is comparable to or smaller than the contribution from the counter ions $Z_{\text{eff}}^{\text{sat}}\rho$. Now, as we increase the volume fraction, we increase the screening, which in turn reduces the Debye length κ^{-1} (see Eq. 2.13) [21]. However, as the particle concentration rises, the particles start to locate (in average) closer together, which then causes a drop in the mean inter particle separation, $\rho^{-\frac{1}{3}}$. According to Eq. 5.4 the former phenomenon reduces Γ_s, whereas the latter increases it.

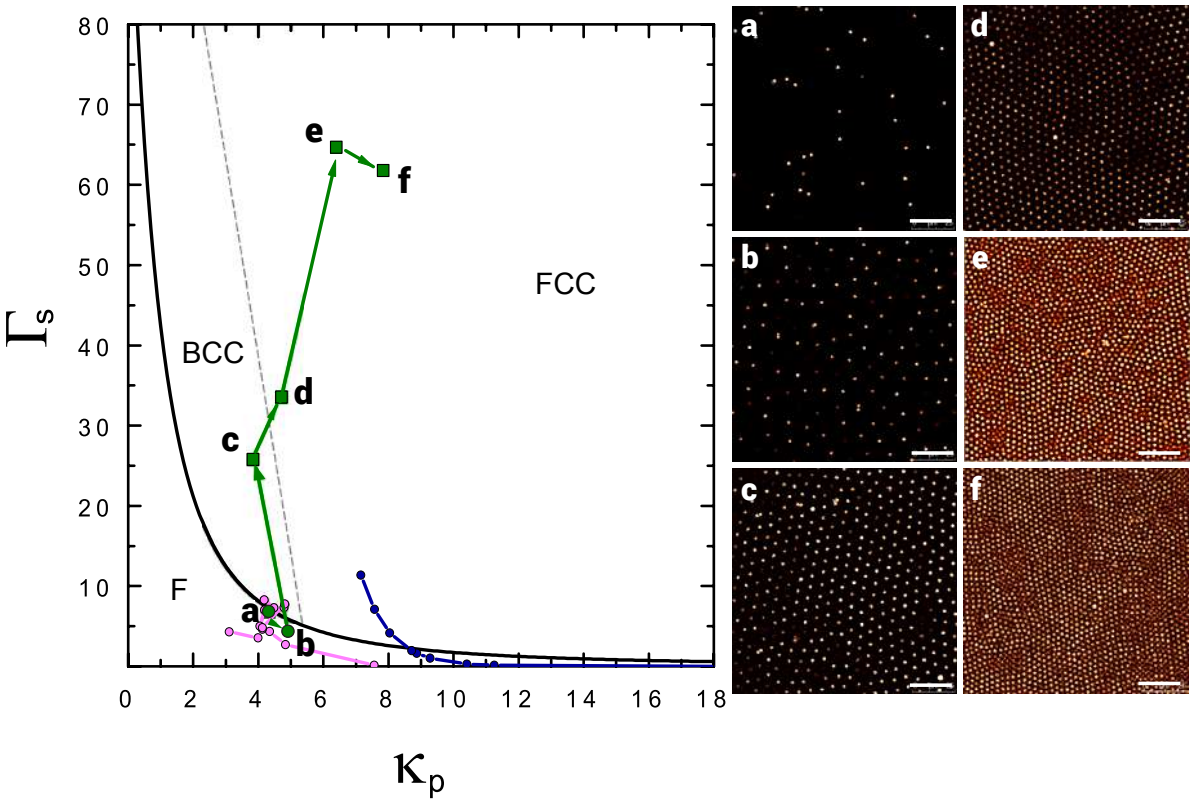

Figure 5.3: Phase diagram of Yukawa system studied in this work in comparison with previous studies [92]. Snapshots in a, b, c, d, e and f correspond to volume fraction ϕ of 0.0055, 0.01, 0.015, 0.04, 0.11 and 0.23, respectively and the state points in (Γ_s, κ_p) representation indicated in the main panel. Lines are as in Fig. 5.1: thick line is the freezing line [Eq. 5.4] and the thin dashed line approximately describes the bcc-fcc transition. Arrows denote increasing volume fraction. Scale bars = 25 μm.

We can now quantify the Debye screening length κ^{-1} = 1.9 μm and the contact potential $\beta\epsilon_Y$ = 1110 at freezing, which corresponds to an effective colloidal charge $Z^{\text{eff}}_{\text{sat}}$ = 850. It is worth highlighting the much larger value of κ^{-1} here observed in comparison to aqueous systems and other previous particle-resolved studies, where it is around 0.200 - 1 μm [122, 143, 21].

Since we have shown that the formation of ordered structures at vey low densities is compatible with the Yukawa theory, we used our parameterisation to estimate the lowest freezing density attainable when no salt is present ($\rho_{\text{salt}} \rightarrow 0$). We found a value around $\phi = 0.0004$ for our system and a Debye length of some 14 μm. Thus, with a total absence of salt, it might be possible to produce crystals at densities ~40 lower than the already small ones reported herein.

5.3.2 Identification of Crystalline Structures at Low Packing Fractions

In order to identify type the of crystalline structure of our ordered lattices, we performed bond orientational order analyses. As aforementioned, for the lower density samples, ϕ < 0.015 (Fig. 5.3 (a) and (b)), we were only able to identify a fluid phase, which presented the characteristics

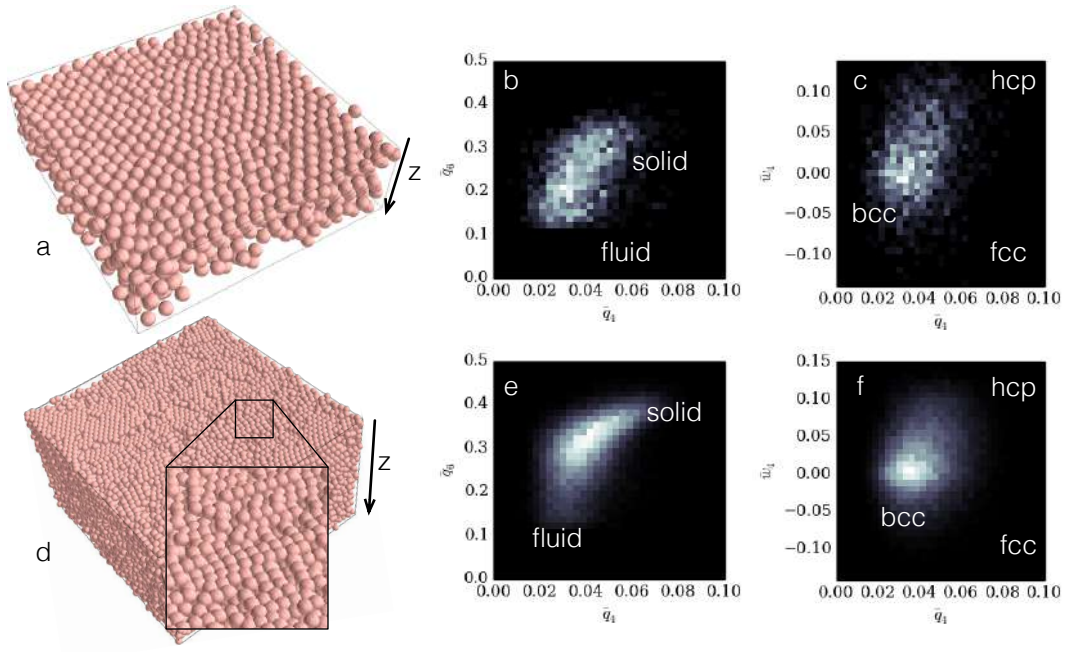

Figure 5.4: Study of the crystalline structure of the crystals found in solutions of highly charged particles. (a) and (d) 3d rendering of the denses crystal observed from the bottom of the sample for (a) volume fraction $\phi = 0.015$ [corresponding to point c in Fig. 5.3] and (d) volume fraction $\phi = 0.23$ [point f in Fig. 5.3]. The radii have been arbitrarily enlarged for better visualisation. In panel (d), a close-up of the ordered surface is highlighted. (b-c) and (e-f) Local bond order parameter diagrams for the two considered volume fractions. In panels (b) and (e) the distribution $P(\bar{q}_4, \bar{q}_6)$ is centred at moderate values corresponding to a solid region, for both packing fractions. Panels (c) and (f) further show that the polymorph of the solid phase, determined via the $P(\bar{q}_4, \bar{w}_4)$ distribution, is bcc also for both packing fractions, with $\phi = 0.23$ showing a higher degree of order.

of a layered liquid along the vertical z axis. On the other hand, ordered structures were identified for packing fractions above ϕ = 0.015, as can be observed in Fig. 5.3 (c-f). The local order analysis of the assemblies is shown in Fig. 5.4, where the top row corresponds to ϕ = 0.015, whereas the bottom row corresponds to a higher concentration, ϕ = 0.23. The graphs comparing the ordered parameters $\bar{q}_6$ and $\bar{q}_4$ confirm the confocal observations, and show that both samples contain a solid phase (Fig. 5.4 (b) and (e)), which is sharper for the highest concentration tested. However, the very limited range of the $\bar{q}_4$ suggest the absence of a fcc crystal. To further confirm this observation, we use an additional order parameter $\bar{w}_4$, which is particularly suitable to differentiate the fcc and hcp hexagonal close-packed structures from the squared bcc. Indeed, we show in Fig 5.4 (c) and (f) that no peak is detected for the hcp and fcc regions, thus the solid phases observed can be identified as bcc. This finding is in agreement with the model predictions for ϕ = 0.015 (Fig. 5.3 (b)), however, for ϕ = 0.23 the model predicts instead a fcc crystal. The same results were found for the packing fractions > 0.04: they all present a bcc ordering when fcc is expected.

We hypothesise that the main reason for such discrepancy is a lack of complete equilibration of the system. We observed that the crystallisation is heterogenous, i.e., it starts at the

regions closer to the walls, where the system appears more crystalline. While the homogenous crystallisation of this system is yet to be studied in detail, following the Ostwald rule of stages, bcc can form first as a metastable phase, leading to the thermodynamically stable hexagonal close-packed polymorph expected, fcc in Yukawa systems [160, 161, 162]. We believe that such phenomena might be the responsible for our findings. Furthermore, in previous work using similar particles with smaller Debye lengths than the ones reported herein, the authors did observe the fluid-bcc-fcc transition [21]. However, we emphasise that the influence of the walls on the type of crystallisation mechanism should not be overlooked. Indeed, the confinement of our samples in square capillaries of 100 μm height, might also play a significant role: under this conditions some preference has been described for square symmetry which in turn might lead to bcc being favoured for our system.

Ways to prove the validity of our hypotheses include the investigation of the crystallisation kinetics in order to determine if certainly our system is approaching and reaches its fcc equilibrium state, along with homogenous crystallisation, to discard any influence of the flat walls of our system. Limitations on the stability of our samples prevented us from running the former experiments, since our systems are only stable for around two days. Differences in the density of the solvent and the particles, along with solvent evaporation and/or ion dissolution from the glass capillary might affect the behaviour of the system.

5.4 Conclusions

Through particle-resolved studies of a colloidal system with an unusually long Debye screening length, we identified crystals at low colloid volume fractions $\phi \sim 0.015$. We quantitatively compared this system with the Yukawa model and we were able to show that its phase behaviour can indeed be described by said theory, i.e., we found that the freezing point of our system is compatible with the model prediction. Furthermore, for packing fractions ≤ 0.015, the predicted fluid and crystalline bcc structure does correspond to the crystal polymorph identified through different bond-orientational order parameters analysis. However, for higher concentrations, the identified ordered structure was also bcc which is not longer compatible with the fcc predictions of the model. Possible reasons for this discrepancy migth include the lack of complete equilibration of the system. Certainly, according to the Ostwald rule of stages, bcc can form before the sample equilibrates to the more favoured fcc structure. Additionally, the square symmetry of the sample confinement might favour bcc ordering in the time-scales studied. These hypotheses can be confirmed through further investigation of the homogenous crystallisation kinetics of our system. However, limitations intrinsic to the nature of our samples, i.e., lack of density matching between the particles and the solvent, along with solvent evaporation, prevented us to further study this phenomenon.

CHAPTER 6

TOWARDS CRITICAL SOFT MATTER USING FLUORESCENT PROTEIN MIXTURES

In this chapter we study experimentally the formation of phase separated bicontinuous networks of a binary mixture of fluorescent enhanced green fluorescent protein (eGFP) and mCherry proteins through salt addition and surface modification of the species. Based on lysozyme studies, we were expecting the behaviour of these proteins to be similar to that of patchy spheres. As such, this system represents the next level of complexity for both monocomponent and hard sphere interactions. The strategies followed were aimed to increase the intra-protein interactions over the inter-protein ones and thus yield a critical soft matter bicontinuous network, with distinctive domains of individual proteins. Firstly, the interactions of the proteins were tested in the presence of sodium chloride, ammonium sulphate, iron and yttrium chloride, where only ammonium sulphate and yttrium chloride precipitated the proteins successfully. Nevertheless, the precipitation yielded mixed protein bi-networks far from the desired critical soft matter structure. Successful protein surface cationisation was performed to increase intra-particle interactions and protein-salt specificity. However, unexpected protein co-precipitation due to complex protein-protein interactions suppressed the formation of critical soft matter gels. These unwanted protein-protein interactions were avoided by forming the individual gels independently. Although these are no longer critical soft matter structures, we did obtain phase separated bicontinuous networks where the proteins preserved their functional structure. Moreover, by adding different amounts of one of the proteins, we were able to modify the percentage of the individual domains forming the structure. To our knowledge, this type of biomaterials has not been reported before. Although further studies of the specificity and strength of the interactions involved in our system are needed, our studies set a precedent for a new methodology to obtain innovative biomaterials with potential medical and technological applications.

6.1 Introduction

6.1.1 Binary Gel Networks

Colloidal or particle gels are elastic and semisolid systems immersed in a liquid medium, where the colloidal particles are partly associated or interconnected with each other through chemical or physical links, forming ramified amorphous structures. The semisolid characteristics of these structures arise as a lack of fluidity due to the network formed by the solid components of the suspension and as such, the structure can withstand mechanical stress [163, 164, 165]. In several materials like colloidal, protein and some polymer solutions, it is known that gelation occurs through spinodal decomposition when the system is quenched into the gas-liquid coexistence region. Here, the system phase separates in two phases with very distinctive dynamics, with the very slow dynamics of the dense liquid leading to dynamical arrest. Similar to other arrested states, i.e. glasses, gel networks are out-of-equilibrium and do not present long-range order [166, 163, 167].

Gel networks can be comprised of several components. In this work, we will focus on studying binary gel networks where two gel phases form the structure. They are relatively new solid-like systems, where the nature of the phases can be fairly similar or different species with diverse properties can form the bi-network. Due to their binary composition, these networks present the physical, chemical and biological characteristics of each component separately, which might improve their properties and hence make them advantageous over single-component gels [168, 169, 170, 165]. Because of their dual properties, gel bi-networks have been widely studied for their applications in the cosmetic, pharmaceutical and food industry. More recently, however, they have become a popular choice for cell and tissue growth scaffolding and to construct matrices for drug delivery [169, 165, 171, 172, 173, 174]. Moreover, they present improved stability as compared to other systems like emulsions or hydrogels. However, phase separation or destabilisation of the gel networks is a current drawback of these systems [169].

Gel bi-networks encompass several types of systems, which include those formed by a mixture of oils and hydrogels, networks formed by joining two different gel strips, two interpenetrating gels, phase separated bicontinuous gels and double networks developed through sequential covalent and non-covalent links [169, 168, 165]. Fig. 6.1 shows some examples of these structures, were the structural differences can be appreciated.

Several methods for their preparation can be found in the literature, which usually involve two separated steps. First, each individual gel is prepared independently to secondly be mixed and sometimes heated, to produce the bi-network [175, 169]. However, recent studies have developed two step methodologies to yield bi-networks, where the different responses of the mixture components to aggregating/precipitating agents or conditions are exploited. In these approaches, the mechanisms for the network formation require that the inter-particle interactions are negligible in comparison with the intra-particle ones [176, 163, 177, 168]. Interestingly, these type of

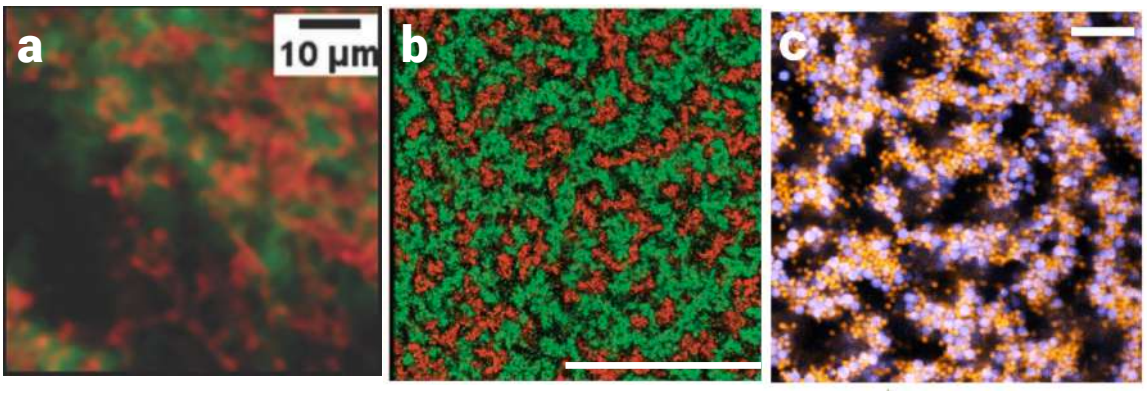

Figure 6.1: Examples of different binary gels. a. Confocal image of interpenetrating BSA (red) and gelatin (green) networks [68]. b. Confocal image of a binary phase separated gel formed by silica particles hybridised through different complementary DNA strains [176]. c. Confocal image of a bicontinuous gel formed by polymethylmethacrylate large (purple) and small (yellow) particles after polymer addition [177].

interactions are a characteristic of critical soft matter discussed earlier (see Chapter 2.2.7).

For example, Blumlein and McManus produced two interpenetrating gel networks when working with bovine serum albumin (BSA) and gelatin. They chose proteins as the bi-network components in order to improve the properties and characteristics of the individual gels, as we will discuss later. The novelty of this approach is that both components are present in the initial mixture and the different responses to heat of each protein present are exploited to hierarchically form interpenetrating gels, as exemplified in Fig. 6.1 (a). In their study, the mixture is heated to 100° C, which produces a BSA gel through spinodal decomposition, whilst gelatin remains in solution. At this point BSA is unfolded and the sulphur groups exposed form disulphide bridges to stabilise the gel. Later, the mixture is cooled down to room temperature, thus an interpenetrating gelatin network is formed around the pre-existing BSA gel [168].

Inspired by Blumlein and McManus methodology, and based on the potential of critical soft matter to form out-of-equilibrium bi-structures with tunable sizes of the component domains (see Chapter 2.2.7), we aim to produce phase separated bicontinuous gels using fluorescent proteins as the model components.

A general scheme for our approach is illustrated in Fig. 6.2, where two different proteins with different surface properties are coarse-grained and represented as patchy particles. The patches correspond to the surface groups and charge heterogeneity present in the proteins. Following critical soft matter ideas, we will utilise a binary mixture of proteins where the intra-protein attractions are stronger than the inter-protein ones. By controlling the forcefield between the proteins through their particular interactions with different salts (grey spheres in Fig. 6.2), we shall be able to favour intra-protein interactions in order to generate critical soft matter gel structures comprised by distinguishable individual protein domains, as shown in (c) in Fig. 6.2. However, unlike the Blumlein and McManus approach, the strategies developed herein are also focused on *preserving the native structure of the proteins to retain their functions*. We will de-

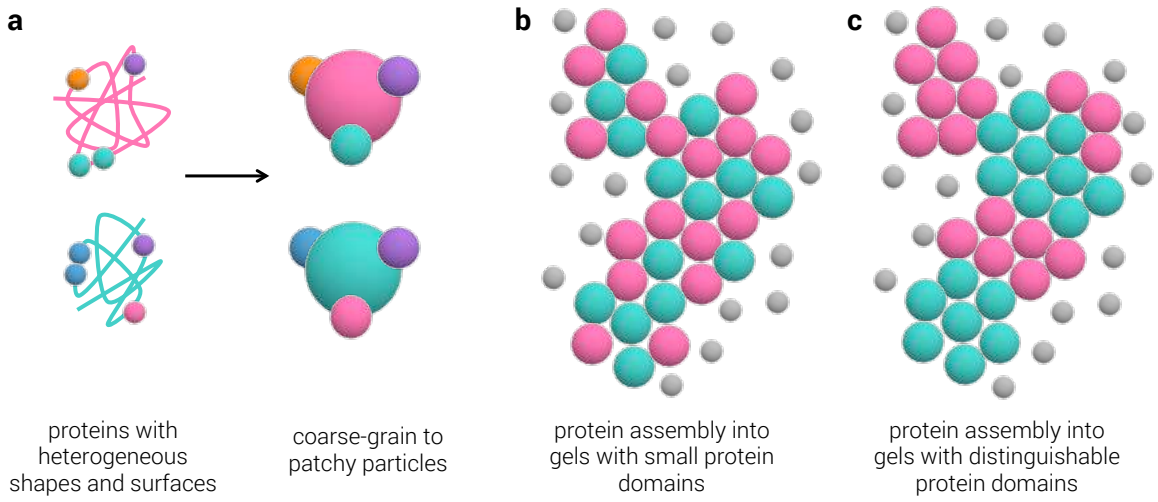

Figure 6.2: General strategy to realise critical soft matter with a mixture of proteins. a. Two different proteins with distinctive surface heterogeneity are coarse-grained to be treated as patchy-particles. b and c. Protein assembly triggered by the addition of a precipitating agent (salt or non-adsorbing polymer) represented as the grey spheres. The proteins are mixed in the structure through small (b) or large distinguishable individual protein (c) domains. Inter-protein interactions dominate in (b), whereas intra-protein attractions dominate in (c). The latter corresponds to critical soft matter gel (see Chapter 2.2.7).

scribe the principles of this strategy and the protein model chosen in the following sections.

6.1.2 Proteins and Protein Interactions

Our objective is to study the optimal self-assembly conditions to yield a critical soft matter gel bi-network in order to produce functional materials. Therefore, we selected proteins as the building blocks, since they present a great versatility of functions and characteristics that provide a wide catalog of potential applications for these innovative materials.

Proteins are bio-macromolecules which constitute essential parts of all living organisms and viruses, since they are involved in *every* process within cells. They consist of one or more polypeptide chains that are in turn composed of several amino acids linked through amide bonds. The sequence of amino acids is specific for each protein and is determined in the genetic code. Once synthesised, the polypeptide chains spontaneously fold and adopt unique 3d shapes stabilised through multiple weak interactions, like hydrogen and ionic bonds, hydrophobic interactions. Covalent bonds may also arise through disulphide bridges. For further details see Chapter 2.3.1 and Fig. 2.11. The final 3d conformation determines the particular biological function of the protein [60].

Proteins can also be regarded as colloidal particles, particularly as patchy spheres that represent their charges, hydrophobicity/hydrophilicity or surface groups (wee Fig. 6.2 (a)). However proteins present a higher level of complexity due to their wide variety of shapes and their large size distributions. Additionally, a single protein also presents heterogenous charge sign

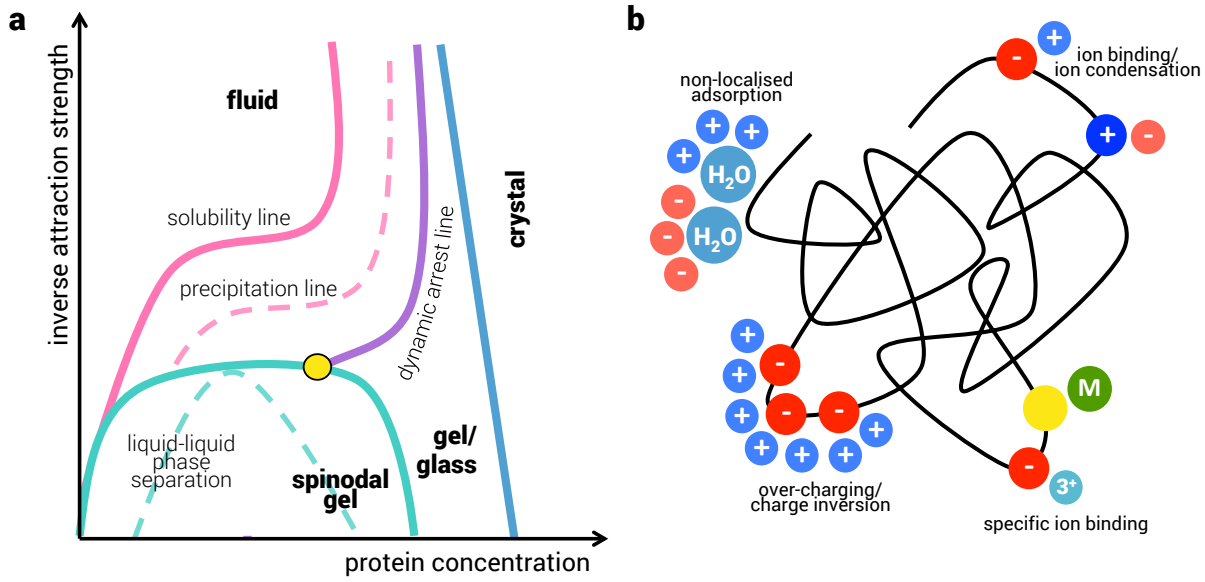

Figure 6.3: Proteins as colloids. a. General phase diagram of globular proteins showing the different condensed phases proteins can present (adapted from [68] and [67]). b. A variety of protein-ion interactions.

and distribution depending on the pH of the medium. The pH where their charge is neutral (same amount of negative and positive charges) is known as the *isoelectric point* (pI). At pHs below their pI, proteins will have a net positive charge, and vice versa, at pHs above, they will have a net negative charge. Furthermore, the surface chemistry of a protein is also heterogenous since proteins usually expose polar and non-polar, and positive and negative charged amino acid groups [178].

In spite of the mentioned complexity, solutions of proteins, like other colloidal systems, may undergo biophysical processes like solubility, aggregation, precipitation, gelation and crystallisation [67, 68]. However, it is important to highlight that proteins will form a condensed phase only if i) they are designed to do so (i.e. viral capsids), if ii) mutations lead to mis-folding or to interactions that produce aggregation (i.e. prions), or if iii) changes in the medium (i.e. temperature, pH, ionic strength) are induced [68]. In general, it is known that protein interactions involve van der Waals, electrostatic, hydrogen bonding, hydrophobic/hydrophilic, volume exclusion and counter-ion interactions [179, 178, 172].

6.1.2.1 Proteins as Colloids

A large number of computational and experimental research on protein phase behaviour has been done on solutions of lysozyme proteins. This globular protein is an enzyme with antimicrobial properties present in animals secretions and eggs, and its popularity arises from its high abundance and stability [180]. Although several models have been used to try to obtain a phase

diagram of the protein, the *patchy colloid model* has shown to be the most successful since it includes the protein inherent anisotropy and short-range attractive interactions [181]. Indeed, Gögelein and coworkers used said model to study lysozyme computationally, where the protein is modelled as long-range repulsive spheres with two short-range attractive patches. This model allowed them to successfully match and describe the transitions and condensed phases formed experimentally by lysozyme solutions as a function of salinity [180].

A theoretical phase diagram for globular proteins is illustrated in Fig. 6.3 a, where several regions can be distinguished. Here, at low protein attraction strength and low protein concentrations, the system is a fluid, i.e., the proteins are in solution due to long-ranged screened electrostatic repulsions that are a consequence of their surface charges [180]. As the protein concentration increases, the proteins cross the solubility line (pink) to the fluid-solid equilibrium region where protein crystals are in coexistence with their supernatant. If instead the attraction strength is increased, short-ranged attractions appear and a gas-liquid phase separation occurs (binodal green line). This phenomenon is experimentally observable as a liquid-liquid phase separation where protein-rich and protein-poor phases can be distinguished, which correspond to liquid and gas phases, respectively. Below the binodal line, we find a spinodal line (dashed green line) and the kinetics of the system will depend on the region where the phase separation occurs. If it happens above the spinodal line, then the phase separation will start as small droplets of dense liquid nucleate and grow until equilibrium. If instead it occurs below the spinodal line, then the phase separation will take place spontaneously (spinodal decomposition) [68, 67]. Finally, at high protein concentrations and fast quenching, the system can present non-equilibrium states similar to gels and glasses of other colloidal systems. Moreover, the dynamic arrest line (purple line) intersects the binodal (yellow circle). At this point the gas-liquid phase separation is affected since the liquid phase cannot form as previously described, and instead the system forms a kinetically trapped gel [67].

6.1.2.2 Interactions Between Proteins and Salts

In order to access all these different phases, the attraction strength between the proteins can be increased through temperature or pH changes, adding depletion agents or, more commonly, through the addition of salts [67, 180]. Salts are generally used to control pH and ionic strength. However, their addition to protein solutions has shown to affect the protein-protein interactions from repulsive to attractive thus leading to the complex phase behaviour [179, 182]. Indeed, protein solubility is affected by the presence of ions: at low salt concentrations anions and cations help neutralise the inherently charged regions of the proteins and thus prevent aggregation. However, as more salt is added to the solution, the surfaces of the proteins will become more charged, losing neutrality and thus aggregating [183]. The ability of anions and cations to stabilise or de-stabilise proteins in solution has been ranked in the Hofmeister Series [184]. This em-

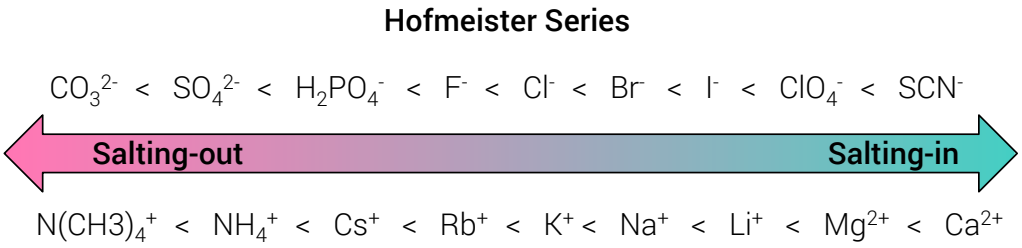

Figure 6.4: Hofmeister series for ions and cations, where their ordering is based on their ability to precipitate negatively charged proteins. Ions have the highest stabilisation ability and thus salt-in proteins increasingly to the right. Conversely, the ions to the left have lower stabilisation power and salt-out proteins [188].

piric categorisation of ions was built by Franz Hofmeister and collaborators back in the 1880s. A more modern Hofmeister series is shown in Fig. 6.4, where the ability to precipitate (salt-out) proteins is the highest for ions on the far left. On the other hand, the ability of ions to solubilise proteins (salt-in) increases towards the right of the series.

The mechanism proposed by which ions from the Hofmeister Series precipitate proteins, amongst others, has to do with preferential solvation, i.e., preferential stabilisation of the added salts in solution over the proteins. This occurs due to exclusion of the salts from the hydration layer of the protein: ions have a larger binding preference to the water and thus displace these molecules from the surface of the macromolecules [185, 186]. Additionally, the presence of salts increases the surface tension of water, which in turn increases the hydrophobic interactions between the water and the proteins. These unfavourable entropic interactions force the proteins to reduce their surface area so contacts with water can be minimised. In addition proteins start interacting with each other through hydrophobic residues, leading to self-association and eventually to precipitation [185, 187]. Finally, the nature of salt interactions with the proteins is highly dependant on the pH of the solution, the protein charge and the type of ion [184].

Moreover, salts might also interact with the proteins directly. Some of the main protein-ion interactions are illustrated in Fig. 6.3, where the most common ones are the ion condensation with charged groups of the exposed amino acid and non-localised adsorption with hydrophobic residues. Additionally, more specific interactions have been described for certain ions, particularly carboxilate, thiol, thioether and imidazol groups have shown to chelate certain heavy metals [189], illustrated as the yellow and green circles in Fig.6.3, respectively. Finally, highly charged areas of the protein might experience over-charging which might lead to charge inversion [66, 190, 191].

Yet, the mechanisms driving the changes in protein-protein and protein-ion interactions are not fully understood. Furthermore considerations regarding on one hand the heterogeneity of the charge, surface charge density and hydrophobicity of the protein; on the other the hydration, valency size and polarisability of the salts involved need to be done [178].

6.1.2.3 Soft Matter Potentials to Study Proteins' Behaviour

In order to further study and understand the complexity of protein-protein interactions in the presence of salts, several soft condensed matter theories have been applied to protein systems. Curtis and collaborators [182] proposed that the interaction potential for a pair of proteins in a salt solution can be obtained by adding the contribution of different potentials evaluated at the centre-to-centre distance *r*:

$$U(r) = U_{HS}(r) + U_{SC}(r) + U_V(r) + U_{AO}(r) + U_A(r) \tag{6.1}$$

where $U_{\mathrm{HS}}(r)$ corresponds to a hard-sphere potential related to an excluded-volume effect from the proteins, $U_{\mathrm{SC}}(r)$ to the screened Coulomb potential arising from electrostatic repulsions, whereas $U_{\mathrm{V}}(r)$ corresponds to the attractive van der Waals forces, $U_{\mathrm{AO}}(r)$ is the depletion potential caused by the salt ions, and finally $U_{\mathrm{A}}(r)$ corresponds to self-association of proteins [182]. Thus, according to this equation, all potentials should be considered to find the interaction between the proteins.

F. Zhang and collaborators conducted studies on the effect of different ionic strengths (I) on protein-protein interactions using BSA as the model protein and small angle X-ray scattering (SAXS) [182]. They found that actually, for small concentrations of NaCl (I < 0.3 M) the repulsive interactions dominate and the system can be described through a screened Coulomb potential. Yet, as the amount of salt increases (I = 0.3-0.5 M) so does the charge screening and the interactions can then be described by a hard sphere model. Finally, at high salt concentrations (I > 0.5 M) medium to long-range attractive forces dominate, and thus the interactions can be described through a square well potential. These interactions arise mainly from protein volume exclusion contributions [182].

This study concluded that depending on the salt concentration, only one (or two) of these contributions will dominate and thus the calculation of the force field can be simplified. Moreover, it showed that in spite of their complexity, protein solutions can be well described through interaction potentials used for colloidal systems.

6.1.3 Fluorescent Proteins as Model Systems

As mentioned earlier, we wish to identify the optimal self-assembly conditions to form phase separated bicontinuous gels based on critical soft matter (CSM) ideas, using proteins to yield innovative functionalities. In order for them to be functional, we ought to preserve the native structure of the building blocks. We therefore decided to use fluorescent proteins for our model system, since any alterations in their native structure as a result of our treatment will be easily detected through changes or loss of the fluorescence.

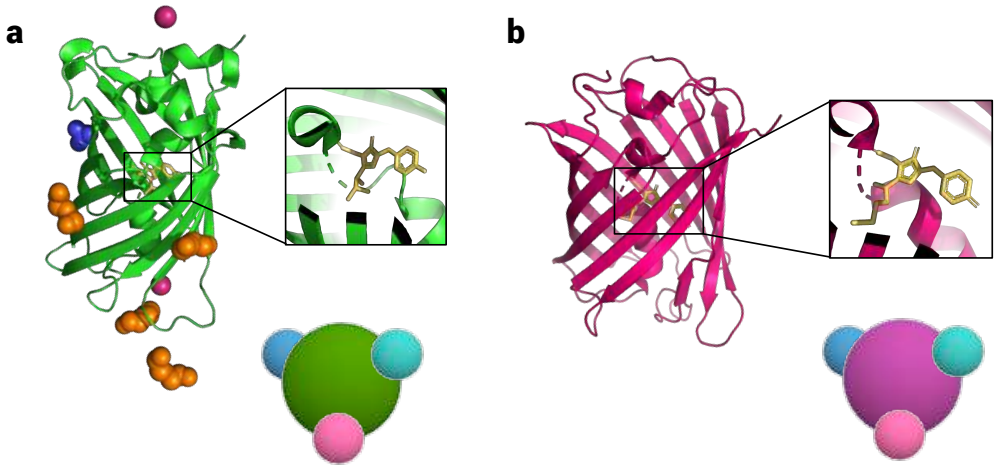

Figure 6.5: Ribbon representation of (a) eGFP and (b) mCherry obtained from Data Protein Bank. In (a) calcium, sulphate and PEG ligands are shown in green, blue and orange, respectively. Insets show the stick representation of the respective chromophores. The inserts show the visualisation of the proteins like patchy particles, where the different bumps represent the surface anisotropy of the proteins that may include charge, functional groups or hydrophobicity.

We chose the *enhanced green fluorescent protein* (eGFP) and *mCherry* as the protein models due to their high stability, availability, high expression rates, and because they present very different excitation and emission wavelengths needed for fluorescence microscopy differentiation.

GFP was derived from the jellyfish *Aequorea victoria* which contains a chromophore (molecule responsible for colour) that fluoresces without the need of substrates or cofactors [192]. The protein wild type was improved into the engineered *eGFP* with a more efficient folding rate which increases the fluorescence. The protein is ~4 nm high and ~3 nm wide, has a molecular weight of 27.7 KDa and presents excitation and emission wavelengths at 488 nm and 509 nm, respectively [193]. A ribbon representation of the protein is shown in Fig. 6.5 (a), where the chromophore *p*-hydroxybenzylideneimidazolinone is shown in yellow and it is located packed in the core of the protein .

On the other hand, mCherry belongs to the 'mFruit' series of red fluorescent proteins family, which were derived from the DsRed protein, isolated from *Dicosoma striata* anemones. This new family presents improvements in protein expression and photo stability, in comparison with the DsRed wild type. mCherry has a similar height and width to eGFP, with a 28.8 KDa of molecular weight. Its excitation and emission wavelengths are at 587 nm and 610 nm, respectively [194]. A ribbon representation of mCherry is illustrated in Fig. 6.5 (b), where also the chromophore is highlighted in yellow and shown to be protected by the β-barrel structure.

Based on the success of the patchy particle model to describe the behaviour of lysozyme [180], we expect that we can treat our proteins as such. This patchy particle model is exemplified as the inserts in Fig. 6.5, where the bumps illustrate the protein surface anisotropy and heterogeneity. In this work, we will exploit experimentally the charge and hydrophobic dispari-

ties between eGFP and mCherry. We hypothesise that due to such differences, each protein will respond differently to the addition of various salts with intra-protein attractions dominating the interactions and thus yielding the desired bicontinous gel network with distinguishable protein domains as illustrated in Fig. 6.2 (c).

6.2 Methods

6.2.1 Production of Fluorescent Proteins eGFP and mCherry

The details for the expression, purification and concentration of both fluorescent proteins are described in Chapter 3.3.1. Briefly, *E. coli* cells were cultured to a desired concentration, then the fluorescent protein expression was induced for 16 h. The cells were then centrifuged and lysed (broken down) to obtain the proteins, which were later purified through affinity chromatography. Finally, the purified eGFP and mCherry were dialysed and concentrated to ~1 mL in dH_2O. No buffer was used to avoid the interaction of the proteins of other ions.

6.2.2 Precipitation of eGFP and mCherry with NaCl

To test the effect of the addition of sodium chloride (NaCl) to protein solutions, different amounts of salt were added to 100 μL of 7 mg/mL of native eGFP and native mCherry solutions to obtain final NaCl concentrations of 0.5, 1, 2, 2.5 and 5 M. Additionally, to test the effect of NaCl on the mutual aggregation of the proteins, a mixture of 8 mg/mL total of native eGFP and native mCherry with 5 M of NaCl was prepared. All samples were mixed for 5 min and analysed immediately after.

6.2.3 Precipitation of eGFP and mCherry with Ammonium Sulphate

Different amounts of ammonium sulphate, $(NH_4)_2SO_4$, Sigma Aldrich) were increasingly added to a 100 μL of 14 mg/mL total mixture of native eGFP and native mCherry to reach final concentrations from 0.3 to 3 M.

Additionally, to test its effect on modified proteins, $(NH_4)_2SO_4$ was added to 50 μL of 7 mg/mL solutions of cationised eGFP and mCherry for a final concentration of 3 M of the salt. All samples were vortexed for 5 min and analysed immediately after.

6.2.4 Precipitation of mCherry Proteins with Iron Chloride

Three different iron chloride ($FeCl_3$) concentrations –5, 10 and 20 mM –were tested against a mCherry solution of 7 mg/mL, by adding the required volumes from a stock solution of the trivalent salt. All samples were mixed using a vortex for 5 min and analysed immediately after.

6.2.5 Precipitation of Native and Cationised eGFP and mCherry with Yttrium Chloride

In order to both study the ability of yttrium chloride (YCl_3, Sigma Aldrich) to precipitate the fluorescent proteins and to confirm the effectivity of the protein cationisation, different salt concentrations (1, 2, 5, 10, 50 mM) were added from YCl_3 stock solutions to 30 μL of 7 mg/mL solutions of native and cationised proteins, separately. The solutions were mixed in a vortex for 5 min and analysed immediately after.

6.2.6 Cationisation of eGFP and mCherry

In order to suppress the interaction of the fluorescent salts with yttrium chloride and gain better control of the interactions of the proteins, the surfaces of eGFP and mCherry were modified. This was done through a cationisation reaction, where positive charges are added to the surface of the proteins, without altering their 3d conformation. This is possible through the reaction of a diamine with the exposed carboxylic groups of acidic aminoacids on the surface the protein, as shown in Fig. 6.11. A 10-fold excess of hexamethylendiamine (HMDA, Sigma Aldrich) from a stock solution at a pH 6.0-6.5 was added to 10 mL of a known concentration of native protein solution. The pH was adjusted to 6.0-6.5 with HCl 1 M. An equal concentration to the protein of 1-Ethyl-3-(3-dimethylaminopropyl)carbodiimide (EDC, Sigma Aldrich) was added to the reaction at two different times: half of the required reagent was added after HMDA and the remaining half after ~3h of reaction. The pH was monitored constantly and adjusted to 6.0-6.5 as required for the first 6 h. The mixture was left stirring at room temperature over night (~18 h). Finally, the solution was filtered through a 0.22 μm syringe filter to remove any precipitates, dialysed against dH_2O for 24 h and concentrated. The degree of cationisation was determined using zeta potential measurements (Zetasizer Nano ZS, Malvern) using 1 mL of 2 mg/mL of native and modified proteins.

6.2.7 Gel Bi-network Formation of Native and Cationised Proteins with Yttrium Chloride and Ammonium Sulphate

Two different strategies were followed to obtain the desired bicontinuous gels and are shown in Fig. 6.14 and 6.16. The first one consisted in mixing initially 30 μL total native eGFP/mCherry and cationised eGFP/mCherry for a total concentration of 10 mg/mL. Then 1.5 μL of a stock solution of 100 mM of YCl_3 were added and the solution was mixed for 5 min. Finally, $(NH_4)_2SO_4$ was added and dissolved for a final concentration of 3 M. Samples of the gels were taken after each salt addition for analysis.

In the second approach we varied two different conditions: the order of the addition of the proteins and their mass ratio. Firstly, an eGFP gel was formed by adding 5mM YCl_3 as described above to a 5 mg/mL solution of only said native protein. Then $(NH_4)_2SO_4$ was added and dis-

solved for a final concentration of 3 M. Finally, 5 mg/mL of cationised mCherry were added to the solution, mixed for 5 min and analysed immediately. The final total protein concentration was kept to 10 mg/mL. Three more samples following this protocol were prepared where the mass ratio of native eGFP:cationised mCherry was varied to 2:1, 5:1 and 10:1.

6.2.8 Imaging of the Assembly Process

All samples were confined to capillaries with a square x-section of of 0.50 x 0.50 mm (Vitcrom) and sealed on the ends with Norland61. CLSM was used to study any gel formation, using also a NA 63x oil immersion objective. The channels used for the proteins were 488 nm for eGFP and 587 nm for mCherry. More than 30 2d images were taken all over the capillaries per sample for characterisation and analysis of the structures found. Scans of the capillary in the z axis were also acquired to analyse the gel structures in 3d, where care was taken to assure the pixel size was equal in all axes (0.10 μm/pixel).

6.2.9 Analysis of the Mixing and Domain Sizes of Native eGFP and Cationised mCherry in the Gel Bi-networks

Confocal optical slices of the obtained gels were analysed individually to measure the percentage of mixing and de-mixing of the gels, along with the sizes of de-mixed domains. Care was taken to obtain images with the same sizes and the intensities of the images was normalised for all of them. Then, the pixels were classified according to their intensities as yellow (mixed proteins), green (eGFP) and red (mCherry). Different intensity thresholds were tested to optimise the results. The percentage of each colour was obtained to study the mixing of the proteins. Additionally, the areas of the identified regions of individual proteins (de-mixed domains) were measured by counting the number of pixels on said domains, which were then converted to μm^2 using the pixel size. Regions with pixel sizes below 10, which corresponded to 1% of the total size of the image, were discarded.

6.3 Results and Discussion

The results and analysis of the gel bi-networks formation are presented in five different sections. First, we tested the ability of two salts from the Hofmeister series, sodium chloride and ammonium sulphate, to precipitate the proteins. Next, we present our results of the precipitation of proteins using the trivalent salts iron chloride and yttrium chloride. We continue with the surface modification of the proteins through cationisation and the outcomes obtained. With all these results, we propose two strategies for the gel bi-network formation and present the structures found. We conclude by analysing the bicontinuous gel composition and size of individual

protein domains according to the different conditions tested. Lastly, we propose some potential future applications for the structures found.

6.3.1 Fluorescent Protein Expression, Purification

We successfully expressed, purified and concentrated ~1 mL of eGFP and mCherry. The final concentrations of each protein were 17 mg/mL for eGFP and 8,82 mg/mL for mCherry. The green and purple colour of the purified protein solutions indicated the presence and correct folding of eGFP and mCherry, respectively. All the different solutions were passed through 0.22 μm filters and the samples were kept at 4° C to avoid any bacterial growth.

6.3.2 Precipitation of Native Proteins with Monovalent Salts of the Hofmeister Series

Based on the differing capacity of salts to aggregate proteins, in this first section we followed the Hofmeister Series to test the efficiency of two different salts with medium (sodium chloride) and high (ammonium sulphate) salting-out properties to form the desired gels.

6.3.2.1 Precipitation of eGFP and mCherry with Sodium Chloride

Since we wish to form gel structures where the proteins preserve their native state for future applications, we started by testing sodium chloride (NaCl), which is located in the medium region of the Hofmeister Series (see Fig. 6.4). This salt has been shown to successfully crystallise proteins like lysozyme [67, 195]. Thus, we first added different salt amounts to individual solutions of eGFP and mCherry. The results are shown in Fig. 6.6, where we do observe the aggregation of both proteins in small clusters, which increase in number and size as we increment the amount of salt. However, even at very high salt concentrations (5 M, Fig. 6.6 left images in panel (a) and (b)), we observe an incomplete aggregation of the protein since the green and red background suggest there is still a significant amount of protein in solution. Additionally, we did not observe percolation of clusters of either protein, required for our main objective.

We interpret these results in the light of the study of different ions and their interactions with proteins carried out by Okur *et al.* [184]. The authors showed that anions with strong attraction to protein surfaces, like Cl^-, are inefficient for salting-out proteins. On the other hand, cations that are highly hydrated, like Na^+, also interact more strongly with the protein, which helps with stabilisation. These are therefore less efficient in precipitating proteins [184]. Thus, both the strong anionic interactions of Cl^- and the relatively highly hydrated Na^+ may prevent protein precipitation of eGFP and mCherry under the conditions tested.

We then moved to test the combination of both proteins in solutions and the effect on their interactions after salt addition. The results are illustrated in Fig. 6.6 (c), and are very similar to the effect observed on the individual solutions, where only small non-percolating clusters are

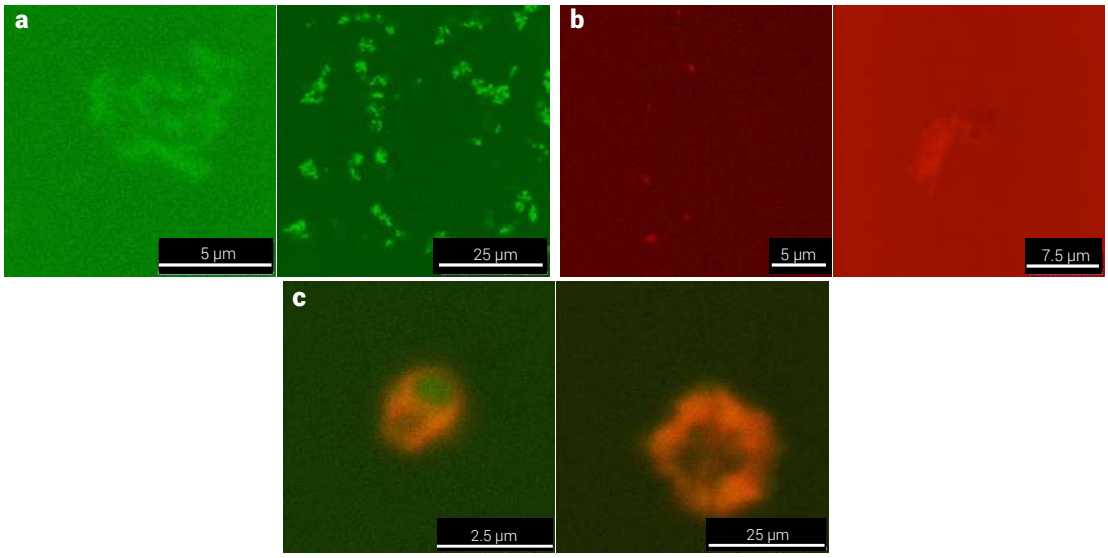

Figure 6.6: Clusters formed through the addition of different amounts of NaCl (0.5 M and 5M left and right, respectively) to a 7 mg/mL solutions of (a) eGFP (green) and (b) mCherry (red) and (c) a mixture of both eGFP and mCherry. No full gel formation nor cluster percolation was observed.

found. Interestingly, some of the clusters are clearly composed by only one protein (Fig. 6.6 (c), left), suggesting that the intra-protein interactions overcome the inter-protein ones, which is one of the conditions for CSM.

6.3.2.2 Precipitation of eGFP and mCherry with Ammonium Sulphate

In view of the results for NaCl, we decided to try a more stabilising salt: ammonium sulphate, $(NH_4)_2SO_4$. This salt is widely used to purify, precipitate and store proteins due to its position on the Hofmesiter Series (see Fig. 6.4 far left) and to its higher solubility in water as compared to phosphate and carbonate salts, which are even further left in the series [185].

Previous studies have already used this salt to precipitate eGFP between ~ 1.5-3 M concentrations (40 to 70% saturation) [196, 192]. We used a saturated concentration of $(NH_4)_2SO_4$ (4 M) to ensure complete precipitation on individual solutions of each protein. The results are shown in Fig. 6.7, where we observe the desired gel-like structures for both proteins. The percolating networks extend for several microns and can be found throughout the capillary in the three dimensions. Additionally, the high contrast (black) background suggests that all protein has been successfully aggregated.

We then moved to test the effect of $(NH_4)_2SO_4$ on the precipitation of a mixture of both proteins (14 mg/mL of total concentration). We decided to test several salt concentrations, with a particular focus on the range between 1 and 2 M, where precipitation first occurs [196]. The results are shown in Fig. 6.8. We first observe that indeed no precipitation occurs before 1 M of $(NH_4)_2SO_4$, and we only start observing small clusters formed solely by eGFP after said con-

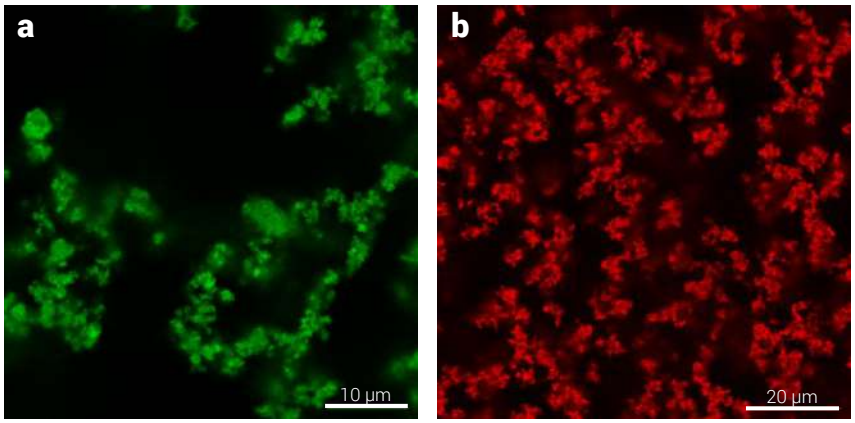

Figure 6.7: Gels formed through the addition of ammonium sulphate (4M) to a 7 mg/mL solutions of eGFP (green) and mCherry (red). The black background suggest that the proteins have fully precipitated.

centration, as shown in the individual protein panels for eGFP (green) and mCherry (red). Interestingly, this trend continues up to 1.5 M of $(NH_4)_2SO_4$, where larger clusters of eGFP are more easily obtained. However, we start observing co-precipitation of the proteins at 1.6 M $(NH_4)_2SO_4$, which is more evident as the salt concentration increases. By 1.8 M all of eGFP has already precipitated (black background in the individual eGFP panel). As more salt is added to the solution, the remaining mCherry continues to precipitate on top of the pre-existing gel and on itself (see figure at 2 M). Full protein aggregation is observed at 3 M of $(NH_4)_2SO_4$ and the gels obtained are a mixture of both proteins, as they appear yellow (overlay of green and red channels), with no domains of individual proteins being clearly identified.

These results suggest that the intra-protein interactions are not sufficiently larger than the inter-protein interactions and thus, the proteins co-precipitate. This phenomenon can be explained by the similarity of the structure of the two proteins, which means that their interactions with $(NH_4)_2SO_4$ are comparable and thus the proteins will precipitate at very close salt concentrations. Indeed, the bi-networks obtained by both I. Zhang *et al.* and Blumlein and collaborators, for example, are based on the very different characteristics and responses of each of the binary

Table 6.1: Comparison of the different properties of proteins eGFP and mCherry

Protein	Isolectric Point[1] (pH)	Charge at pH 7 (mV)	No. of Aspartate[2] Residues	No. of Glutamate[2] Residues	Total Acidic Residues	Cystein[2] Residues	Other[2] Residues
native eGFP	5.80	-14	17	15	32	2	2x Ca^{2+} 1x SO_4^{2-} 4x PEG
native mCherry	5.48	-6.1	12	21	33	0	0

[1] Protein Innovagen Protein Calculator
[2] Protein Data Bank

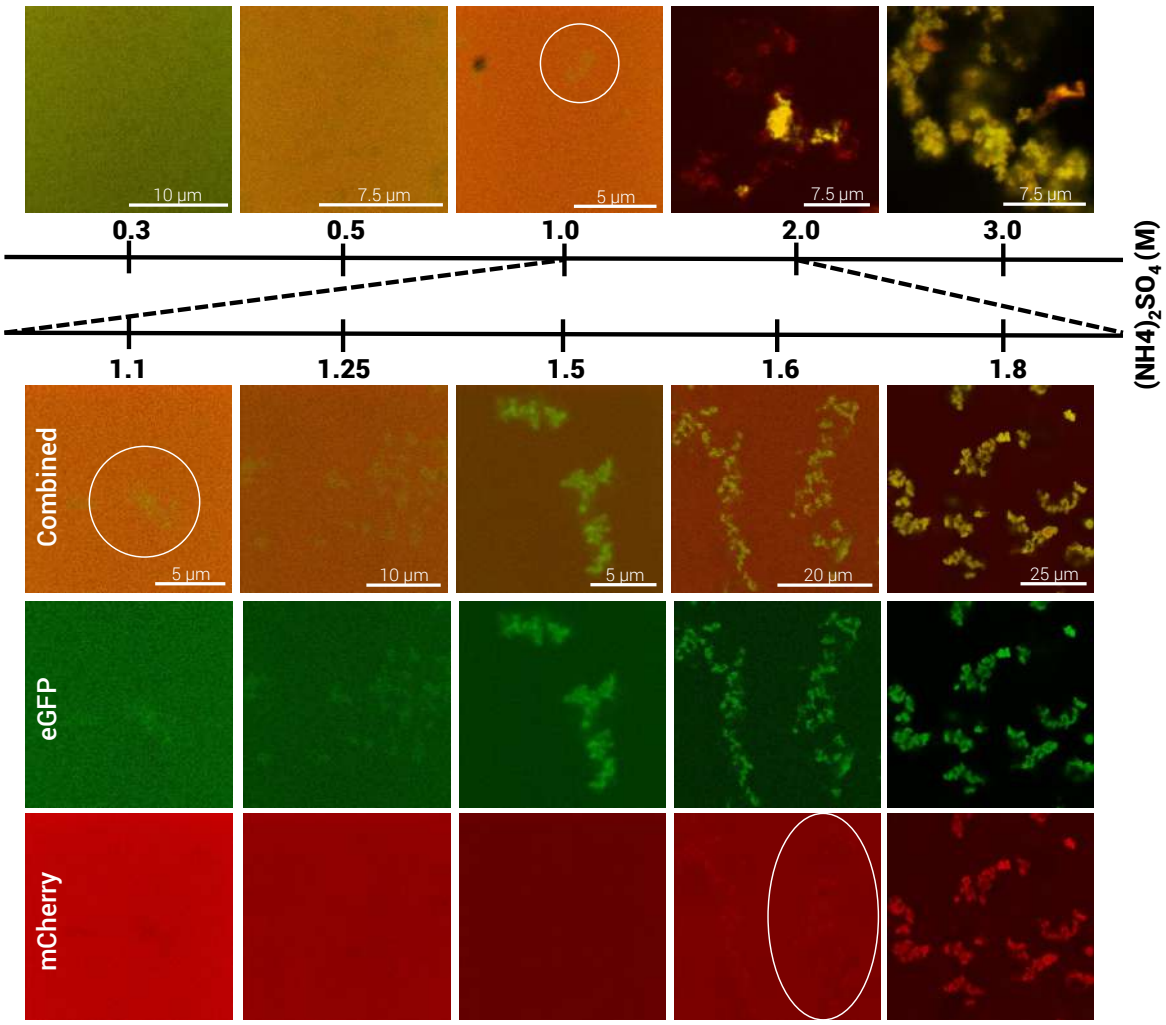

Figure 6.8: Gels formed through the addition of different amounts of ammonium sulphate to a 1:1 mixture of 8 mg/mL total protein of eGFP (green) and mCherry (red). The top images are an overlay of the channels. No precipitation is observed before 1 M of the salt, concentration after which small clusters of only eGFP are observed. The sizes and number of such clusters increase as the more salt is added to the solution. Moreover, as shown in the individual eGFP (green) and mCherry (red), these clusters are only formed by the former protein. However at 1.6 M we start seeing mCherry co-precipitation and deposition. At 1.8 M all eGFP has fully precipitated (black background on eGFP individual channel) and mCherry does it by 3 M of ammonium sulphate. The bi-networks are formed by a mixture of both proteins. The circled regions highlight the structures found.

components of the system to depletion interactions and heat, respectively [177, 168].

Table 6.1 shows the main properties of eGFP and mCherry proteins, where we can observe that they present a very similar negative charge at the pH studied. Additionally, the amount of acidic residues on the surface (aminoacids with carboxylic groups that confer the negative charge) is very similar. Only a few differences are present in eGFP. One of these is a site for a sulphate group (shown in blue in Fig. 6.5), which might explain why this protein precipitates before mCherry. However, the amount of these specific sites is too low (1 per protein) to have a larger impact.

Thus, the interactions of these proteins with $(NH_4)_2SO_4$ are not different or specific enough to yield precipitation at non-overlapping concentrations of the salt. Based on these results, it is clear that in order to obtain the bi-network desired, we need to aim for both specific salt-protein interactions and to modify the proteins to make them 'more different' between each other. The following sections will describe the strategies followed to fulfil both aims.

6.3.3 Precipitation of eGFP and mCherry with Trivalent Salts

F. Zhang and collaborators have extensively studied the interactions of trivalent salts with globular proteins [66, 190, 197, 198, 199, 112, 191]. In their studies they have found that these salts tend to successfully precipitate and crystallise negatively charged proteins without affecting their structure. Their studies comprise both a variety of trivalent salts (iron, aluminium and yttrium chloride) and a variety of globular proteins (BSA, ovoalbumin, β-lactoglobulin). They have described their phase diagrams over a range of salt and protein concentrations and have identified three different regimes for most of them. The first regime corresponds to proteins in solution. The second corresponds to liquid-liquid phase separation where clusters and crystals of the proteins appear. Finally, the third regime corresponds also to proteins in solution. This re-entrant solution arises as salt saturation causes a charge inversion on the proteins [66, 190, 197, 198, 199, 112]. Moreover, they have proposed a mechanism for the salt-protein interaction in which the trivalent cations form specific metal ion bridges with the surface-exposed carboxylic groups of the acidic residues of the protein. The metal ions then act as cross-linkers between the proteins so that aggregation or crystallisation occurs [190]. These interactions are more precise than those of the salts from the Hofmeister Series.

Based on these studies, we decided to test the ability of trivalent salts to precipitate eGFP and mCherry in order to have better control of these specific salt-protein interactions.

6.3.3.1 Precipitation of mCherry with Iron Chloride

We started the analysis by adding different concentrations of iron chloride ($FeCl_3$) to mCherry. Based on previous work, we tested 5, 10 and 20 mM of said salt [198]. However, immediately after the addition of $FeCl_3$ we observed a colour change on the solution, which was more evident at $FeCl_3$ concentrations above 10 mM, as shown in Fig. 6.9 (a). When looking at the samples under the microscope, we were only able to observe small protein clusters at 5 mM $FeCl_3$ (Fig. 6.9 (b)), whereas we were not able to detect fluorescence from the rest of the samples. This loss of fluorescence suggests denaturalisation of the protein.

A reason for the loss of the functional conformation of the protein might be a change of the pH of the solution. Indeed, Roosen-Runge *et al.* [198] showed that the Fe^{3+} cation lowers the pH of the solution dramatically due to ion hydrolysis. Even concentrations as small as 10 M $FeCl_3$ can bring down the pH to ~ 2.5 [198], a pH at which mCherry might not be stable anymore. Due

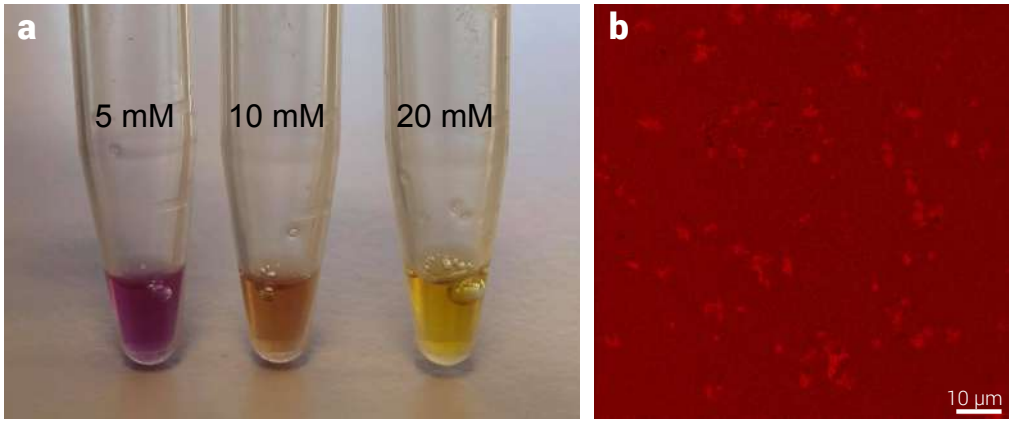

Figure 6.9: Effect of iron chloride addition to a solution of mCherry. a. Protein denaturation when the iron chloride concentrations are above 10 mM. b. Non-percolating clusters found at iron chloride 5 mM.

to this de-naturalising effect and to the fact that eGFP is more sensitive to pH changes [200], we decided not to proceed with further experiments or to test $FeCl_3$ with eGFP or a mixture of the proteins.

6.3.3.2 Precipitation of eGFP and mCherry with Yttrium Chloride

In the same study, Roosen-Runge and co-workers found that yttrium chloride (YCl_3) precipitates globular proteins successfully, without lowering the pH dramatically [198]. Inspired by this, we tried different concentrations of this salt with eGFP and mCherry. The results are illustrated in Fig. 6.10, where the green images correspond to eGFP and the red ones to mCherry. We first observed that even at small concentrations like 1 mM, eGFP starts aggregating and by 2 mM all the protein has precipitated in the gel-like structures desired and similar to the ones obtained with $(NH_4)_2SO_4$. These structures are preserved as we increase the salt concentration and we do not observe re-entrant solution.

However, the precipitation profile is not the same for mCherry. At 1 mM of YCl_3 we also observe some aggregation (highlighted by the circle in the figure), which continued at 2 mM, without full precipitation as observed with eGFP. Furthermore, as we continued increasing the salt concentration, we stopped observing any aggregates. This phenomenon has been described previously [66, 190, 198], where the precipitation of proteins with trivalent salts only occurred within a window of concentrations. Outside that range, the proteins were in solution. The studies suggested these results could be due to a saturation of metallic cations in the surface of the protein. This leads to a charge inversion, which makes the proteins stable again and thus they re-entrant solution, as mentioned earlier [66, 190, 198]. A similar saturation effect could be taking place to mCherry.

This outcome is surprising as, according to Table 6.1, both proteins present the same amount of acidic residues that interact with the trivalent ion. A possible factor for the difference in the

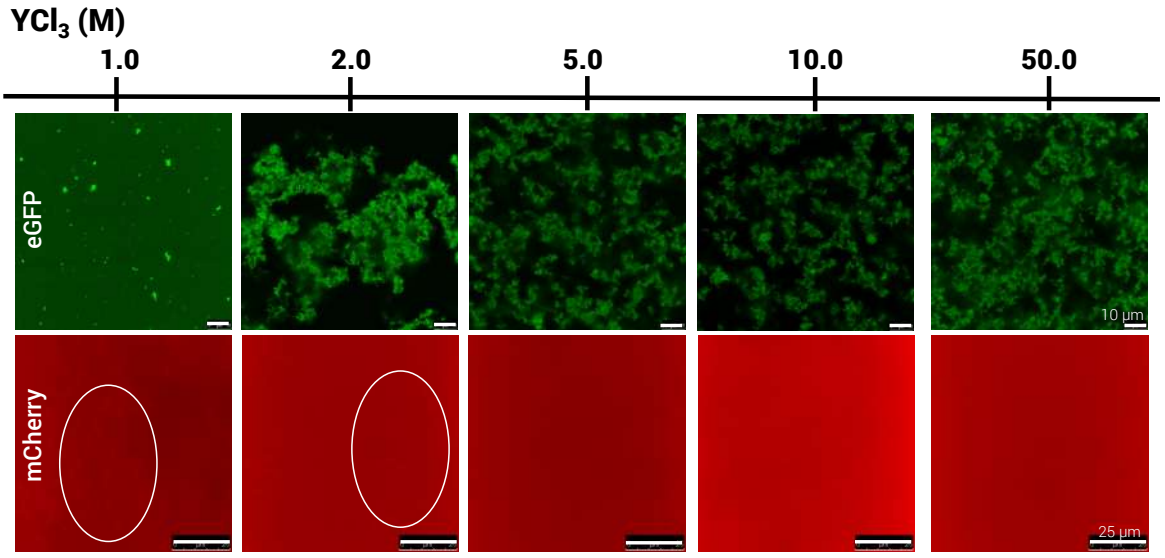

Figure 6.10: Gels formed through the addition of different concentrations of yttrium chloride (YCl_3) to 7 mg/mL solutions of eGFP (green) and mCherry (red). We observe small cluster formation already at 1 mM of YCl_3 for both proteins. Full eGFP precipitation is observed and preserved at YCl_3 concentrations > 2 mM. Conversely, for mCherry no full precipitation is observed and at YCl_3 concentrations > 5 mM we do not observe any precipitate or clusters, probably due to re-entrant solution [66, 190, 198]. Scale bars are 10 μm for eGFP and 25 μm for mCherry.

behaviour could be the number and surface distribution of the carboxylic groups, which might facilitate faster surface saturation or prevent proper bridging with the metal ions. Indeed, when studying the linking of BSA and yttrium molecules, F. Zhang and coworkers found that although the dimer of said protein contained more than 50 surface-exposed acidic residues, only a few of them ordered in a way that allowed their simultaneous linking with the same cation [190]. Moreover, they found that this orientation-dependent bridging of a neighbouring side chain and the metal is essential for protein crystallisation [190]. Presumably, the number of mCherry residues that cluster effectively to form the proper bridges with yttrium cations is lower than eGFP and thus we do not observe the same precipitation profile. Further studies on the charge distribution of mCherry and their spatial interactions with yttrium cations are necessary for a better understanding.

Nevertheless, as we did observe precipitation of YCl_3 with eGFP, we thus have successfully found a salt that interacts specifically with one of the components of our binary mixture.

6.3.4 Surface Modification of the Native Proteins through Cationisation

The results of the salt addition to eGFP and mCherry solutions are summarised in Table 6.2, where we can see that from our four candidates, only $(NH_4)_2SO_4$ and YCl_3 formed the desired gels with eGFP. The addition of the former salt to mCherry also produced the wanted gels, however, this was not the case for YCl_3. Finally, when $(NH_4)_2SO_4$ was added to a mixture of eGFP and mCherry, gels with mixed proteins were observed and not the bicontinuous desired structures

Table 6.2: Addition of different salts to eGFP and mCherry solutions and mixtures

Salt	eGFP	mCherry	eGFP + mCherry
NaCl	only clusters	only clusters	individual clusters
$(NH_4)_2SO_4$	gels	gels	mixed gels
$FeCl_3$	X	denaturation	X
YCl_3	gels	precipitation + re-entrant solution	X

presumably due to a lack of specificity in the protein-salt interactions.

In light of these results, an alternative strategy to yield the desired gel bi-networks was to modify the proteins so they can interact in a different manner with the salts tested herein.

As previously mentioned, the trivalent cations interact specifically with the negative charges of the surface of the protein, which are provided by the presence of carboxylic groups from acidic residues. A related study showed that positively charged proteins did not precipitate regardless of the salt and the concentration used [66]. We thus decided to manipulate the charges of the proteins in order to prevent their interaction with YCl_3, to further increase the specificity of this salt with our system components.

One way to easily manipulate the proteins' charge is by modifying the pH of the solution. As mentioned before, at pH below the isoelectric point of the protein, they have a net positive charge, whereas at pH above it, the proteins have a negative charge [178]. The respective values of pI of eGFP and mCherry are listed on Table 6.1, where we can see that they are fairly similar (~ 0.4 difference), which limits the pH range where we can manipulate the charges. Moreover, the addition of YCl_3 would modify the pH and in turn may affect the protein and salt interactions.

Another way to modify the charges of the proteins without disrupting their structure is through the chemical addition of certain charged ions. This procedure is called *cationisation* when the added charges are positive or *anionisation* when they are negative. Since with this procedure we wish to avoid the proteins interaction with yttrium chloride, we performed cationisation on our native proteins. To understand this process, we need to discuss the chemistry of cationisation.

6.3.4.1 Cationisation Reaction

The reaction mechanism for cationisation is shown in Fig. 6.11, where the exposed carboxylic groups of glutamic and aspartic acid residues are highlighted on the surface of the protein. Once a diamine is added to the solution, these acidic residues will react with one of the terminal amino groups present in a diamine (hexamethylendiamine, in this case), through a nucleophilic substitution reaction to produce an amide bond [201]. This means, that the -OH group of the carboxylic acid is substituted by the primary amine [202]. This reaction will confer a positive charge to the protein through the remaining free amine group of the original diamine as shown

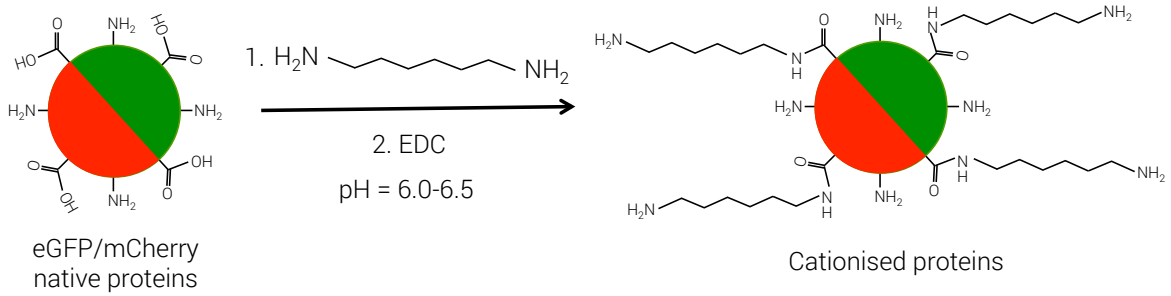

Figure 6.11: Cationisation reaction of eGFP and mCherry. The carboxylic groups of the acidic residues on the surface of the protein react with one of the amino groups of the hexamethylendiamine to form an amide bond, adding the unreacted amino terminal from the diamine to the surface of the protein and thus a positive charge. A 10x excess of hexamethylendiamine was added to a protein solution, followed by two separated additions of the crosslinker 1-ethyl-3-(3-dimethylaminopropyl)carbodiimide hydrochloride (EDC).

in the figure. Remarkably, this reaction occurs only with the acidic groups in the surface of the protein. Furthermore, it occurs in mild pH conditions (6.0-6.5) and at room temperature, which prevents protein denaturation. This reaction has the flexibility and potential to introduce other functional groups through a different amine precursor [203].

In our case, the hexamethylenediamine was added in excess to ensure the reaction of all carboxylic groups available. Additionally, 1-ethyl-3-(3-dimethylaminopropyl)carbodi-imide hydrochloride (EDC) serves as an activator of the carboxylic groups: it reacts first with them to form an active acyl group (R-C=O) which can be easily displaced through a nucleophilic attack from the diamine [202]. We added EDC at two different times to improve the yields of the reaction. We also monitored the pH to ensure the right reaction conditions and protein stabilisation. Once the reaction time concluded, the proteins were dialysed and concentrated.

We did not observe any changes in the colour of the solution, which suggested that the protein native structure was preserved throughout the different steps of the reaction. We then corroborated the success of the reaction by measuring the charge of the proteins through zeta potential measurements. The results are shown in Table 6.3, where we do observe a higher positive charge for both cationised proteins, in comparison with their native negative counterparts. Interestingly, we can see that such increment is larger for mCherry than for eGFP, which might be a consequence of using a higher protein concentration, or availability of mCherry sites to be cationised.

6.3.4.2 Precipitation of Cationised Proteins with Yttrium Chloride

Once we have obtained the cationised proteins, we continue to test if we have effectively 'blocked' the interaction between YCl_3 and the proteins. We thus mixed solutions of each cationised protein against the same concentrations of the salts as before for the native proteins. We could not observe any aggregation for both proteins at any concentration tested, as shown in Fig.

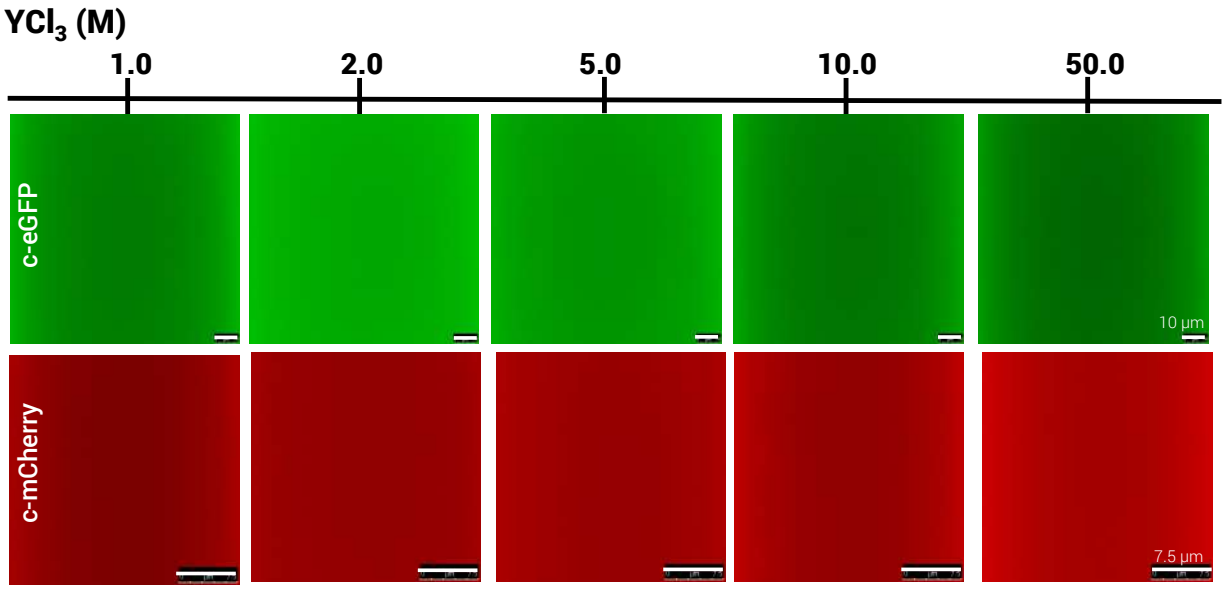

Figure 6.12: Evaluation of the cationisation reaction on native eGFP (green) and mCherry (red) against the addition of different amounts of YCl_3. No cluster formation, nor precipitation is observed for both proteins regardless of the salt concentration, showing the successful cationisation of the proteins. Scale bars are 10 μm for eGFP and 7.5 μm for mCherry.

6.12. Here, only the fluorescence from the protein in solution can be observed, which in turn shows that the protein kept its tertiary conformation in spite of the surface modification.

These results show that we can effectively prevent the interaction of a protein with a particular salt through an easy surface modification, without altering its native and functional conformation.

6.3.4.3 Precipitation of Cationised Proteins with Ammonium Sulphate

Finally, we tested if the addition of positive charges to the proteins affected their precipitation with $(NH_4)_2SO_4$. Thus, we added 3 M of this salt to a 8 mg/mL solution of each cationised protein. Images of the results obtained are shown in Fig. 6.13 where it can be clearly observed that both cationised proteins successfully precipitate with said salt. Moreover, they form gel

Table 6.3: Comparison between the charges of native and cationised eGFP and mCherry

Protein	Native Charge (mV)	Charge after Cationisation (mV)
eGFP	-14	+1.9
mCherry	-6.1	+8

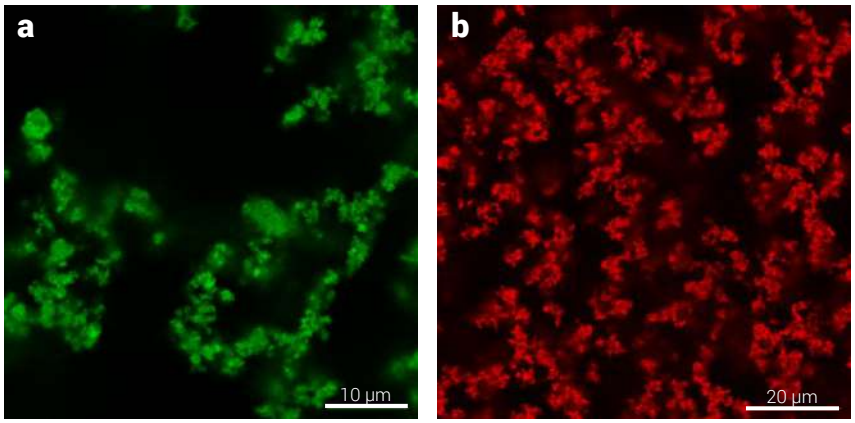

Figure 6.13: Evaluation of the cationisation reaction on native eGFP (green) and mCherry (red) against the addition of 3 M of $(NH_4)_2SO_4$. Both proteins still precipitate with this salt in spite of the surface modification.

structures similar to their native counterparts, which shows that cationisation did not affect this particular interaction. Furthermore, these results further suggest that the proteins precipitate in the presence of $(NH_4)_2SO_4$ as a consequence of preferential solvation and enhancement of hydrophobic interactions, rather than the interactions with charged regions.

Thus, we have a system where native proteins precipitate through specific interactions with YCl_3, whereas cationised proteins do not. However, the latter still precipitate readily with $(NH_4)_2SO_4$. We will use these specific and differential interactions to yield the bicontinuous gels.

6.3.5 Gel Bi-network Formation

Previously, we discussed a gel bi-network formation strategy consisting in a two step process where a primary gel is formed by one of the proteins with the other one remaining in solution. Then, the latter protein is precipitated too, forming an interlinked gel with the pre-existing one.

Based on this procedure and our results discussed above, we present in this section two different strategies to produce the desired bi-networks, the analysis of the composition of the structures found and its potential for future applications.

6.3.5.1 Two Step Salt Addition for Critical Soft Matter Realisation of a Mixture of Native and Cationised Proteins

Our initial strategy is very similar to the one proposed by Blumlein and coworkers [168] mentioned above, and is illustrated in Fig. 6.14, where only one of the mixtures is shown. Here, equal amounts of the native eGFP and cationised mCherry (*mixture a*) or cationised eGFP and native mCherry (*mixture b*) are mixed. This is followed by the addition of YCl_3, where we expect that only the native proteins form a gel, whereas the cationised ones remain in solution. Then $(NH_4)_2SO_4$ is dissolved into the mixture to precipitate the cationised proteins in solution, which

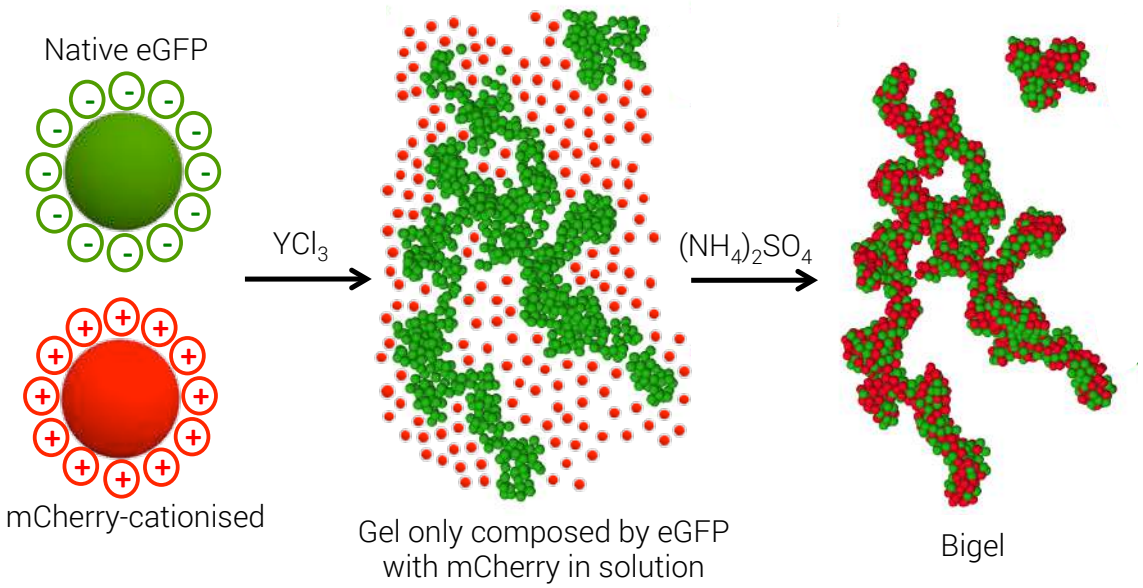

Figure 6.14: Scheme of the proposed protocol for yielding critical soft matter gels. *Mixture b* composed by native eGFP and cationised mCherry is illustrated here, but the same procedure was used for *mixture a*. The proteins are mixed in equal concentrations. 5 mM of yttrium chloride is added to form a gel solely formed by native eGFP, leaving cationised mCherry in solution. Finally, ammonium sulphate is added to precipitate the latter protein and thus form phase separated bicontinuous gel, with distinctive native eGFP and mCherry domains.

we expect to do so in the form of small domains deposited on the preexisting gel in order to form the phase separated bicontinuous network shown in the figure.

We followed then the scheme in Fig. 6.14 using 30 μL of 8 mg/mL of total protein, and salt concentrations of 5 mM of YCl_3 and 3 M of $(NH_4)_2SO_4$.The results of each step of the procedure are summarised in Fig. 6.15, where the top figures belong to *mixture a* and the bottom ones to *mixture b*. For *mixture a* we observed slight turbidity when we mixed cationised eGFP and native mCherry before any salt addition, which we have not seen before with other mixtures. Moreover, we did not observe it in *mixture b* when we mixed native eGFP and cationised mCherry. When we observed both mixtures under the confocal, we found clusters formed by both proteins in both cases, however, the sizes and number of clusters formed on the *mixture a* were much larger and numerous than the ones observed in *mixture b*, where only a few small clusters were found (Fig. 6.15, left). This cluster formation most likely arises from the proteins having opposite charges which makes them attractive. The reason it is much more evident with *mixture a* could be from less charging of the proteins (see Table 6.3) which might make them less stable.

In spite of these findings, we continued with the different salt additions, where we also observed interesting results. As aforementioned, we were expecting to observe a gel formed only by the native protein, however, as can be observed in the middle panels of Fig. 6.15, for the case of *mixture a* the previously observed clusters now formed a protein gel network that covered most of the bottom of the capillary and extended for a few microns in the z axis. We have not

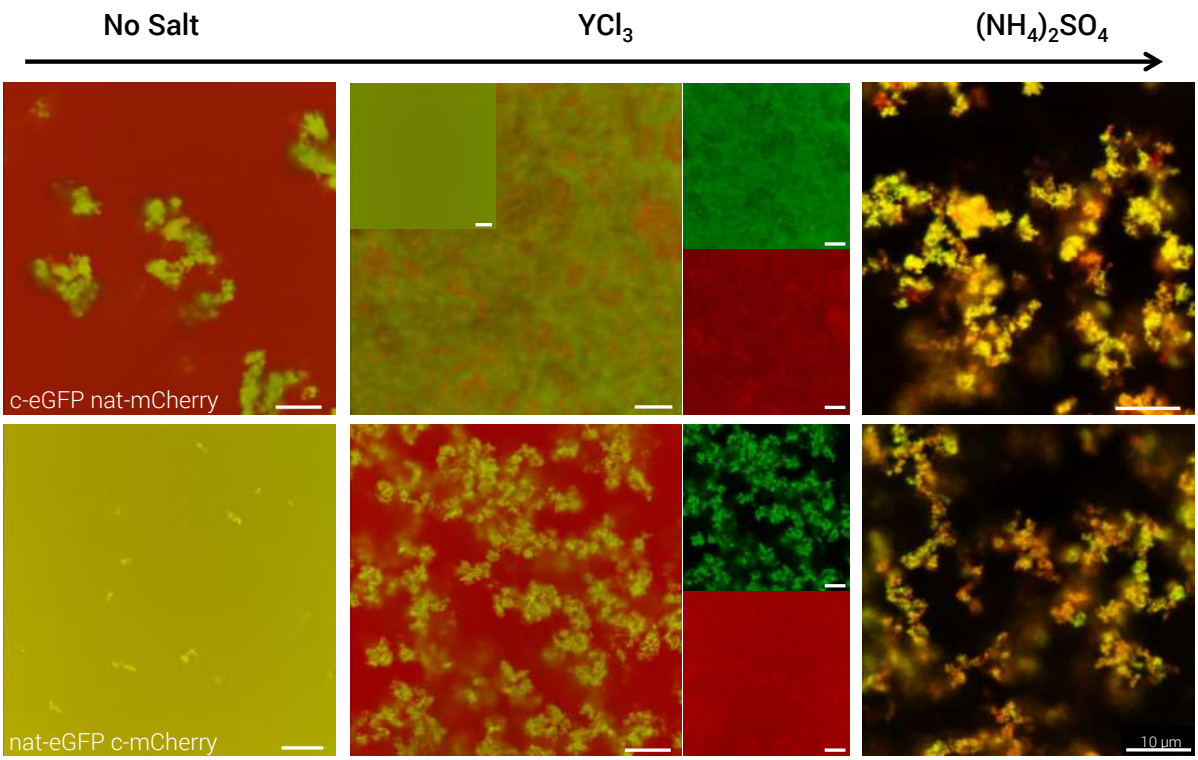

Figure 6.15: Gel bi-network formation following the two step salt addition protocol. Top images correspond to a mixture of cationised eGFP and native mCherry (*mixture a*), whereas the bottom images correspond to a mixture of native eGFP and cationised mCherry (*mixture b*). We observed cluster formation without any salt addition due to the oppositely charges of the proteins (left panel). After the addition of yttrium chloride, for *mixture a* we observe the formation of a extended network formed by both proteins (middle panel), network which 're-structures' to a mixed protein gel after the addition of ammonium sulphate (right panel). For *mixture b*, we did obtain full precipitation and gel formation of native eGFP. However, we also observed unexpected co-precipitation of cationised mCherry after the addition of yttrium chloride (middle panels, separated channels). The insert corresponds to a mixture of cationised eGFP, cationised mCherry and yttrium chloride, where no precipitation is observed. When ammonium sulphate is added, the rest of mCherry precipitates to form a also a mixed protein gel. The structures formed by both mixtures are similar to the ones obtained previously with ammonium sulphate and unmodified proteins. Scale bars correspond to 10 μm.

seen such a precipitate with any of the of the conditions previously tested. These structures might arise as unexpected interactions of the salt and the oppositely charged particles. On the other hand, for *mixture b*, we did observe full gel formation of native eGFP as expected. However, we also observed unexpected co-precipitation of cationised mCherry. These results suggest that the presence of a precipitating native protein affects the interactions of the cationised one and co-precipitation occurs.

Protein co-precipitation has been studied mainly due to its correlation with the pathology of important diseases such as Parkinson's and Alzheimer's. Konno and collaborators investigated the effect of induced precipitation of soluble proteins by Alzheimer's β(25-35) amyloid fibril. They found that clustering of the amyloid peptide was required to induce non-specific co-aggregation for all the soluble proteins tested and that the co-precipitant proteins bounded to the surface

of the amyloid [204]. We hypothesise that similarly, the precipitating native proteins lead to co-precipitation of the cationised ones, rather than un-expected interactions of the latter with the salt. In order to test this hypothesis, we mixed cationised eGFP and cationised mCherry and added YCl_3 under the same concentrations as above. We did not observe any cluster or precipitate formation (insert in Fig. 6.15), which indicates that the precipitation of cationised proteins, similarly to the case studied by Konno *et al.* [204], is indeed induced by the precipitating native protein in the presence of YCl_3. However, the co-precipitation does not denature the proteins as we still observe fluorescence, similarly to Konno *et al.* [204]. Moreover, in said study, the authors found that electrostatic interactions were one of the factors for protein co-aggregation [204]. Since our proteins in both mixtures have opposite charges, electrostatic interactions might also contribute to co-precipitation. In the future, it is worth-pursuing simulation work or further protein surface modification with another functional group to shed light into the mechanisms and nature of protein-protein interactions involved in this phenomenon.

Finally, after the addition of $(NH_4)_2SO_4$, we observed gels very similar to the ones obtained with a mixture of unmodified proteins, where both proteins are mixed or deposited one on top of the other (yellow colour from overlaying of the two channesl) and few individual protein domains can be distinguished (small green and red areas) as shown in Fig. 6.15 right panels. The appearance of such structures is particularly surprising for *mixture a*, as the structures found on the previous step are quite different. This 're-structuring' of the precipitate might be due to a larger strength interaction of the proteins with $(NH_4)_2SO_4$, and suggests that the protein-YCl_3 interactions are weaker and reversible. Equally, further studies into the particular interactions when both proteins and both salts are present might help to explain this complex phenomenon.

Our results clearly indicate that major and more complex interactions surface when a mixture of oppositely charged proteins interact with salts, and suggest that further and different modifications might be needed to decrease or avoid protein-protein interaction to yield the desired bicontinuous networks.

6.3.5.2 Two Step Salt and Protein Addition for a Bicontinuous Network Formation of a Mixture of Cationised eGFP and Native mCherry

The major limitation to produce critical soft matter gels appears to be the unexpected interactions between the proteins. So, in order to avoid them, we decided to modify the addition of the mixture components, keeping the same concentrations of both proteins and salts. The new protocol is illustrated in Fig. 6.16. Here, we first form a gel with the native protein and YCl_3. We then add $(NH_4)_2SO_4$ to precipitate cationised mCherry, which we add at last. We decided to keep using cationised mCherry to avoid undesired interactions with YCl_3. As native mCherry did not form the desired gels with YCl_3 (see Fig. 6.10 red panels and Section 6.3.3.2), we decided to focus only on the behaviour of native eGFP and cationised mCherry mixtures.

The results of this new strategy are summarised in Fig. 6.17, where it can be seen that struc-

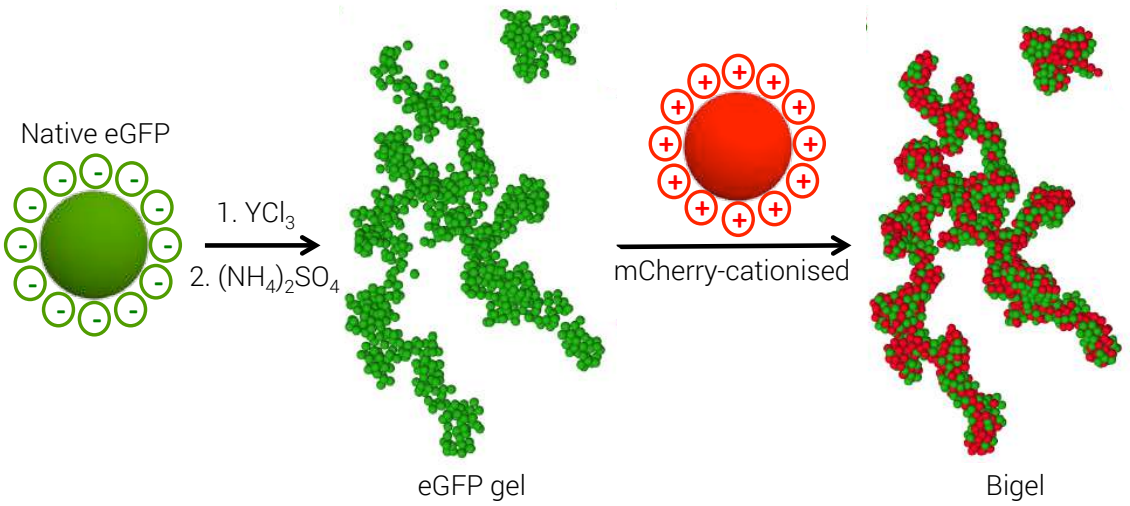

Figure 6.16: Scheme of the proposed alternative protocol for yielding critical soft matter gels. Native eGFP and was mixed on its own with 5 mM of yttrium chloride is added to form a gel. 3 M of ammonium sulphate is added followed by the addition of cationised mCherry which precipitates with ammonium sulphate already in the solution, forming the expected gel bi-networks with distinctive native eGFP and mCherry domains.

tures very close to the desired bicontinuous gels were obtained. However, it is important to highlight that in this methodology we are no longer exploiting critical soft matter self-assembly principles, i.e., different responses of the system components to an external stimuli according to their intra-particle interactions [53]. Thus the structures found are *not* critical soft matter gels. In Fig. 6.17 we can clearly distinguish green and red-only domains (native e-GFP and cationised mCherry, respectively), which indicate that they are solely composed by one of the proteins. However, there are still large yellow areas, which indicate that cationised mCherry deposited directly on the surface of the preexisting native eGFP gel, areas which we will refer as 'mixture' in the following sections. Both observations are clearer at higher magnifications (Fig. 6.17 (b)).

The changes on the addition of the mixture components, which were aim to avoid protein-protein co-precipitation, allowed us to obtain structures very close to the desired ones. However, we were expecting that most cationised mCherry formed clusters and precipitated on its own before depositing or interacting on the preexisting gel. It is evident from our results that there is still a strong competition between intra and inter-protein interactions, the latter being more predominant. This could be a consequence of using $(NH_4)_2SO_4$ to precipitate the cationised mCherry, which, as discussed earlier, does not interact specifically with the protein, providing little room for fine control of the interactions and protein precipitation.

In order to increase the strength of mCherry intra protein interactions and decrease the protein mixing, a different surface modification with an alternative functional group can be performed. Alternatively, a salt that might precipitate proteins through unique interactions with an amino (or other) groups can be sought.

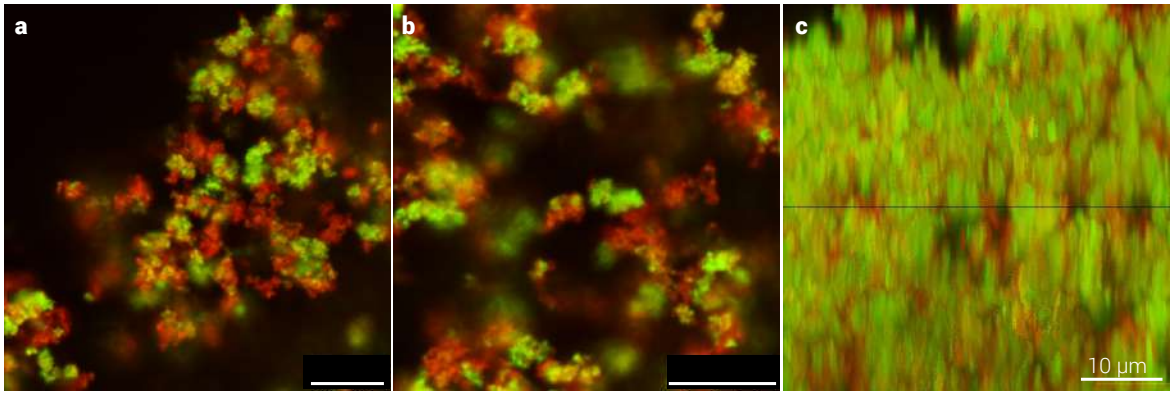

Figure 6.17: Gel bi-network formation following the two step protein addition protocol using native eGFP (green) and cationised mCherry (red). Left and central panel: xy projections. Although deposition of cationised mCherry is still present (yellow colour areas), clear domains of individual protein aggregation are distinguished (only green or only red areas). This is more evident as we look closer into the gel structure (b). (c) xz projection, where the domains appear like enlarged ellipsoids. These structures are very close to the desired CSM-gels.

6.3.6 Analysis of the Mixing and Domain Sizes of Native eGFP and mCherry Cationised in the Bi-networks

We then move to compare qualitatively the two different bi-networks that we obtained through our two strategies to study if there are indeed significant differences in their composition. Additionally, we tested further concentration conditions to see if we could further manipulate the sizes of the individual domains. We did the qualitative study by classifying the intensity of the image pixels as green for the native eGFP, red for cationised mCherry and yellow for protein co-precipitation (first strategy) or cationised mCherry deposited on the native eGFP gel (second strategy). This was done by intensity normalisation and by applying different green/yellow, red/yellow and green/red intensity thresholds, which were optimised to produce reliable tracking and pixel-colour assignation. An example of the different images analysed for the different conditions is illustrated in Fig. 6.18, were the upper line shows the original confocal images and the bottom line the analysed ones. It is clear that the areas of individual protein domains (green and red) are assigned successfully. Yellow and slightly orange regions are also effectively identified as mixed-protein sections. It is important to mention that these studies were done on 2d images. Although 3d scans were obtained for all samples, the intrinsic lack of density and refractive index matching, along with sample sedimentation, generated aberrant images in the z axis, as shown in Fig. 6.17, (c).

6.3.6.1 Percentage Distribution of Co-precipitation or *Covered* and *Un-covered* Gel on the Native eGFP by Cherry Cationised Bicontinous Network

We first compared the two strategies followed to yield the bi-networks. Histograms of the percentage distribution of the mixed (yellow), native eGFP (green) and cationised mCherry (red)

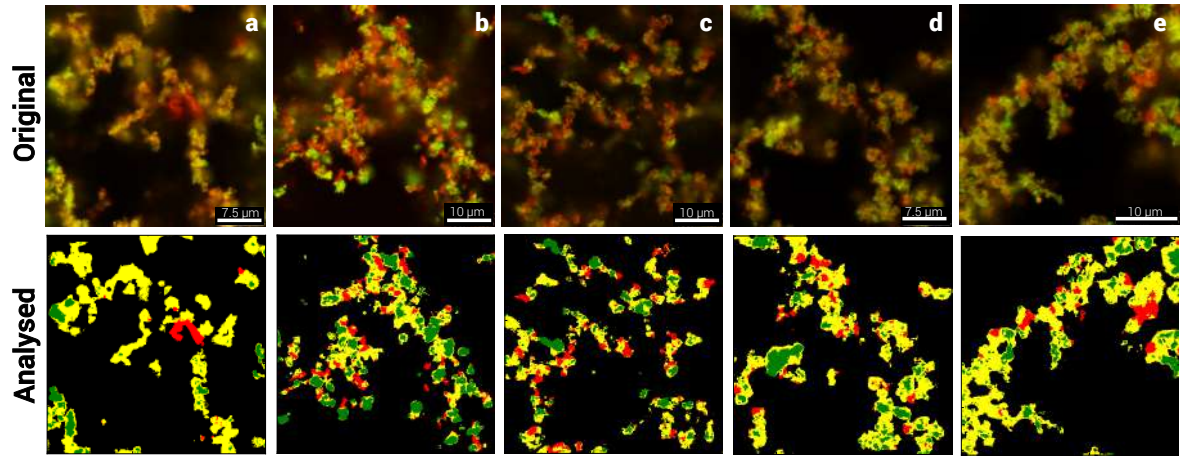

Figure 6.18: Comparison between the original images (top row) and the ones produced by the structure analysis (bottom row). It is clear that the code effectively identifies the de-mixed zones where only one of the proteins is present (green for native eGFP and red for cationised mCherry) and zones were there is deposition of cationised mCherry on the pre-existing native eGFP gel (yellow colour).

proteins in the gels are shown in Fig. 6.19, where the lines correspond to the first procedure and the filled histograms to the second one. It is clear from the histograms, that effectively the late addition of cationised mCherry enabled us to decrease the level of protein-protein co-precipitation and protein deposition on the gel. In the case of the first protocol, around ~80% of the pre-existing gel is covered by or co-precipitated with cationised mCherry, leaving only ~15% of 'free' native eGFP gel and thus only ~5% of the gel is formed by cationised mCherry individual clusters. On the other hand, the second strategy effectively reduced the gel coverage to almost half of the previous protocol (~40%), and the regions of 'un-coated' gel and individual protein clusters increased almost by two, reaching almost ~40% for free native eGFP gel and ~20% for cationised mCherry.

These results suggest that we can, up to a certain extent, control the percentage of 'gel coverage' by simply changing the order of the protein addition and might be particularly useful for future applications, where the functionality of the system requires a particular coverage of the pre-existing gel.

6.3.6.2 Domain Sizes of Bicontinuous Networks formed by Native eGFP and mCherry Cationised

We finally tested if we were also able to control the extent of the native eGFP gel coverage and the domain sizes of the regions with individual native eGFP and cationised mCherry. In order to do this, we decreased the concentration of cationised mCherry to a half, a fifth and a tenth of the correspondent of eGFP, which was kept at 5 mg/mL. We used the second strategy to obtain the bicontinuous gels. Furthermore, changes in these values might give an indication of which of the interactions is preferred as follows: if the amount of regions identified as mCherry increases

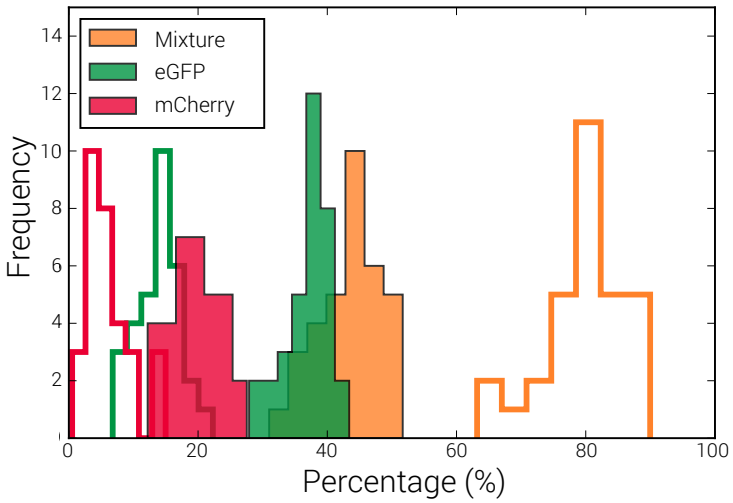

Figure 6.19: Comparison of the percentage distribution of individual regions of native eGFP (green), cationised mCherry (red) and covered gel (yellow) according to the production strategy. Adding the salts in two consecutive steps produceds an ~80% coverage and thus less than ~20% of free protein, as indicated by the lines. Differently, adding the cationised mCherry as the final step, produces less coverage of the original native eGFP gel, which reaches only ~40%, leaving ~40% of the pre-existing gel and ~20% of cationised mCherry free, as shown by the filled histograms.

or remains the same as the quantity of this protein is reduced, it might suggest that there is a slight preference for intra-protein interactions. *Per contra*, if the gel coverage augments as less cationised mCherry is added, then the inter-protein interactions are preferred.

Fig. 6.20 shows the results obtained. The first graph corresponds to the different percentages according to the different ratios tested for cationised mCherry, the graph in the centre corresponds to native eGFP, whereas the right graph corresponds to the gel coverage. The different native eGFP and cationised mCherry ratios 1:1, 2:1, 5:1 and 10:1 are coloured in pink, purple, blue and turquoise, respectively. As we decreased the amount of cationised mCherry, so did the percentage of uncovered native eGFP gel (Fig. 6.20 centre), whereas the percentage of covered gel increased (Fig. 6.20 right). Yet no significant differences are observed between 5:1 and 10:1 ratios (Fig. 6.20 blue and turquoise). Although a similar trend to 'free' native eGFP is observed for cationised mCherry, it seems that there are also not significant differences between 1:1 and 2:1 ratios (Fig. 6.20 left pink and purple colours). This is surprising as, according to the other two analysed conditions, more cationised mCherry is covering the prexisting gel at 2:1 ratio, and thus the sizes of only cationised mCherry regions should have been reduced at this condition too. A reason that might explain this phenomenon is that the coverage of the gel by cationised mCherry is more extended but thinner. An equally extended but thinner cationised mCherry layer might also explain why there are no significant differences between the 5:1 and 10:1 ratios (Fig. 6.20 blue and turquoise).

Unfortunately, neither the kinetics of the precipitation, nor the thickness of the deposited mCherry layer can be followed or resolved with our current microscopy techniques. However,

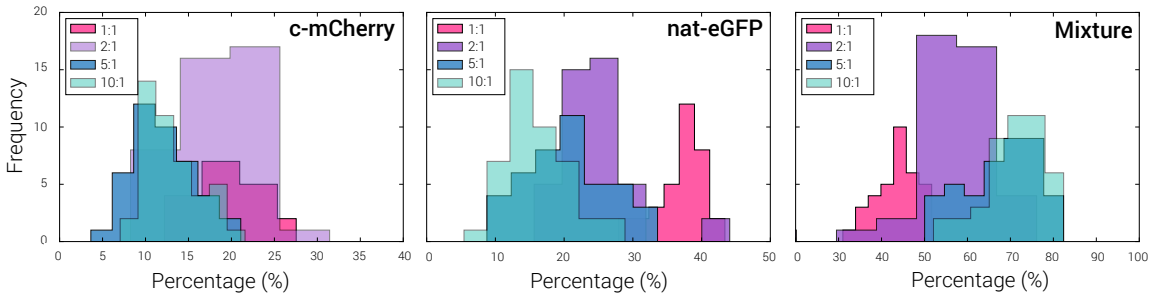

Figure 6.20: Comparison of the distribution of the percentages of individual regions of cationised mCherry (left), native eGFP (middle) and coated gel (right) in the bi-network when the native eGFP: cationised mCherry concentration ratio of the proteins is varied from 1:1 (pink), 2:1 (purple), 5:1 (blue) and 10:1 (turquoise). In general, the percentages of 'free' protein decrease as the amount of mCherry decreases, whereas the gel coverage increases.

simulations of these conditions might help to prove if our hypothesis is correct and elucidate the actual mechanism for the formation of the gel bi-networks.

Finally, we measured the sizes of only the native eGFP and cationised mCherry domains to see if their distribution also changed with the different protein ratios tested. To do this analysis, the pixel neighbours of already colour-assigned pixels were counted and the number of pixels per domain was obtained. They were then converted to micrometers according to the pixel size. The histograms with the distribution results are shown in Fig. 6.21, where the left panel shows the size distribution of native eGFP domains, and the right panel shows the correspondent ones for cationised mCherry. The plots show that the amount of small areas is higher for cationised mCherry than for native eGFP, and that more areas with sizes above $\sim 8\ \mu$m are observed for latter. For this protein, we can see that the size distribution is smaller as the amount of cationised mCherry is decreased. This decrease in both number and size of native eGFP domains is more evident for the 5:1 and 10:1 ratios (blue and turquoise colours, respectively) as compared to equal amounts (pink) of the proteins (Fig. 6.21 (a)). This coincides with the suggestion that we obtain a larger gel coverage as the amount of cationised protein added is reduced. However, this trend is not clearly observed for cationised mCherry domains. It only seems that there is a smaller size distribution when the concentration of this protein is reduced 10 times (turquoise), since the distribution for the rest of the concentrations looks similar, as shown in Fig. 6.21 (b). Thus, although the actual coverage of the pre-existing gel might be manipulable, the actual size of the individual protein domains of the second protein does not seem to be so with our current proposal.

In order to overcome these limitations, we would need to study precisely the strength as well as the actual motives involved in the interactions between the proteins and the salts. This may not only allow us to yield the desired gel coverage, but also to tune the sizes of the individual protein domains.

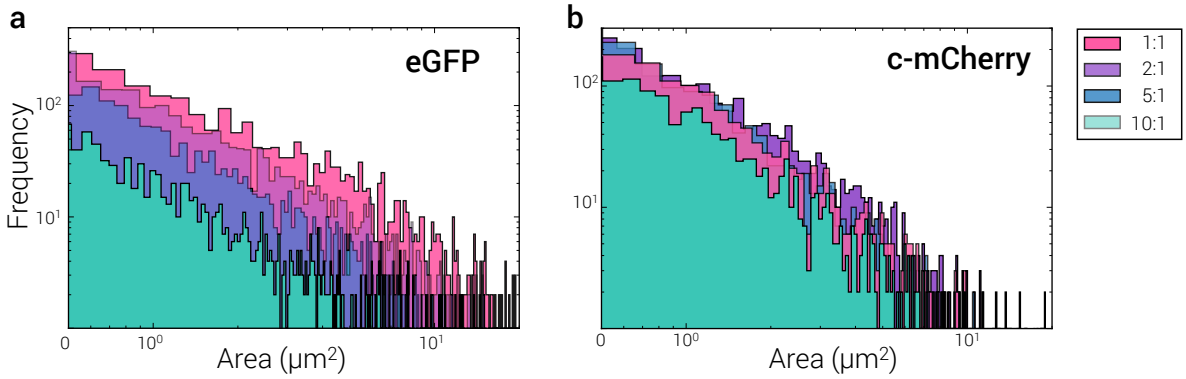

Figure 6.21: Comparison of the distribution of the domain area size of individual regions of native eGFP (a) and cationised mCherry (b) in the bicontinuous gels. The native eGFP: cationised mCherry concentration ratio of is varied from 1:1 (pink), 2:1 (purple), 5:1 (blue) and 10:1 (turquoise). Although there is a general increase on the number of smaller area sizes as the concentration of cationised mCherry is decreased, not a strong or monotonic correlation between the distribution of areas and the different concentration ratios can be drawn for mCherry domain sizes.

Although we still lack precise control and differentiation of the protein-protein and protein-salt interactions to yield critical soft matter gel structures, to our knowledge, this is the first realisation of phase separated bicontinous protein gel where the proteins preserve their native structure. Our study highlights the complexity of protein interactions and the need for further studies to understand them in order to achieve the desired structures. However, it also opens the door for further research to obtain innovative functional biomaterials using the strategies proposed herein.

6.3.7 Potential Applications of the Bi-networks Produced

We envision several bio-composite applications for our bicontinous gel networks. The first one has to do with its structure which can serve as scaffolding for tissue engineering. In this regard, gels have largely shown to be good templates for cellular and tissue development, and currently the most popular material to do so are hydrogels. These are systems where the 3d network is formed by a cross-linked hydrophillic polymer capable of swelling or de-swelling reversibly in water [205, 165, 174]. However, these materials present some drawbacks regarding their low tensile strength, limitations on their versatility, costs, batch reproducibilty and toxicity [174].

Several critical characteristics of the scaffolds are needed for proper growth, differentiation and development of the cells and tissue. These characteristics will be determined by the type of cell and tissue or interest. The first one includes the mechanical properties of the gels, like stiffness and elasticity [172, 173]. The second characteristic involves their ability to mimic the function of the extracellular matrix (ECM), in particular, to have growth factors that allow cells and tissue development [171, 173]. Also, low immunogenicity and biocompatibility are essential

for *in vivo* applications. Finally, the scaffolds need to be easy and safe to degrade [173]. With the versatility of our protein gels, the specific characteristics of the proteins forming the composite, as well as their interactions, can be tuned or engineered to yield the required properties. As such, the Young's Modulus and porosity can be tailored to the required ones. In addition, since the proteins in our bi-networks preserve their function, proteins from the ECM can be chosen and incorporated to the gel structure, making the structures bioactive. Lastly, proteins are intrinsically biocompatible [168] and they can be enzymatically processed and hence cleared without forming toxic byproducts.

One of the current limitations of genetic engineered proteins to form gels is the scale-up ability and costs [172]. As a result, the proteins typically selected to yield the gel structures are limited to natural structural (fibrous) proteins, like elastin, keratin, collagen and gelatin [171, 168, 172]. Our easy and cheap strategy has shown that at protein concentrations ~10 mg/mL, micron-sized bi-network structures can be readily achieved, and that no prerequisite of the structural characteristics of the proteins involved is needed to form these long networks.

Furthermore, the potential applications of the structures found in this work exceed those of scaffolding. Since the proteins in the formed gels preserved their native configuration and their function, we can use this strategy to produce innovative devices through bio-networks with optical, electrical, chemical, antimicrobial or energy storage properties. Proteins with enzymatic, charge-carrying, antibiotic and light-harvesting abilities can be designed *de novo* and finely assembled into micron-sized porous networks through the methodology proposed herein.

Lastly, our protein precipitation protocol combined with ultra-high resolution real-space imaging might also help to study the aggregation mechanisms of proteins relevant to diseases like Parkinson's or Alzheimer's, which may contribute to their understanding and treatment.

6.4 Conclusions

Several experimental conditions were tested to obtain phase separated bicontinuous networks through salt addition and surface modification of the fluorescent proteins eGFP and mCherry. Using fluorescent proteins as the model system allowed the identification of the conditions that preserved or affected their native structure, which is essential for future applications of these biomaterials. Here, ammonium sulphate was able to produce percolating gel structures of several microns of individual solutions of both proteins, without denaturalising them. However, only mixed gel networks were obtained when the proteins were precipitated together with said salt, and no individual regions of each species were clearly distinguished. This could be due to non-specific interactions between the proteins and the salt, as well as the intrinsic similarities between eGFP and mCherry. When using yttrium chloride, which presents higher protein-ion specificity, percolating gels very similar to the ones observed with ammonium sulphate were obtained for eGFP at concentrations as low as 2 mM. However, for mCherry only clusters were

identified and the protein seemed to reentrant solution at yttrium chloride concentrations above 5 mM. The difference in behaviour could be a consequence of a distinct charge distribution on the surface of the proteins. Alternatively, surface cationisation for both proteins was conducted in order to prevent their precipitation with yttrium chloride and hence gain more control over the protein-salt interactions. This reaction successfully modified the net charge of both proteins from negative to positive and the precipitation of both cationised proteins with yttrium chloride was effectively prevented.

Critical soft matter gels with distinctive protein domains were expected to form by adding yttrium chloride and ammonium sulphate in two separate steps to a solution of native eGFP/mCherry and cationised mCherry/eGFP. Unexpected protein co-precipitation occurred as a result of complex interactions between the oppositely charged proteins. In contrast, by forming the gels individually, the desired bi-networks were obtained, where cationised mCherry precipitated on top of the pre-existing native eGFP gel. This coverage was not homogenous and thus individual protein domains of both native eGFP and cationised mCherry were clearly identified throughout the structure. Furthermore, the gel coverage was easily manipulated by decreasing the amount of mCherry added. Yet, we did not observe a correlation between these changes and the sizes of the individual domains. Our results emphasise the larger complexity of protein-salt interactions in comparison with other colloidal systems, and highlight the need for further studies to understand better the specific interactions involved in these systems to obtain the desired structures. In spite of this, to our knowledge, our structures are the first phase separated bicontinous networks formed by functional proteins. The method proposed herein is easy, cheap, versatile and scalable, and hence it sets a precedent to develop new strategies to produce a novel class of innovative functional biomaterials.

6.5 Acknowledgments

The expression and purification of GFP and mCherry were carried out in collaboration with Dr. Ross Anderson and Dr. Angélique Coutable of the School of Biochemistry at the University of Bristol. Dr. Coutable performed the expression and purification of GFP, and supervised and help with the correspondent procedures for mCherry. The cationisation of the proteins was also done with her help and under her supervision.

Nicholas Wood provided the code to analyse the data.

CHAPTER 7

DEVELOPMENT FLUORESCENT MAGNETIC NANOPARTICLES FOR THE REALISATION OF CRITICAL SOFT MATTER

The work presented herein was carried-out in collaboration with Dr. Steve Whitelam and Dr. Jeff Urban, based at the Molecular Foundry, in Berkeley California, USA. The first syntheses of magnetic nanoparticles where performed in Dr. Urban's facilities under Dr. Jason Forster's supervision. This was done in accordance to the accepted project 'Critical Soft Matter: Making a New Type of Functional Multicomponent Material'.

Herein we present the development of core shell fluorescent silica magnetic nanoparticles. They constitute one component of a binary system containing bare and magnetic silica spheres for the realisation of critical soft matter, where individual domains of each component can be distinguished in the final assembly, due to higher attractive forces between like particles. By coating fluorescent silica spheres with magnetic iron oxide nanoparticles, we expect to be able to control the assembly of the system using magnetic fields. The fluorescence of the particles will allow us to follow them and characterise their final assemblies. Magnetic iron oxide nanoparticles with 16.8 ± 1.6 nm in diameter were synthesised through thermal decomposition of an iron salt, and were successfully linked to the surface of commercial 500 nm fluorescent silica spheres, via previous chemical modification of their respective surfaces. A final coating with silica was done to provide further stability. However, this step only produced aggregates, likely arising from particle attraction and poor steric stabilisation. Although more stabiliser and different stirring strategies were followed, clusters were not prevented. In spite of this, when a mixture of the synthesised magnetic particles and bare silica spheres were exposed to a magnet, the clusters of the former particles moved quickly towards it. This suggests that our particles have potential to be used for yielding critical soft matter assemblies. Further work regarding the improvement of the stability of the particles is then worth pursuing.

7.1 Introduction

7.1.1 Magnetic Nanoparticles

In recent years, nanostructured materials have acquired a great interest due to promising applications in a myriad of fields, from electronics, to high-density data storage to drug and gene delivery and diagnosis and cancer treatment. From the large variety of nanoparticles that may serve as building blocks of such structures, magnetic nanoparticles emerge as one of the most suitable ones for such purposes [56]. Thus, in the last decades there has been a great development and progress of chemical syntheses and methodologies for the large scale production of these nanoparticles for their integration in functional devices [206, 207].

Magnetic nanoparticles are those who respond to an applied magnetic field and they can be classified according to their magnetic susceptibility (χ), which is a magnitude of the effectiveness of the applied magnetic field to induce a magnetic dipole. χ is defined as

$$\chi = M/H \tag{7.1}$$

where M is the induced magnetisation and H the applied field. If the material presents a $\chi \sim 10^{-6}$-10^{-5} it is classified as diamagnetic; if its $\chi \sim 10^{-5}$-10^{-3}, then the material is paramagnetic; but if χ lies between $\sim 10^{-2}$ and 10^{6}, then it is ferromagnetic [2]. These characteristics depend strongly on their size and shape.

In order for these functional nanoparticles to be used for the mentioned applications, the size, location, alignment and spacing within the device is essential [207]. Highly ordered super structures of magnetic species can be achieved using magnetic fields [207, 2]. This type of guided self-assembly route is driven by dipole-dipole interactions which can be modulated to be attractive or repulsive according to the angle of the magnetic field. Additionally, the interactions can be quickly initiated and reversed by either permanent or temporary electromagnets and are independent of other experimental conditions like pH, solvent nature or composition and temperature. Finally the magnetic field strength can be precisely tuned for fine manipulation of individual particles or collective motion of the system [74].

The assembly process in these materials arises from the competition of van der Waals attractions, electrostatic repulsions, Brownian motion and attractions between magnetic dipoles. When a magnetic field is applied, these latter attractions overcome the rest forces and the nanoparticles will align their magnetic dipole moments along the direction of the applied field. Thus the magnetic field acts as the physical parameter responsible for the self-assembly of the system components. The final structures usually appear in linear chains or special superlattices, which can be influenced by the size, shape and concentration of the particles as well as the direction of the magnetic field [207, 2].

The preferred materials for its manipulation with magnetic fields are ferromagnetic nanoparticles. These kind of particles and their respective interactions are described in Chapter 2.3.2

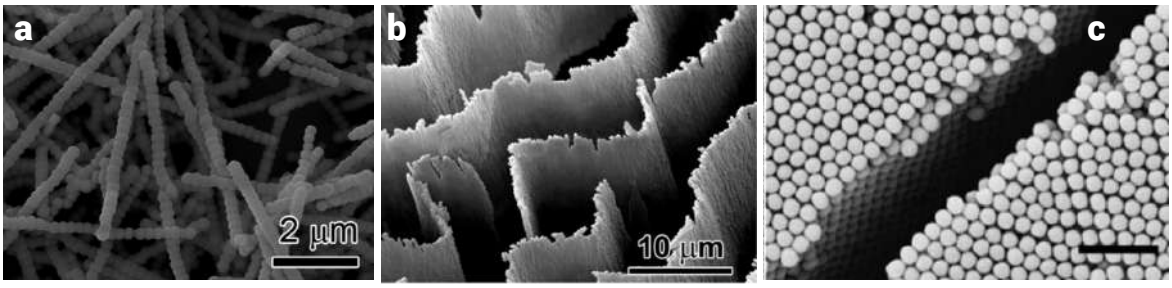

Figure 7.1: Examples of different assemblies formed by magnetic nanoparticles under an external magnetic field. a. Scanning electron microscopy of 1-dimension chains formed by iron oxide nanoparticles fixed with a coating of silica [74]. b. Scanning electron microscopy of 2-dimension structures of silica coated iron oxide nanoparticles [74]. c. Scanning electron microscopy of 3-dimensional crystals of silica spheres coated with iron oxide nanoparticles and carbon (scale bar: 1 μm) [208]

and illustrated in Fig. 2.14. For these, the magnetic dipole moment induced by an external magnetic field can be characterised by

$$m = \mu_0 \chi H V \tag{7.2}$$

where μ_0 is the magnetic permeability of vacuum, H is the local magnetic field and V is the volume of the particle.

In these systems dipole-dipole interactions govern the attraction and repulsion between particles, given by [56]:

$$U_{dd}(\vec{r}) = \frac{m_1 \cdot m_2 - 3(m_1 \cdot \vec{r})(m_2 \cdot \vec{r})}{4\pi\mu_0 r^3} \tag{7.3}$$

where $\vec{r}$ is the vector parallel to the corresponding vector connecting particle 1 and 2 [56] illustrated Fig. 2.14 (a turquoise). Additionally, magnetised particles can act as small magnets, with magnetic field varying with the particle separation (r^{-3}) and the magnitude of m [56]. If $m_1 = m_2$, then the generated field can be described by:

$$H = \frac{3\vec{r}(m \cdot \vec{r}) - m}{4\pi\mu_0 r^3} \tag{7.4}$$

As such, by controlling the magnetic field strength, the inter-particle repulsive and attractive forces, along with the local concentration of the species, colloidal magnetic particles can assemble in 1, 2 or 3 dimensions [74, 2]. Examples of the different assemblies are shown in Fig. 7.1 [74, 208]. As above mentioned, 1-dimensional chain structures arise when the dipole-dipole interactions overcome thermal fluctuations and the particles align parallel to the direction of the magnetic field (Fig. 7.1 (a)). The periodicity of the chains can also be manipulated by the external field and repulsive interactions. However, when the concentration of the particle chains

increases, the system becomes thermodynamically unstable. In order to overcome this, the chains aggregate into 2-dimensional zig-zag multi-chains (Fig. 7.1 (b)). If the particle concentration and inter-particle potential are further increased, then 2-dimensional structures can form 3-dimensional ones. Additionally, particle attractions towards areas where the magnetic field is maximised can generate 'nucleation sites' for a 3-dimensional ordered structure to grow from [74]. Such methodology was used by Cheng and collaborators to yield crystalline assemblies of silica spheres coated with iron oxide nanoparticles and carbon [208] and are shown in Fig. 7.1 (c).

However, it is often desired to have structures with particular patterns or where the magnetic nanoparticles are placed in a certain disposition within the material. Several techniques to yield a particular distribution of magnetic particles include modifications or complex orientation of the magnetic field, along with magnetised patterns [74], templates or microlitographic techniques. Nevertheless, these techniques tend to be unpractical for large-scale production [209].

Regarding simulation studies of out-of-equilibrium assemblies formed by a binary mixture of particles with higher intra particle attraction strengths, Whitelam and coauthors [53] found that, according to their growth rate, different assemblies in 3 dimensions can be obtained (see Chapter 2.2.7). Interestingly, at fast growing rates the assemblies presented particle domain fluctuations that resemble the structures found in systems near their critical point, and thus called these assemblies *critical soft matter*. Their ability to tune the sizes of said individual particle domains stands out as a promising new experimental route to yield 3-dimensional structures. These are formed of particle mixtures with particular and controllable spatial arrangements of particle domains in 3-dimensions, a characteristic required for some technological applications of magnetic nanoparticles.

We hypothesise that by using critical soft matter principles in a mixture of inert and magnetic silica spheres, we can yield structures with periodic spatial clusters of magnetic nanoparticles. A general scheme for our suggestion is illustrated in Fig. 7.2. The magnetic particles consist of a central fluorescent silica sphere covered with iron oxide magnetic nanoparticles and coated with a silica shell. The fluorescent core will allow us to follow the dynamics and final assemblies of the particles. We expect that due to the magnetic functionalisation of one of the species, their behaviour will be different to the naked silica spheres when exposed to an external magnetic field. Moreover, by controlling the attraction forces between the particles through a magnetic field, we expect to favour intra-particle interactions. As such, different magnetic field strengths and increase rate might allow us to yield critical soft matter structures, where the final assemblies are composed by configurable and distinguishable particle domains, as shown in (c) in Fig. 7.2.

The present chapter will only focus on the different synthetic strategies followed for the development of the core shell fluorescent magnetic species summarised in Fig. 7.4 . Future work on the design of the sample cell and magnetic field is still required.

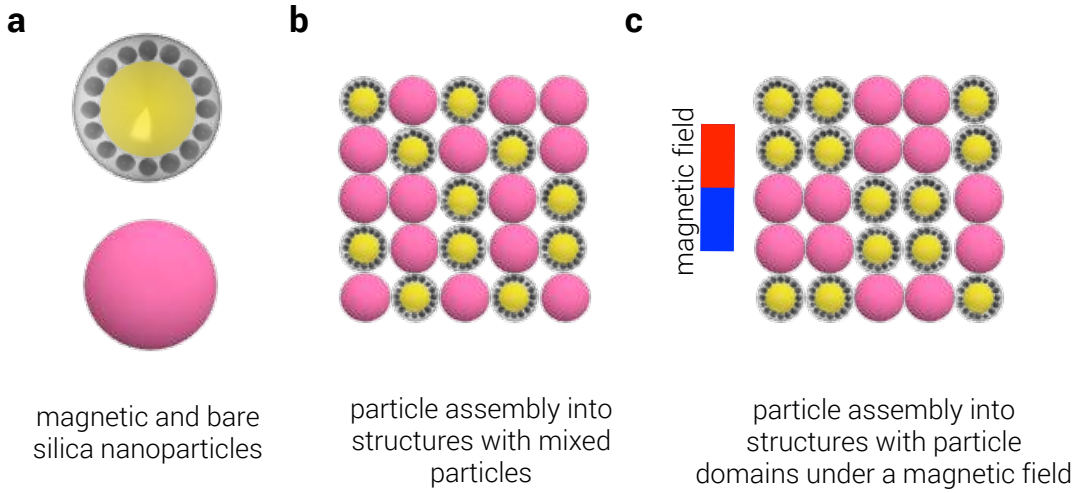

Figure 7.2: General strategy to realise critical soft matter utilising a magnetic nanoparticles. a. Mixture of magnetic silica nanoparticles (above) with bare silica ones (pink). Here, fluorescent silica cores are decorated with iron oxide nanoparticles and coated with a silica shell. b and c. Particle assemblies in the lack (b) and presence (c) of a magnetic field. The particles are well mixed in the structure in the former, whereas they form distinguishable particle domains in the latter, depending on the field strength and its increase rate. c. corresponds to critical soft matter assemblies.

7.1.2 Synthesis of Magnetic Responsive Nanoparticles

In order to realise the aforementioned binary system, we needed to synthesise magnetic responsive nanoparticles. Recently, great success has been achieved in the chemical synthesis of monodispersed magnetic nanoparticles [210, 208]. The increase of interest in this type of particles arises from the fact that they exhibit different electrical, optical, chemical and magnetic properties in comparison with their bulk counterparts [210, 211]. 2-20 nm magnetic nanoparticles in particular have had an increasing interest due to their potential applications in storage devices, aerospace devices, contrast enhancement imaging, waste water treatment, bioprocessing, drug delivery and catalysis [212, 210, 213, 211].

The most common elements to obtain magnetic nanoparticles from are iron, cobalt and nickel. Since much of the development of these particles is dedicated to biomedical applications, magnetic iron oxides are usually the preferred one due to its availability, physicochemical stability, compatibility, low cost and low human and environmental toxicity [214, 213]. Several iron salts (nitrates, chlorides, sulphates and carbonates) and organometallic compounds can be the source of iron atoms, however, the former tend to be more popular, due to their low costs and low toxicity [215].

From the eight different polymorphs of iron oxides hematite (α-Fe_2O_3), magnetite (Fe_3O_4) and maghemite (γ-Fe_2O_3), shown in Fig. 7.3, are the ones that present magnetic properties. From these, magnetite is commonly the final product of most syntheses. From the figure, we can observe that in magnetite (centre) oxygen atoms (red) form an fcc closed packed lattice and iron atoms (black and red) sit on its tetrahedral and octahedral sites [212]. It contains both

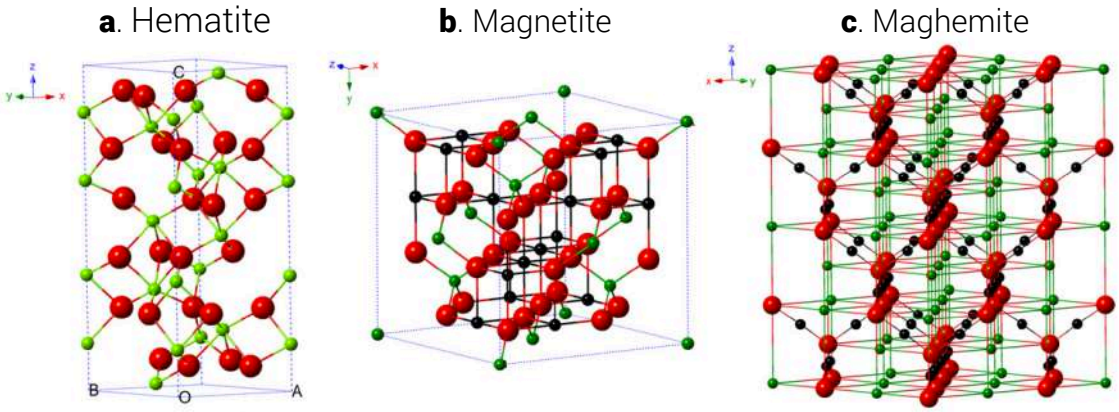

Figure 7.3: Crystal structure of magnetic polymorphs of iron oxide. Black balls are Fe^{2+}, green balls are Fe^{3+} and red balls are O^{2-}. Reproduced from Wu *et al.* [206].

divalent (Fe^{2+}) and trivalent (Fe^{3+}) iron atoms in a Fe^{2+}/Fe^{3+} = 1/2 stoichiometry [206].

Different methodologies involving hydroxide co-precipitation, sonochemical deposition, microemulsion, sol-gel reactions and thermal decomposition have been developed for the production of these particles [214, 210, 213, 211, 212]. For a detailed review of these methods, the reader is referred to Wu *et al.* [213] and Campos *et al.* [211]. From these strategies, the thermal decomposition is nowadays preferred due to its ecological and large scale production of magnetic nanoparticles using non-toxic and inexpensive precursors. Moreover, high control over the size and polydispersity of the particles is achievable [214, 215, 210]. In this procedure, magnetic nanoparticles are produced by controlled oxidation of an iron precursor at high temperatures and usually under inert atmosphere conditions [215, 213, 211]. One of its drawbacks, is that the resulting nanoparticles are usually insoluble in polar media.

Additionally, surface coating or functionalisation of the magnetic particles is generally required to improve their stability and solubility, or to prevent their oxidation and corrosion. The choice of surface modification will depend on the final applications intended for the particles [214, 213]. Amongst the most popular we can find silica coating, polymer grafting, biomolecule deposition or encapsulation [214, 213]

Control over the size, shape and polydispersity of the magnetic particles is often achieved by adjusting the reaction temperature and duration, as well as the concentration of the reagents and other species involved in the syntheses, like surfactants or stabilising polymers [215, 210]. In particular, a narrow size distribution is highly desired, as in order to obtain high quality and long range ordered structures, the size uniformity of the building blocks is important [78, 208]. To achieve narrow size distributions, the nucleation and growth stages of the nanoparticle formation need to be finely separated [215, 210]. Although much research has been devoted to develop procedures that fulfil that characteristic, fine control over these processes is often challenging [211, 213].

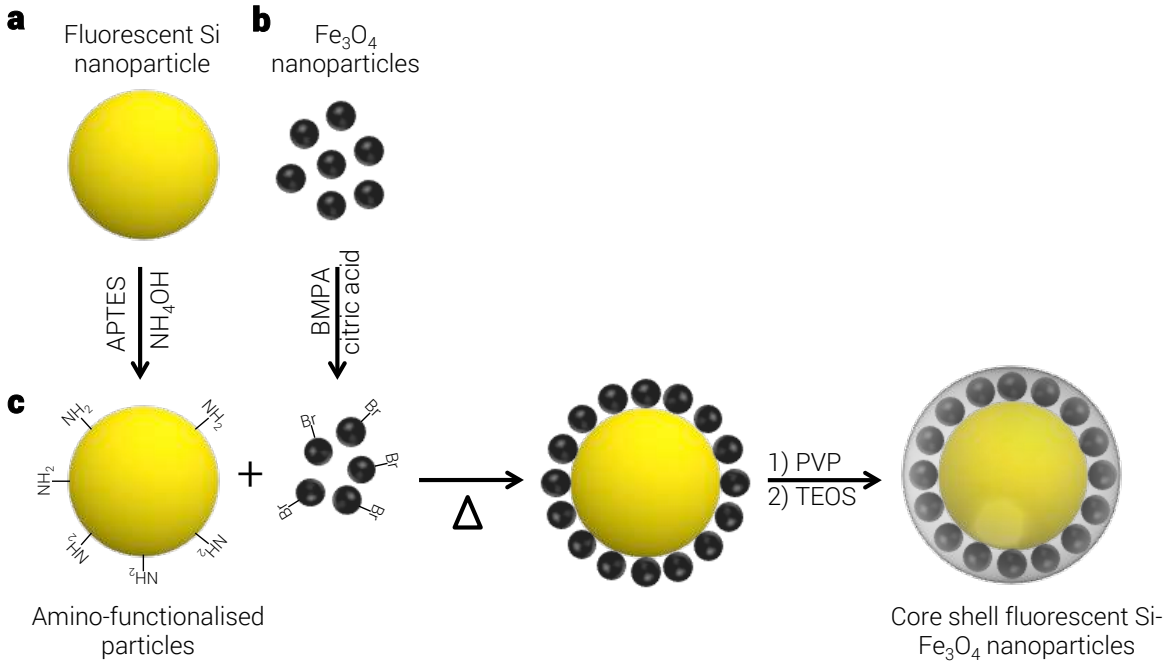

Figure 7.4: Schematic diagram of the steps followed to synthesise fluorescent silica-iron oxide nanoparticles. Briefly, fluorescent silica nanoparticles were coated with amino-groups to allow the functionalisation of their surface with previously synthesised iron-oxide nanoparticles coated with bromide groups. The funcionalised particles were finally coated with a thin silica shell for stabilisation.

An easy way to prepare magnetic responsive species with small size distributions is by using monodispersed spheres as a template and to decorate their surfaces with smaller magnetic nanoparticles. Besides, Cheng and coauthors found that silica particles with magnetic shells were better for forming assemblies, in comparison to their magnetic core colloidal counterparts [208]. Therefore, we decided to use this approach to produce our magnetic components.

Based on the above considerations, the magnetic building blocks developed herein consist of fluorescent silica particles (core) functionalised on their surface with iron oxide nanoparticles and coated with a silica shell. Here, the fluorescent core will allow us to characterise both the particles' behaviour and the structures formed under a magnetic field, using confocal laser scanning microscopy. Their responsiveness to the external field will be provided by the magnetic shell of iron oxide nanoparticles. Finally, the outer silica coating will add further stability to the particles and will also allow us to redisperse and match the refractive index of our species in solvents of interest. Fig. 7.4 shows the general steps involved in this methodology. In summary, the surfaces of monodisperse fluorescent silica spheres and in-house synthesised iron oxide nanoparticles are functionalised with reactive groups (amino and bromide moieties, respectively) to link the particles together and yield fluorescent silica cores decorated with magnetic nanoparticles. These particles are then coated with a silica shell for further stability.

We expect that these steps will produce monodisperse magnetic responsive nanoparticles

which, in combination with non-responsive spheres, will allow the future realisation of critical soft matter and thus, the future development of functional nanomaterials.

7.2 Methods

7.2.1 Synthesis of Fluorescent Silica-Iron Oxide Nanoparticles

The different chemical and surface modification reactions followed to yield the core-shell fluoresent magnetic nanoparticles are detailed in this section.

7.2.1.1 Functionalisation of Fluorescent Silica Nanoparticles with Amino groups

Plain fluorescent silica nanoparticles (FS-np) of 500 nm of diameter with a green fluorophore (excitation and emission wavelengths of 485 and 510 nm, respecitvely) were purchased from Kisker Biotech GmbH & Co. KG (PSI-G0.5). The as-received particles were then functionalised with amino groups based on the procedure proposed by Kyeong and collaborators [216] (Fig. 7.4 (a)). Briefly, 800 μL of the silica dispersion was washed and resuspended in 20 mL of ethanol (Fischer Scientific) for a final concentration of 25 mg/mL. 200 μL of (3-aminopropyl)triethoxysilane (APTES, Alfa Aesar) were added slowly to the suspension and left stirring at 200 rpm for 30 min. Finally, 100 μL of amonium hydroxyde (NH_4OH 30%, Sigma Aldrich) were added drop-wise. The reaction was left stirring at room temperature for 18 h, time after which the particles were washed in ethanol through three centrifugation cycles (Eppendorf Centrifuge 5804 R) of 5 min at 5000 rpm. To finish, the particles were resuspended in 10 mL of ethanol.

7.2.1.2 Synthesis of Iron Oxide Nanoparticles

To synthesise the magnetic nanoparticles, an iron oleate complex was first obtained by dissolving and degassing iron chloride hexahydrated (Sigma Aldrich) and sodium oleate (Sigma Aldrich) in a solvent mixture of ethanol, deionised water and n-hexane (Fisher Scientific). The reaction was held for 4 h at 70° C under inert atmosphere. The upper organic layer obtained was washed with water three times and the remaining solvents were evaporated with a rotary evaporator at 40° C for 2 h. The resulting waxy product was dissolved in dioctyl ether (Sigma Aldrich) and an excess of oleic acid (Sigma Aldrich) was added. Thermal decomposition of the complex has carried out by increasing the temperature to 290° C, temperature at which the reaction proceeded for 30 min. Finally, the nanoparticles were precipitated with 30 mL of ethanol, centrifuged at 5000 rpm for 10 min and washed with 20 mL of chloroform. This precipitation and washing cycles were repeated three times and the particles were finally resuspended in 20 mL of chloroform (Fisher Scientific) [215].

7.2.1.3 Functionalisation of Iron Oxide Nanoparticles with Bromide groups

The obtained iron oxide nanoparticles were further funcitonalised with bromide groups on their surface to allow their reaction with the amino groups covering the fluorescent silica cores. In order to do so, we followed the procedure proposed by Lee *et al.* [217], and illustrated in Fig. 7.4 (b). Here 5 mL of the synthesised iron-oxide nanoparticles were sonicated for 10 min. 0.5 g 2-Bromo-2-methyl-propionic acid (BMPA, Sigma Aldrich) and 0.5 g of citric acid (Sigma Aldrich) were dissolved in 15 mL of a 50/50 v/v mixture of chloroform and dimethylformamide (DMF, Sigma Aldrich) solution. The sonicated iron oxide nanoparticles were mixed with the BMPA-citric acid solution. The mixture was heated at 30° C and left to react over night. The particles were washed through three centrifugation cycles of 5 min at 5000 rpm, and were resuspended in 10 mL of ethanol.

7.2.1.4 Deposition of Iron Oxide Nanoparticles on Fluorescent Silica Cores

In order to cover the surface of the fluorescent silica spheres with metallic nanoparticles, we also followed the method proposed by Kyeong *et al.* [216], with slight modifications. Firstly, 10 mL of the amino-functionalised FS-np were sonicated for 10 min. Under vigorous stirring, 500 μL of the bromide-coated iron oxide nanoparticles suspension were added drop-wise to the fluorescent silica dispersion, and the reaction was heated at 80° C. After 3 h, a second addition of 500 μL of the bromide-coated iron oxide nanoparticles was done. This modification helped to prevent aggregation. The reaction continued for another 3 h, time after which the particles were washed in ethanol through three centrifugation cycles of 2 min at 5000 rpm. Finally, the particles were resuspended in 5 mL of ethanol. These steps are showed in Fig. 7.4 (c). The success of the deposition was characterised through transmission electron microscopy.

7.2.1.5 Silica Coating of Fluorescent Silica-Iron Oxide Nanoparticles

Finally, the fluorescent magnetic particles were coated with a thin layer of silica in order to enhance their stability. The procedure to achieve the coating is divided in two steps. First, the particles were coated with polyvinylpyrrolidone (PVP, 360K MW, Sigma) to avoid aggregation. Slight modifications were made to the coating method introduced by Q. Zhang and collaborators [218]. Here a 10 mg/mL solution of PVP was prepared in water and 5 mL of the fluorescent magnetic nanoparticles were added slowly under vigorous stirring. The mixture was allowed to stand under vigorous stirring for 24 h. Once the time had concluded, the particles were washed with ethanol through three cycles of 5 min centrifugation at 5000 rpm, and redispersed in 5 mL of ethanol.

The second step consisted of adding the silica precursor to form the silica shell. The procedure followed was reported by Kyeong and collaborators [216], with some modifications. 3 mL of the above suspension were added to 2 mL of dH_2O and sonicated for 10 min. Under vigorous

stirring, a solution of 10 μL of tetraethyl orthosilicate (TEOS, Sigma Aldrich) in 90 μL of ethanol was added drop-wise to the suspension. The mixture was left stirring for 30 min at room temperature, time after which 150 μL of NH_4OH 30% were added drop-wise. After 1.5 h a second addition of an equal TEOS-ethanol solution was added slowly. The reaction was left to proceed for 12 h at room temperature. The coated particles were washed three times with ethanol via 2 min centrifugation cycles at 5000 rpm and were finally resuspended in 5 mL of ethanol. The final product was also characterised through transmission electron microscopy.

7.2.1.6 TPM Coating of Core Shell Fluorescent Silica-Iron Oxide Nanoparticles

Finally, to allow the particles' resuspension in low-polarity solvents, they were coated with 3-(trimethoxysilyl)propyl methacrylate (TPM), following Liz-Marzán and authors methodology [219] with some modifications. Here, to a 3 mL of the core shell magnetic nanoparticles were added 2 mL of dH_2O and sonicated for 10 min. Under vigorous stirring, an excess of TPM was added drop-wise to the suspension (500 μL). The mixture was left stirring for 30 min at room temperature, time after which 100 μL of NH_4OH 30% were added drop-wise. The reaction was left stirring for 45 min at room temperature. The particles were washed through cycles of centrifugation and were finally resuspended in tetrahydrofurfuryl alcohol (THFFA). The final suspension was characterised through confocal laser scanning microscopy.

7.3 Results and Discussion

We present the results of the synthesis of the particles in three different main sections. We start with the different chemical procedures followed to obtain the core shell magnetic nanoparticles, which include iron oxide nanoparticle synthesis followed by their surface functionalisation with bromide motifs; and the functionalisation of fluorescent silica nanoparticles with amino groups. This was followed by the deposition of metallic nanoparticles on the surface of the fluorescent silica nanoparticles and finalised with the silica coating of the magnetic functionalised fluorescent silica cores. We then present the results regarding the mixing of our magnetic nanoparticles with bare fluorescent silica spheres and their response to a magnet. We finish with our conclusions.

7.3.1 Synthesis of Core Shell Magnetic Fluorescent Nanoparticles

As illustrated in Fig. 7.4, the final functional nanomaterial wanted consists of a fluorescent silica nanoparticle core functionalised with iron oxide magnetic spheres deposited on its surface and coated with a silica shell. In one hand, the fluorescent core will allow us to observe and follow the assemblies of the particles through confocal microscopy. On the other hand, the magnetic

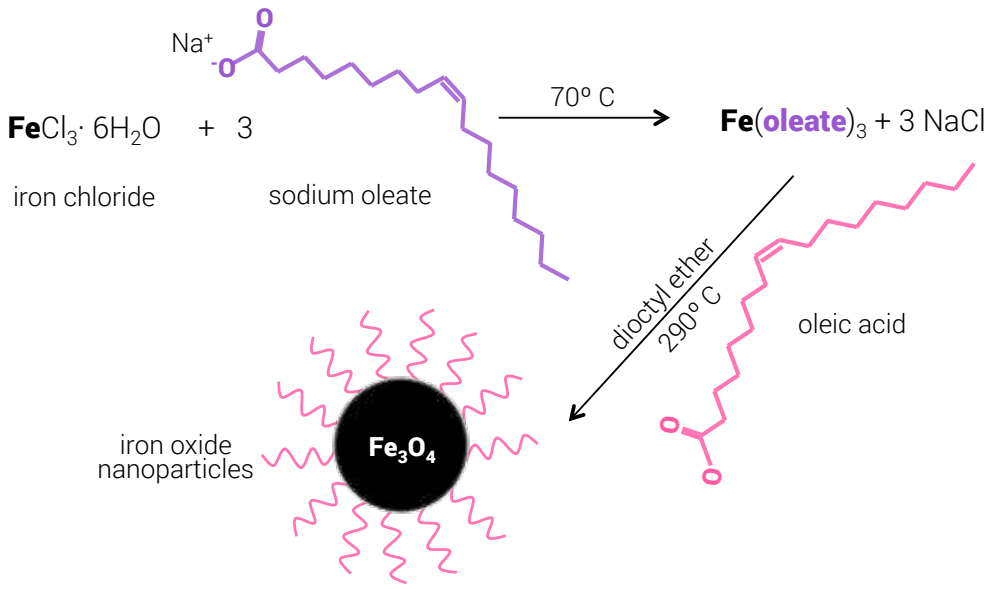

Figure 7.5: Synthesis of iron oxide nanoparticles. First, an iron oleate complex is formed through an iron salt and sodium oleate. Then, thermal decomposition of the complex in a high boiling point solvent generates iron oxide nanoparticles. Oleic acid is added in excess to stabilise the magnetic nanoparticles.

iron oxide nanoparticles coating will allow us to manipulate the self-assembly of the particles. Finally, the final silica shell would provide further stabilisation to the particles.

7.3.1.1 Synthesis of Iron Oxide Nanoparticles

We started by synthesising magnetic iron oxide nanoparticles following the procedure introduced by Park and coauthors [215]. This reaction is illustrated in Fig. 7.5 and consists on the thermal decomposition of a previously synthesised iron-oleate complex in the presence of oleic

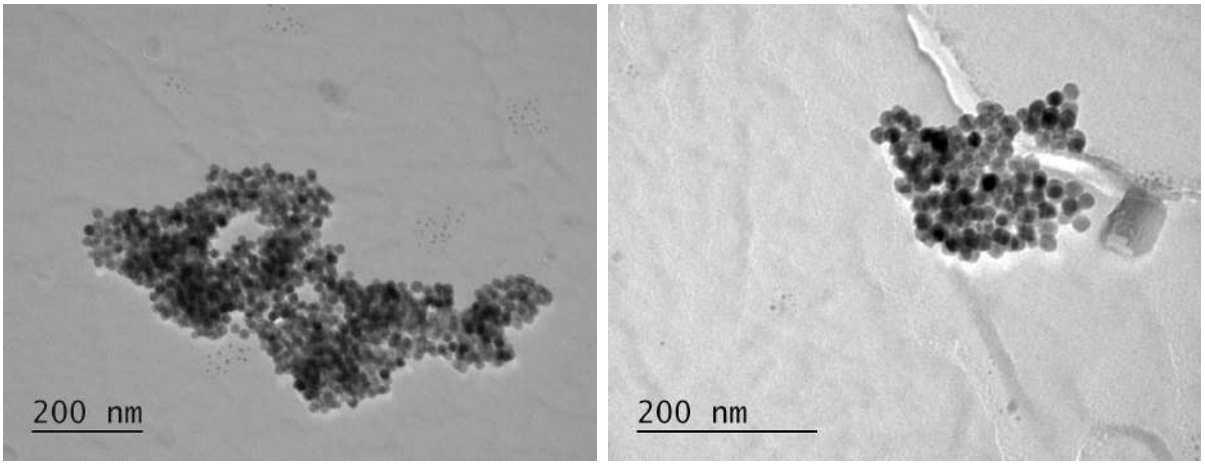

Figure 7.6: Transmission electron microscope images of synthesised iron oxide nanoparticles with 16.8 ± 1.6 nm of diameter.

acid, which acts as a surfactant to help with particle stabilisation.The complex is derived from a reaction of a iron chloride and sodium oleate and is necessary to allow the solubility of iron molecules in high boiling point organic solvents. The thermal decomposition occurs under inert atmosphere conditions at very high temperatures, which are required to break iron-oleate bonds and allow controlled iron oxidation and crystallisation. Indeed, particle nucleation starts between 200° and 240° C with the dissociation of one of the three oleate ligands of the iron molecule. Further nuclei growth occurs at higher temperatures with a major growth at ~ 300° C [220, 215]. Fine control of the temperature and its increase rate are essential for obtaining spherical monodisperse magnetic nanoparticles. Finally, the sizes can be controlled depending on the solvent used. We used dioctyl ether with a boiling poing = 286-287° C, which according to the authors, should produce magnetic particles with sizes around 12 nm [215].

The final particles obtained were characterised using transmission electron microscopy (TEM) and their sizes were determined using the open source image processing software Fiji. The particles are shown in Fig. 7.6 and present a diameter of 16.8 nm with a polydispersity of 9.5%. The heater used for this reaction only reached ~285° C and we were not able to control the heat rate as suggested by Park and coauthors [215]. Although this temperature was sufficient to observe reflux and oxidise the iron salt, larger particle sizes and broad size dispersion might be a consequence of such limitations.

7.3.1.2 Deposition of Iron Oxide Nanoparticles onto Fluorescent Silica Spheres

The next step was to obtain magnetically functionalised fluorescent silica nanoparticles. In order to do so, iron oxide nanoparticles need to be covalently bonded to the surface of the fluorescent silica spheres. To do this, it was necessary to add reactive groups to the surface of each system. We followed two procedures for the functionalisation of each species.

First we added bromide groups on the surface of our magnetic nanoparticles following Lee *et al.* [217]. Here, the oleic acid coated iron oxide nanoparticles are added to a solution containing citric acid (CA) and 2-bromo-2methylpropionic acid (BMPA). The ligand exchange reaction and surface functionalisation are depicted in Fig. 7.7 (1). First, oleic acid ligands are displaced from the surface and exchanged by CA groups (Fig. 7.7 (1a)), which presents multiple carboxylic groups and hence is a stronger ligand. CA provides both stabilisation and hydroxyl groups for their reaction with BMPA (Fig. 7.7 (1b)). This reaction produces iron oxide nanoparticles with bromide groups on the surface [221, 217] (Fig. 7.7 (1c)).

Second, we modified the surface of the purchased fluorescent silica nanoparticles (Kisker Biotech GmBH & Co. KG) by adding amino groups through a silanisation via 3-aminopropyltriethoxysilane (APTES) shown in Fig. 7.7 (2) [216]. This process is known as the Stöber method and here the silica precursor, APTES, is hydrolysed in ethanol with ammonia (NH_4OH), which serves as a catalyst. The hydrolysis produces a mixture of ethoxysilanols, where the alkyl groups of APTES (CH_3–CH_2-) have been substituted for hydrogens, forming hydroxyl groups (OH) as

1. Functionalisation of Fe_3O_4 nanoparticles with bromide groups

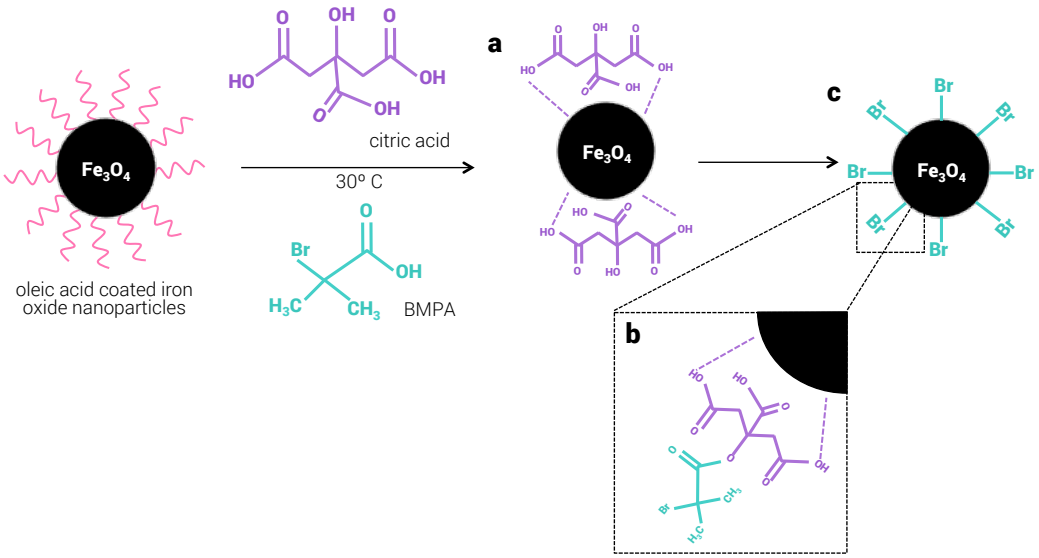

2. Functionalisation of fluorescent silica spheres with amino groups

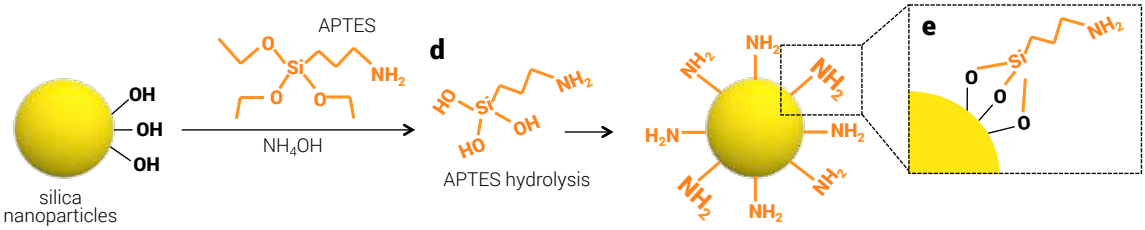

3. Br-Fe_3O_4 nanoparticles deposited on NH_2-fluorescent silica spheres

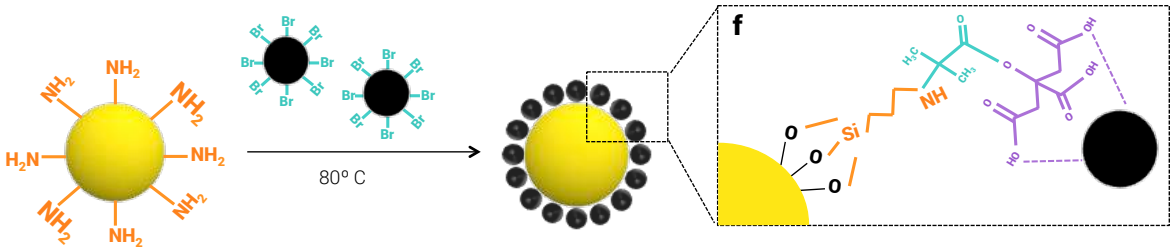

Figure 7.7: Schematic illustration of the methods followed for the deposition of iron oxide nanoparticles on fluorescent silica spheres. 1. Functionalisation with bromide groups of iron oxide nanoparticles coated with oleic acid. The metallic spheres first react with citric acid, where a change of ligands occurs (a). Then the hydroxyl group (OH) of citric acid forms an ester with the carboxylic group of 2-bromo-2-methyl-propionic acid (BMPA) (b), thus leaving bromide groups in the surface of the iron oxide nanoparticles (c) [221]. 2. Functionalisation of fluorescent silica spheres with amino groups through the Stöber method where 3-aminopropyltriethoxysilane (APTES) first hydrolyses (d) and then reacts with the hydroxyl groups (OH) present on the surface of the silica particles forming a -Si-O-Si bond (e). 3. Deposition of bromide functionalised iron oxide nanoparticles on the surface of amino modified fluorescent silica particles through an amine alkylation between the amino and bromide groups (f).

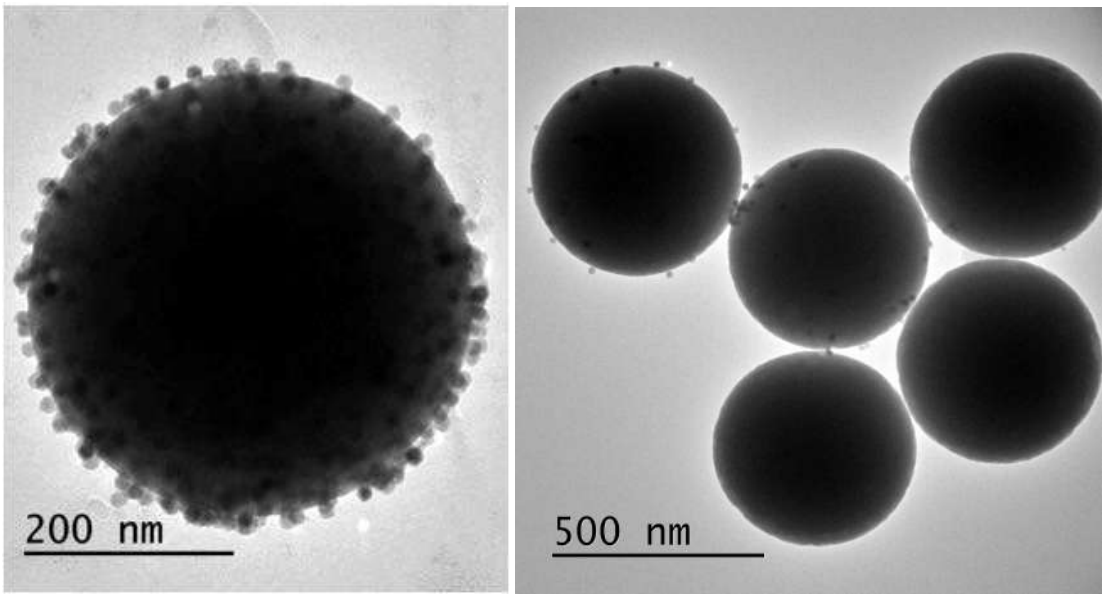

Figure 7.8: Transmission electron microscope images of deposited iron oxide nanoparticles on fluorescent silica spheres. Left, fully covered silica nanoparticle versus partially covered spheres on the right.

shown in Fig. 7.7 (2d). These react with the correspondent ones present in the surface of the fluorescent nanoparticles to form Si -O- Si linkages [222], illustrated in Fig. 7.7 (2e). This reaction leaves the amino groups of APTES free for further reactions.

Immediately after the modification of each particle, both functionalised species were mixed and heated up for an amine alkylation reaction, as illustrated in Fig. 7.7 (3). Here, the bromide group of the iron oxide nanoparticles reacts with the amine group of the fluorescent silica spheres to give an alkyl-substituted amine [223], as shown in Fig. 7.7 (3f). This covalent bond allows the deposition of iron oxide nanoparticles on the surface of fluorescent silica spheres.

Once the reaction was completed, the particles were washed and characterised using TEM. A picture of the species obtained is shown in Fig. 7.8, where the successful coating is clearly observed (left). Moreover, we observed very few unbound iron oxide nanoparticles, which suggests that most of the magnetic nanoparticles were effectively deposited on the surface of the fluorescent silica ones. Additionally, the high polydispersity of the particles did not seem to affect their deposition. However, it is important to mention that again we observed iron oxide nanoparticles attached to the magnetic bar used to stir the mixture.

In addition, although most of the particles looked like the picture shown in the left panel, there were also some with much less coverage, as shown on the right panel of the same figure. This could be due to poor functionalisation of any of the species or lack of availability of magnetic nanoparticles due to preferential deposition on the stirring bar.

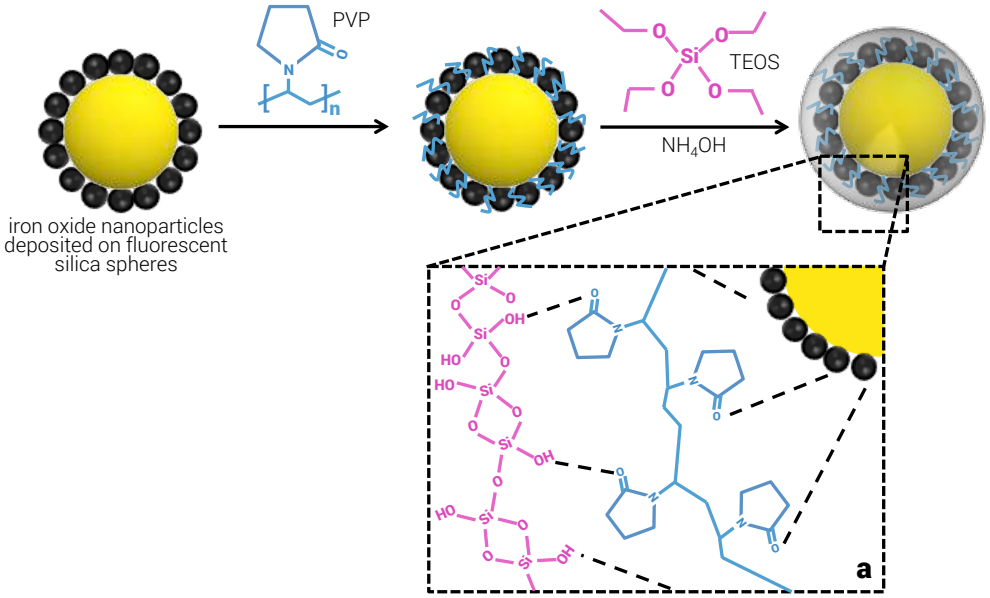

Figure 7.9: Schematic representation of the silica coating of deposited iron oxide nanoparticles on fluorescent silica spheres. The first step consists on coating the particles with polyvinylpyrrolidone (PVP) through hydrogen bonds (dashed lines). Hydrogen bonds are also formed between PVP and hydrolysed tetraethyl orthosilicate (TEOS) to form the silica shell (a).

7.3.1.3 Silica Coating of Core Shell Silica Magnetic Nanoparticles

Since we obtained satisfactory results, we continued with the final step of the synthesis that consisted on adding a silica shell to the functionalised particles as shown in Fig. 7.9. This was possible through the hydrolysis and association of a silica precursor on the surface of the magnetic fluorescent silica spheres. Again we used the Stöber process, however, tetraethyl orthosilicate (TEOS) was the silica precursor utilised in this case. To help with particle stabilisation and TEOS deposition, a thin coating of the polymer polyvinylpyrrolidone (PVP) on the spheres was provided first. PVP is a popular amphiphilic, nonionic polymer broadly used to stabilise colloidal particles [224]. It has the ability to form hydrogen bonds with both the surface of the particle and the Si-OH groups from TEOS hydrolysis, which promotes steric stabilisation and favours the growth of the silica shell [225, 224]. Once the particles were coated with the polymer, TEOS was hydrolysed in a basic pH to allow the reaction to proceed, similar to the APTES reaction and illustrated in Fig. 7.9 (a).

Two step additions of TEOS were made to avoid the formation of small silica spheres (secondary nucleation) and the results are shown in Fig. 7.10. On the left hand side, an image of the first TEOS addition is shown, where a thin layer of silica can be distinguished. Interestingly, the images suggest a preferential deposition of this primary layer on the top of the magnetic nanoparticles, although this might be due to spatial restrictions (the magnetic nanoparticles are much more exposed and easy to 'reach' than the surface of the sphere) rather than an actual preference for these species. On the right hand side of the image, successfully and completely

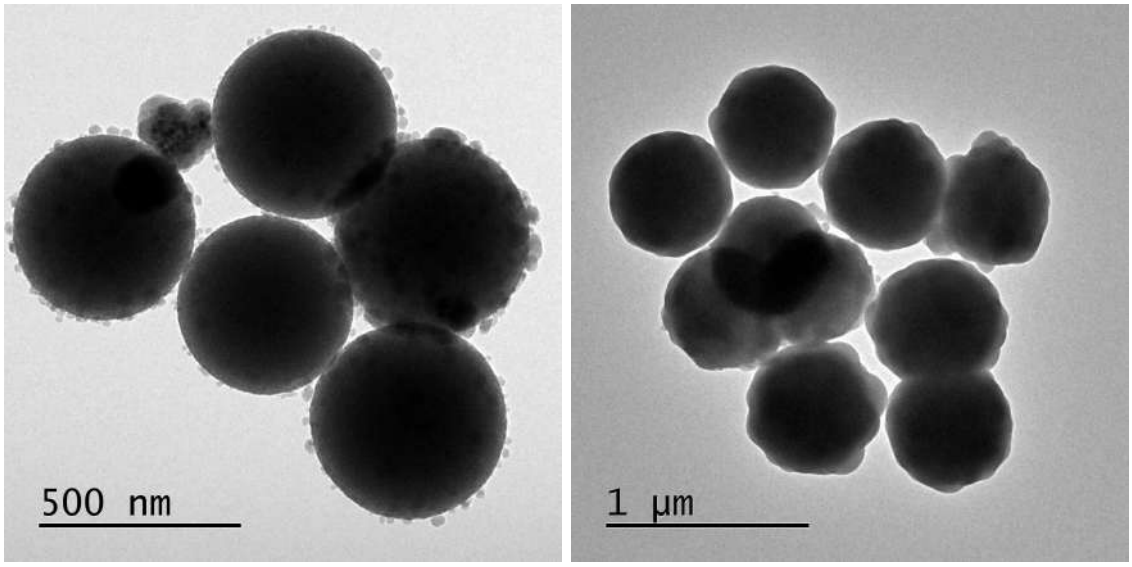

Figure 7.10: Transmission electron microscope images of silica coating of fluorescent silica spheres functionalised iron oxide nanoparticles. Left, first thin silica layer. Right, thicker silica coating, particle aggregation is already observed.

coated particles can be observed. We did not observe a white pellet nor smaller spheres, characteristic of secondary nucleation, thus, our spatial addition of TEOS was successful in preventing such phenomenon. However, throughout the sample only clusters like the one shown were observed, and only few particles were on their own, which suggests they were aggregated.

Different strategies were followed to improve the undesired aggregation, which consisted on: bath and tip sonication after the reaction concluded, adding more PVP to the reaction and more spaced TEOS addition. However, no improvements were obtained. One of the reasons of using PVP as the stabiliser has to do with the ability it has shown to form hydrogen bonds with the surface of the particles. Additionally, a PVP coating has shown to be effective for subsequent silica shell deposition [225, 224]. However, we did not observe a good stabilisation of the particles and a large amount of aggregation was found (see Fig. 7.10). We hypothesise this could be due to not using the optimum PVP molecular weight or the lack of interaction sites for said polymers on our particles. Indeed, Graf and collaborators found that the length of the PVP does affect the stability of the particles. Their studies showed that the appropriate length of the polymer to prevent aggregation and promote a silica shell depends directly on the size of the particle: it needs to be long enough to provide effective steric repulsion, but short enough to form a homogenous layer to allow a smooth silica deposition [224]. Presumably, the molecular weight of the PVP used did not fulfil these characteristics. Thus, in order avoid cluster formation, the optimum length of PVP for our spheres needs to be found.

On the other hand, we can see from Fig. 7.7 (3f) that only some hydrogen atoms seem to be available for hydrogen bridging. These pertain to the citric acid on the surface of iron oxide nanoparticles along with some of the ones belonging to unreacted amino groups present in the

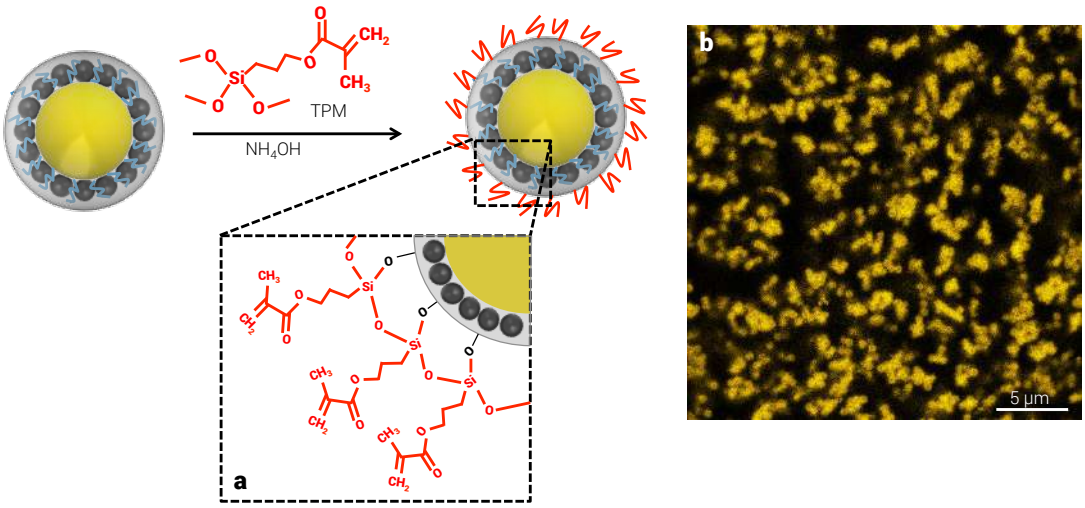

Figure 7.11: Schematic representation of the 3-(trimethoxysilyl)propyl methacrylate (TPM) coating of core shell silica magnetic nanoparticles. a. Hydrolysed TPM associates with the hydroxyl groups present on the particles after the silica coating forming Si-O-Si bonds. b. Confocal snapshot of the TPM coated particles in tetrahydrofurfuryl alcohol (THFFA).

fluorescent silica spheres. However, the number or spatial availability of these hydrogens might not be sufficient for proper hydrogen bond formation. Different polymers or another surfactant can be tested to prove this hypothesis.

Finally, since we still observed some particle deposition on the magnetic bar, we decided to change the stirring method in case the presence of a magnet affected the particle stability inducing attractive interactions. First, we bubbled the mixture with nitrogen, but because the solvent used is a mixture of water and ethanol, the latter evaporated too fast and even more aggregation was observed. So, we tried mechanic stirring using a vortex, nevertheless, the stirring was not efficient enough and we observed particle sedimentation due to high difference between the particles' and solvent's densities. Using an overhead stirrer shaft with teflon propellers might prevent both the magnetic attraction and particle sedimentation. Another alternative to achieve mixture homogenisation is sonication [79].

Therefore, we were only able to obtain clusters of silica coated of core shell silica magnetic nanoparticles. Thus, carrying out the suggestions stated above to prevent particle aggregation is necessary to achieve a stable system.

7.3.2 First Tests of Magnetic Response of Silica Coated Core Shell Silica Magnetic Nanoparticles

Although we did not obtain individual magnetic silica nanoparticles, we continued with some experiments to test the potential of our system to yield critical soft matter assemblies. The final core shell magnetic nanoparticles were suspended in ethanol. This solvent does not match the refractive index of the particles necessary to avoid van der Waals interactions to prevent even

Table 7.1: Steps followed to produce core shell fluorescent silica magnetic nanoparticles

Synthesis Step	Result	Reference
Magnetic nanoparticles	Spherical iron oxide nanoparticles of 16.8 ± 1.6 nm	[215]
Iron oxide deposition on fluorescent silica particles	Effective fluorescent silica spheres decoration	[216] [217]
Silica coating	Particles aggregation	[216] [218]
Silica coating with more PVP	Particle aggregation	[216] [218]
Silica coating mixing through nitrogen bubbling	Solution drying and particle aggregation	[216]
Silica coating mixing with vortex	Particle precipitation	[216]
TPM coating	Effective aggregates dispersion in THFFA	[219]

further aggregation and necessary for good quality imaging. Thus, we changed the solvent to tetrahydrofurfuryl alcohol (THFFA), with a refractive index of 1.45 similar to the correspondent one of silica 1.458 [226]. However, this is an organic solvent and hence steric stabilisation is required for the system, since the silica coated particles present charge stabilisation through hydroxyl groups on the surface. Thus, 3-(trimethoxysilyl)propyl methacrylate (TPM) was grafted on the surface of the core shell magnetic nanoparticles according to Liz-Marzan *et al.* [219], and as shown in Fig. 7.11. TPM is also a silane similar to APTES and TEOS and the coating reaction proceeds in the same way: TPM is hydrolysed in the presence of ethanol and ammonia, and then it associates with other hydroxyl groups that may pertain to other TPM molecules or to the surface of the silica coated core shell silica magnetic nanoparticles (Fig. 7.11 (a)) [219, 227]. The coated particles were then re-dispersed in THFFA.

A confocal image of the particles obtained is shown in Fig. 7.11 (b), where the spheres appear in large clusters, in spite of several bath and tip sonication cycles. Since we also observed some particle aggregation after their silica coating (see Fig. 7.10), it is hard to determine if the TPM grafting process also contributed to it.

A summary of all the different syntheses and strategies followed to produce the magnetic particles is shown in Table 7.1.

In spite of the undesired clustering, we continued to test the response of our core shell magnetic nanoparticles in the presence of a magnet. Hence, we mixed these particles with the same amount of previously synthesised ~ 540 nm bare rhodamine silica spheres already modified with TPM in THFFA. The way we prepared the sample was to first obtain a pellet through centrifugation of a particle dispersion for each system. We then assume the concentration of the pellet corresponds to a random close packing of the particles (ϕ = 0.64) and weighted the correspondent masses of each system to have the same number of each species in a total packing

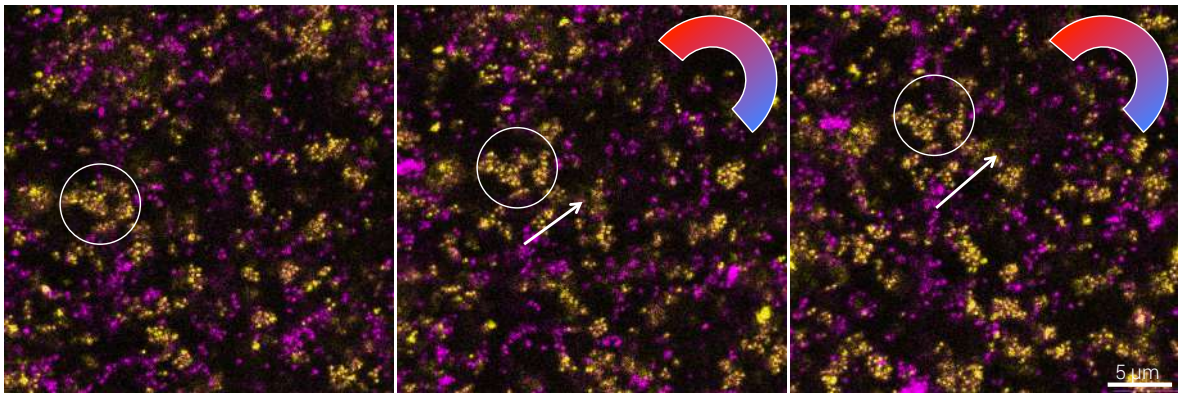

Figure 7.12: Confocal scanning microscopy images of silica coated of fluorescent silica spheres functionalised iron oxide nanoparticles (yellow) mixed with bare silica nanoparticles (magenta) when a magnet (middle and right panel) is approached to the particles. The highlighted cluster is a guide to observe the movement.

fraction of 50%. From the images in Fig. 7.12, we can observe that our sample is more diluted than the expected. This could be due to an inherent problem of the system: the matching of the refractive index of the particles and THFFA. Indeed, once the particles are resuspended in such medium they can not be distinguish from it with a naked eye, and thus finding the pellet and eliminating the supernatant it is non-trivial. This is specially hard for our core shell magnetic nanoparticles. Hence, residual solvent might be the reason our final particle concentration is smaller.

Clear clusters of both particles can be observed in Fig. 7.12 where the yellow ones correspond to our synthesised core shell magnetic nanoparticles and the magenta spheres to bare silica particles. Different bath and tip sonication cycles were applied to the sample in order to potentially eliminate the clusters, however this was not achieved. The aggregation might have arisen from the silica coating process or from poor TPM functionalisation and centrifugation cycles.

In order to test the response of our magnetic nanoparticles in the mixture, we placed a small magnet next to the sample. Before the magnet was placed nearby, typical Brownian motion was observed for the clusters. As soon as the magnet touched the sample, the particles started moving fast towards it, getting out from the plane and out of sight. Interestingly, they also dragged some non magnetic particles with them. This is illustrated in Fig. 7.12, where the circle focus on a cluster formed by core shell magnetic nanoparticles as a reference. The first image corresponds to the sample just before the magnet was put close, whereas the middle and right images correspond to the moment the particles started moving towards the magnet. In the images the movement of other clusters from both particles can also be seen.

Although this is only a preliminary easy test, with little control on the magnetic field strength and direction, it does show that the dynamics of our synthesised core shell magnetic nanoparticles can be altered by the presence of an external magnetic field and shows that further work to

improve the stability of the particles is worth pursuing to achieve critical soft matter assemblies with these materials.

7.4 Conclusions

Different chemical techniques were followed in order to yield functional core shell fluorescent silica magnetic nanoparticles. These particles consist on a fluorescent silica core decorated with magnetic iron oxide nanoparticles and coated with a silica shell. Magnetic iron oxide nanoparticles with a size of 16.8 nm with a polydispersity of 9.5% were successfully synthesised through the thermal decomposition of an iron oleate, previously obtained through the reaction of an iron salt with an oleate precursor. The size distribution could be due to poor control over the temperature and its rate increase. However, this polydispersity had no effect on the subsequent steps. These involved the functionalisation with reactive groups of both the iron oxide and the 500 nm commercial fluorescent silica nanoparticles' surfaces to allow their linkage. The former were coated with bromide groups, whereas the latter were functionalised with amino moieties. Mixing both particles successfully yielded fluorescent silica spheres decorated with iron oxide nanoparticles. To further stabilise the particles, these were firstly coated with the polymer polyvinylpyrrolidone followed by a silica shell. However, these procedures only produced aggregates, most likely due to poor polymer coating and inherent particle attraction. Different strategies to prevent such phenomenon were tested. These included adding more stabiliser and using alternative stirring methods in order to avoid magnetic bars that could induce particle attraction. However, they did not produce different results. In spite of this, we tested the potential of our aggregates to be used to yield critical soft matter. When mixed with bare fluorescent silica particles and exposed to a magnet, the core shell fluorescent magnetic nanoparticles quickly moved towards it. These results suggest that the developed particles can effectively be manipulated through a magnetic field. Thus, further stabilisation techniques are worth pursuing to eventually yield structures with critical soft matter characteristics.

7.5 Acknowledgments

The synthesis of iron oxide nanoparticles was carried out in collaboration with Dr. Jeff Urban and Dr. Jason Forster of the Molecular Foundry at the Lawrence Berkeley National Laboratory, University of Berkeley, California, USA. Dr. Forster helped and supervised the synthesis of the magnetic nanoparticles.

Dr. James Hallett and Peter Crowther kindly provided the bare rhodamine silica nanoparticles with TPM coating.

CHAPTER 8

SUMMARY, CONCLUSIONS AND FURTHER WORK

8.1 Thesis Overview

The research described in the previous chapters focuses on studying the self-assembly process and the final assemblies formed by different systems with increasing interaction complexity. First, the assemblies of a mixture of particles with different sizes and hard sphere interactions were studied in Chapter 4. This system is followed by a mono-component dispersion of particles with long-range repulsions, investigated in Chapter 5. The two subsequent chapters describe the strategies undergone towards the realisation of a particular kind of structure studied theoretically and called *critical soft matter*. The first strategy consisted of using two fluorescent proteins with short-range attractions induced through salt addition studied in Chapter 6. The second strategy involves the development of core shell fluorescent silica magnetic nanoparticles, which is covered in Chapter 7.

This final section highlights the main results found for each system and proposes further research based on this work.

8.2 Non-Equilibrium Interstitial Solid Solutions of Hard Spheres

The crystallisation of a binary mixture of hard spheres with a size ratio of 0.39 was studied experimentally and computationally in Chapter 4. Particle-resolved studies along with the use of bond-order orientational analyses allowed us to identify interstitial solid solutions (ISS) in coexistence with a fluid phase as the final structures in the experiments, in accordance with related studies [26, 13]. Here the large species form exclusively the ordered close-packed structure comprised of a mixture of fcc and hcp lattices. The small species are located randomly and

in an incomplete fashion in the octahedral holes of these ordered phases. The ISS were formed through heterogeneous nucleation in a total packing fraction range from ϕ_{tot} = 0.52 to 0.64, with the higher concentrations crystallising in shorter times.

Complementary simulation work performed in the same concentration range showed the same final assemblies and allowed us to overcome some experimental limitations. However, we observed crystallisation in a smaller total packing fraction range: from ϕ_{tot} = 0.563 to 0.610. This is likely due to the fact that the crystallisation was homogenous for the simulations.

The quality of the ordered structures was evaluated in both experiments and simulations. The crystal quality was determined by identifying whether the crystal pertains to a large crystalline domain (higher quality) or if the system is polycrystalline (poor quality). The crystals obtained through heterogenous nucleation, i.e., in the experiments, presented higher quality than the ones obtained through homogenous crystallisation. This is likely due to the presence of flat walls that facilitate nucleation and layering, thus improving orientation in the former.

Furthermore, simulations allowed us to follow the crystallisation process, to quantify the composition of the interstitial solid solutions and to study the dynamics of the particles once the structures were formed.

With the information provided, a possible mechanism for the formation of the interstitial solid solutions obtained was suggested: the large particles start nucleating from the fluid and form ordered close-packed structures separately from the small particles, which in turn quickly become trapped within the interstitial sites of the forming lattice, filling it partially and irregularly. As a consequence, a different composition between the coexisting ordered and fluid phases arises, where the former is small-poor and the latter is small-rich. These compositional fluctuations prevent further crystal growth, which was indeed observed. Once the interstitial solid solutions stopped growing, we studied the dynamics of the particles and found that both species do not present movement in the crystalline phase. Moreover, under the conditions studied herein, the small particles remain localised and do not penetrate the crystalline structure, nor do they hop from one octahedral hole to another. This might be due to a close-packing of the ordered phase, which prevents the small species from occupying the available interstitial sites and reaching the equilibrium composition described before for a similar system [26, 13]. Here, the maximum occupancy of the octahedral holes is ~ 14%, which is smaller than said predictions.

Therefore, our interstitial solid solutions are long-lived out-of equilibrium structures. We thus have identified some conditions that might prevent the formation of equilibrium structures. These are worth considering for future experiment and device design. The present studies might also help with further understanding of why crystals of binary spheres are hard to obtain experimentally.

Further experimental and simulation work where fast close-packing of the crystallising species can be slowed down, like sedimentation studies, might allow us to overcome the present limitations and to reach the equilibrium composition.

8.3 Colloidal Crystals at Low Packing Fractions

In chapter 5, particle-resolved studies were conducted to study a one-component system with long-range repulsion. Assuming an effective charge of $Z\lambda_B/\sigma$ = 6, and the counter ions then set at maximum, a Debye screening length of κ^{-1} = 1.9 μm was calculated. This large value of κ^{-1} is likely due to solvent cyclohexyl bromide partial and spontaneous dissociation into cyclohexane and hydrobromic acid. Further partial dissociation of the latter into bromide ions and protons allows for the interaction of hydrogen ions with the surface of the colloidal species, providing them positive charges [21, 39]. This charging phenomenon yielded crystals at particle volume fractions as low as $\phi \sim 0.015$. Quantitative comparison of the results obtained with the Yukawa model showed that the phase behaviour of this system was comparable with the one predicted by the model. We used the Yukawa theory to estimate the lowest freezing density if no salt was present in the system and found it to be around ϕ= 0.0004 with a Debye length of ~ 14 μm.

The crystalline structure of the assemblies found was identified using different bond-orientational order parameters. For $\phi \leq 0.015$ the fluid and crystal bcc structure found coincided with the model predictions. However, this was not the case for higher particle concentrations: the bcc crystal polymorph persisted, which was no longer compatible with the fcc crystal expected. Two main reasons for this discrepancy were suggested. The first one has to do with a lack of equilibration of the system. Indeed, following the Ostwald rule of stages, we might have identified a metastable bcc phase prior to the equilibrated fcc structure predicted for Yukawa systems. The second reason for the unexpected bcc structure found might be the influence of the confinement of the sample into square capillaries, which might favour square symmetries over hexagonal ones.

Intrinsic limitations of our system which include lack of particles and solvent density matching, along with solvent evaporation, prevented us from investigating longer experimental times. In order to confirm the hypotheses proposed, further studies of the kinetics of homogenous crystallisation are required.

8.4 Realisation of Critical Soft Matter

Based on the theoretical study of a binary mixture carried out by Whitelam *et al.* [53], we explored a new self-assembly route to yield out-of-equilibrium structures where the assemblies present particle component fluctuations resembling systems near their critical point, thus being denominated *critical soft matter*. This new route and its structures have potential applications to reproduce nature's far-from-equilibrium processes, assemblies and purposes and thus constitute a new type of functional materials.

One of the characteristics required of the systems to yield such structures is that the particle attractions between the equal species need to be higher than those corresponding to different

species (a-a and b-b attractive interactions > a-b). Also, control over the structure and rate formation is also necessary. Two systems were proposed to yield these type of structures.

8.4.1 Mixture of Fluorescent Proteins

The first system investigated to produce critical soft matter structures was a mixture of two fluorescent proteins: enhanced GFP (eGFP) and mCherry. These proteins served as a model system that allowed us to test the stability of the proteins throughout the different methodologies tested, which is vital for potential applications of these biomaterials. The several experimental conditions explored in order to obtain bi-continuous gel networks with distinctive protein domains through the addition of different salts are detailed in Chapter 6.

Ammonium sulphate produced the desired individual gels when added to protein solutions of eGFP and mCherry. However, when this salt was added to a mixture of both proteins, mixed gels of both proteins were obtained and not the aimed bi-continous gel with characteristic eGFP and mCherry individual domains. This likely arose from non-specific interactions between the salt and each protein as well as the inherent similarities between eGFP and mCherry.

Therefore, the strategies that followed were focused on both increasing the specificity of the salt-protein interactions and on increasing the difference between the two proteins. For the former objective, yttrium chloride, a trivalent salt which interacts specifically with negative charges on the surface of proteins, was tested. It successfully formed gel networks when added to a eGFP solution, but not with mCherry, where only large clusters and re-entrant solution was observed. This might be due to differences in the charge distribution between the proteins. For the second objective, the methodology carried out to further differentiate the proteins was to chemically modify their surface by adding positive charges. Through this modification the interaction between yttrium chloride and the positive proteins was effectively prevented, i.e., the proteins remained in solution.

In order to yield the bi-continuous gels, the following strategy was designed: yttrium chloride was added to a mixture of native and modified proteins, where only the native (and negatively charged) proteins would form gels. Then, the addition of ammonium sulphate would precipitate the modified protein still in solution. However, unexpected interactions between the oppositely charged proteins appeared and solely mixed gels with only few distinctive domains were obtained. Therefore, an alternative strategy was applied, where first a gel of native eGFP was formed in the presence of yttrium chloride, followed by the subsequent addition of ammonium sulphate and positive mCherry. Although these structures were *not* obtained through critical soft matter principles, to our knowledge, this is the first realisation of bi-continous gels of two proteins that retain their functional structure. Moreover, control over the coverage of the primary eGFP gels was also obtained by changing the concentration of mCherry.

Using the easy, cheap, scalable and versatile methodology proposed in Chapter 6, struc-

tures with a large variety of potential applications can be obtained. These applications include scaffolding for tissue growth; innovative biomaterials with optical, electrical, chemical, biological, anti-microbial or energy storage functions; and even the study of diseases which involve protein aggregation like Alzheimer's and Parkinson's.

However, the results obtained also highlight the complexity of protein interactions and the lack of precise control over the interactions between the proteins and the proteins with salts. Thus, the first future steps to yield the wanted materials would be to study precisely the proteins' motives involved in the interactions as well as their strength. Small angle X-ray scattering together with colloidal potentials and patchy particle models might shed light into these parameters. Once the interactions and their strength required have been identified to yield the desired structures, protein design technologies can help to provide the building blocks with such properties and with specific functionalities.

8.4.2 Synthesis of Fluorescent Magnetic Nanoparticles

Chapter 7 covers the different chemical techniques employed to synthesise core shell fluorescent silica magnetic nanoparticles, where the core is comprised of a fluorescent silica sphere decorated with magnetic iron oxide nanoparticles and coated with a thin layer of silica. These magnetic-responsive particles constitute one of the components of a binary mixture with potentially higher intra-particle attractions than inter-particle interactions, with the other component being bare fluorescent silica spheres.

Magnetic iron oxide nanoparticles of 16.8 nm (9.5% polydispersity) were firstly obtained through thermal decomposition of an iron-oleate, obtained *a priori* by reacting iron (III) chloride with sodium oleate. Secondly, they were functionalised with bromide groups. Finally, magnetic fluorescent particles were obtained through successful linking of iron oxide nanoparticles to the surface of fluorescent silica spheres through covalent bonds . These were formed between the bromide motifs of the former and amine moieties previously deposited on the latter. Further particle stabilisation was provided through coating the particles with a polymer (PVP) followed by a silica shell. Although secondary nucleation was effectively prevented, this procedure only yielded clusters of the particles, likely arising from poor polymer coating and intrinsic particle attraction. The former may be due to a lack of insufficient hydrogen bonding between PVP and the particles, or to an inadequate molecular weight of the polymer to prevent aggregation.

Larger amounts of polymer were tested to improve particle stabilisation. These were accompanied by different mixing strategies were the use of a magnet was avoided and included nitrogen bubbling and vortex stirring. None of these various strategies improved the cluster formation and particle aggregates were invariably obtained.

The particle aggregates were successfully resuspended in an organic solvent that matches their refractive index, however, clusters were still observed. When mixing our magnetic clusters

with bare silica particles and exposing such a suspension to a magnet, the former started to move quickly towards it. This result suggest that the system has indeed potential to be manipulated to yield mixed structures with tunable particle size domains and thus, further work in this direction is worth pursuing.

Further control over the size and size dispersion of the magnetic nanoparticles can be achieved through a better control of the temperature and its rate increase. However, the main limitation of our approach is the lack of individual stability of the final core shell fluorescent magnetic particles. Several approaches can be taken in order to avoid particle aggregation. It is worth investigating the optimum molecular weight of PVP to yield effective particle stabilisation [224]. Additionally, other polymers or surfactants that do not rely on hydrogen bond formation between them and the particle might improve particle stability. Alternatively, an overhead stirrer shaft or sonication [79] might provide homogenous stirring without using a magnet.

Once the individual stability of the particles has been achieved, the next steps for yielding the desired structures include the manipulation of the assemblies through control of the attractive interactions that favour intra-particle association over inter-particle association. Manipulation of the strength of an external magnetic field, along with its rate increase, might potentially provide such control.

8.4.3 General Conclusion

In Chapter 1 we introduced the relevance of studying self-assembly processes to both understand physical, chemical and biological phenomena, and to exploit their outstanding potential for the production of functional materials with a myriad of applications. However, the lack of comprehension of the actual mechanisms and specific interactions involved –and required – between the system components to yield particular structures, has limited its exploitation. In this work, we studied experimentally the self-assembly and final structures of a range of colloidal model systems in an effort to contribute with the understanding of these processes and their outcomes. The systems we considered presented a variety of components and several interactions. They included binary hard spheres (also studied computationally), a one-component system with long-range repulsions and binary protein solutions with short-range attractions. The worked carried-out in this thesis sheds light into further understanding of self-built complex systems, highlighted the main current limitations and proposed future work worth pursuing. Moreover, some of the strategies developed herein might serve as inspiration and constitute the first steps for the design and further development of novel types of promising functional materials.

Bibliography

[1] J. A. Pelesko, *Self-Assembly The Science of Things That Put Themselves Together*. Champman and Hall, 2007.

[2] L. Hu, R. Zhang, and Q. Chen, "Synthesis and assembly of nanomaterials under magnetic fields," *Nanoscale*, vol. 6, no. 23, pp. 14 064–14 105, 2014. [Online]. Available: http://dx.doi.org/10.1039/C4NR05108D

[3] P. J. Krommenhoek and J. B. Tracy, "Magnetic field-directed self-assembly of magnetic nanoparticle chains in bulk polymers," *Particle & Particle Systems Characterization*, vol. 30, no. 9, pp. 759–763, 2013. [Online]. Available: https://doi.org/10.1002/ppsc.201300101

[4] G. M. Whitesides and B. Grzybowski, "Self-assembly at all scales," *Science*, vol. 295, no. 5564, p. 2418, 03 2002. [Online]. Available: http://science.sciencemag.org/content/295/5564/2418.abstract

[5] S. Tibbits, "Design to self-assembly," *Architectural Design*, vol. 82, no. 2, pp. 68–73, 2012. [Online]. Available: https://doi.org/10.1002/ad.1381

[6] P. Sharma, "Self-assembly of colloidal particles," *Resonance*, vol. 23, no. 3, pp. 263–275, 2018. [Online]. Available: https://doi.org/10.1007/s12045-018-0616-0

[7] G. F. Swiegers, S. Balakrishnan, and J. Huang, *Assemblies and Self-Assembly*. Elsevier, 2016. [Online]. Available: http://www.sciencedirect.com/science/article/pii/B978012409547211710X

[8] S. Chidambaram, N. Kasi, and S. Muthusamy, *Self-assembly of Nanostrctures: Nanostructure, Nanosystems and Nanostructured Materials*, 2013.

[9] Z. Xu, L. Wang, F. Fang, Y. Fu, and Z. Yin, "A review on colloidal self-assembly and their applications," *Current Nanoscience*, vol. 12, no. 6, pp. 725–746, 2016.

[10] M. van der Linden, "Long-range repulsive charged colloids in and out of equilibrium," Ph.D. dissertation, Utrecht University, 2013.

[11] T. Tadros, *Electrical Phenomena at Interfaces and Biointerfaces*. Wiley-Blackwell, 2012, no. 10, ch. Electrostatic and Steric Stabilization of Colloidal Dispersions, pp. 153–172.

[12] B. Li, D. Zhou, and Y. Han, "Assembly and phase transitions of colloidal crystals," *Nature Reviews Materials*, vol. 1, p. 15011, 01 2016. [Online]. Available: http://dx.doi.org/10.1038/natrevmats.2015.11

[13] L. Filion, "Self-assembly in colloidal hard-sphere systems," Ph.D. dissertation, Utrecht University, 2011.

[14] R. Jones, *Soft Condensed Matter*, 2nd ed., ser. Oxford Master Series in Condensed Matter Physics. Oxford University Press, 2002.

[15] M. Meissner, "Microfluidics on the colloidal scale," Ph.D. dissertation, University of Bristol, 2017.

[16] I. Williams, "Colloids in optically defined confinement," Ph.D. dissertation, University of Bristol, 2013.

[17] P. Segre, *Fluids, Colloids and Soft Materials: An Introduction to Soft Matter Physics*. Wiley, 2016, no. 4, ch. Fluctuations in Particle Sedimentation, pp. 43–58.

[18] E. Hadjittofis, S. C. Das, G. G. Z. Zhang, J. Y. Y. Heng, Y. Qiu, Y. Chen, G. G. Z. Zhang, L. Yu, and R. V. Mantri, *Chapter 8 - Interfacial Phenomena*. Boston: Academic Press, 2017, pp. 225–252. [Online]. Available: http://www.sciencedirect.com/science/article/pii/B978012802447800008X

[19] R. M. Pashley and M. E. Karaman, *Van der Waals Forces and Colloid Stability*. Wiley-Blackwell, 2005, pp. 127–151. [Online]. Available: https://onlinelibrary.wiley.com/doi/abs/10.1002/0470014709.ch7

[20] N. I. Lebovka, *Aggregation of Charged Colloidal Particles*. Berlin, Heidelberg: Springer Berlin Heidelberg, 2014, pp. 57–96. [Online]. Available: https://doi.org/10.1007/12_2012_171

[21] M. E. Leunissen, "Manipulating colloids with charge and electric fields," Ph.D. dissertation, University of Utrecht, 2007.

[22] I. Rios de Anda, A. Statt, F. Turci, and C. P. Royall, "Low-density crystals in charged colloids: comparison with yukawa theory," *Contributions to Plasma Physics*, vol. 55, no. 2-3, pp. 172–179, 2015. [Online]. Available: http://dx.doi.org/10.1002/ctpp.201400099

[23] P. N. Pusey, "The effect of polydispersity on the crystallization of hard spherical colloids," *Journal de Physique*, vol. 48, no. 5, pp. 709–712, 1987.

[24] M. D. Eldridge, P. A. Madden, P. N. Pusey, and P. Bartlett, "Binary hard-sphere mixtures: a comparison between computer simulation and experiment," *Molecular Physics*, vol. 84, no. 2, pp. 395–420, 02 1995. [Online]. Available: http://dx.doi.org/10.1080/00268979500100271

[25] L. Filion and M. Dijkstra, "Prediction of binary hard-sphere crystal structures," *Physical Review E*, vol. 79, no. 4, p. 046714, 04 2009. [Online]. Available: https://link.aps.org/doi/10.1103/PhysRevE.79.046714

[26] L. Filion, M. Hermes, R. Ni, E. C. M. Vermolen, A. Kuijk, C. G. Christova, J. C. P. Stiefelhagen, T. Vissers, A. van Blaaderen, and M. Dijkstra, "Self-assembly of a colloidal interstitial solid with tunable sublattice doping," *Physical Review Letters*, vol. 107, no. 16, p. 168302, 10 2011. [Online]. Available: http://link.aps.org/doi/10.1103/PhysRevLett.107.168302

[27] P. N. Pusey and W. van Megen, "Phase behaviour of concentrated suspensions of nearly hard colloidal spheres," *Nature*, vol. 320, pp. 340 EP –, 03 1986. [Online]. Available: http://dx.doi.org/10.1038/320340a0

[28] C. P. Royall, W. C. K. Poon, and E. R. Weeks, "In search of colloidal hard spheres," *Soft Matter*, vol. 9, no. 1, pp. 17–27, 2013. [Online]. Available: http://dx.doi.org/10.1039/C2SM26245B

[29] W. G. T. Kranendonk and D. Frenkel, "Thermodynamic properties of binary hard sphere mixtures," *Molecular Physics*, vol. 72, no. 3, pp. 715–733, 02 1991. [Online]. Available: https://doi.org/10.1080/00268979100100521

[30] M. Dijkstra, *Entropy-Driven Phase Transitions in Colloids: From spheres to anisotropic particles*. Wiley-Blackwell, 2014, ch. 2, pp. 35–71. [Online]. Available: https://onlinelibrary.wiley.com/doi/abs/10.1002/9781118949702.ch2

[31] N. Hunt, R. Jardine, and P. Bartlett, "Superlattice formation in mixtures of hard-sphere colloids," *Physical Review E*, vol. 62, no. 1, 2000.

[32] A. P. Hynninen, L. Filion, and M. Dijkstra, "Stability of ls and ls2 crystal structures in binary mixtures of hard and charged spheres," *The Journal of Chemical Physics*, vol. 131, no. 6, p. 064902, 2009. [Online]. Available: https://aip.scitation.org/doi/abs/10.1063/1.3182724

[33] É. Ducrot, M. He, G.-R. Yi, and D. J. Pine, "Colloidal alloys with preassembled clusters and spheres," *Nature Materials*, vol. 16, p. 652, 02 2017. [Online]. Available: http://dx.doi.org/10.1038/nmat4869

[34] K. P. Velikov, C. G. Christova, R. P. A. Dullens, and A. van Blaaderen, "Layer-by-layer growth of binary colloidal crystals," *Science*, vol. 26, no. 5565, 2002.

[35] A. P. Hynninen, J. H. J. Thijssen, E. C. M. Vermolen, M. Dijkstra, and A. van Blaaderen, "Self-assembly route for photonic crystals with a bandgap in the visible region," *Nature Materials*, vol. 6, p. 202, 02 2007. [Online]. Available: http://dx.doi.org/10.1038/nmat1841

[36] E. Boattini, M. Ram, F. Smallenburg, and L. Filion, "Neural-network-based order parameters for classification of binary hard-sphere crystal structures," *Molecular Physics*, pp. 1–10, 06 2018. [Online]. Available: https://doi.org/10.1080/00268976.2018.1483537

[37] J. V. Sanders, "Close-packed structures of spheres of two different sizes i. observations on natural opal," *Philosophical Magazine A*, vol. 42, no. 6, pp. 705–720, 12 1980. [Online]. Available: https://doi.org/10.1080/01418618008239379

[38] M. Dijkstra, R. van Roij, and R. Evans, "Phase diagram of highly asymmetric binary hard-sphere mixtures," *Physical Review E*, vol. 59, no. 5, pp. 5744–5771, 05 1999. [Online]. Available: https://link.aps.org/doi/10.1103/PhysRevE.59.5744

[39] M. E. Leunissen, C. G. Christova, A.-P. Hynninen, C. P. Royall, A. I. Campbell, A. Imhof, M. Dijkstra, R. van Roij, and A. van Blaaderen, "Ionic colloidal crystals of oppositely charged particles," *Nature*, vol. 437, no. 7056, pp. 235–240, 09 2005. [Online]. Available: http://dx.doi.org/10.1038/nature03946

[40] W. H. Evers, B. D. Nijs, L. Filion, S. Castillo, M. Dijkstra, and D. Vanmaekelbergh, "Entropy-driven formation of binary semiconductor-nanocrystal superlattices," *Nano Letters*, vol. 10, no. 10, pp. 4235–4241, 10 2010. [Online]. Available: https://doi.org/10.1021/nl102705p

[41] E. V. Shevchenko, D. V. Talapin, N. A. Kotov, S. O'Brien, and C. B. Murray, "Structural diversity in binary nanoparticle superlattices," *Nature*, vol. 439, no. 7072, pp. 55–59, 01 2006. [Online]. Available: http://dx.doi.org/10.1038/nature04414

[42] M. J. Murray and J. V. Sanders, "Close-packed structures of spheres of two different sizes ii. the packing densities of likely arrangements," *Philosophical Magazine A*, vol. 42, no. 6, pp. 721–740, 12 1980. [Online]. Available: https://doi.org/10.1080/01418618008239380

[43] P. Bartlett, R. H. Ottewill, and P. N. Pusey, "Superlattice formation in binary mixtures of hard-sphere colloids," *Phys. Rev. Lett.*, vol. 68, p. 3801, 1992.

[44] V. J. Anderson and H. N. W. Lekkerkerker, "Insights into phase transition kinetics from colloid science," *Nature*, vol. 416, p. 811, 04 2002. [Online]. Available: http://dx.doi.org/10.1038/416811a

[45] C. Zhao, G. Yuan, D. Jia, and C. C. Han, "Macrogel induced by microgel: bridging and depletion mechanisms," *Soft Matter*, vol. 8, no. 26, pp. 70–36–7043, 2012.

[46] J. Chen, S. R. Kline, and Y. Liu, "From the depletion attraction to the bridging attraction: The effect of solvent molecules on the effective colloidal interactions," *The Journal of Chemical Physics*, vol. 142, no. 8, p. 084904, 2018/08/03 2015. [Online]. Available: https://doi.org/10.1063/1.4913197

[47] H. Lekkerkerker and R. Tuinier, *Colloids and the Depletion Interaction*, ser. Lecture Notes in Physics. Springer-Verlag, 2011.

[48] P. Theodorakis, N. Fytas, G. Kahl, and C. Dellago, "Self-assembly of dna-functionalized colloids," *Condensed Matter Physics*, vol. 18, no. 2, pp. 1–24, 2015.

[49] L. Belloni, "Colloidal interactions," *Journal of Physics: Condensed Matter*, vol. 12, no. 46, p. R549, 2000. [Online]. Available: http://stacks.iop.org/0953-8984/12/i=46/a=201

[50] Y. Liang, N. Hilal, P. Langston, and V. Starov, "Interaction forces between colloidal particles in liquid: Theory and experiment," *Advances in Colloid and Interface Science*, vol. 134-135, pp. 151–166, 2007. [Online]. Available: http://www.sciencedirect.com/science/article/pii/S0001868607000632

[51] Z. Xu and R.-H. Yoon, "The role of hydrophobia interactions in coagulation," *Journal of Colloid and Interface Science*, vol. 132, no. 2, pp. 532–541, 1989. [Online]. Available: http://www.sciencedirect.com/science/article/pii/0021979789902671

[52] C. L. Klix, K.-i. Murata, H. Tanaka, S. R. Williams, A. Malins, and C. P. Royall, "Novel kinetic trapping in charged colloidal clusters due to self-induced surface charge organization," *Scientific Reports*, vol. 3, pp. 2072 EP –, 06 2013. [Online]. Available: https://doi.org/10.1038/srep02072

[53] S. Whitelam, L. O. Hedges, and J. D. Schmit, "Self-assembly at a nonequilibrium critical point," *Physical Review Letters*, vol. 112, no. 15, p. 155504, 04 2014. [Online]. Available: http://link.aps.org/doi/10.1103/PhysRevLett.112.155504

[54] H. Gleiter, "Nanostructured materials: basic concepts and microstructure," *Acta Materialia*, vol. 48, no. 1, pp. 1–29, 2000. [Online]. Available: http://www.sciencedirect.com/science/article/pii/S1359645499002852

[55] Z. Fu, Y. Xiao, A. Feoktystov, V. Pipich, M.-S. Appavou, Y. Su, E. Feng, W. Jin, and T. BrÃŒckel, "Field-induced self-assembly of iron oxide nanoparticles investigated using small-angle neutron scattering," *Nanoscale*, vol. 8, no. 43, pp. 18 541–18 550, 2016.

[56] S. Singamaneni, V. N. Bliznyuk, C. Binek, and E. Y. Tsymbal, "Magnetic nanoparticles: recent advances in synthesis, self-assembly and applications," *Journal of Materials Chemistry*, vol. 21, no. 42, pp. 16 819–16 845, 2011. [Online]. Available: http://dx.doi.org/10.1039/C1JM11845E

[57] G. A. Ozin, K. Hou, B. V. Lotsch, L. Cademartiri, D. P. Puzzo, F. Scotognella, A. Ghadimi, and J. Thomson, "Nanofabrication by self-assembly," *Materials Today*, vol. 12, no. 5, pp. 12–23, 2009. [Online]. Available: http://www.sciencedirect.com/science/article/pii/S1369702109701567

[58] Q. Luo, C. Hou, Y. Bai, R. Wang, and J. Liu, "Protein assembly: Versatile approaches to construct highly ordered nanostructures," *Chemical Reviews*, vol. 116, no. 22, pp. 13 571–13 632, 11 2016. [Online]. Available: https://doi.org/10.1021/acs.chemrev.6b00228

[59] T. Vo-Dinh, *Protein Nanotechnology*. Totowa, NJ: Humana Press, 2005, pp. 1–13. [Online]. Available: https://doi.org/10.1385/1-59259-858-7:001

[60] G. Walsh, *Proteins: Biochemistry and Biotechnology*, 2nd ed., G. Walsh, Ed. Wiley-Blackwell, 2004.

[61] J. E. Padilla, C. Colovos, and T. O. Yeates, "Nanohedra: Using symmetry to design self assembling protein cages, layers, crystals, and filaments," *Proceedings of the National Academy of Sciences*, vol. 98, no. 5, p. 2217, 02 2001. [Online]. Available: http://www.pnas.org/content/98/5/2217.abstract

[62] Y. He, Y. Tian, A. E. Ribbe, and C. Mao, "Antibody nanoarrays with a pitch of 20 nanometers," *Journal of the American Chemical Society*, vol. 128, no. 39, pp. 12 664–12 665, 10 2006. [Online]. Available: https://doi.org/10.1021/ja065467+

[63] J. Sun, C. DuFort, M.-C. Daniel, A. Murali, C. Chen, K. Gopinath, B. Stein, M. De, V. M. Rotello, A. Holzenburg, C. C. Kao, and B. Dragnea, "Core-controlled polymorphism in virus-like particles," *Proceedings of the National Academy of Sciences*, vol. 104, no. 4, p. 1354, 01 2007. [Online]. Available: http://www.pnas.org/content/104/4/1354.abstract

[64] D. W. Watkins, J. M. X. Jenkins, K. J. Grayson, N. Wood, J. W. Steventon, K. K. Le Vay, M. I. Goodwin, A. S. Mullen, H. J. Bailey, M. P. Crump, F. MacMillan, A. J. Mulholland, G. Cameron, R. B. Sessions, S. Mann, and J. L. R. Anderson, "Construction and in vivo assembly of a catalytically proficient and hyperthermostable de novo enzyme," *Nature Communications*, vol. 8, no. 1, p. 358, 2017. [Online]. Available: https://doi.org/10.1038/s41467-017-00541-4

[65] L. Ma, F. Li, T. Fang, J. Zhang, and Q. Wang, "Controlled self-assembly of proteins into discrete nanoarchitectures templated by gold nanoparticles via monovalent interfacial engineering," *ACS Applied Materials & Interfaces*, vol. 7, no. 20, pp. 11 024–11 031, 05 2015. [Online]. Available: https://doi.org/10.1021/acsami.5b02823

[66] F. Zhang, S. Weggler, M. J. Ziller, L. Ianeselli, B. S. Heck, A. Hildebrandt, O. Kohlbacher, M. W. A. Skoda, R. M. J. Jacobs, and F. Schreiber, "Universality of protein reentrant condensation in solution induced by multivalent metal ions," *Proteins: Structure, Function, and Bioinformatics*, vol. 78, no. 16, pp. 3450–3457, 2010. [Online]. Available: https://doi.org/10.1002/prot.22852

[67] A. Dumetz, A. M. Chockla, E. W. Kaler, and A. M. Lenhoff, "Protein phase behavior in aqueous solutions: Crystallization, liquid-liquid phase separation, gels, and aggregates," *Biophysical Journal*, vol. 94, no. 2, pp. 570–583, 2018/07/20 2008. [Online]. Available: http://dx.doi.org/10.1529/biophysj.107.116152

[68] J. J. McManus, P. Charbonneau, E. Zaccarelli, and N. Asherie, "The physics of protein self-assembly," *Current Opinion in Colloid & Interface Science*, vol. 22, pp. 73–79, 2016. [Online]. Available: http://www.sciencedirect.com/science/article/pii/S1359029416300292

[69] S. James, M. K. Quinn, and J. J. McManus, "The self assembly of proteins; probing patchy protein interactions," *Physical Chemistry Chemical Physics*, vol. 17, no. 7, pp. 5413–5420, 2015. [Online]. Available: http://dx.doi.org/10.1039/C4CP05892E

[70] T. K. Singh, S. K. Øiseth, L. Lundin, and L. Day, "Influence of heat and shear induced protein aggregation on the in vitro digestion rate of whey proteins," *Food & Function*, vol. 5, no. 11, pp. 2686–2698, 2014. [Online]. Available: http://dx.doi.org/10.1039/C4FO00454J

[71] L. Huang, Y. Zhang, and H. Li, "Self-assembly of globulin nanofibrils at various ionic strength: Microstructure and gels," *American Journal of Nanomaterials*, vol. 2, no. 1, pp. 8–12, 2014. [Online]. Available: http://pubs.sciepub.com/ajn/2/1/3

[72] G. Singh, H. Chan, T. Udayabhaskararao, E. Gelman, D. Peddis, A. Baskin, G. Leitus, P. Král, and R. Klajn, "Magnetic field-induced self-assembly of iron oxide nanocubes," *Faraday Discussions*, vol. 181, pp. 403–421, 2015. [Online]. Available: http://dx.doi.org/10.1039/C4FD00265B

[73] A. Yadollahpour and S. Rashidi, "Magnetic nanoparticles: A review of chemical and physical characteristics important in medical applications," *Oriental Journal of Chemistry*, vol. 31, pp. 25–30, 2015.

[74] M. Wang, L. He, and Y. Yin, "Magnetic field guided colloidal assembly," *Materials Today*, vol. 16, no. 4, pp. 110–116, 2013. [Online]. Available: http://www.sciencedirect.com/science/article/pii/S1369702113001089

[75] G. Lumay, S. Dorbolo, and N. Vandewalle, "Compaction dynamics of a magnetized powder," *Physical Review E*, vol. 80, no. 4, p. 041302, 10 2009. [Online]. Available: https://link.aps.org/doi/10.1103/PhysRevE.80.041302

[76] J. B. Tracy and T. M. Crawford, "Magnetic field-directed self-assembly of magnetic nanoparticles," *MRS Bulletin*, vol. 38, no. 11, pp. 915–920, 2013. [Online]. Available: https://www.cambridge.org/core/article/magnetic-fielddirected-selfassembly-of-magnetic-nanoparticles/6866BE9C12579AFE7CE79868031BFFD3

[77] H. N. Wang, A. Mararenko, G. Cao, Z. Gai, K. Hong, P. Banerjee, and S. Zhou, "Multifunctional 1d magnetic and fluorescent nanoparticle chains for enhanced mri, fluorescent cell imaging, and combined photothermal/chemotherapy," *ACS Applied Materials and Interfaces*, vol. 6, no. 17, pp. 15 309–15 317, 2014.

[78] A. Ahniyaz, Y. Sakamoto, and L. Bergström, "Magnetic field-induced assembly of oriented superlattices from maghemite nanocubes," *Proceedings of the National Academy of Sciences*, vol. 104, no. 45, p. 17570, 11 2007. [Online]. Available: http://www.pnas.org/content/104/45/17570.abstract

[79] T. Ding, K. Song, K. Clays, and C.-H. Tung, "Fabrication of 3d photonic crystals of ellipsoids: Convective self-assembly in magnetic field," *Advanced Materials*, vol. 21, no. 19, pp. 1936–1940, 2009. [Online]. Available: https://doi.org/10.1002/adma.200803564

[80] F. Zhang and C.-C. Wang, "Fabrication of one-dimensional iron oxide/silica nanostructures with high magnetic sensitivity by dipole-directed self-assembly," *The Journal of Physical Chemistry C*, vol. 112, no. 39, pp. 15 151–15 156, 10 2008. [Online]. Available: https://doi.org/10.1021/jp804452r

[81] G. A. B. Confalonieri, V. Vega, A. Ebbing, D. Mishra, P. Szary, V. M. Prida, O. Petracic, and H. Zabel, "Template-assisted self-assembly of individual and clusters of magnetic nanoparticles," *Nanotechnology*, vol. 22, no. 28, p. 285608, 2011. [Online]. Available: http://stacks.iop.org/0957-4484/22/i=28/a=285608

[82] G. Bosma, C. Pathmamanoharan, E. H. A. de Hoog, W. K. Kegel, A. van Blaaderen, and H. N. W. Lekkerkerker, "Preparation of monodisperse, fluorescent pmma-latex colloids by dispersion polymerization," *J. Coll. Interf. Sci.*, vol. 245, no. 2, pp. 292–300, Jan. 2002.

[83] R. Rice, "Novel colloid interactions using pmma," Master's thesis, School of Chemistry, University of Bristol, 2012.

[84] M. N. Bannerman, R. Sargant, and L. Lue, "Dynamo: A free o(n) general event-driven simulator," *J. Comp. Chem.*, vol. 32, pp. 3329–3338, 2011.

[85] Y.-L. Hsiao, E. E. Maury, J. M. DeSimone, S. Mawson, and K. P. Johnston, "Dispersion polymerization of methyl methacrylate stabilized with poly(1,1-dihydroperfluorooctyl acrylate) in supercritical carbon dioxide," *Macromolecules*, vol. 28, no. 24, pp. 8159–8166, 11 1995. [Online]. Available: https://doi.org/10.1021/ma00128a028

[86] A. P. Richez, H. N. Yow, S. Biggs, and O. J. Cayre, "Dispersion polymerization in non-polar solvent: Evolution toward emerging applications," *Progress in Polymer Science*, vol. 38, no. 6, pp. 897–931, 2013. [Online]. Available: http://www.sciencedirect.com/science/article/pii/S0079670012001232

[87] M. H. Nada, "Scanning electron microscopy," *BAOJ Microbio*, vol. 1, p. 005, 2015.

[88] L. Reimer, *Scanning Electron Microscopy Physics of Image Formation and Microanalysis*, 1st ed., ser. Springer Series in Optical Sciences. Springer-Verlag, 1985, vol. 45.

[89] J. A. Bonham, "Microgel particles in non-aqueous colloid-polymer mixtures," Ph.D. dissertation, University of Bristol, 2016.

[90] L. Reimer, *Transmission Electron Microscopy Physics of Image Formation and Microanalysis*, 3rd ed., ser. Springer Series in Optical Sciences. Springer-Verlag, 1993, vol. 36.

[91] V. Prasad, D. Semwogerere, and E. R. Weeks, "Confocal microscopy of colloids," *Journal of Physics: Condensed Matter*, vol. 19, no. 11, p. 113102, 2007. [Online]. Available: http://stacks.iop.org/0953-8984/19/i=11/a=113102

[92] A. Ivlev, H. Löwen, G. Morfill, and C. P. Royall, *Complex Plasmas and Colloidal Dispersions: Particle-resolved Studies of Classical Liquids and Solids*. World Scientific Co., Singapore Scientific, 2012.

[93] W. Schumann, *Plasmids: Current Research and Future Trends*. Caister Academic Press, 2008, ch. Escherichia coli Cloning and Expression Vectors, pp. 1–24.

[94] J. R. Beckwith, "Regulation of the lac operon," *Science*, vol. 156, no. 3775, pp. 597–604, 1967.

[95] R. Schleif, "Regulation of the l-arabinose operon of escherichia coli," *Trends in Genetics*, vol. 16, no. 12, pp. 559–565, 2000. [Online]. Available: http://dx.doi.org/10.1016/S0168-9525(00)02153-3

[96] H. Block, B. Maertens, A. Spriestersbach, N. Brinker, J. Kubicek, R. Fabis, J. Labahn, F. Schäfer, R. R. Burgess, and M. P. Deutscher, *Chapter 27 Immobilized-Metal*

Affinity Chromatography (IMAC): A Review. Academic Press, 2009, vol. 463, pp. 439–473. [Online]. Available: http://www.sciencedirect.com/science/article/pii/S0076687909630275

[97] A. Beckett and J. Stenlake, *Practical Pharmaceutical Chemistry Part II*, 4th ed. The Athlone Press London, 1988, ch. Introduction.

[98] M. Kaishima, J. Ishii, T. Matsuno, N. Fukuda, and A. Kondo, "Expression of varied gfps in saccharomyces cerevisiae: codon optimization yields stronger than expected expression and fluorescence intensity," *Scientific Reports*, vol. 6, p. 35932, 10 2016. [Online]. Available: http://dx.doi.org/10.1038/srep35932

[99] L. Yankun, S. A. M., A. Hui-wang, and C. R. E., "Identification of sites within a monomeric red fluorescent protein that tolerate peptide insertion and testing of corresponding circular permutations," *Photochemistry and Photobiology*, vol. 84, no. 1, pp. 111–119, 2007. [Online]. Available: https://doi.org/10.1111/j.1751-1097.2007.00206.x

[100] S. Bhattacharjee, "Dls and zeta potential –what they are and what they are not?" *Journal of Controlled Release*, vol. 235, pp. 337–351, 2016. [Online]. Available: http://www.sciencedirect.com/science/article/pii/S0168365916303832

[101] S. Salgin, U. Salgin, and S. Bahadir, "Zeta potentials and isoelectric points of biomolecules: the effects of ion types and ionic strengths," *Int. J. Electrochem Sci*, vol. 7, pp. 12 404–12 414, 2012.

[102] J. D. Clogston and A. K. Patri, *Zeta Potential Measurement*. Totowa, NJ: Humana Press, 2011, pp. 63–70. [Online]. Available: https://doi.org/10.1007/978-1-60327-198-1_6

[103] A. J. Dunleavy, "Applying information theory to super-cooled liquids," Ph.D. dissertation, University of Bristol, 2014.

[104] K. Sandomirski, E. Allahyarov, H. Lowen, and S. U. Egelhaaf, "Heterogeneous crystallization of hard-sphere colloids near a wall," *Soft Matter*, vol. 7, no. 18, pp. 8050–8055, 2011. [Online]. Available: http://dx.doi.org/10.1039/C1SM05346A

[105] A. E. Saunders and B. A. Korgel, "Observation of an ab phase in bidisperse nanocrystal superlattices," *ChemPhysChem*, vol. 6, no. 1, pp. 61–65, 2005. [Online]. Available: http://dx.doi.org/10.1002/cphc.200400382

[106] A. T. Pham, R. Seto, J. Schonke, D. Y. Joh, A. Chilkoti, E. Fried, and B. B. Yellen, "Crystallization kinetics of binary colloidal monolayers," *arXiv:1605.05389*, 2016.

[107] A. B. Schofield, P. N. Pusey, and P. Radcliffe, "Stability of the binary colloidal crystals ab2 and ab13," *Physical Review E*, vol. 72, no. 3, pp. 031 407–, 09 2005. [Online]. Available: http://link.aps.org/doi/10.1103/PhysRevE.72.031407

[108] E. Trizac, M. D. Eldridge, and P. MaMadden, "Stability of the ab crystal for asymmetric binary hard sphere mixtures," *Mol. Phys.*, vol. 90, p. 675, 1997.

[109] E. C. M. Vermolen, A. Kuijk, L. C. Filion, M. Hermes, J. H. J. Thijssen, M. Dijkstra, and A. van Blaaderen, "Fabrication of large binary colloidal crystals with a nacl structure," *Proceedings of the National Academy of Sciences*, vol. 106, no. 38, pp. 16 063–16 067, 2009. [Online]. Available: http://www.pnas.org/content/106/38/16063.abstract

[110] C. Christova, "Binary colloidal crystals," Ph.D. dissertation, Utrecht University, 2005.

[111] J. V. Sanders and M. J. Murray, "Ordered arrangements of spheres of two different sizes in opal," *Nature*, vol. 275, no. 5677, pp. 201–203, 09 1978. [Online]. Available: http://dx.doi.org/10.1038/275201a0

[112] K. Zhang, W. W. Smith, M. Wang, Y. Liu, J. Schroers, M. D. Shattuck, and C. S. O'Hern, "Connection between the packing efficiency of binary hard spheres and the glass-forming ability of bulk metallic glasses," *Physical Review E*, vol. 90, no. 3, p. 032311, 09 2014. [Online]. Available: http://link.aps.org/doi/10.1103/PhysRevE.90.032311

[113] C. P. Royall and S. R. Williams, "The role of local structure in dynamical arrest," *Physics Reports*, vol. 560, pp. 1–75, 2 2015. [Online]. Available: http://www.sciencedirect.com/science/article/pii/S0370157314004062

[114] R. W. Cahn, *The Coming of Materials Science*, ser. Pergamon Materials Series. Pergamon, Oxford, 2009, vol. 5.

[115] B. van der Meer, E. Lathouwers, F. Smallenburg, and L. Filion, "Diffusion and interactions of interstitials in hard-sphere interstitial solid solutions," *The Journal of Chemical Physics*, vol. 147, no. 23, p. 234903, 2017. [Online]. Available: https://doi.org/10.1063/1.5003905

[116] Verhoeven John D., *Steel metallurgy for the non-metallurgist*. Materials Park, Ohio : ASM International, 2007.

[117] H. M. Syed, C. J. Webb, and E. M. Gray, "Hydrogen-modified superconductors: A review," *Progress in Solid State Chemistry*, vol. 44, no. 1, pp. 20–34, 2016. [Online]. Available: http://www.sciencedirect.com/science/article/pii/S0079678616000030

[118] E. Vermolen, "Manipulation of colloidal crystallization," Ph.D. dissertation, Utrecht University, 2008.

[119] C. P. Royall, A. A. Louis, and H. Tanaka, "Measuring colloidal interactions with confocal microscopy," *J. Chem. Phys.*, vol. 127, p. 044507, 2007.

[120] M. N. Bannerman and L. Lue, "Transport properties of highly asymmetric hard-sphere mixtures," *The Journal of Chemical Physics*, vol. 130, no. 16, 2009. [Online]. Available: http://scitation.aip.org/content/aip/journal/jcp/130/16/10.1063/1.3120488

[121] F. H. Stillinger and B. D. Lubachevsky, "Crystalline—amorphous interface packings for disks and spheres," *Journal of Statistical Physics*, vol. 73, no. 3, pp. 497–514, 1993. [Online]. Available: http://dx.doi.org/10.1007/BF01054337

[122] C. P. Royall, M. E. Leunissen, and A. van Blaaderen, "A new colloidal model system to study long-range interactions quantitatively in real space," *Journal of Physics: Condensed Matter*, vol. 15, no. 48, p. S3581, 2003. [Online]. Available: http://stacks.iop.org/0953-8984/15/i=48/a=017

[123] C. P. Royall, S. R. Williams, and H. Tanaka, "The nature of the glass and gel transitions in sticky spheres," *ArXiv e-prints*, Sep. 2014.

[124] A. J. Dunleavy, K. Wiesner, R. Yamamoto, and C. P. Royall, "Mutual information reveals multiple structural relaxation mechanisms in a model glass former," *Nature Communications*, vol. 6, p. 6089, 01 2015. [Online]. Available: http://dx.doi.org/10.1038/ncomms7089

[125] M. Leocmach and H. Tanaka, "A novel particle tracking method with individual particle size measurement and its application to ordering in glassy hard sphere colloids," *Soft Matter*, vol. 9, no. 5, pp. 1447–1457, 2013. [Online]. Available: http://dx.doi.org/10.1039/C2SM27107A

[126] W. Lechner and C. Dellago, "Accurate determination of crystal structures based on averaged local bond order parameters," *J. Chem. Phys.*, vol. 129, p. 114707, 2009.

[127] S. Jungblut and C. Dellago, "Crystallization of a binary lennard-jones mixture," *The Journal of Chemical Physics*, vol. 134, no. 10, p. 104501, 2011. [Online]. Available: http://aip.scitation.org/doi/abs/10.1063/1.3556664

[128] C. J. Fullerton and R. L. Jack, "Optimising self-assembly through time-dependent interactions," *ArXiv e-prints*, Sep. 2016.

[129] D. Klotsa and R. L. Jack, "Controlling crystal self-assembly using a real-time feedback scheme," *The Journal of Chemical Physics*, vol. 138, no. 9, p. 094502, 2013. [Online]. Available: http://aip.scitation.org/doi/abs/10.1063/1.4793527

[130] D. Turnbull, "Kinetics of heterogeneous nucleation," *The Journal of Chemical Physics*, vol. 18, no. 2, pp. 198–203, 1950. [Online]. Available: http://aip.scitation.org/doi/abs/10.1063/1.1747588

[131] R. Backofen and A. Voigt, "A phase field crystal study of heterogeneous nucleation – application of the string method," *The European Physical Journal Special Topics*, vol. 223, no. 3, pp. 497–509, 2014. [Online]. Available: https://doi.org/10.1140/epjst/e2014-02105-3

[132] N. DeCristofaro and R. Kaplow, "Interstitial atom configurations in stable and metastable fe-n and fe-c solid solutions," *Metallurgical Transactions A*, vol. 8, no. 1, pp. 35–44, 1977. [Online]. Available: http://dx.doi.org/10.1007/BF02677261

[133] F. C. Campbell, Ed., *Elements of Metallurgy and Engineering Alloys*. Materials Park, OH: ASM International, 2008, ch. Solid Solutions.

[134] P. Montero de Hijes, P. Rosales-Pelaez, C. Valeriani, P. N. Pusey, and E. Sanz, "Brownian versus newtonian devitrification of hard-sphere glasses," *Physical Review E*, vol. 96, no. 2, p. 020602, 08 2017. [Online]. Available: https://link.aps.org/doi/10.1103/PhysRevE.96.020602

[135] R. P. A. Dullens and W. K. Kegel, "Reentrant surface melting of colloidal hard spheres," *Physical Review Letters*, vol. 92, no. 19, pp. 195 702–, 05 2004. [Online]. Available: https://link.aps.org/doi/10.1103/PhysRevLett.92.195702

[136] T. Schillng, H. J. Schoepe, M. Oettel, G. Opletal, and I. Snook, "Precursor-mediated crystallization process in suspensions of hard spheres," *Phys. Rev. Lett.*, vol. 105, p. 025701, 2010.

[137] O. Bakunin, *Turbulence and Diffusion Scaling Versus Equations*, ser. Springer Series in Synergetics. Springer-Verlag, 2008.

[138] K. Yoshizawa, T. Okuzono, T. Koga, T.Taniji, and J. Yamanaka, "Exclusion of impurity particles during grain growth in charged colloidal crystals," *Langmuir*, vol. 27, pp. 13 420–13 427, 2011.

[139] C. Likos, "Effective interactions in soft condensed matter physics," *Phys. Rep.*, vol. 348, pp. 267–439, 2001.

[140] E. Verwey and J. Overbeek, *Theory of the Stability of Lyophobic Colloids*. Elsevier, Amsterdam, 1948.

[141] H. Loewen, C. P. Royall, A. Ivlev, and G. E. Morfill, "Charged colloidal suspensions and their link to complex plasmas," *Proc. 6th ICPDP, Am. Inst.*, vol. 1397, p. 201, 2011.

[142] A. P. Hynninen and M. Dijkstra, "Phase diagrams of hard-core repulsive yukawa particles," *Phys. Rev. E*, vol. 68, p. 021407, 2003.

[143] C. P. Royall, M. E. Leunissen, A.-P. Hynninen, M. Dijkstra, and A. van Blaaderen, "Re-entrant melting and freezing in a model system of charged colloids," *The Journal of Chemical Physics*, vol. 124, no. 24, 2006.

[144] S. A. Khrapak, B. A. Klumov, P. Huber, V. I. Molotkov, A. M. Lipaev, V. N. Naumkin, H. M. Thomas, A. V. Ivlev, G. E. Morfill, O. F. Petrov, V. E. Fortov, Y. Malentschenko, and S. Volkov, "Freezing and melting of 3d complex plasma structures under microgravity conditions driven by neutral gas pressure manipulation," *Physical Review Letters*, vol. 106, no. 20, p. 205001, 05 2011. [Online]. Available: https://link.aps.org/doi/10.1103/PhysRevLett.106.205001

[145] M. O. Robbins, K. Kremer, and G. S. Grest, "Phase diagram and dynamics of yukawa systems," *J. Chem. Phys*, vol. 88, pp. 3286–3312, 1987.

[146] S. Hamaguchi, R. T. Farouki, and D. H. E. Dubin, "Triple point of yukawa systems," *Phys. Rev. E*, vol. 56, pp. 4671–4682, 1997.

[147] S. Alexander, P. M. Chaikin, P. Grant, G. J. Morales, P. Pincus, and D. Hone, "Charge renormalisation, osmotic-pressure, and bulk modulus of colloidal crystals - theory," *J. Chem. Phys.*, vol. 80, pp. 5776–5781, 1984.

[148] E. Trizac, L. Bocquet, and M. Aubouy, "Simple approach for charge renormalization in highly charged macroions," *Phys. Rev. Lett.*, vol. 89, no. 24, p. 248301, 2002.

[149] K. Ito, H. Yoshida, and N. Ise, "Void structure in colloidal dispersions," *Science*, vol. 263, pp. 66–68, 1994.

[150] G. M. Kepler and S. Fraden, "Attractive potential between confined colloids at low ionic strength," *Phys. Rev. Lett.*, vol. 73, pp. 356–359, 1994.

[151] A. E. Larsen and D. G. Grier, "Like-charge attractions in metastable colloidal crystallites," *Nature*, vol. 385, pp. 230–233, 1997.

[152] Y. Han and D. G. Grier, "Confinement-induced colloidal attractions in equilibrium," *Phys. Rev. Lett.*, vol. 91, p. 038302, 2003.

[153] J. Baumgartl and C. Bechinger, "On the limits of digital video microscopy," *Europhys. Lett.*, vol. 71, pp. 487–493, 2005.

[154] J. Baumgartl, J. Arauz-Lara, and C. Bechinger, "Like-charge attraction in confinement: myth or truth?" *Soft Matter*, vol. 2, no. 8, pp. 631–635, 2006.

[155] R. van Roij and J. P. Hansen, "Van der waals-like instability in suspensions of mutually repelling charged colloids," *Phys. Rev. Lett.*, vol. 77, pp. 3082–3085, 1997.

[156] R. van Roij and J.-P. Dijkstra, M. aHansen, "Phase diagram of charge-stabilized colloidal suspensions: van der waals instability without attractive forces," *Phys. Rev. E*, vol. 59, pp. 2010–2025, 1998.

[157] A. Yethiraj and A. van Blaaderen, "A colloidal model system with an inteaction tunable from hard sphere to soft and dipolar," *Nature*, vol. 421, pp. 513–517, 2003.

[158] C. L. Klix, C. P. Royall, and H. Tanaka, "Structural and dynamical features of multiple metastable glassy states in a colloidal system with competing interactions," *Phys. Rev. Lett.*, vol. 104, p. 165702, 2010.

[159] E. B. Sirota, H. D. Ou-Yang, S. K. Sinha, P. M. Chaikin, J. D. Axe, and Y. Fujii, "Complete phase diagram of a charged colloidal system," *Phys. Rev. Lett.*, vol. 62, pp. 1524–1527, 1989.

[160] C. Desgranges and J. Delhommelle, "Polymorph selection during the crystallization of yukawa systems," *J. Chem. Phys.*, vol. 126, p. 144509, 2007.

[161] J. Nyvlt, "The ostwald rule of stages," *Cryst. Res. Technol.*, vol. 30, no. 4, pp. 443–449, 1995.

[162] T. Threlfall, "Structural and thermodynamic explanations of ostawld's rule," *Organic Process Research and Development*, vol. 7, pp. 1017–1027, 2003.

[163] F. Varrato, L. Di Michele, M. Belushkin, N. Dorsaz, S. H. Nathan, E. Eiser, and G. Foffi, "Arrested demixing opens route to bigels," *Proceedings of the National Academy of Sciences*, vol. 109, no. 47, p. 19155, 11 2012. [Online]. Available: http://www.pnas.org/content/109/47/19155.abstract

[164] B. Behera, S. S. Sagiri, K. Pal, K. Pramanik, U. A. Rana, I. Shakir, and A. Anis, "Sunflower oil and protein-based novel bigels as matrices for drug delivery applications—characterization and in vitro antimicrobial efficiency," *Polymer-Plastics Technology and Engineering*, vol. 54, no. 8, pp. 837–850, 06 2015. [Online]. Available: https://doi.org/10.1080/03602559.2014.974268

[165] A. Shakeel, F. R. Lupi, D. Gabriele, N. Baldino, and B. De Cindio, "Bigels: A unique class of materials for drug delivery applications," *Soft Materials*, vol. 16, no. 2, pp. 77–93, 04 2018. [Online]. Available: https://doi.org/10.1080/1539445X.2018.1424638

[166] E. Zaccarelli, "Colloidal gels: equilibrium and non-equilibrium routes," *Journal of Physics: Condensed Matter*, vol. 19, no. 32, p. 323101, 2007. [Online]. Available: http://stacks.iop.org/0953-8984/19/i=32/a=323101

[167] C. P. Royall, S. R. Williams, and H. Tanaka, "Vitrification and gelation in sticky spheres," *The Journal of Chemical Physics*, vol. 148, no. 4, p. 044501, 2018. [Online]. Available: https://doi.org/10.1063/1.5000263

[168] A. Blumlein and J. J. McManus, "Bigels formed via spinodal decomposition of unfolded protein," *Journal of Materials Chemistry B*, vol. 3, no. 17, pp. 3429–3435, 2015. [Online]. Available: http://dx.doi.org/10.1039/C5TB00131E

[169] V. Sing, D. Qureshi, S. Nayak, and K. Pal, *Polymeric Gels: Characterization, Properties and Biomedical Applications*, 1st ed., ser. Biomaterials. Woodhead Publishing, 2018, no. 10, ch. Bigels.

[170] J. P. Gong, Y. Katsuyama, T. Kurokawa, and Y. Osada, "Double-network hydrogels with extremely high mechanical strength," *Advanced Materials*, vol. 15, no. 14, pp. 1155–1158, 2003. [Online]. Available: https://doi.org/10.1002/adma.200304907

[171] Q. Lu, X. Wang, S. Lu, M. Li, D. L. Kaplan, and H. Zhu, "Nanofibrous architecture of silk fibroin scaffolds prepared with a mild self-assembly process," *Biomaterials*, vol. 32, no. 4, pp. 1059–1067, 2011. [Online]. Available: http://www.sciencedirect.com/science/article/pii/S0142961210012858

[172] X. Hu, P. Cebe, A. S. Weiss, F. Omenetto, and D. L. Kaplan, "Protein-based composite materials," *Materials Today*, vol. 15, no. 5, pp. 208–215, 2012. [Online]. Available: http://www.sciencedirect.com/science/article/pii/S1369702112700913

[173] A. Schloss, D. Williams, and L. Regan, *Protein-Based Hydrogels for Tissue Engineering. In: Protein-based Engineered Nanostructures*, ser. Advances in Experimental Medicine and Biology. Springer-Verlag, 2016, vol. 940, pp. 167–177.

[174] B. Sri. M, A. Vadithya, and A. Chatterjee, *As A Review on Hydrogels as Drug Delivery in the Pharmaceutical Field*, 2012, vol. 1.

[175] F. R. Lupi, L. Gentile, D. Gabriele, S. Mazzulla, N. Baldino, and B. de Cindio, "Olive oil and hyperthermal water bigels for cosmetic uses," *Journal of Colloid and Interface Science*, vol. 459, pp. 70–78, 2015. [Online]. Available: http://www.sciencedirect.com/science/article/pii/S0021979715301089

[176] L. Di Michele, F. Varrato, J. Kotar, S. H. Nathan, G. Foffi, and E. Eiser, "Multistep kinetic self-assembly of dna-coated colloids," *Nature Communications*, vol. 4, p. 2007, 06 2013. [Online]. Available: http://dx.doi.org/10.1038/ncomms3007

[177] I. Zhang, R. Pinchaipat, N. B. Wilding, M. A. Faers, P. Bartlett, R. Evans, and C. P. Royall, "Composition inversion in mixtures of binary colloids and polymer," *The Journal of Chemical Physics*, vol. 148, no. 18, p. 184902, 2018/07/20 2018. [Online]. Available: https://doi.org/10.1063/1.5023393

[178] J. Zhang, *Protein-Protein Interactions - Computational and Experimental Tools*. InTech, 2012, no. 18, ch. Protein-Protein Interactions in Salt Solutions, pp. 359–376.

[179] A. H. Elcock and J. A. McCammon, "Calculation of weak protein-protein interactions: The ph dependence of the second virial coefficient," *Biophysical Journal*, vol. 80, no. 2, pp. 613–625, 2001. [Online]. Available: http://www.sciencedirect.com/science/article/pii/S0006349501760420

[180] C. Gögelein, "Phase behaviour of proteins and colloid-polymer mixtures," Ph.D. dissertation, Dusseldorf University, 2008.

[181] J. Cai and A. M. Sweeney, "The proof is in the pidan: Generalizing proteins as patchy particles," *ACS Central Science*, vol. 4, no. 7, pp. 840–853, 07 2018. [Online]. Available: https://doi.org/10.1021/acscentsci.8b00187

[182] F. Zhang, M. W. A. Skoda, R. M. J. Jacobs, R. A. Martin, C. M. Martin, and F. Schreiber, "Protein interactions studied by saxs: Effect of ionic strength and protein concentration for bsa in aqueous solutions," *The Journal of Physical Chemistry B*, vol. 111, no. 1, pp. 251–259, 01 2007. [Online]. Available: https://doi.org/10.1021/jp0649955

[183] K. C. Duong-Ly, S. B. Gabelli, and J. Lorsch, *Chapter Seven - Salting out of Proteins Using Ammonium Sulfate Precipitation*. Academic Press, 2014, vol. 541, pp. 85–94. [Online]. Available: http://www.sciencedirect.com/science/article/pii/B9780124201194000070

[184] H. I. Okur, J. Hladílková, K. B. Rembert, Y. Cho, J. Heyda, J. Dzubiella, P. S. Cremer, and P. Jungwirth, "Beyond the hofmeister series: Ion-specific effects on proteins and their biological functions," *The Journal of Physical Chemistry B*, vol. 121, no. 9, pp. 1997–2014, 03 2017. [Online]. Available: https://doi.org/10.1021/acs.jpcb.6b10797

[185] P. T. Wingfield, "Protein precipitation using ammonium sulfate," *Current Protocols in Protein Science*, vol. Appendix 3, 2001. [Online]. Available: http://www.ncbi.nlm.nih.gov/pmc/articles/PMC4817497/

[186] S. N. Timasheff, *Solvent Stabilization of Protein Structure*. Totowa, NJ: Humana Press, 1995, pp. 253–269. [Online]. Available: https://doi.org/10.1385/0-89603-301-5:253

[187] Y. Kita, T. Arakawa, T.-Y. Lin, and S. N. Timasheff, "Contribution of the surface free energy perturbation to protein-solvent interactions," *Biochemistry*, vol. 33, no. 50, pp. 15 178–15 189, 12 1994. [Online]. Available: https://doi.org/10.1021/bi00254a029

[188] N. Schwierz, D. Horinek, U. Sivan, and R. R. Netz, "Reversed hofmeister series—the rule rather than the exception," *Current Opinion in Colloid & Interface Science*, vol. 23, pp. 10–18, 2016. [Online]. Available: http://www.sciencedirect.com/science/article/pii/S1359029416300474

[189] T. L. Blundell and J. A. Jenkins, "The binding of heavy metals to proteins," *Chemical Society Reviews*, vol. 6, no. 2, pp. 139–171, 1977. [Online]. Available: http://dx.doi.org/10.1039/CS9770600139

[190] F. Zhang, G. Zocher, A. Sauter, T. Stehle, and F. Schreiber, "Novel approach to controlled protein crystallization through ligandation of yttrium cations," *Journal of Applied Crystallography*, vol. 44, no. 4, pp. 755–762, 2011. [Online]. Available: https://doi.org/10.1107/S0021889811017997

[191] F. Zhang, F. Roosen-Runge, A. Sauter, M. Wolf, R. M. J. Jacobs, and F. Schreiber, "Reentrant condensation, liquid-liquid phase separation and crystallization in protein solutions induced by multivalent metal ions," *Pure and Applied Chemistry*, vol. 86, no. 2, pp. 191–202, 2014.

[192] Y. R. Sindarovska, Y. Sheludko, I. M. Gerasymenko, M. Bannikova, and N. Kuchuk, "Purification of recombinant gfp produced by agrobacterium-mediated transient expression in nicotiana excelsior," *Cytology and Genetics*, vol. 42, pp. 86–89, 04 2008.

[193] J. A. J. Arpino, P. J. Rizkallah, and D. D. Jones, "Crystal structure of enhanced green fluorescent protein to 1.35 å resolution reveals alternative conformations for glu222," *PLoS ONE*, vol. 7, no. 10, p. e47132, 2012. [Online]. Available: http://www.ncbi.nlm.nih.gov/pmc/articles/PMC3473056/

[194] D. W. Piston, R. E. Campbell, R. N. Day, and M. W. Davidson. (2018, June) Anthozoa fluorescent proteins. [Online]. Available: http://zeiss-campus.magnet.fsu.edu/articles/probes/anthozoafps.html

[195] M. Ries-Kautt and A. Ducruix, "Relative effectiveness of various ions on the solubility and crystal growth of lysozyme," *The Journal of Biological Chemistry*, vol. 264, no. 2, pp. 745–748, 1989.

[196] A. V. Yakhnin, L. M. Vinokurov, A. K. Surin, and Y. B. Alakhov, "Green fluorescent protein purification by organic extraction," *Protein Expression and Purification*, vol. 14, no. 3, pp. 382–386, 1998. [Online]. Available: http://www.sciencedirect.com/science/article/pii/S1046592898909810

[197] L. Ianeselli, F. Zhang, M. W. A. Skoda, R. M. J. Jacobs, R. A. Martin, S. Callow, S. Prévost, and F. Schreiber, "Protein,àí-protein interactions in ovalbumin solutions studied by small-angle scattering: Effect of ionic strength and the chemical nature of cations," *The Journal of Physical Chemistry B*, vol. 114, no. 11, pp. 3776–3783, 2010. [Online]. Available: https://doi.org/10.1021/jp9112156

[198] F. Roosen-Runge, B. S. Heck, F. Zhang, O. Kohlbacher, and F. Schreiber, "Interplay of ph and binding of multivalent metal ions: Charge inversion and reentrant condensation in protein solutions," *The Journal of Physical Chemistry B*, vol. 117, no. 18, pp. 5777–5787, 05 2013. [Online]. Available: https://doi.org/10.1021/jp401874t

[199] E. Jordan, F. Roosen-Runge, S. Leibfarth, F. Zhang, M. Sztucki, A. Hildebrandt, O. Kohlbacher, and F. Schreiber, "Competing salt effects on phase behavior of protein solutions: Tailoring of protein interaction by the binding of multivalent ions and charge screening," *The Journal of Physical Chemistry B*, vol. 118, no. 38, pp. 11 365–11 374, 09 2014. [Online]. Available: https://doi.org/10.1021/jp5058622

[200] G. P. Doherty, K. Bailey, and P. J. Lewis, "Stage-specific fluorescence intensity of gfp and mcherry during sporulation in bacillus subtilis," *BMC Research Notes*, vol. 3, pp. 303–303, 2010. [Online]. Available: http://www.ncbi.nlm.nih.gov/pmc/articles/PMC2994887/

[201] J. Futami, M. Kitazoe, T. Maeda, E. Nukui, M. Sakaguchi, J. Kosaka, M. Miyazaki, M. Kosaka, H. Tada, M. Seno, J. Sasaki, N.-H. Huh, M. Namba, and H. Yamada, "Intracellular delivery of proteins into mammalian living cells by polyethylenimine-cationization," *Journal of Bioscience and Bioengineering*, vol. 99, no. 2, pp. 95–103, 2005. [Online]. Available: http://www.sciencedirect.com/science/article/pii/S138917230570339X

[202] N. Nakajima and Y. Ikada, "Mechanism of amide formation by carbodiimide for bioconjugation in aqueous media," *Bioconjugate Chemistry*, vol. 6, no. 1, pp. 123–130, 01 1995. [Online]. Available: https://doi.org/10.1021/bc00031a015

[203] K. A. Totaro, X. Liao, K. Bhattacharya, J. I. Finneman, J. B. Sperry, M. A. Massa, J. Thorn, S. V. Ho, and B. L. Pentelute, "Systematic investigation of edc/snhs-mediated bioconjugation reactions for carboxylated peptide substrates," *Bioconjugate Chemistry*, vol. 27, no. 4, pp. 994–1004, 04 2016. [Online]. Available: https://doi.org/10.1021/acs.bioconjchem.6b00043

[204] T. Konno, "Amyloid-induced aggregation and precipitation of soluble proteins: An electrostatic contribution of the alzheimer's beta(25–35) amyloid fibril," *Biochemistry*, vol. 40, no. 7, pp. 2148–2154, 02 2001. [Online]. Available: https://doi.org/10.1021/bi002156h

[205] E. M. Ahmed, "Hydrogel: Preparation, characterization, and applications: A review," *Journal of Advanced Research*, vol. 6, no. 2, pp. 105–121, 2015. [Online]. Available: http://www.sciencedirect.com/science/article/pii/S2090123213000969

[206] W. Wu, Z. Wu, T. Yu, C. Jiang, and W.-S. Kim, "Recent progress on magnetic iron oxide nanoparticles: synthesis, surface functional strategies and biomedical applications,"

Science and Technology of Advanced Materials, vol. 16, no. 2, p. 023501, 04 2015. [Online]. Available: https://doi.org/10.1088/1468-6996/16/2/023501

[207] C. Jiang, C. W. Leung, and P. W. T. Pong, "Magnetic-field-assisted assembly of anisotropic superstructures by iron oxide nanoparticles and their enhanced magnetism," *Nanoscale Research Letters*, vol. 11, no. 1, p. 189, 2016. [Online]. Available: https://doi.org/10.1186/s11671-016-1406-9

[208] K. Cheng, Q. Chen, Z. Wu, M. Wang, and H. Wang, "Colloids of superparamagnetic shell: synthesis and self-assembly into 3d colloidal crystals with anomalous optical properties," *CrystEngComm*, vol. 13, no. 17, pp. 5394–5400, 2011. [Online]. Available: http://dx.doi.org/10.1039/C0CE00825G

[209] P. Camargo, Z. Li, and Y. Xia, "Colloidal building blocks with potential for magnetically configurable photonic crystals," *Soft Matter*, vol. 3, no. 10, pp. 1215–1222, 2007.

[210] T. Hyeon, "Chemical synthesis of magnetic nanoparticles," *Chemical Communications*, no. 8, pp. 927–934, 2003. [Online]. Available: http://dx.doi.org/10.1039/B207789B

[211] E. A. Campos, D. V. B. S. Pinto, J. A. I. S. d. Oliveira, E. d. C. Mattos, and R. d. C. A. L. Dutra, "Synthesis, characterization and applications of iron oxide nanoparticles - a short review," *Journal of Aerospace Technology and Management*, vol. 7, pp. 267 – 276, 09 2015. [Online]. Available: http://www.scielo.br/scielo.php?script=sci_arttext&pid=S2175-91462015000300267&nrm=iso

[212] A. K. Gupta and M. Gupta, "Synthesis and surface engineering of iron oxide nanoparticles for biomedical applications," *Biomaterials*, vol. 26, no. 18, pp. 3995–4021, 2005. [Online]. Available: http://www.sciencedirect.com/science/article/pii/S0142961204009317

[213] W. Wu, Q. He, and C. Jiang, "Magnetic iron oxide nanoparticles: Synthesis and surface functionalization strategies," *Nanoscale Research Letters*, vol. 3, no. 11, p. 397, 2008. [Online]. Available: https://doi.org/10.1007/s11671-008-9174-9

[214] J. Kudr, Y. Haddad, L. Richtera, Z. Heger, M. Cernak, V. Adam, and O. Zitka, "Magnetic nanoparticles: From design and synthesis to real world applications," *Nanomaterials*, vol. 7, no. 9, p. 243, 09 2017. [Online]. Available: http://www.ncbi.nlm.nih.gov/pmc/articles/PMC5618354/

[215] J. Park, K. An, Y. Hwang, J.-G. Park, H.-J. Noh, J.-Y. Kim, J.-H. Park, N.-M. Hwang, and T. Hyeon, "Ultra-large-scale syntheses of monodisperse nanocrystals," *Nature Materials*, vol. 3, p. 891, 11 2004. [Online]. Available: http://dx.doi.org/10.1038/nmat1251

[216] S. Kyeong, C. Jeong, H. Kang, H.-J. Cho, S.-J. Park, J.-K. Yang, S. Kim, H.-M. Kim, B.-H. Jun, and Y.-S. Lee, "Double-layer magnetic nanoparticle-embedded silica particles for efficient bio-separation," *PLOS ONE*, vol. 10, no. 11, pp. e0 143 727–, 11 2015. [Online]. Available: https://doi.org/10.1371/journal.pone.0143727

[217] J. E. Lee, N. Lee, H. Kim, J. Kim, S. H. Choi, J. H. Kim, T. Kim, I. C. Song, S. P. Park, W. K. Moon, and T. Hyeon, "Uniform mesoporous dye-doped silica nanoparticles decorated with multiple magnetite nanocrystals for simultaneous enhanced magnetic resonance imaging, fluorescence imaging, and drug delivery," *Journal of the American Chemical Society*, vol. 132, no. 2, pp. 552–557, 01 2010. [Online]. Available: https://doi.org/10.1021/ja905793q

[218] Q. Zhang, T. Zhang, J. Ge, and Y. Yin, "Permeable silica shell through surface-protected etching," *Nano Letters*, vol. 8, no. 9, pp. 2867–2871, 09 2008. [Online]. Available: https://doi.org/10.1021/nl8016187

[219] L. M. Liz-Marzán, M. Giersig, and P. Mulvaney, "Synthesis of nanosized gold,àísilica core,àíshell particles," *Langmuir*, vol. 12, no. 18, pp. 4329–4335, 01 1996. [Online]. Available: https://doi.org/10.1021/la9601871

[220] R. Hufschmid, H. Arami, R. M. Ferguson, M. Gonzales, E. Teeman, L. N. Brush, N. D. Browning, and K. M. Krishnan, "Synthesis of phase-pure and monodisperse iron oxide nanoparticles by thermal decomposition," *Nanoscale*, vol. 7, no. 25, pp. 11 142–11 154, 07 2015. [Online]. Available: http://www.ncbi.nlm.nih.gov/pmc/articles/PMC5198837/

[221] M. Lattuada and T. A. Hatton, "Functionalization of monodisperse magnetic nanoparticles," *Langmuir*, vol. 23, no. 4, pp. 2158–2168, 02 2007. [Online]. Available: https://doi.org/10.1021/la062092x

[222] M. T. Swihart, *Nanothecnology in Biology and Medicine. Methods, Devices and Applications*. Taylor & Francis, 2007, no. 4, ch. Silicaon Nanoparticles for Biophotonics.

[223] A. Johnson, *Invitation to Organic Chemistry*. Jones and Bartlett Publishers, 1999.

[224] C. Graf, D. L. J. Vossen, A. Imhof, and A. van Blaaderen, "A general method to coat colloidal particles with silica," *Langmuir*, vol. 19, no. 17, pp. 6693–6700, 08 2003. [Online]. Available: https://doi.org/10.1021/la0347859

[225] R. Xie, C. Wang, L. Xia, H. Wang, T. Zhao, and Y. Sun, "Controlled preparation of co3o4 porous-sio2 nanocomposites for fischer–tropsch synthesis," *Catalysis Letters*, vol. 144, no. 3, pp. 516–523, 2014. [Online]. Available: https://doi.org/10.1007/s10562-013-1187-z

[226] J.-H. So, W.-K. Oh, and S.-M. Yang, "Microstructure and phase behavior of concentrated silica particle suspensions," *Korean Journal of Chemical Engineering*, vol. 21, no. 5, pp. 921–928, 2004. [Online]. Available: https://doi.org/10.1007/BF02705572

[227] A. P. Philipse and A. Vrij, "Preparation and properties of nonaqueous model dispersions of chemically modified, charged silica spheres," *Journal of Colloid and Interface Science*, vol. 128, no. 1, pp. 121–136, 1989. [Online]. Available: http://www.sciencedirect.com/science/article/pii/0021979789903913